

MAGNETOM Flash

The Magazine of MR

Issue Number 1/2011

ISMRM Edition

Not for distribution in the US.

SIEMENS

Technology

Towards Clinical 7T MRI
Page 32

Clinical

MRI of the Lung
Page 6

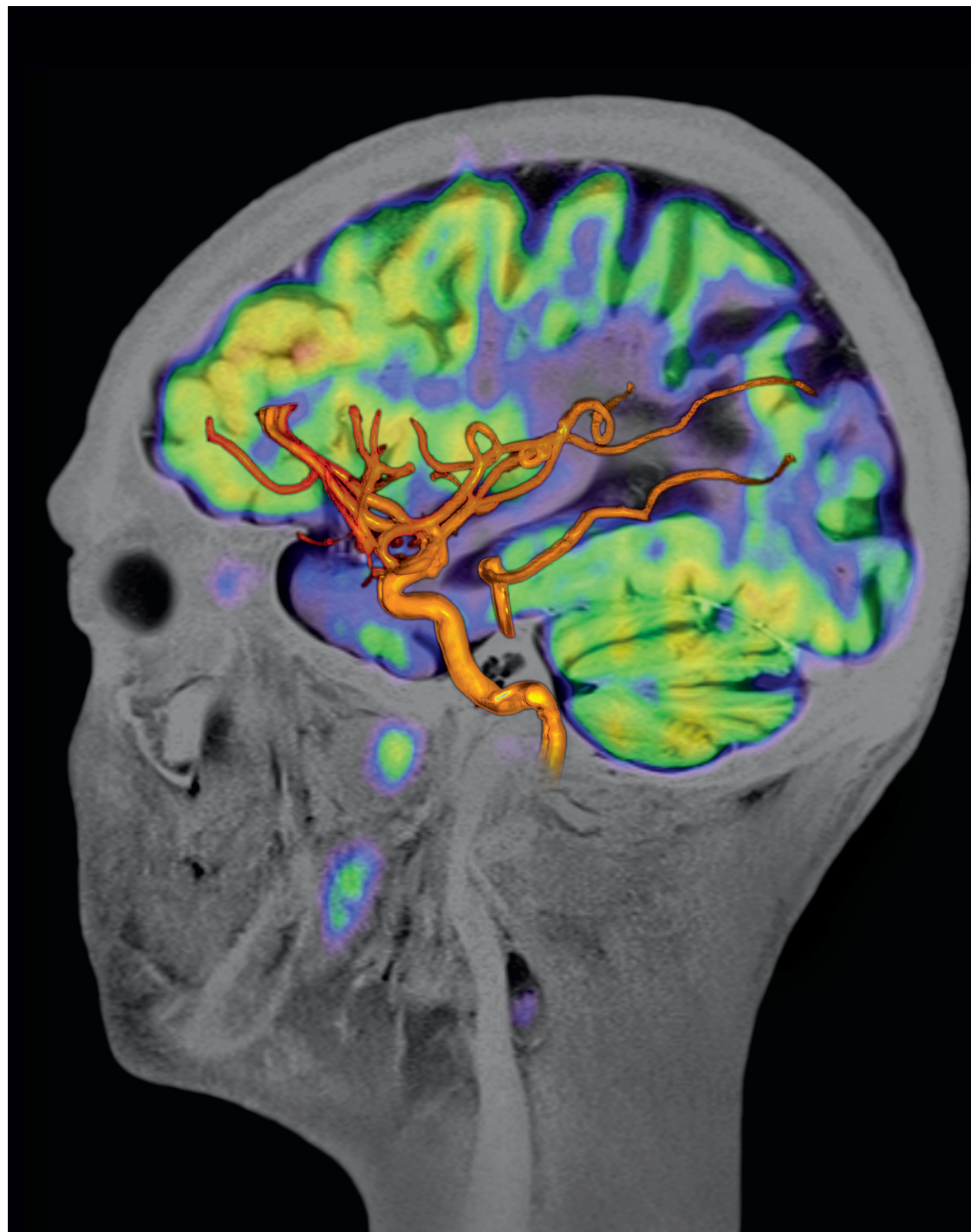
MAGNETOM Skyra: The
Mannheim Perspective
Page 24

Snowboarding Injuries
to the Middle Subtalar
Joint
Page 60

Integrated Whole-Body
MR/PET Imaging
Page 102

How I do it

FAQs on Diffusion-
Weighted Imaging
Page 84



Matthias Lichy, MD



Dear MAGNETOM user,

Technology is fascinating because of its potential to offer solutions to our daily problems.

Imaging technologies, however, face challenges from several factors such as speed, availability in clinical routine and even patient comfort. Some of these challenges have meant that in the last century positron-emission tomography (PET) was a rarely applied technology in a clinical setting; it proved time-consuming and without the potential to provide important information about anatomy and therefore about, for example, therapy-induced side-effects like thrombosis or pneumonia.

However, by integrating the anatomical information derived from computed tomography (CT) with PET, we acquire much more diagnostic information than would be available by applying these components individually. This combination also overcomes some limitations of a pure PET exam by integrating CT data for PET attenuation correction, which significantly reduces examination time. Today PET/CT is recognized as an imaging technique which can answer clinically relevant questions in multiple scenarios such as lung cancer; it clearly improves patient care and also, indirectly, therapy outcome.

In its first days, magnetic resonance imaging (MRI) was recognized mainly for providing best soft tissue contrast. But it was already known that MRI could do more than providing detailed anatomical information about,

for example, biochemical processes through the use of MR spectroscopy. With the inventions such as MR contrast-media, together with the refinement of sequence techniques, MRI is nowadays able to provide both qualitative and quantitative functional information about perfusion and diffusion, as well as motion, such as cardiac wall motion and ejection volume.

Further developments in therapy have, however, triggered new questions from clinicians. Multimodality MRI already plays an important role in understanding disease biology in daily routine. But to provide further, deeper insight into metabolism such as glucose consumption or amino acid synthesis and several functional aspects of tissue like oxygenation or receptor expression, PET is still the imaging modality of choice because of its intrinsic high sensitivity to the probes used within picomolar range.

Of course, some information derived from PET and MRI will be interdependent, ranging from complimentary to contradictory. Thanks to Biograph mMR, we can now combine MRI and PET into one easy-to-handle system and obtain understanding of aspects of the biology of diseases at a single point in time.

Matthias Lichy, MD

Editorial Board

We appreciate your comments.

Please contact us at magnetomworld.med@siemens.com



Antje Hellwich
Associate Editor



Wellesley Were
MR Business Development
Manager Australia and New
Zealand



Dr. Sunil Kumar S.L.
Senior Manager Applications,
Canada



Christiane Bernhardt
Head Outbound Marketing
Erlangen, Germany



Milind Dhamankar, MD
Sr. Director, MR Product
Marketing, Malvern, PA, USA



Michelle Kessler
US Installed Base Manager
Malvern, PA, USA



Gary R. McNeal, MS (BME)
Advanced Application Specialist,
Cardiovascular MR Imaging
Hoffman Estates, IL, USA



Peter Kreisler, PhD
Collaborations & Applications,
Erlangen, Germany

Review Board

Okan **Ekinci**, MD, Center of Clinical Competence – Cardiology

Jens-Christoph **Georgi**, PhD, Global Marketing Manager Biograph mMR

Christian **Geppert**, PhD, Application Development Breast Applications

Wilhelm **Horger**, Application Development Oncology

Jürgen **Kampmeier**, PhD, MR/PET

Berthold **Kiefer**, PhD, Oncological and Interventional Applications

Lars **Lauer**, PhD, Orthopedic Applications

Heiko **Meyer**, PhD, Neuro Applications

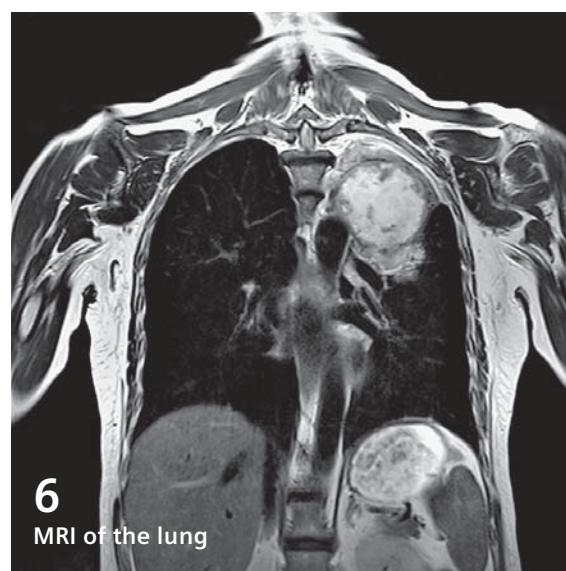
Edgar **Müller**, Cardiovascular Applications

Silke **Quick**, Global Marketing Manager Women's Health

Ignacio **Vallines**, PhD, Global Marketing Manager Neurology and Orthopedics

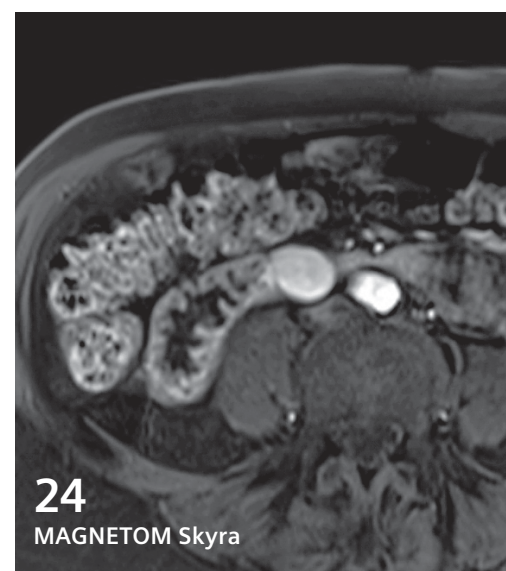
Heike **Weh**, Clinical Data Manager

Content



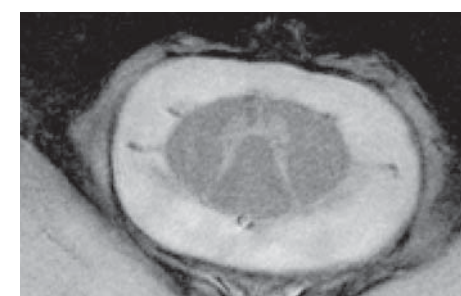
6

MRI of the lung



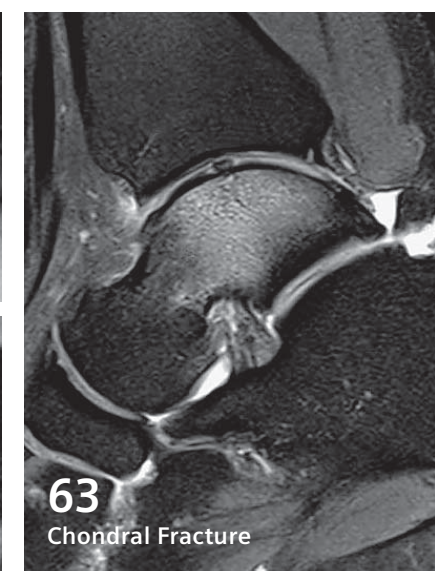
24

MAGNETOM Skyra



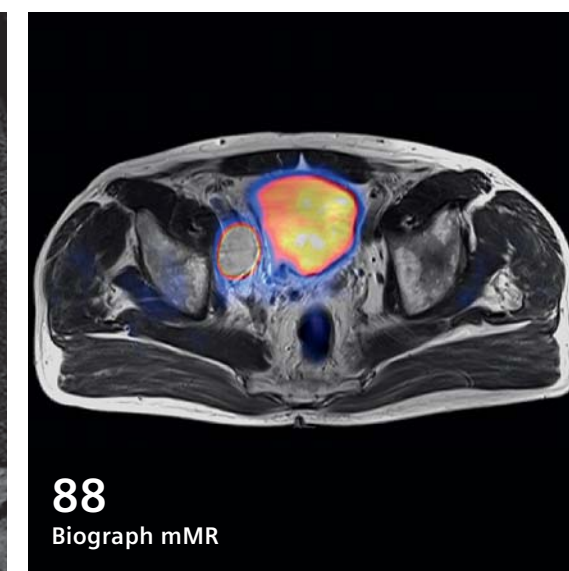
32

7T MRI



63

Chondral Fracture



88

Biograph mMR

Further information

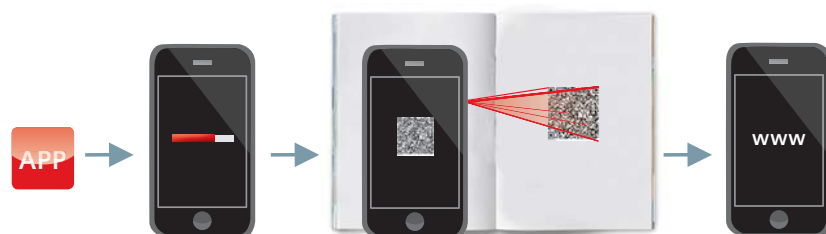


MAGNETOM_World

→ The Quick Response (QR) codes in this issue link you with external resources and offer further information on the subject. Dig in.

...that's how it works

- You need an iPhone (3GS or higher) or a Smartphone using Android. We recommend a mobile with a camera using at least 2 Megapixel.
- Install a code reader application on your device (there are a number of code readers downloadable e.g. at i-nigma).
- Start the code reader application on your device, point and shoot the camera at the mobile code.
- After scanning it with your camera phone, you will have instant access to the encoded information straight on the display of your mobile device. Enjoy the content.



Clinical Lung Imaging

- 6 MRI of the Lung – ready ... get set ... go!
Juergen Biederer, et al.
- 16 Case Report: Lung Imaging with MRI
Juergen Biederer

Clinical

- 24 MAGNETOM Skyra: The Mannheim Perspective
Henrik J. Michaely, Stefan O. Schoenberg

Technology

- 32 Towards Clinical 7T MRI
Graham C. Wiggins, Daniel K. Sodickson

Technology Neuro

- 50 MRI-Based Pattern Recognition Methods for Dementia Diagnostics
Stefan Klöppel

Clinical Woman's Health

- 54 STIR versus SPAIR in Breast Imaging: a Case-Based Discussion
Yien Sien Lee, et al.

Technology

- 56 Fat Suppression Techniques – a Short Overview
Wilhelm Horger, Berthold Kiefer

Clinical MSK

- 60 Case Report: Snowboarding Injuries to the Middle Subtalar Joint. The Sustentacular Talocalcaneal Articulation
Anna K. Chacko, Charles P. Ho
- 63 Case Report: Chondral Fracture of the Talar Dome and Diastasis of the Os Trigonum
Anna K. Chacko, Charles P. Ho

How I do it

- 66 Long Bone Imaging Distal Lower Limbs utilizing Tim Technology and the Tim User Interface
James Hancock
- 75 Long Bone Imaging Proximal Lower Limbs utilizing Tim Technology and the Tim User Interface
James Hancock
- 84 Frequently Asked Questions: Diffusion-Weighted Imaging
Joachim Graessner

Product News

- 88 Whole-Body MR/PET Hybrid Imaging: Technical Considerations, Clinical Workflow, and Initial Results
Harald H. Quick, et al.

Clinical mMR

- 102 Integrated Whole Body MR/PET Imaging. First Examples of Clinical Application
Alexander Drzezga, et al.

Life

- 112 Clinical Perspective of the 7th MAGNETOM World Summit
Matthias P. Lichy.

Cover

- 115 Simultaneous MR/PET Examination
Nina Schwenzer

The information presented in MAGNETOM Flash is for illustration only and is not intended to be relied upon by the reader for instruction as to the practice of medicine. Any health care practitioner reading this information is reminded that they must use their own learning, training and expertise in dealing with their individual patients. This material does not substitute for that duty and is not intended by Siemens Medical Solutions to be used for any purpose in that regard. The treating physician bears the sole responsibility for the diagnosis and treatment of patients, including drugs and doses prescribed in connection with such use. The Operating Instructions must always be strictly followed when operating the MR System. The source for the technical data is the corresponding data sheets.

MRI of the Lung – ready... get set ... go!

J. Biederer¹; C. Hintze¹; M. Fabel¹; P. M. Jakob²; W. Horger³; J. Graessner³; B.D. Bolster, Jr.³; M. Heller¹

¹University Hospital Schleswig-Holstein, Campus Kiel, Department of Diagnostic Radiology, Kiel, Germany

²University of Wuerzburg, Department of Experimental Physics 5 and Magnetic Resonance Bavaria e.V., Wuerzburg, Germany

³Siemens AG, Healthcare

Introduction

Magnetic resonance imaging (MRI) of the lung is a powerful evolving tool for scientific and clinical application. The key technique for MRI of lung morphology is based on resonant high-frequency signal of protons in tissues and liquids, so-called Proton- or ¹H-MRI. Empowered by recent technical advances, MRI has challenged its well-known limitations as defined by the low proton density in the lung and the fast signal decay due to susceptibility artifacts at air-tissue inter-

faces. The new modality in chest imaging is much appreciated, even in spite of the excellent performance of modern multiple row detector computed tomography (CT) scanners and the far lower price of X-ray. Being superior to X-ray and matching CT in detection of nodular and infiltrative lung disease, offering additional functional imaging capacities and all this without radiation exposure to the patient, lung MRI has become a valuable method for examinations in

children and during pregnancy, for young patients with diseases which warrant frequent follow-up examinations or for any other application that would need to avoid radiation exposure, such as scientific studies, commercial clinical trials (therapy control) or assessment of patients for legal medical opinions.

Clinical method

Fast sequences, preferably for breath-hold imaging with reasonably high spa-

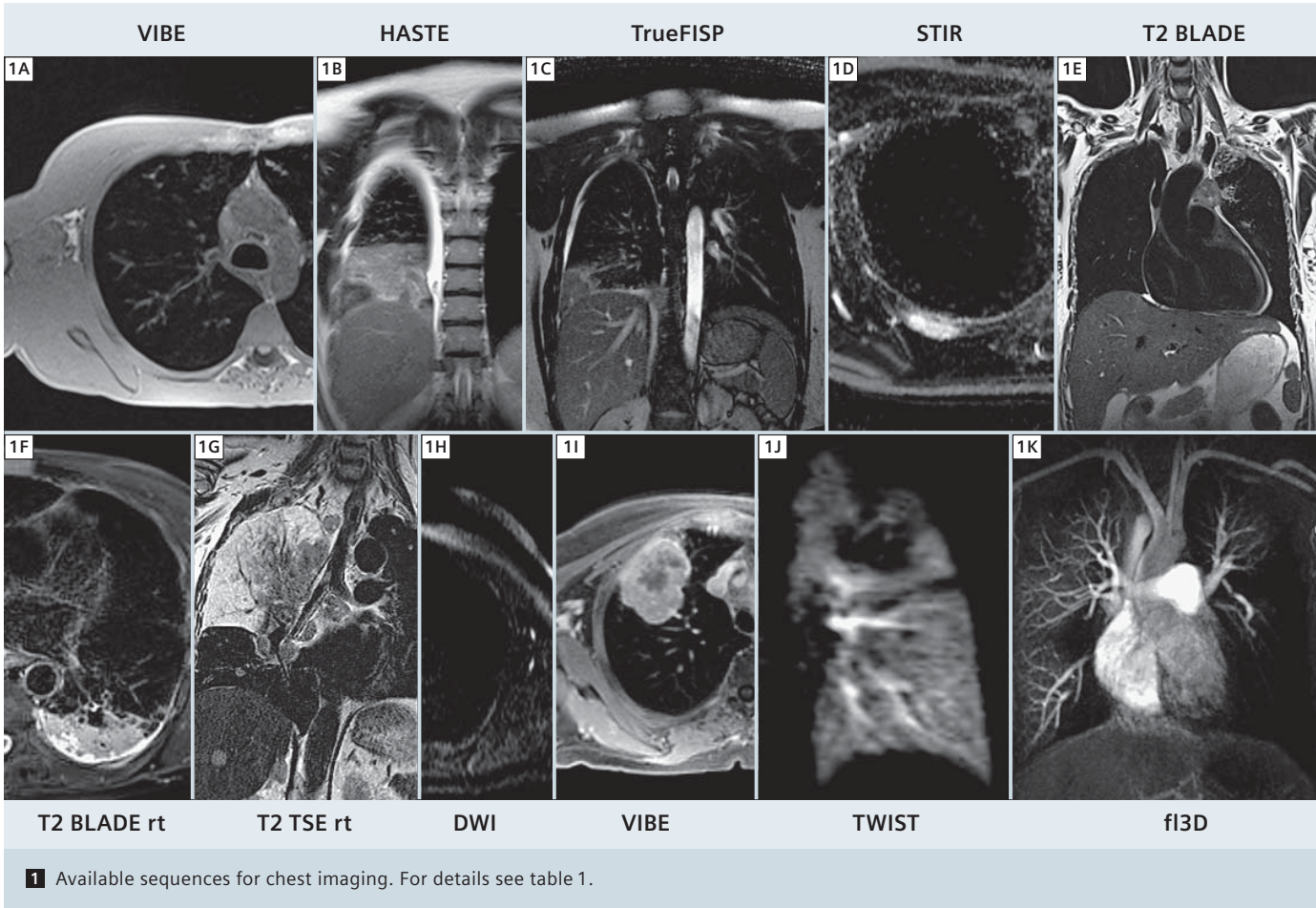


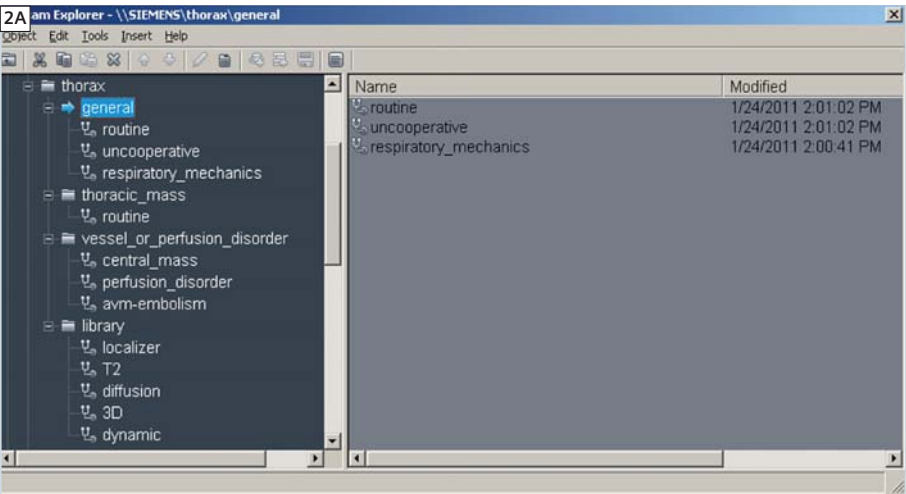
Table 1: Sequences for lung MRI						
Sequence	Key pathology	Respiration manoeuvre	Spatial resolution	Temporal resolution	1.5T	3T
VIBE	pulmonary nodules	breathhold	high	low	+	+
HASTE	infiltrates	breathhold	low	high	+	+
TrueFISP	pulmonary embolism	free breathing	moderate	high	+	(–)
STIR or T2 BLADE fs	lymph nodes bone metastases	multiple breathholds	moderate	low	+	+
T2 BLADE	nodules and masses	multiple breathholds	moderate	moderate	+	+
T2 BLADE rt* T2 TSE rt*	masses	free breathing	moderate-high	low	+	+
DWI	nodules and masses	multiple breathholds	low	low	+	+
TWIST	perfusion deficit	breathhold	low	high	++	+
fl 3D	embolism AVM	breathhold	high	low	+	++

*rt = respiratory triggered

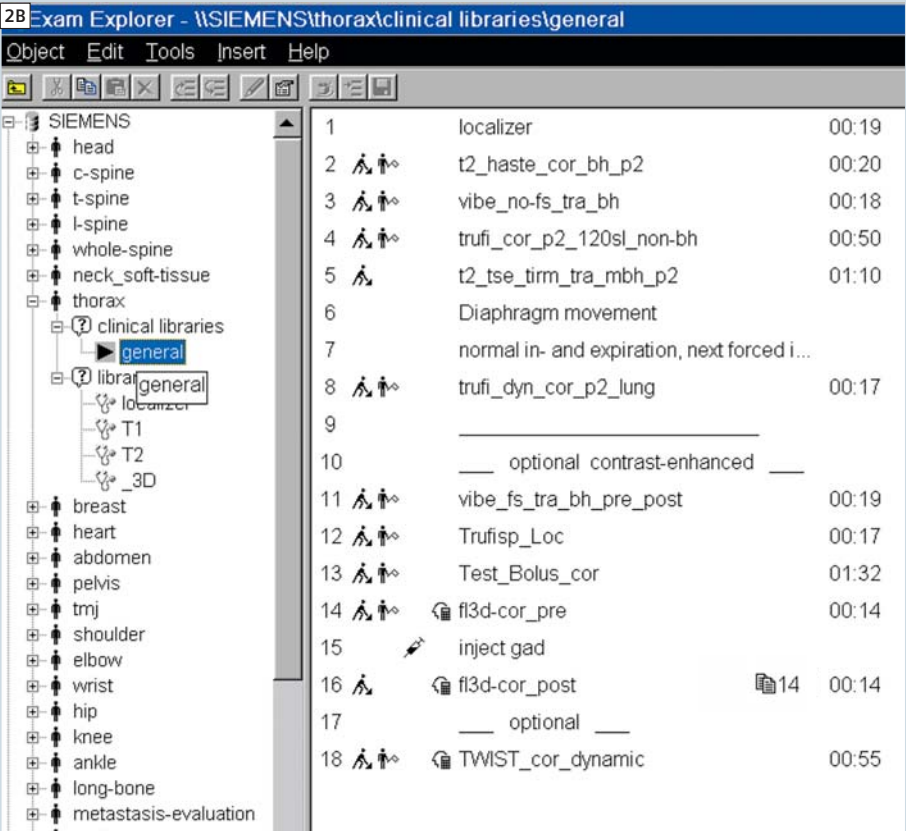
tial resolution and short echo time (TE), able to receive as much lung signal as possible within the short interval before signal decay are a technical challenge for both, hardware and sequence design [1]. Combining fast breathhold acquisitions with parallel imaging (iPAT = integrated Parallel Acquisition Techniques), high temporal resolution MR angiography (TWIST = time-resolved angiography with stochastic trajectories) rotating phase encoding (BLADE) and Navigator technology (PACE = prospective acquisition correction), lung MRI has become a fairly robust technique for broad clinical application [2]. Nowadays, the Siemens MAGNETOM user can select from a ‘buffet’ of protocols that have been optimized for imaging lung diseases (Fig. 1). A quick summary of the specific properties of the sequences is listed in Table 1. Suggested complete push-button

protocols for specific pathologies are arranged in a protocol list at the scanner and are practically ready to go. Figure 2A shows the improved protocol tree with syngo MR D11D. Figure 2B gives a list of protocols that are implemented with software version syngo MR B17. The packages cover different aspects of lung pathology, from general purpose, to specific sequence combinations for imaging thoracic masses and high resolution angiography, to functional imaging with dynamic first pass lung perfusion imaging. The rationale for the protocol suggestion was to combine different sequence techniques to cover different weighting (T1, T2, balanced T1/T2), to appreciate the particular strengths of different techniques, to cover all planes in at least one acquisition and to have diagnostic quality in at least 3/5 series in the worst case

(e.g. uncooperative patient). Room times from 15 minutes for a basic protocol, 20 minutes for a contrast-enhanced study, to up to 30 minutes for a comprehensive study including perfusion imaging, angiography and post-contrast volumetric imaging are adjusted to the needs of clinical workflow. Alternatives for patients who have difficulties holding their breath are offered. Free breathing real time imaging with TrueFISP and navigator-triggered acquisitions with BLADE T2-TSE allow for excellent image quality even in non-compliant patients. For practical reasons, it is not needed to use ECG-triggering and the non-contrast enhanced basic protocol covers most clinical questions. Robustness against cardiac pulsation and respiratory motion is achieved by short acquisition time and (multi-)breathhold-imaging or respiratory triggering.



2A Protocol trees for chest imaging in the Exam Explorer window.

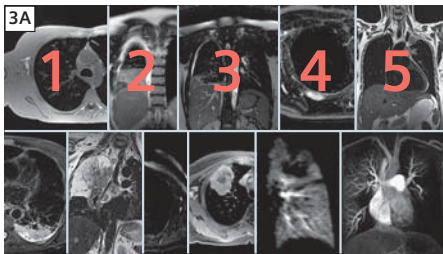


2B Chest imaging protocols as already installed with syngo MR B17.

‘General’ – the lung imaging protocol for general purposes

The first branch of the protocol tree contains a package for general purposes (Fig. 3). It will be used for most lung pathologies and large parts of it are integrated into the other protocol branches. The non-contrast-enhanced ‘**General Routine**’ protocol (in-room time 15 min) comprises a coronal T2-weighted HASTE (T2w single-shot half-Fourier TSE) sequence with a high sensitivity for infiltrates and a transversal VIBE (T1w 3D-GRE) sequence with a high sensitivity for small nodular lesions (in particular the contrast-enhanced, fat saturated VIBE). Both are acquired in a single breathhold. This is followed by a coronal steady-state free precession sequence (TrueFISP) in free breathing. This sequence adds functional information on pulmonary motion during the respiratory cycle and heart function. Size, shape and patency of the central pulmonary vessels can be assessed. This part of the protocol is highly sensitive for central pulmonary embolism and gross cardiac or respiratory dysfunction [3]. A further advantage is the excellent robustness to motion. Despite potential susceptibility and off resonance artifacts the morphologic quality in lung imaging challenges the image quality of other parts of the protocol, e.g. of the VIBE sequence. A motion-compensated coronal BLADE (multi-breathhold T2w TSE) is added to improve depiction of masses with chest wall invasion and mediastinal pathology such as masses, lymph nodes or cysts (Fig. 4).

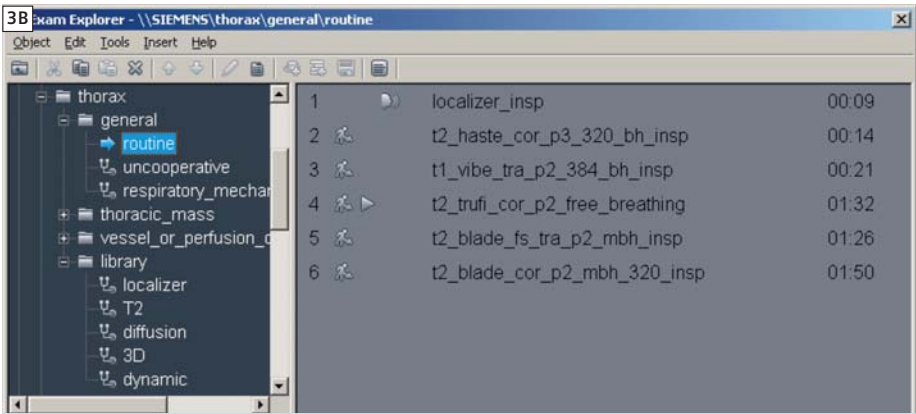
The protocol variant ‘**Respiratory Mechanics**’ includes an additional coronal series to be placed on top of the diaphragm and acquired during instructed breathing with a temporal resolution of 3 images per second. This can be used for specific questions such as diaphragmatic palsy or lung tumor motion, e.g. to detect attachment and infiltration of a lesion to the chest wall. A final multi-breathhold transversal fat-saturated T2w TSE visualizes enlarged lymph nodes and skeletal lesions.



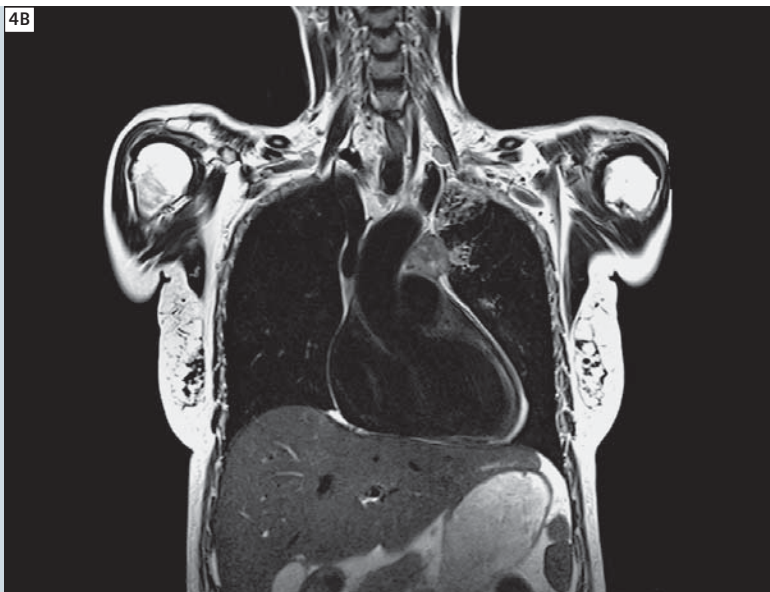
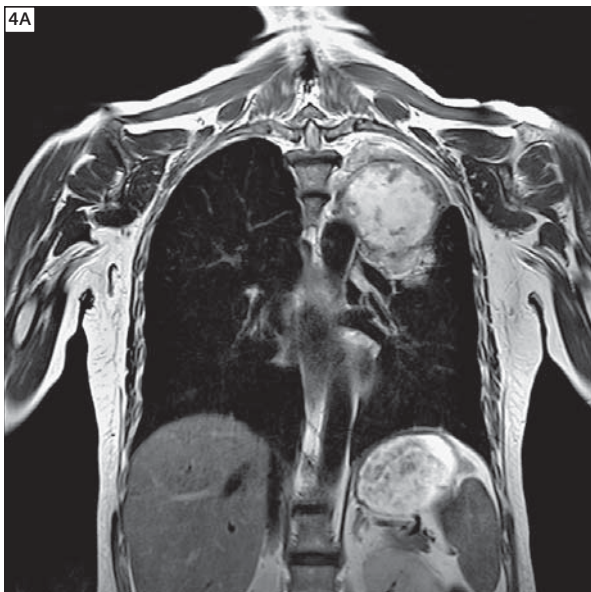
3A Selection of sequences for a ‘General-Routine’ protocol from the list offered in Fig. 1 and Tab. 1.

1: T1w VIBE, 2: T2w HASTE, 3: TrueFISP, 4: STIR or T2 BLADE fs, 5: T2 BLADE

In-room time 15 minutes



3B Detail of the protocol tree for general lung examinations.

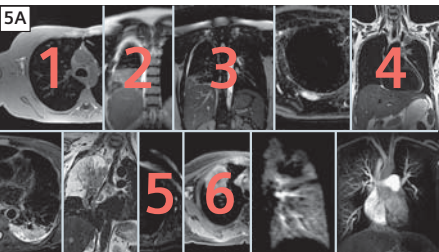


4 Coronal multi-breathhold T2 BLADE acquisition in a patient with a large lung cancer in the left upper lobe and mediastinal lymph node metastases.

The protocol variation ‘**Uncooperative**’ (to be used for patients who have difficulties holding their breath) comprises respiration-triggered versions of the T2-weighted TSE sequences (BLADE). Their application increases the total in-room time by approx. 10 minutes. This non-contrast enhanced ‘**General-Routine**’ study covers the majority of clinical indications: Pneumonia, atelectasis, pulmonary nodules and masses, mediastinal masses (lymphoma, goiter, cyst, thymoma), phrenic nerve palsy, cystic fibrosis, tuberculosis, interstitial

lung disease, acute pulmonary embolism. Detection rates for pulmonary infiltrates with the basic protocol match CT and make MRI a valuable alternative in particular for children, young patients and pregnant women. The sensitivity for lung nodules reaches 80–90% for lesions >4 mm (100% for >8 mm). Both capacities are appreciated in follow-up studies of cystic fibrosis patients using dedicated scores for the extent of disease. In lung cancer patients, MRI contributes to staging and atelectasis. Administration of contrast material contributes to detect

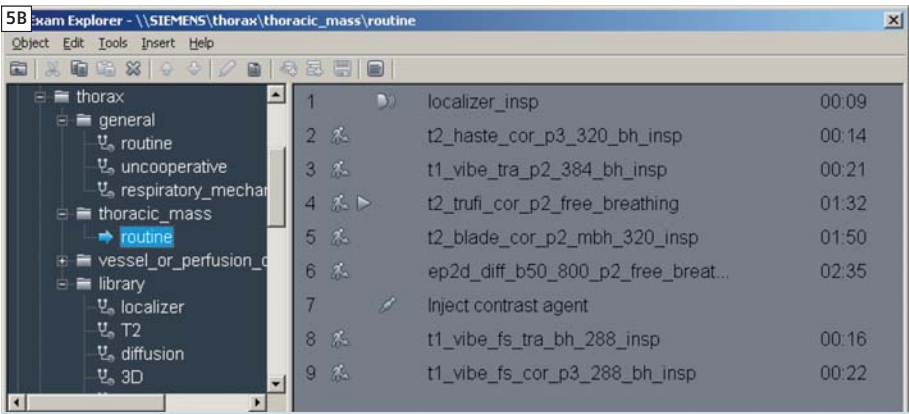
tumor necrosis, chest wall or mediastinal invasion and pleural reaction/carcinosis. In many cases the further assessment of an unclear pulmonary or mediastinal mass, a pleural effusion of unclear origin or pulmonary embolism will warrant further contrast enhanced protocol elements. This is covered with the protocol branch ‘**Thoracic Mass**’ which comprises the basic protocol plus additional contrast-enhanced fat-saturated breathhold-VIBE sequences (3D GRE) in transverse and coronal orientations. To cut down on imaging time, the transverse fat-sat-



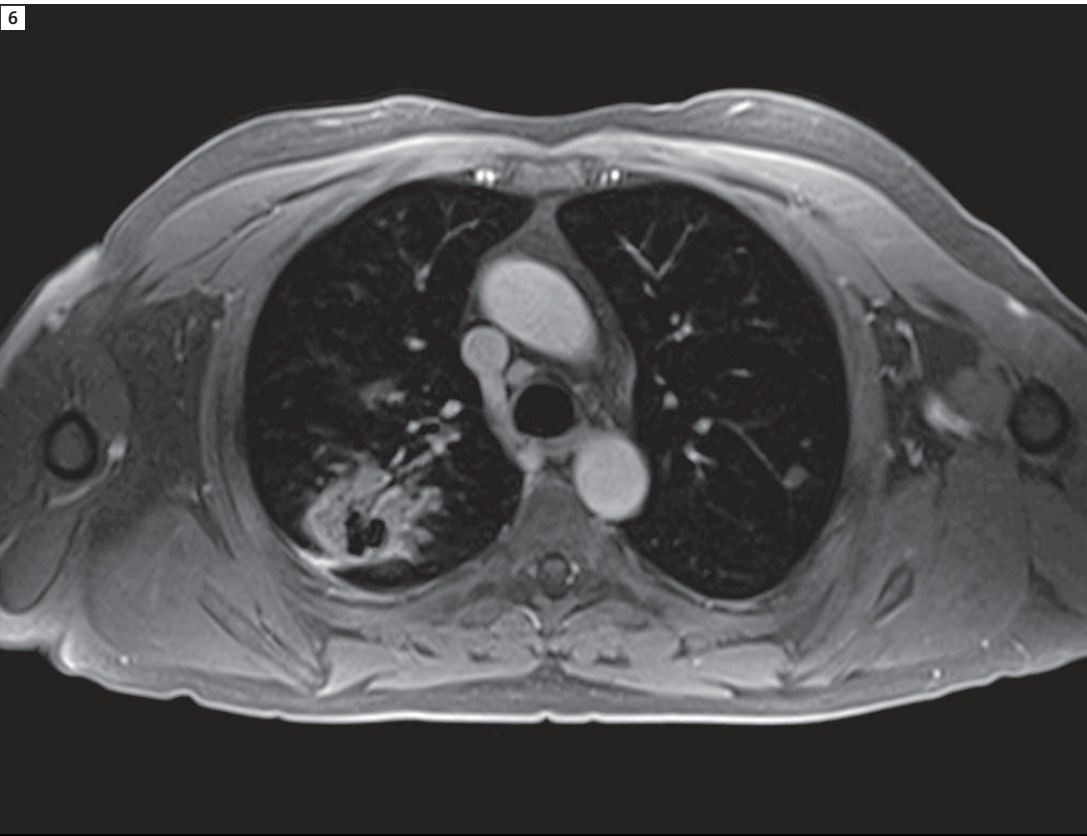
5A Sequence selection for the 'Thoracic Mass' protocol.

1: T1w VIBE, 2: T2w HASTE, 3: TrueFISP, 4: T2w BLADE, 5: DWI, 6: T1w VIBE contrast enhanced

In-room time 20 minutes



5B Protocol tree 'Thoracic Mass'.

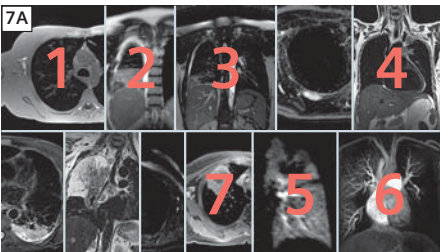


6 Contrast-enhanced VIBE of a lung granuloma in Wegener's disease. Note central necrosis with air-filled defect inside the large mass.

urated BLADE (multi-breathhold T2w TSE) is skipped in this protocol. Therefore total room time is not more than 20 min. Recognizing the potential value of diffusion-weighted imaging of the lung, the interested user will also find a sugges-

tion for an optional EPI-DWI sequence in this protocol branch. The indications for the contrast-enhanced 'Thoracic Mass' study include lung carcinoma, vasculitis (e.g. Wegener's granulomatosis, see figure 6), and masses of

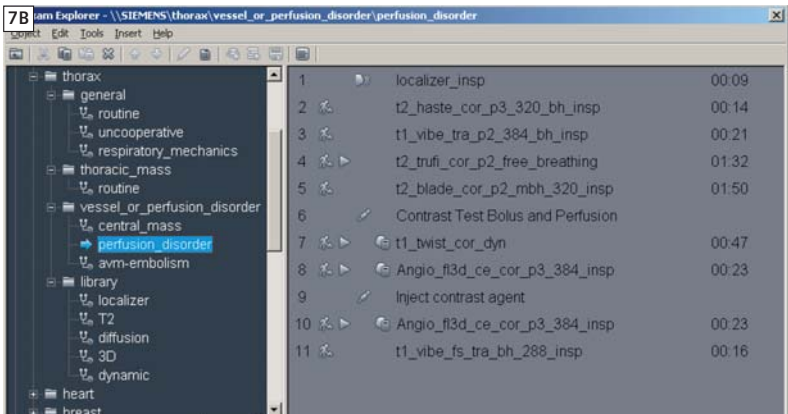
the mediastinum or mediastinitis. Contrast enhancement is also recommended in the case of pleural processes (unclear pleural effusion, empyema, abscess, pleural spread of carcinoma, mesothelioma). With their origin in 3D FLASH angiogra-



7A Sequence selection for the 'Vessel or Perfusion Disorder' protocol

1: T1w VIBE, 2: T2w HASTE, 3: TrueFISP, 4: T2w BLADE, 5: TWIST perfusion, 6: fl 3D ceMRA, 7: T1w VIBE contrast enhanced

In-room time 20 minutes



7B Protocol tree 'Perfusion Disorder'.

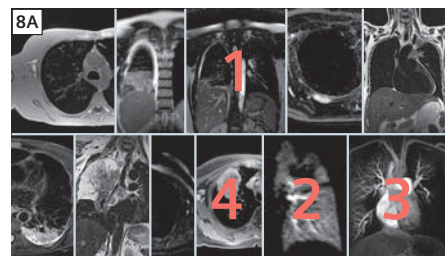
phy, the volumetric VIBE acquisitions have angiographic capacities with excellent visualization of pulmonary vasculature. Therefore, the additional VIBE acquisitions can serve as 'backup-angiogram' in case the image quality of the *k*-space centered FLASH 3D angiogram is impaired by respiratory motion, coughing or mis-timed contrast injection. This contributes to the sensitivity of the 'Thoracic Mass' program also for pulmonary embolism, which is a frequent condition in tumor patients.

'Vessel or Perfusion Disorder' – ceMRA and perfusion imaging of the chest

The collection of protocols for chest MRI is completed by a dedicated branch for the assessment of lung perfusion disorders (Fig. 7). The key sequence for imaging pulmonary vasculature is a T1-weighted 3D FLASH angiography with *k*-space centering of the contrast bolus. Three breathhold acquisitions (first a pre-contrast, followed by two contrast enhanced centered on the peak signal of the pulmonary artery and centered on the peak signal of the aorta) are used to produce subtracted 3D data

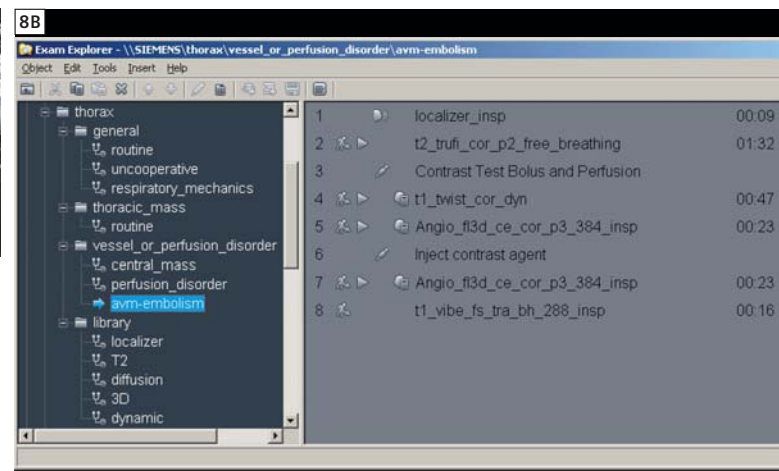
sets for comprehensive viewing with a 3D-tool for multiplanar reformation (MPR) or maximum intensity projections (MIP). Optimum results will be achieved with an automatic power injection of a T1-shortening contrast agent (0.1 mmol/kg at 5 ml/s followed by a 20 ml sodium chloride chaser to produce a compact bolus). The optimum timing for contrast bolus injection can be identified with a simple test bolus injection and sequential single slice acquisitions. However, the protocol includes far more: A dynamic study of lung perfusion with full anatomic coverage. The applied TWIST sequence is the time-resolved variant of high resolution breathhold 3D FLASH angiography. Based on iPAT and data sharing, it allows for a 3D data acquisition with a temporal resolution of 1.5 seconds per image during free breathing. The resulting 4D data set can be displayed with the '4D-InSpace' application of a multi modality workplace, which allows to scroll through the series in a single image position or to scroll through the images of a 3D data set obtained at a single time point. For practical use, time stamps on the images directly indicate the interval between the start of acquisition (equal to the start of test bolus injection) to be used for timing of the high spatial resolution angiogram. To save storage

capacities, it is recommended to select a single subtracted 3D data set at peak lung perfusion and a MIP series documenting the time course of contrast dynamics. Those willing to wait the additional 1–2 minutes computing time required for the reconstruction of 4D-TWIST (compared to single slice test bolus monitoring) are rewarded with a comprehensive lung perfusion study with excellent temporal resolution but still far higher spatial resolution than any scintigraphic technique. This time-resolved multiphase ceMRA is independent from the bolus timing and is therefore not only favorable in patients with severe respiratory disease and very limited breathhold capabilities, but also improves arterial-venous discrimination, e.g. in anomalies and shunts.

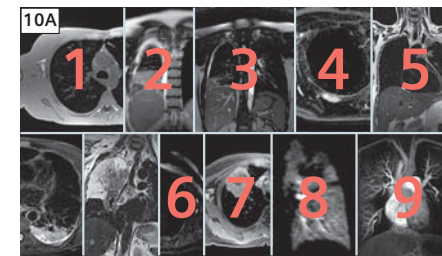


8A Sequence selection for the 'AVM-Embolism' protocol.
1: TrueFISP, 2: TWIST perfusion, 3: fl 3D ceMRA, 4: T1w VIBE contrast enhanced

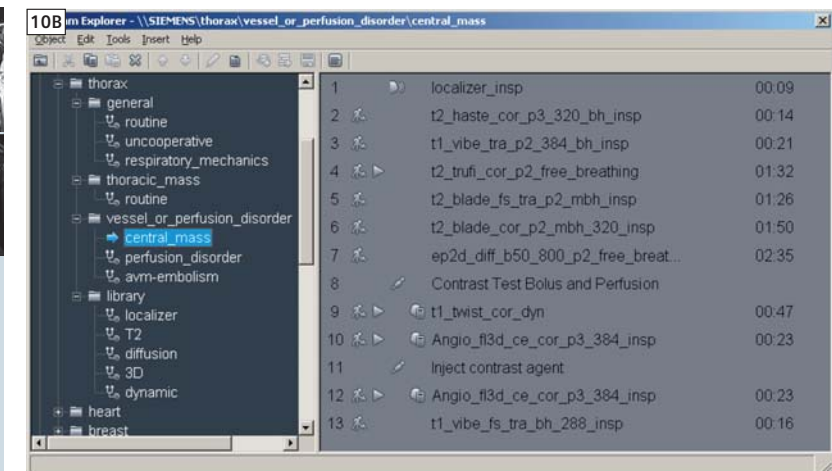
in-room time 15 minutes



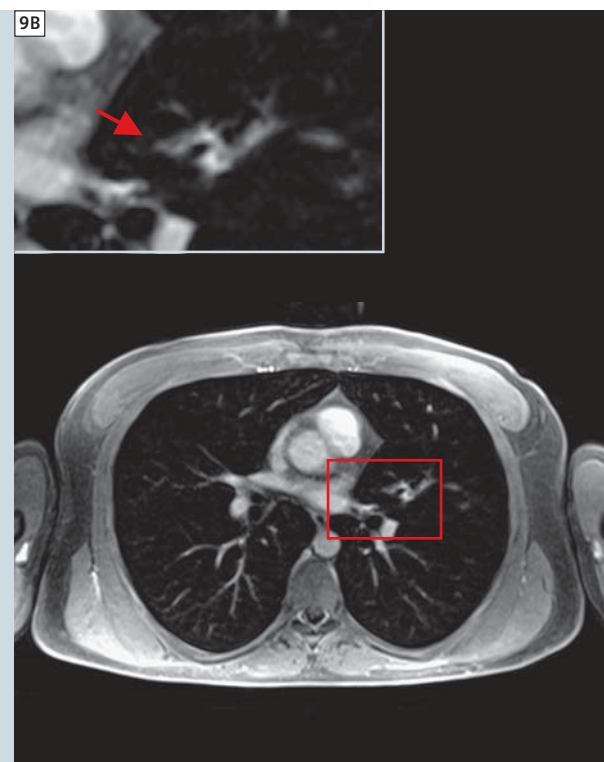
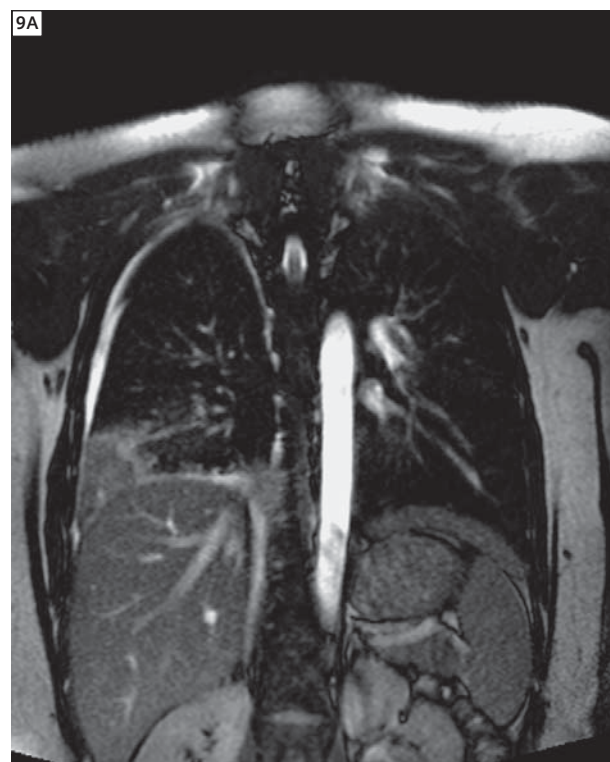
8B Protocol tree 'AVM-Embolism'.



10A Sequence selection for the 'Central Mass' protocol.
1: T1w VIBE, 2: T2w HASTE, 3: TrueFISP, 4: T2w STIR, 5: T2w BLADE, 6: DWI, 7: TWIST perfusion, 8: fl 3D ceMRA, 9: T1w VIBE contrast enhanced
In-room time 30 minutes



10B Protocol tree 'Central Mass'.



9 Two cases of acute pulmonary embolism. On the left a case with massive embolism and large thrombi detected with the TrueFISP series, on the right a small embolus within a segmental vessel, in this case detected with the VIBE.

The indications covered with the '**Vessel or Perfusion Disorder**' protocol include acute and chronic pulmonary embolism (PE), arterio-venous (AV) malformation (e.g. Osler's disease), lung sequestration, pulmonary arterial aneurysm, abnormalities of pulmonary venous drainage and any other pathology of lung vasculature. Specific indications for the TWIST perfusion appreciate the fact that this is the only part of the protocol which indirectly

visualizes defects or absence of lung parenchyma due to emphysema or pneumothorax. Furthermore, functional lung perfusion impairment due to hypoventilation and hypoxic vasoconstriction can be easily detected (air-trapping in bronchiolitis, mucous impaction in cystic fibrosis). At this point, MRI includes specific functional information that would be difficult to obtain with CT. However, conditions such as acute pul-

monary embolism are an emergency. This requires immediate interaction and will not allow for typical scheduling lead times for an MR scanner. An abbreviated version of the protocol was prepared for this purpose (Fig. 8): It is limited to four sequences focusing on lung vessel imaging and lung perfusion. This can be accomplished within 15 minutes in-room-time which is considered acceptable to be squeezed into a full MR sched-

ule during the day. Nevertheless, this short examination provides comprehensive information on pulmonary embolism combining perfusion imaging with the diagnostic scope of a scintigraphy and lung vessel angiography comparable to CT scanning (Fig. 9). An important point is to start the examination with TrueFISP non-contrast enhanced series. In case of severe embolism the diagnosis can be made within the first 60 seconds of the examination with the option to immediately stop imaging at that time and to proceed to intensive treatment without any time loss compared to CT scanning.

'Central Mass' – have it all!

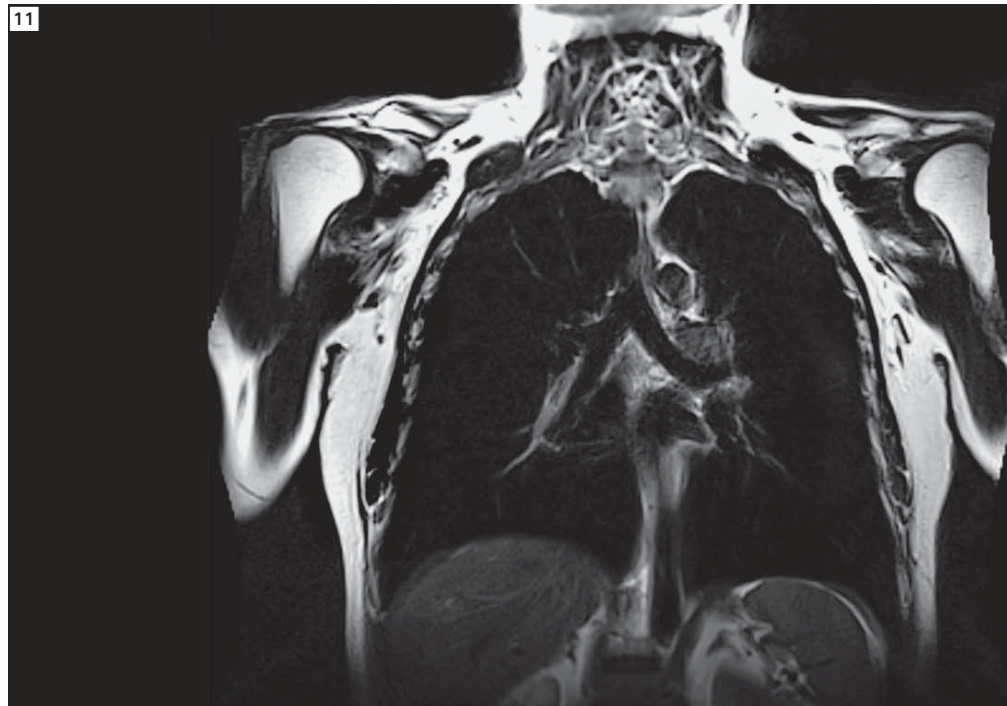
'**Central Mass**' is the most comprehensive package of the protocol tree, containing elements of all the aforementioned branches. It accounts for vessel involvement by central lung or mediastinal tumors with possible consequences for lung perfusion. This includes T2-weighted fat-saturated BLADE sequences as well as DWI. Typically, it would be used for the diagnosis of central masses with infiltration into the pulmonary arteries or aorta. 'Central Mass' is also a 'have it all' protocol for all cases in which one would like to cover any possible aspect with comprehensive imaging – however, since this takes approximately 30 minutes in-room-time, for daily routine and the majority of indications it would be practicable to use selective protocols.

Protocol adaptations for 3 Tesla

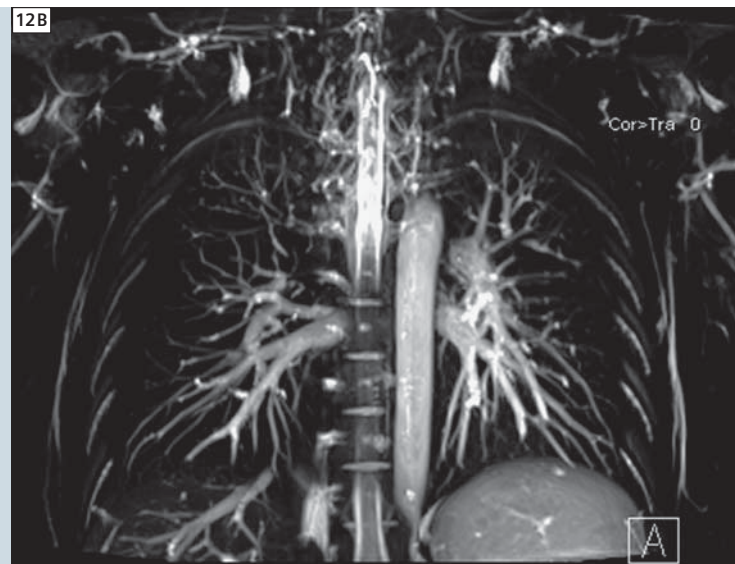
Originally, lung MRI protocols were developed for 1.5 Tesla systems. The majority of available publications are based on work with this field strength. Since high performance 3 Tesla scanners have become the benchmark on the clinical stage, serious effort was invested into transferring lung MRI technology to the higher field strength. Initially, it was discussed that increased susceptibility artifacts would make lung imaging even more difficult on these systems. However, systematic experimental work and application fine tuning have paved the road to the successful introduction of lung imaging into the high field world [4, 5]. In general, proton MRI of the lung is based on the effect that most relevant pathologies have intense signal and give optimum contrast against the black background of lung tissue. Consequently, transfer of the protocols to a 3T system has even improved the lesion to background contrast in infiltrative as well as solid lung lesions for all FLASH and TSE sequence types. In particular, lung nodule detection with the VIBE sequence as well as the detection of infiltrates with HASTE and STIR is improved on 3T images. This opens the perspective to invest the higher signal into higher spatial resolution or even faster image acquisition schemes. Contrast-enhanced studies after i.v. injection reach equal quality

and with optimized technology first pass perfusion studies can be performed in a similar fashion [6]. Changes of image quality with transfer of the aforementioned sequence concept to 3T are therefore acceptable or even positive for most sequence types.

The exception concerns TrueFISP images, which show significant motion- and flow-related artifacts at the higher field strength. Delineation of vessel walls and other structures is still good, but lesion/background contrast does not improve. In combination, the effects result in an inhomogeneous signal of the pulmonary artery trunk and the large lobar vessels. Therefore, exclusion of severe pulmonary embolism with a quick free breathing TrueFISP acquisition on a 3T system is not favorable. To fill this gap in the protocol, a respiration-triggered SPACE-STIR sequence was adjusted for the visualization of central pulmonary vessels without contrast injection. The triggered acquisition scheme produces images of central mediastinal vessels with bright signal within 4-5 min and can be used on 1.5T as well as 3T. Due to triggering, the acquisition is robust even in uncooperative patients. The respiration-triggered SPACE-STIR sequence might therefore replace the free breathing TrueFISP throughout the whole protocol tree, although sensitivity and specificity for pulmonary emboli are subject to ongoing patient studies (Fig. 12).



11 Coronal multi-breathhold T2w BLADE; healthy volunteer, 3T MAGNETOM Verio.



12 Coronal respiration triggered SPACE STIR acquisition in a 67-year-old man, using a 1.5T MAGNETOM Avanto (left). 30-year-old healthy volunteer using a 3T MAGNETOM Skyra (right).

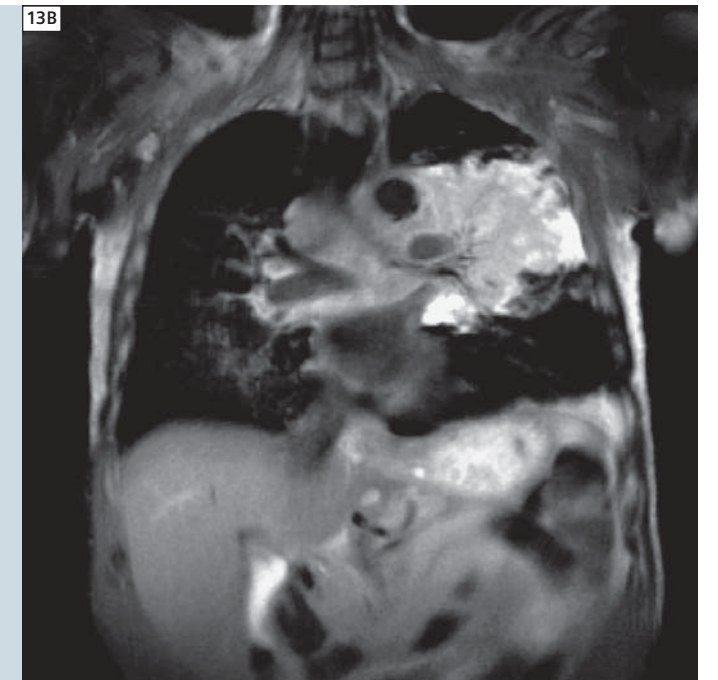
Future perspectives

A quick glance at the current investigations on proton MRI of lung pathology illustrates the trend towards further improvement in robustness and reproducibility of image quality. Free-breathing self-navigated sequence designs, radial k -space methods including ultra-short-echo-time imaging and dynamic as well as quantitative lung imaging protocols for improved anatomical and functional lung assessment are currently under investigation.

A consortium of medical physics and radiology departments at Würzburg, Kiel, Heidelberg and Mannheim supported

by the German Research Foundation (Deutsche Forschungsgemeinschaft; DFG) is currently on the way to developing 2D- and 3D imaging protocols based on the Siemens MAGNETOM Avanto platform for high-resolution lung MRI. One key sequence for 3D-MRI of the lung with full volume coverage is a self-navigated T1-weighted 3D FLASH with quasi-random k -space ordering. Under free-breathing condition five to seven full 3D acquisitions are acquired using additionally sampled non-spatially encoded DC-signals at the center of k -space as navigator. This approach is

rather time efficient, since it does not require separate RF excitations, and the DC-signal at the center of k -space contains sufficient information to reliably detect motion. Therefore, there are double benefits: Almost motion-free parallel acquisition of multiple breathing phases will either allow for detail motion analysis or for morphologic imaging without patient compliance. A key modification necessary for self-navigation was an extra data acquisition immediately after each imaging echo. Typical imaging parameters for the 3D-flash technique are: TE 1.2 msec, TR 3.8 msec, 7°,



13 Lung cancer patient with a tumor in the left upper lobe, adjacent atelectasis and pleural effusion. (A) Self-navigated coronal 3D FLASH of the posterior thorax, free-breathing. (B) Coronal radial TSE image of the same patient at carina level, free-breathing.

matrix : 256 x 320 x 44, FOV 370 x 450 x 220 mm³, resolution 1.4 x 1.4 x 5 mm³, total acquisition time 375 s (Fig. 13). In the same trend, Fourier decomposition ventilation-perfusion scanning is being developed as a robust technology for regional assessment of lung function with a non-contrast enhanced free breathing acquisition scheme. Periodic changes of parenchyma signal with inspiration depth (highest signal with lowest pulmonary air content in expiration) and heart action (lowest signal with maximum blood flow in systole) will be evaluated separately to produce ventilation and perfusion maps with comparable quality to a V/Q SPECT without the use of contrast media or radiation exposure to the patient [7]. Just these two examples indicate the dynamic development in the field of lung MRI and its bright future perspectives. In conclusion, lung MRI has made it from a niche technology to the doorsteps of clinical routine imaging. On MAGNETOM Aera and MAGNETOM Skyra lung protocols are ready to go! For key clinical questions lung MRI not only matches X-ray and CT, it offers additional func-

tional imaging capacities. The protocol tree offers solutions for tricky problems of daily routine and makes MRI more than a good option for pediatrics and science. Dedicated parts of the protocol are fairly robust accounting for respiratory motion and heart action even in uncooperative patients. Experience with this young technology, e.g. in comparison with CT, is growing rapidly in an increasing number of centers worldwide. The perspectives for further developments are excellent and the degrees of freedom to adapt the suggested protocols for the users own purposes are large. Get ready ... get set ... go!

References

- 1 Puderbach M, Hintze C, Ley S, Eichinger M, Kauczor HU, Biederer J (2007) MR Imaging of the Chest. A practical approach at 1.5 T. *European Journal of Radiology Eur J Radiol.* 64:345-355.
- 2 Biederer J, Puderbach M, Hintze C (2006) A Practical Approach to Lung MRI at 1.5 T. *Magnetom Flash 2/2006:38-43* (Siemens MR Customer Magazine, Siemens AG, München).
- 3 Kluge A, Gerriets T, Müller C, Ekinici O, Neumann T, Dill T, et al. [Thoracic real-time MRI: experience from 2200 examinations in acute and ill-defined thoracic diseases]. *Rofo* 2005; 177(11):1513-21.

- 4 Fink C, Puderbach M, Biederer J, Fabel M, Dietrich O, Kauczor HU, Reiser M, Schönberg S (2007) Lung MRI at 1.5T and 3T: Observer preference study and lesion contrast using five different pulse sequences. *Investigative Radiology* 42: 377-383.
- 5 Fabel M, Wintersperger BJ, Dietrich O, Eichinger M, Fink C, Puderbach M, Kauczor HU, Schoenberg SO, Biederer J (2009) MRI of respiratory dynamics with 2D steady-state free-precession and 2D gradient echo sequences at 1.5 and 3 Tesla: an observer preference study. *European Radiology* 19:391-399.
- 6 Attenberger UI, Ingrisch M, Dietrich O, Herrmann K, Nikolaou K, Reiser MF, et al. (2009) Time-resolved 3D pulmonary perfusion MRI: comparison of different k -space acquisition strategies at 1.5 and 3 T. *Invest Radiol.* 44:525-531.
- 7 Bauman, G., Puderbach, M., Deimling, M., Jellus, V., Chedf hotel, C., Dinkel, J., Hintze, C., Kauczor, H., und Schad, L. R. (2009) *Magn Reson Med* 62, 656-664.

Contact

Prof. Dr. med. Jürgen Biederer, MD
Department of Diagnostic Radiology
University Hospital Schleswig-Holstein,
Campus Kiel
Arnold-Heller-Street 3, Haus 23
24105 Kiel
Germany
Phone: + 49 431-597-3153
juergen.biederer@rad.uni-kiel.de

Case Series: Lung Imaging with MRI

J. Biederer, MD

University Hospital Schleswig-Holstein, Campus Kiel, Department of Diagnostic Radiology, Kiel, Germany

Background

MR imaging (MRI) of the lung can be applied in a variety of clinical scenarios. It is not only a feasible alternative to computed tomography (CT) of the lung – especially to avoid unnecessary radiation burden in young patients – but it can easily provide additional diagnostically relevant information on physiological parameters such as perfusion or respiratory dynamics. Diffusion-weighted imaging can even add biological information about cell density.

This case series aims to provide an insight into typical applications of MRI and to visualize characteristic findings. On page 6 of this issue of MAGNETOM Flash you will find a detailed review on lung imaging protocols available with the Siemens MR scanners.

Materials and methods

All images shown in this case series were acquired at 1.5 Tesla (MAGNETOM Avanto) with a combination of the body and integrated spine coil using software version *syngo* MR B17.

Sequence parameters were adapted to patient needs. Selected parameters of some of the shown sequences were as follows:

Coronal T2w HASTE (breathhold)

TR / TE = 228 / 20 ms, SL = 8 mm, FOV = (500*500) mm², matrix = (192p*320) px²

Transversal T1w VIBE

(no fat-saturation ; breathhold)

TR / TE = 3.23 / 1.15 ms, SL = 4 mm, FOV = (384*450) mm², matrix = (384*512i) px²

Transversal T1w VIBE

(fat-saturated; breathhold)

TR / TE = 3.3 / 1.18 ms, SL = 4 mm, FOV = (350*400) mm², matrix = (448*512i) px²

Coronal TrueFISP (free-breathing)

TR / TE = 412.8 / 1.16 ms, SL = 4 mm, FOV = (450*450) mm², matrix = (512*512i) px²

Transversal T2w TSE (SPAIR, breathhold)

TR / TE = 2040 / 116 ms, SL = 6 mm, FOV = (380*380) mm², matrix = (256*256) px²

Coronal T2w TSE

(BLADE, free-breathing)

TR / TE = 2040 / 123 ms, SL = 5 mm, FOV = (480*480) mm², matrix = (320*320) px²

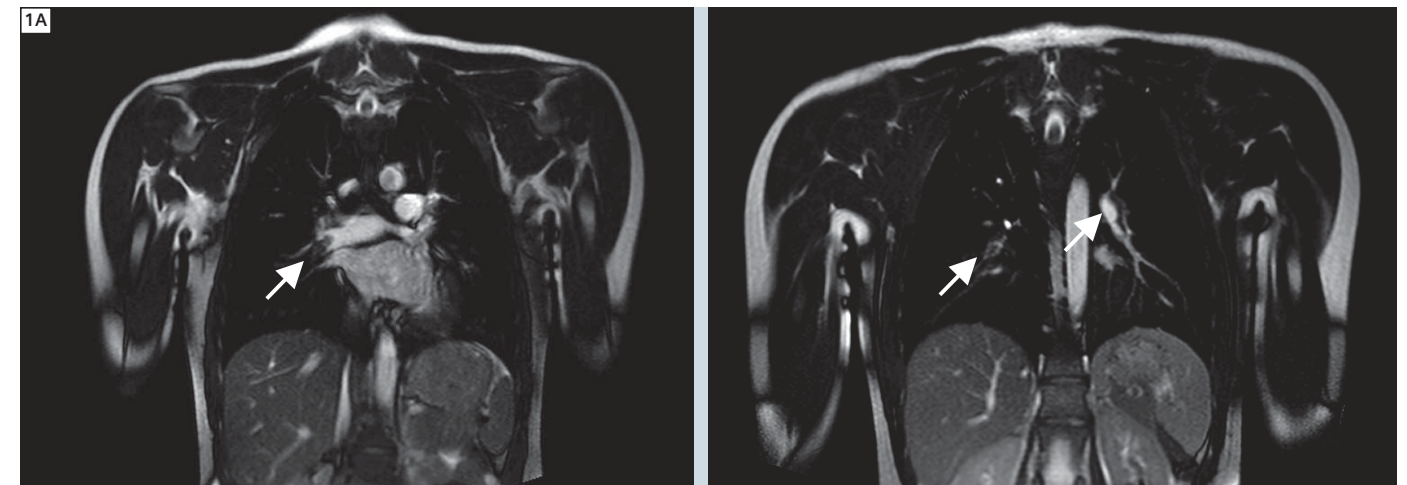
Transversal DWI (free-breathing; three b-values 50, 400, 800 s/mm²)

TR / TE = 5983 / 79 ms, SL = 8 mm, FOV = (248*379) mm², matrix = (115p*192) px²

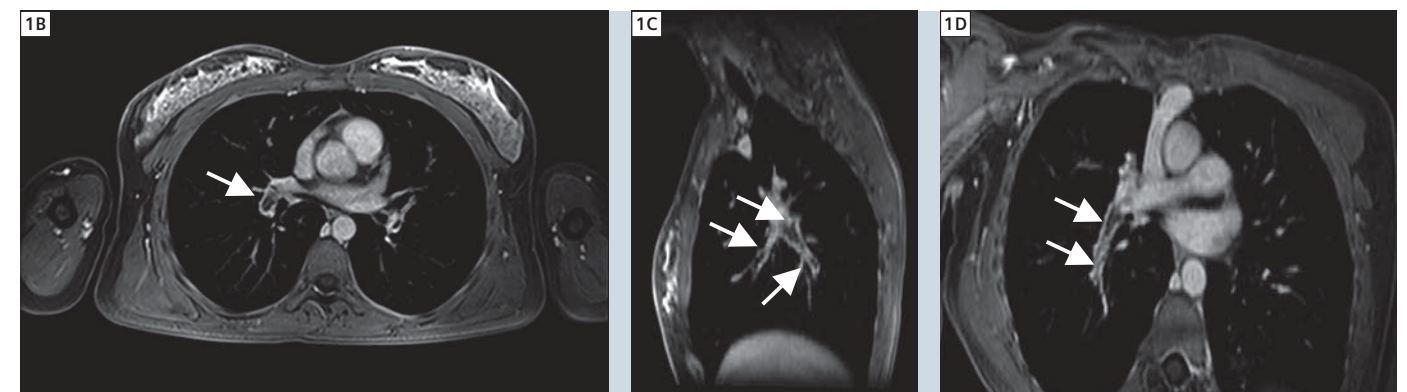
Case 1

Young female patient with bilateral acute pulmonary embolism

An 18-year-old female patient presented with clinical suspicion (dyspnoea and elevated D-dimeres) of acute lung artery embolism. To avoid unnecessary radiation exposure, this patient was referred immediately to our MR unit.



1A Coronal TrueFISP images; the emboli are already well delineated (arrows).



1B Transversal, ...

1C ... oblique sagittal,

1D ... oblique coronal contrast-enhanced 3D VIBE images visualize the right thrombus in greater detail (arrows).

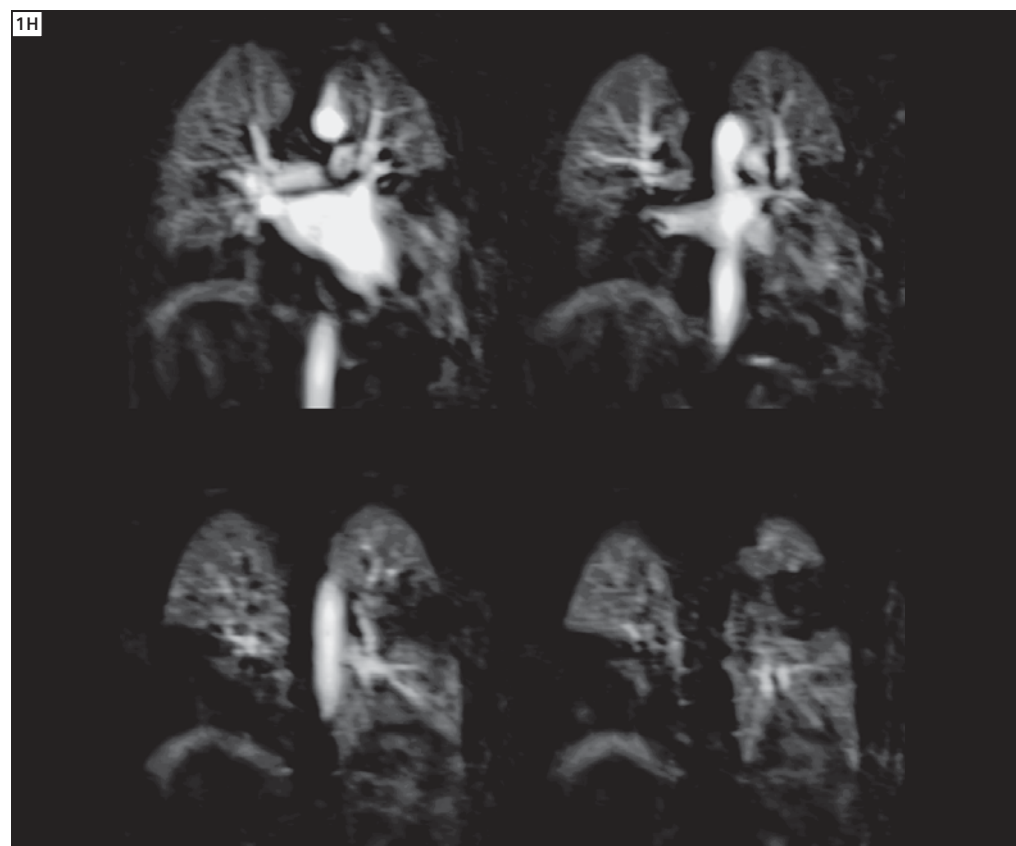


1E–G Corresponding reconstructions of the left side thrombus; an infarction pneumonia can be seen in this area (marked by *).

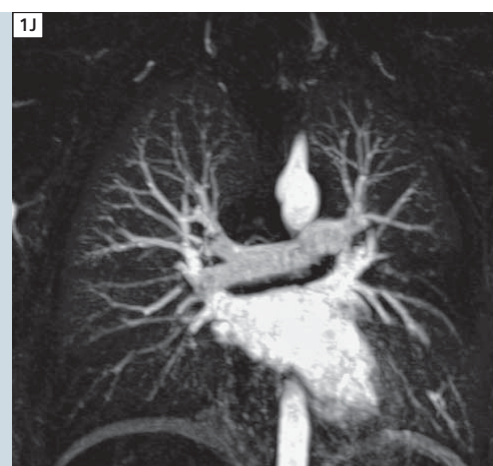
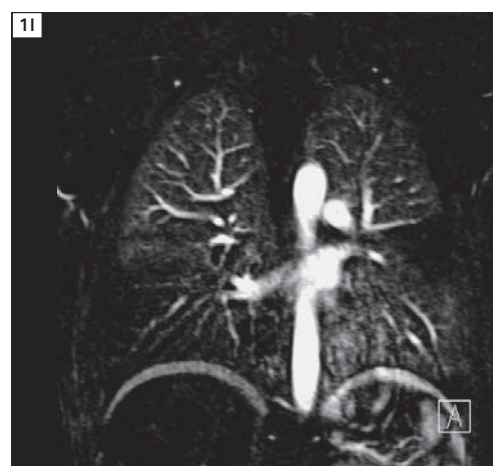
Imaging findings show an acute embolism of the right lower lobe segment and partially also on the left side. The thrombus is already visible in the coronal True-

FISP images. However, post-contrast 3D data show the extension of the emboli in much greater detail. A dynamic contrast enhanced T1w 3D scan with high

temporal resolution (syngo TWIST) was performed to evaluate the degree of perfusion defects caused by the emboli.



1H Parenchymal phase derived from the perfusion scan; corresponding perfusion defects to the emboli are well delineated.



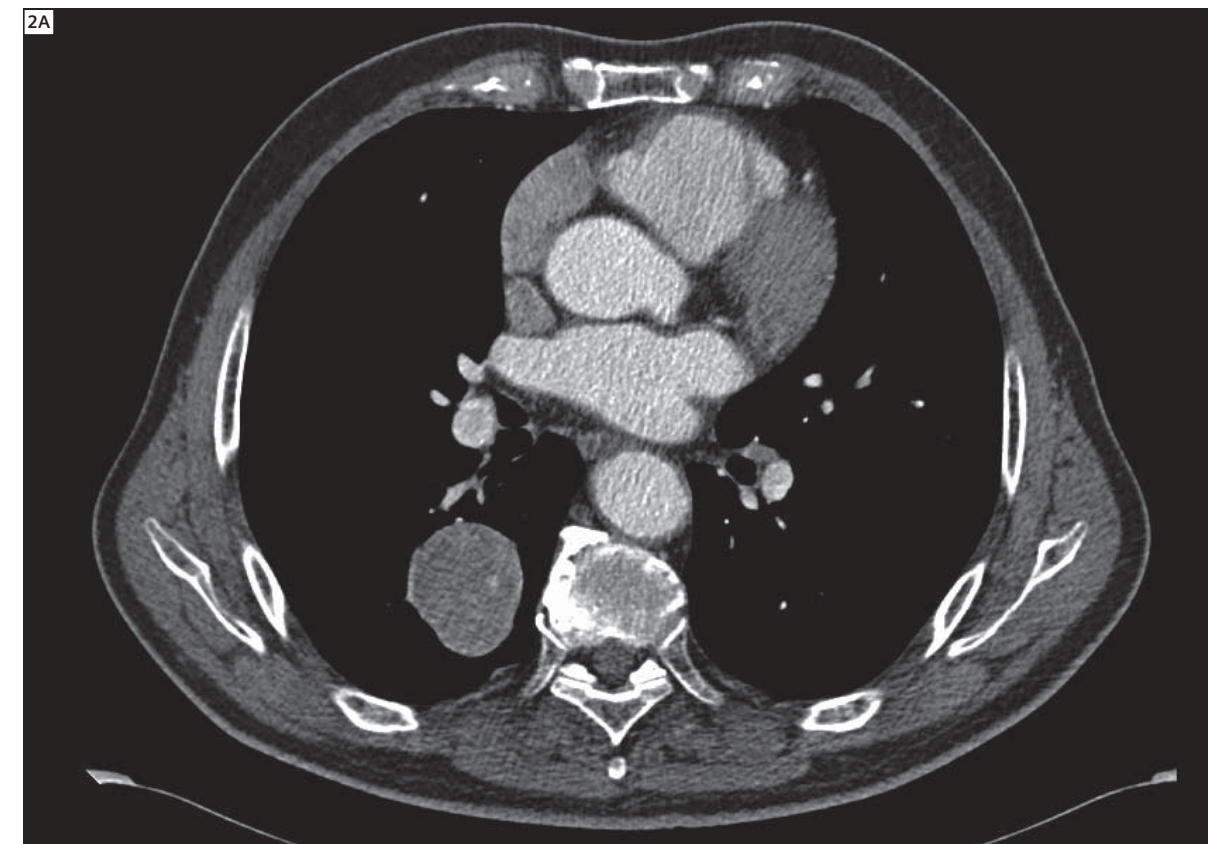
1I-K Coronal thick-slice maximum intensity projections (MIP) demonstrating filling defects of the corresponding vessel segments.

Case 2 Rule out of vessel malformation of the lung

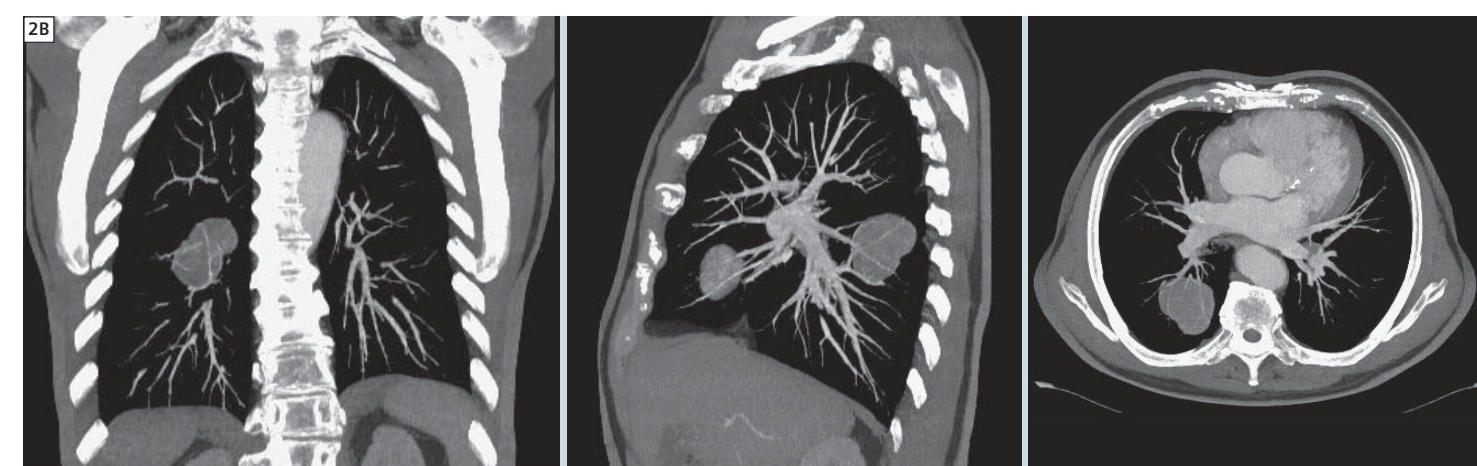
Lung MRI of a 77-year-old male patient is shown with a suspicious lesion in the right lung. A clear rule out of an arterio-

venous malformation was not possible with the already performed diagnostic tests and the patient was therefore

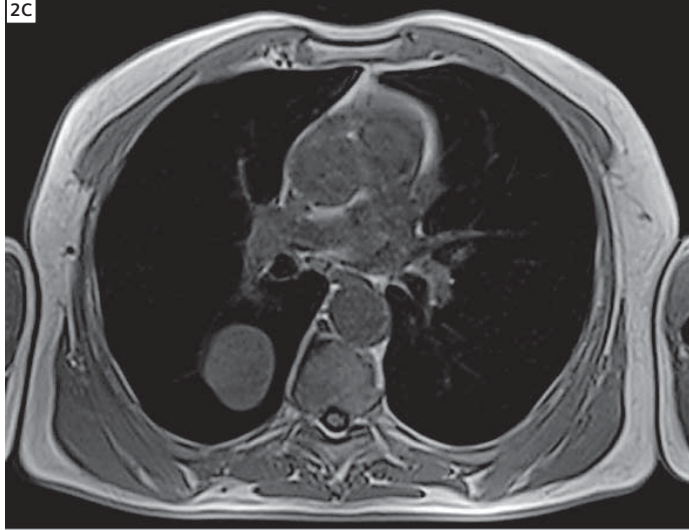
referred to our institute. A well delineated, ellipsoid shaped lesion can be seen. Based on morphological features, a



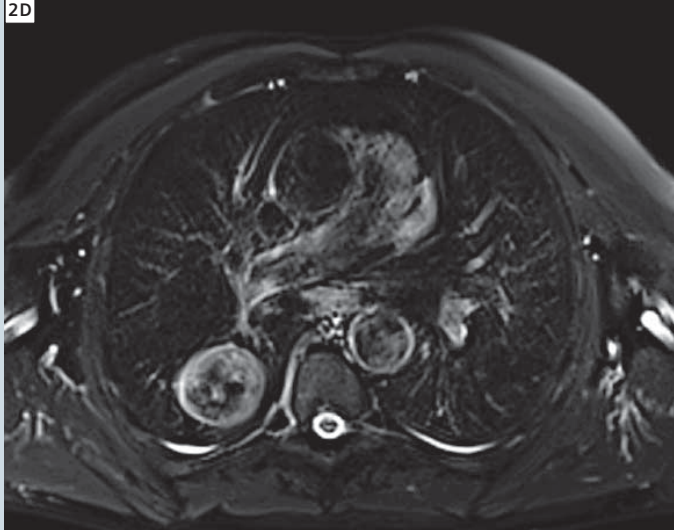
2A Contrast enhanced CT scan showing well delineated but enhancing lesion within the right lung.



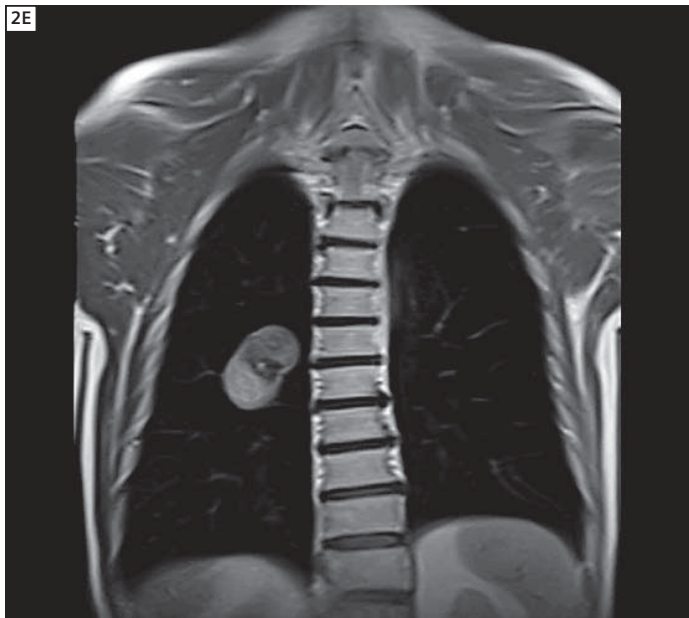
2B Thick-slice multiplanar reconstruction (MPR) showing close relationship of the lesion to arterial lung vessels.



2C Native transversal T1w MRI, ...



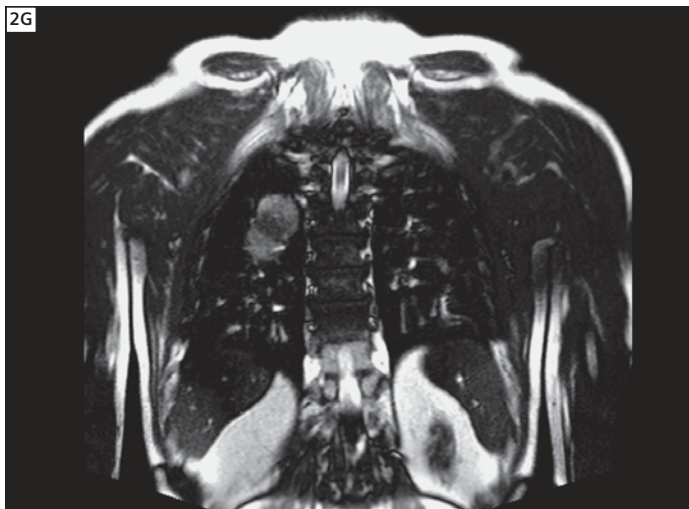
2D ... corresponding T2w TSE with fat saturation.



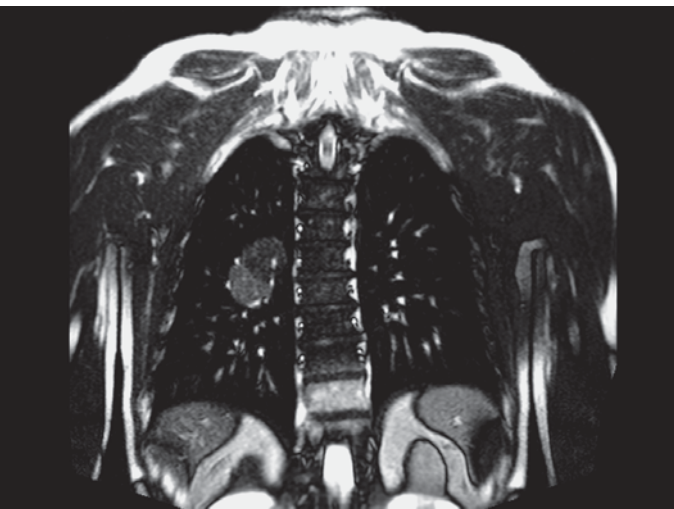
2E Coronal HASTE and ...



2F ... coronal T2w TSE showing different but well delineated components of the tumor, supporting the suspicion of hamartoma.

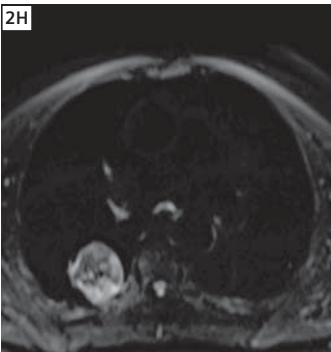


2G Coronal TrueFISP acquired during free-breathing demonstrating free degree of movement during the breathing cycle.

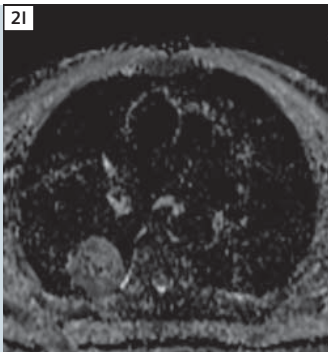
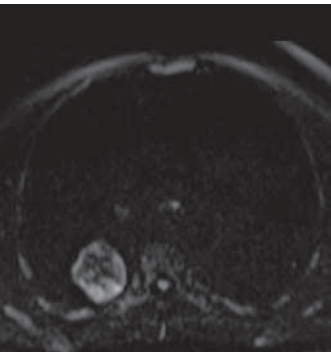
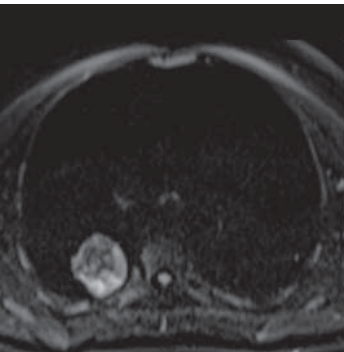


hamartoma is possible. While the tumor has a close relationship to several arterial vessels, dynamic MRI could rule out a vessel malformation (no arterio-venous malformation, no aneurysm). Contrast-media enhancement of the

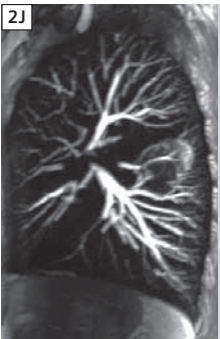
lesion, however, has to be interpreted as a sign of potential malignancy and further invasive evaluation was warranted (surgical resection).



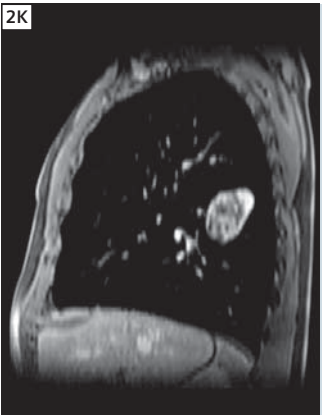
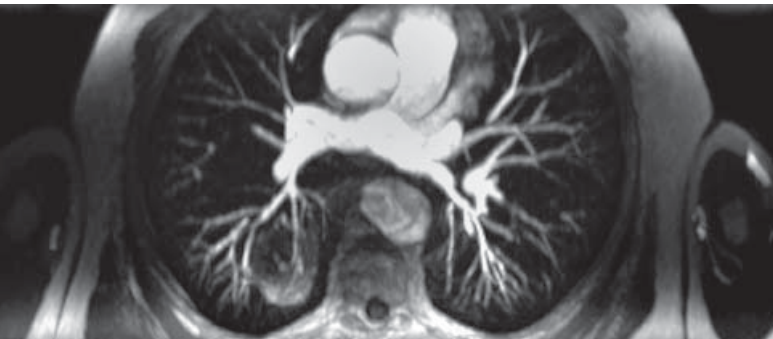
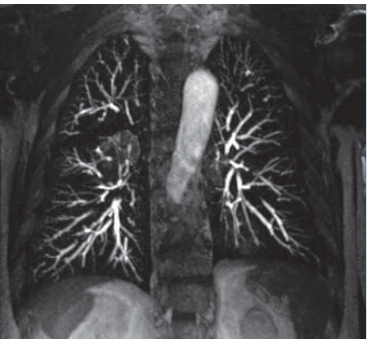
2H Original b-value images derived from DWI exam (right b = 0, middle b = 400, left b = 800 s/mm²), ...



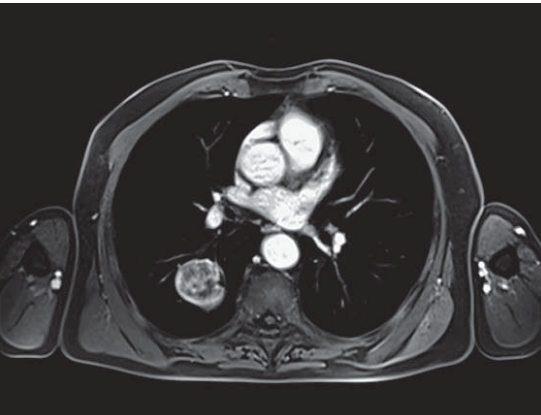
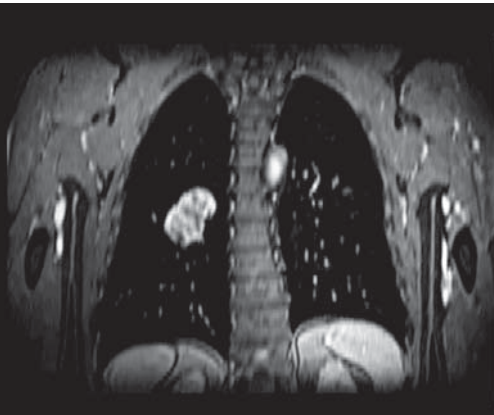
2I ... Liecorresponding ADC map.



2J Multiplanar thick-slice MIP of late-arterial dynamic scan showing relationship to arterial vessels and contrast-media enhancement as potential sign of malignancy; no imaging feature of AVM / aneurysm can be visualized.

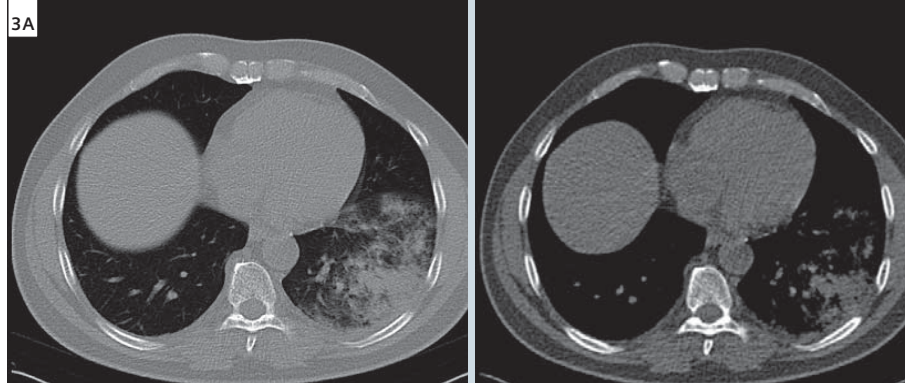


2K Multiplanar reconstruction based on late-phase 3D T1w VIBE demonstrating inhomogenous but evident contrast enhancement.

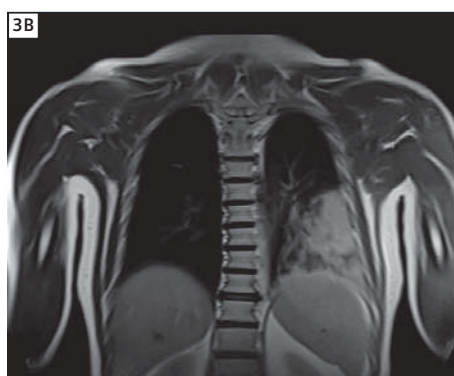


Case 3 Pneumonia

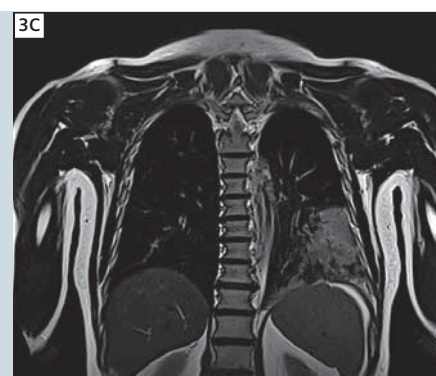
A 66-year-old male volunteer was diagnosed with pneumonia a few days previously. This case clearly shows the potential of MRI to detect and evaluate inflammatory processes of the lung. In addition to the pneumonia of the left lower lobe, a slight apical effusion and reactive mediastinal / hilar lymphadenopathy (not shown) is present. No signs of malignancy and / or masking of lesions by the infiltrate can be found.



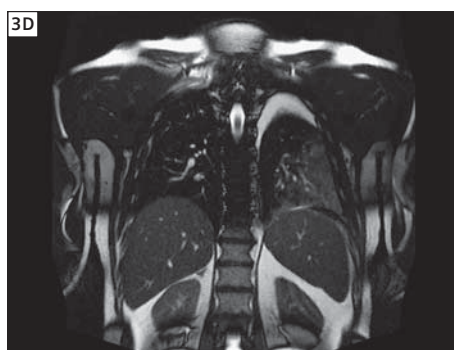
3A Native low-dose CT of the lung.



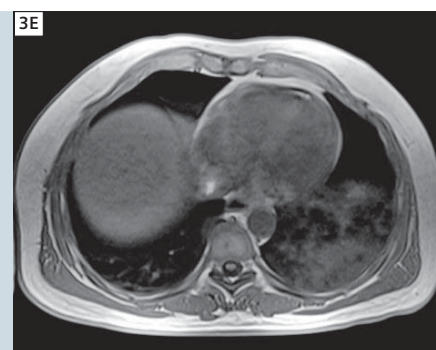
3B Coronal HASTE.



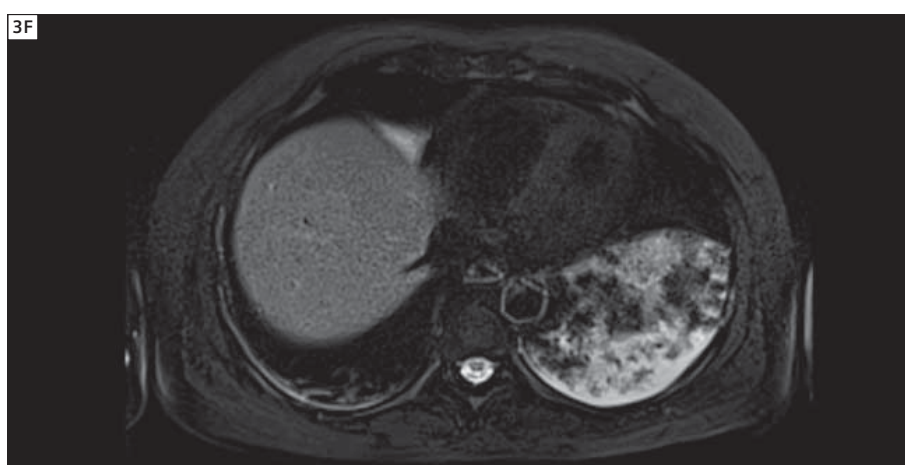
3C Corresponding T2w TSE.



3D Coronal TrueFISP at a different slice position showing additional apical pleural effusion.



3E Native T1-weighted image.



3F Corresponding T2-weighted TSE with fat saturation at comparable height of the lung to the CT images in figure 3A.

Case 4 Sarcoidosis

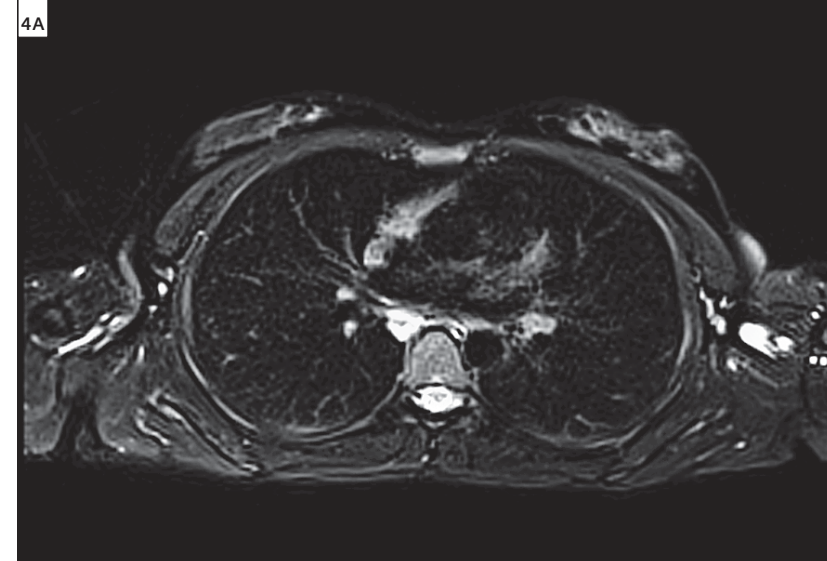
This 25-year-old woman underwent MRI for the follow-up of a proven sarcoidosis. The protocol was adapted to also evaluate the supraclavicular and nuchal lymph node stages, which were unsuspecting (therefore not shown). Best visualized by fat-saturated T2w MRI, however, multiple mediastinal and hilar lymph nodes are visible. The lung parenchyma is normal and no pleural effusions can be seen. However, a reduction of the degree of bihilar lymphadenopathy was diagnosed compared to CT and in accordance with clinical parameters, recurrent inflammation of the sarcoidosis stage 1 was concluded.

Conclusion

This short case series shows that MRI of the lung is capable of assisting in the detection and diagnosis of a large range of lung pathologies. With growing experience in the application of MRI in the lung, it can play an important role in future diagnostic set-up of lung pathologies, especially in younger patients.

Contact

Prof. Dr. med. Jürgen Biederer, MD
Department of Diagnostic Radiology
University Hospital Schleswig-Holstein,
Campus Kiel
Arnold-Heller-Street 3, Haus 23
24105 Kiel
Germany
Phone: + 49 431-597-3153
juergen.biederer@rad.uni-kiel.de



4A Transversal T2w TSE with fat saturation showing bihilar lymphadenopathy.



4B Coronal T2w TSE (BLADE technique).

MAGNETOM Skyra: The Mannheim Perspective

Henrik J. Michaely; Stefan O. Schoenberg

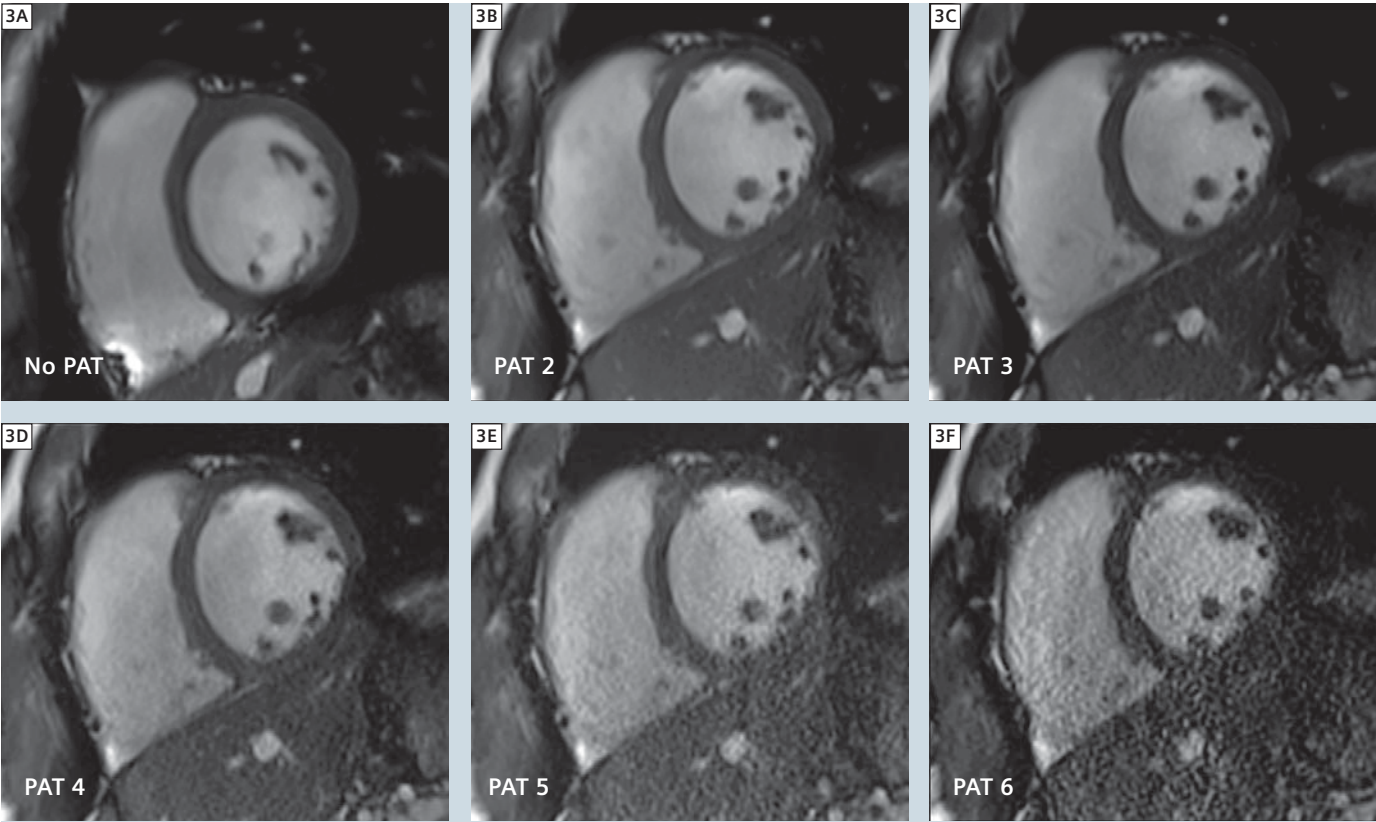
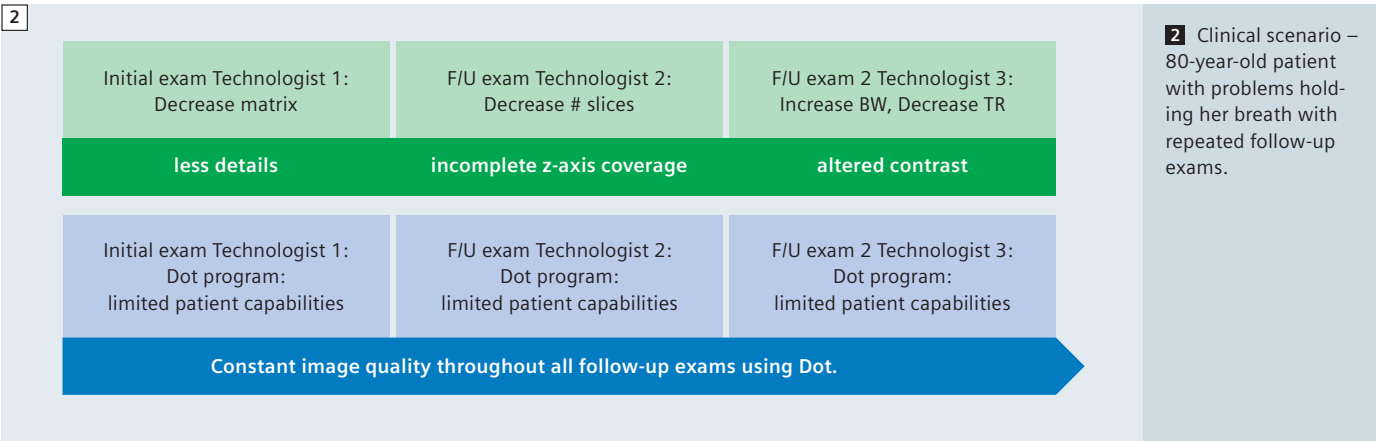
Institute of Clinical Radiology and Nuclear Medicine, University Medical Center Mannheim, University of Heidelberg, Germany

Introduction

For over one year the 3T MAGNETOM Skyra has been used for scientific projects and clinical imaging at the University Medical Center (UMM) Mannheim. The UMM Mannheim was the first site in the world to install the Skyra. In order to meet the high requirements for state-of-the-art imaging with high spatial resolution and fast scan times, a fully equipped version of the Skyra with XQ gradients and 64 independent receive channels was installed. The small space requirement of the Skyra meant that it could be installed completely within the previous technical cabinet of a former 1T Siemens MAGNETOM Harmony. This enabled us to install the Skyra as the fourth scanner in our MR-facility, alongside a 1.5T MAGNETOM Sonata, a 1.5T MAGNETOM Avanto and a 3T MAGNETOM Trio. This allows us to easily switch patients between the scanners and to run all four scanners with just a small number of technologists. The scanner was installed in such a way that the dockable table can be moved out of the scanner room in the shortest possible way in order to facilitate patient transport into and out of the scanner. All four scanners are operated from 7 am to 8 pm, hence yielding a high patient throughput. The focus of our hospital is translational research in the fields of abdominal imaging and oncologic imaging while all other imaging areas such as musculoskeletal imaging and neurologic imaging are also offered.



1 MAGNETOM Skyra with MoodLight illumination installed in Mannheim.



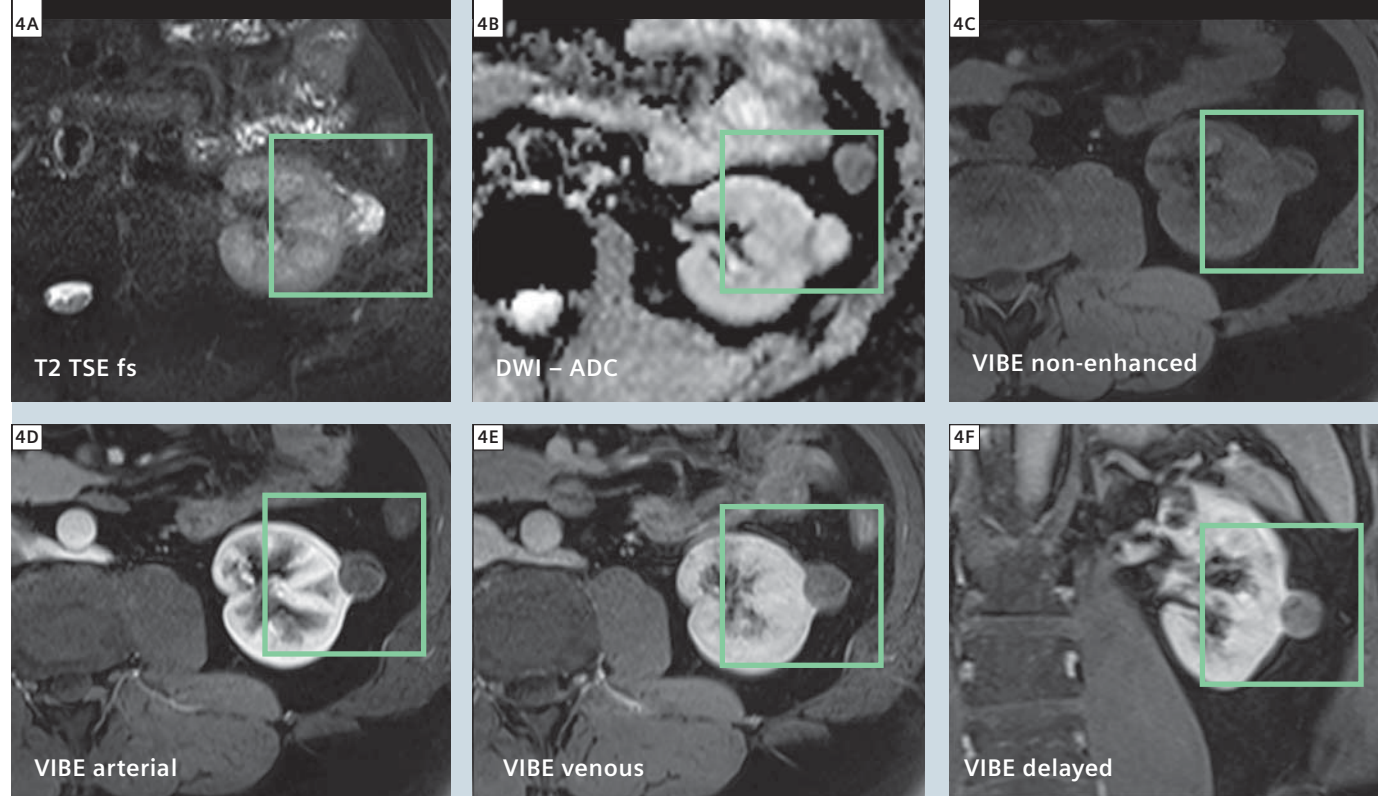
3 Using up to 30 coil elements for cardiac studies (18-element body matrix coil and 12 elements of the 32-element spine matrix coil) allows for high parallel imaging factors (up to 4) in clinical routine applications. With further developments even higher PAT factors of 5–6 will be clinically available.

Patient acceptance

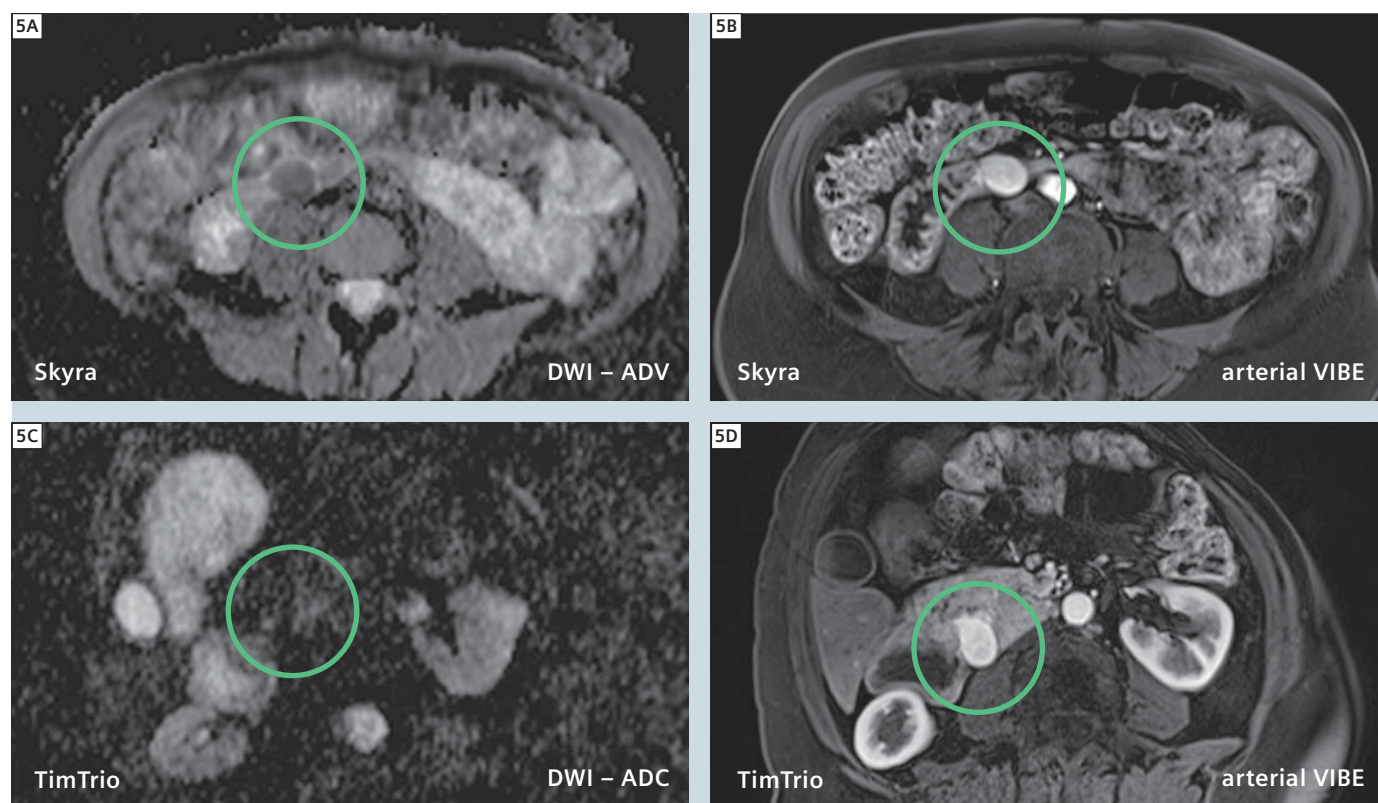
Except for the MAGNETOM Skyra all our MR-units are characterized by a 60 cm-wide bore with a length of between 160 cm and 213 cm. So far, 15% of patients have declined an examination because of claustrophobia. Another 5% of our patients could not be exam-

ined because of a too big circumference of the abdomen not allowing a positioning of the patients in the conventional MR-scanners. For these two reasons, one of the prerequisites for the fourth scanner to be installed was a wide bore and a maximum of patient comfort.

Patient comfort also included installation of the Illumination MoodLight feature. In summary, the MAGNETOM Skyra combines a 70 cm Open Bore and 173 cm short system design with variable bright outside illumination and light strips inside the bore that further



4 Histologically proven carcinoma of the cyst wall which can only be appreciated in the ADC map where a local restriction of the diffusion can be seen. The contrast-enhanced studies do not allow a delineation of this lesion.



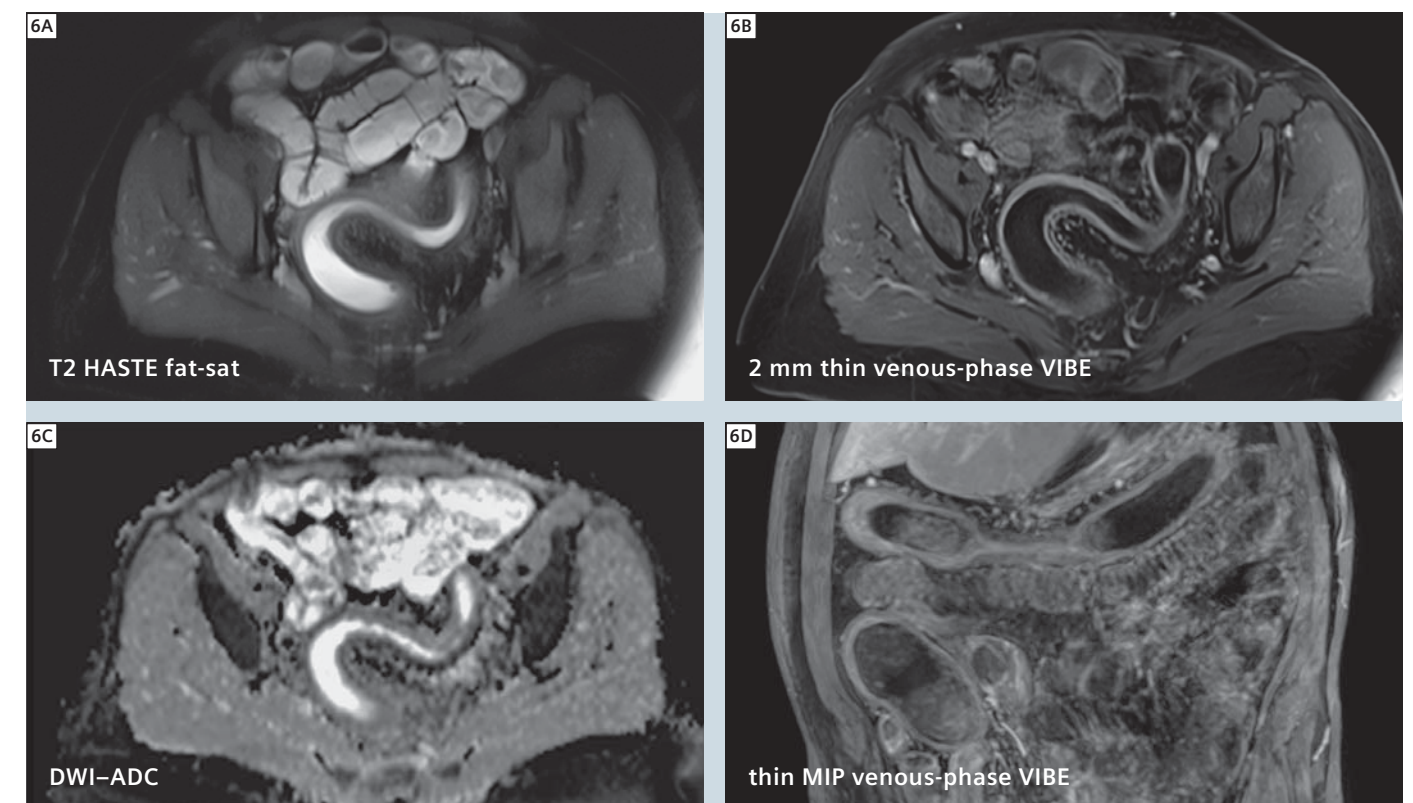
5 Intraindividual comparison study acquired at the 3T MAGNETOM Trio with Tim (lower row) and the 3T MAGNETOM Skyra (upper row, 6 months later). A hypervascular mass can be clearly seen on both arterial phase VIBE images while only the DWI-imaging acquired at the Skyra allows characterizing the mass. Surgery revealed a gastrointestinal stromal tumor (GIST).

decrease patients' anxiety. So far, not a single patient declined an examination in the Skyra due to claustrophobia, which is particularly important for patients in longitudinal research studies. In contrast, a whole new group of patients could be acquired in the meantime: claustrophobic patients and obese patients who could only be examined in low-field open 1T scanners. Approximately 25% of all patients currently examined on the Skyra belong to this latter group. A further potential benefit of the system which has not been fully exploited so far is the imaging of anesthetized patients requiring close medical surveillance. The open and wide bore enables an easy surveillance of the patient with the potential for, e.g., optimal access to a respiratory tube.

User interface

The MAGNETOM Skyra is equipped with a new software platform, *syngo* MR D11 (current version D) that has provided technologists with several positive changes. The MR D11 platform is based on the well-known MR B and MR A *syngo* versions running on all current Siemens MR scanners and hosts various features. The user interface (UI) has been graphically overhauled with unchanged *syngo* functionality so that clinical and research users familiar with *syngo* can immediately start working. Beyond the visible changes in the UI, further technical improvements have been implemented that aim mainly at facilitating and accelerating the actual process of image acquisition. Some well-known features of *syngo* such as AutoCoilSelect have been extended to now include AutoPosition and automated localizers. Based on the registra-

tion of the patient (height/weight) and the body part/exam chosen for the examination the Skyra can automatically start the acquisition and hence save time and – furthermore – unnecessary mouse clicks. The most powerful new tools, however, are the so called Dot (Day optimizing throughput) engines. The Dot engines represent a complete customizable system of automatization, standardization and guidance for technologists. In neuro-imaging, for example, the Dot engine automatically aligns the images and chooses the appropriate FOV. Based on the examination strategies as defined by the user, different protocols will be employed: a standard head exam, an exam based on BLADE sequences in the case of non-cooperative patients or dedicated sequences in case of a special exam focus. In cardiac imaging the Dot

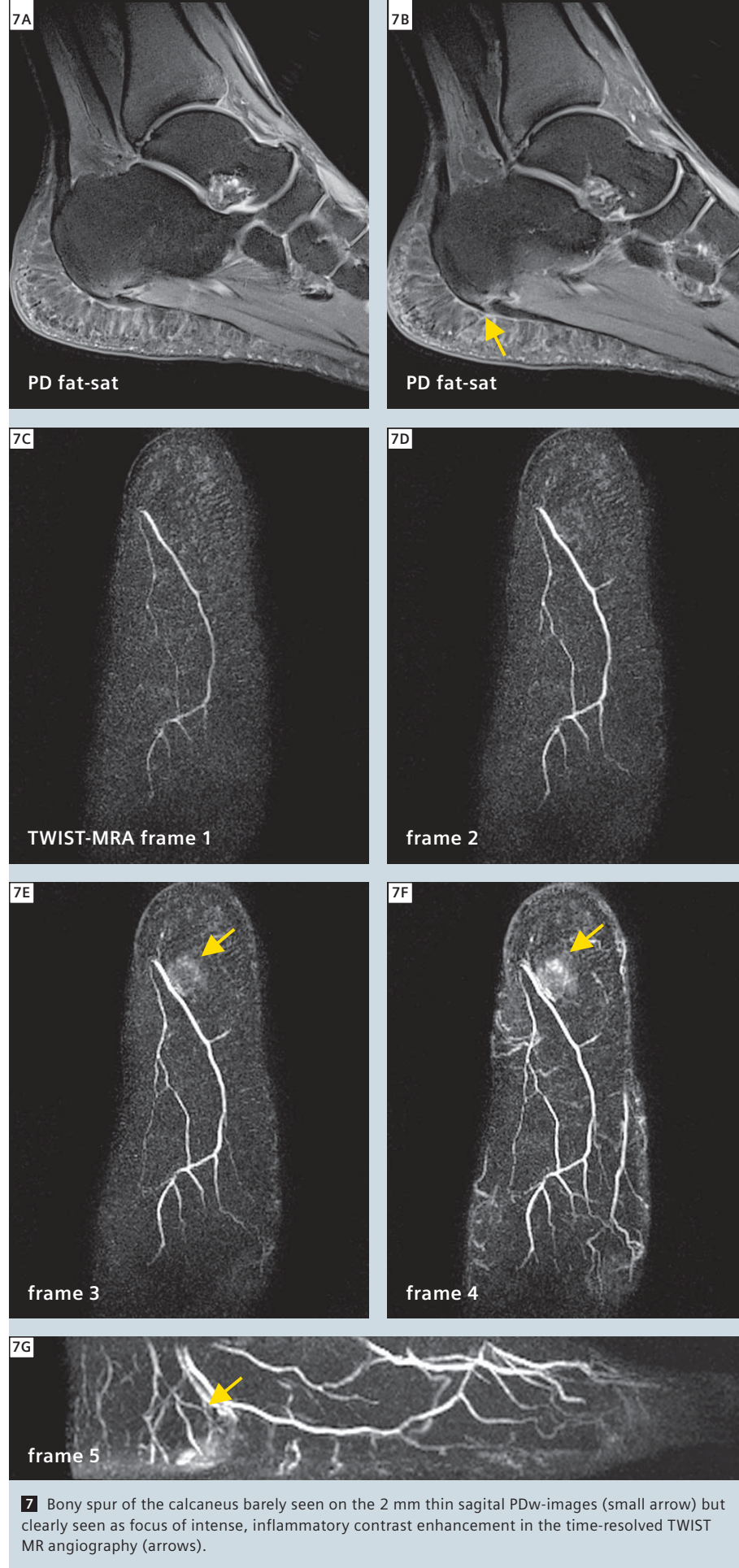


6 Long-segment inflammatory changes in the entire colon of a patient suffering from ulcerative colitis. Bowel wall thickening can be seen in the T2w-images as well as in the T1w-images post contrast but also in the DWI-sequence where a restriction of the diffusion can clearly be seen. Please note the normal appearance of the small bowel.

engines provide special guidance images that support less experienced technologists in the complex positioning for cardiac exams. Also, a single mouse click will change, for example, the cardiac gating of all following sequences. Overall, the main benefit of the Dot engines is not to obviate the need for technologists but to decrease the complexity of MR and to further standardize MR-examinations. It allows follow-up examinations to be conducted with the same parameter settings and hence with constant image quality over time, which is particularly important for quantitative evaluation of lesions in therapeutic clinical and research studies.

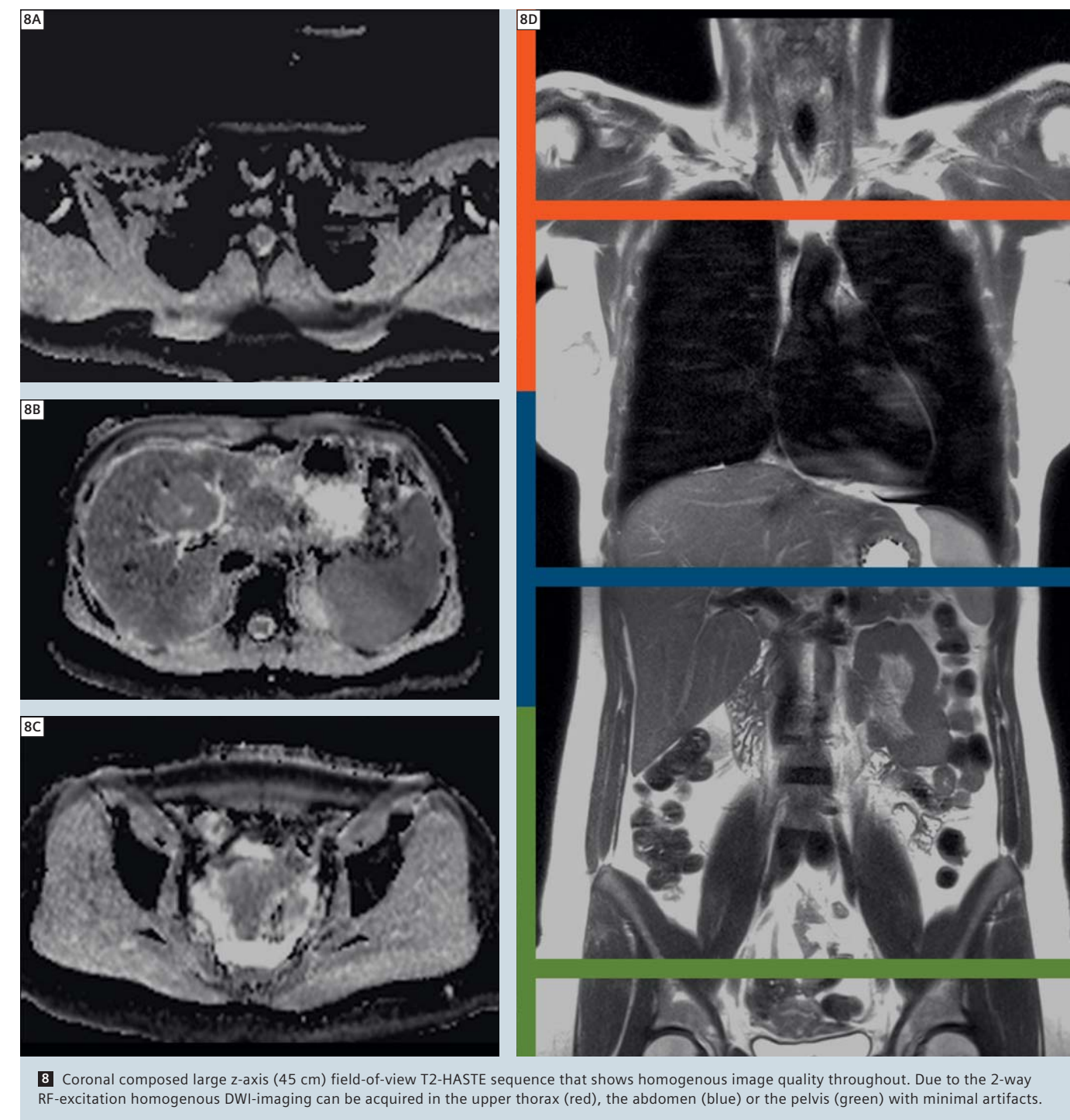
Imaging capabilities

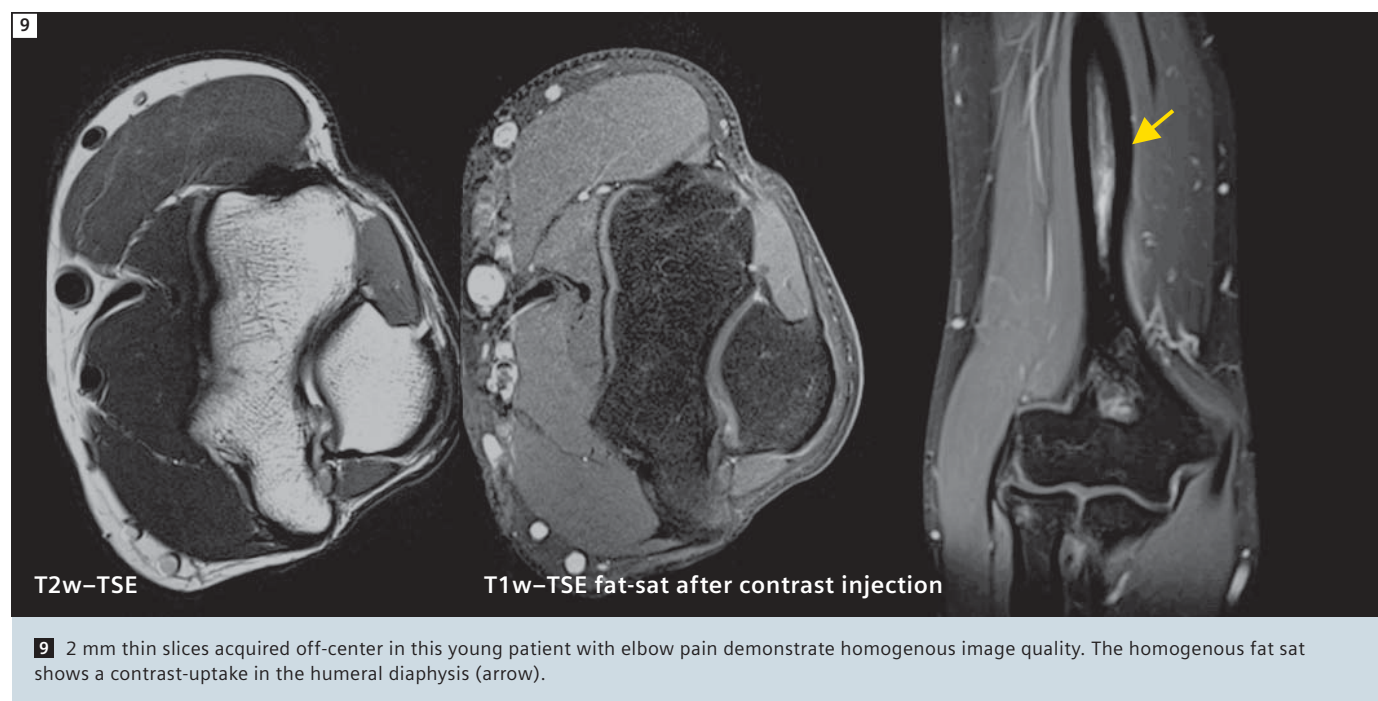
The MAGNETOM Skyra overcomes typical B_1 -inhomogeneities that used to degrade image quality in the spine, abdomen or neck region by a two-way RF-transmission, the TimTX TrueForm technology. Compared to conventional 3T MR-scanners the number of non-diagnostic MR-examinations of the upper abdomen or of the neck could be reduced to virtually zero. While T1w-imaging is less affected by field inhomogeneities (if no fat-sat is applied) T2w-sequences and diffusion-weighted imaging (DWI) massively profit from the two-way excitation in the abdomen. Non-diagnostic image quality of abdominal T2w-sequences has not occurred on our system so far. DWI is notorious for ghosting artifacts in the presence of field inhomogeneities.



With conventional 3T MR-scanners only 30–40% of all examinations yielded robust image quality – whereas Skyra has sustainably increased robustness, leading to a technical success rate of more than 85%. The robustness of abdominal DWI with MAGNETOM Skyra can now be compared to the robust-

ness of 1.5T acquisitions – yet higher b-values of up to 1200 of good quality can be acquired with Skyra. The high SNR achieved with Skyra can also be accounted for by the newly designed multi-element coils ranging, for example, from an 18-channel body matrix coil over a 20-element head and neck





coil to dedicated 16-element extremity coils. The two 18-element body matrix coils mean that large-field-of-view imaging of the abdomen with isotropic voxel size of 1.3–1.7 mm (depending on patient size) has become the clinical standard. The 45 cm z-axis FOV enables depiction of the entire abdomen in patients with, for example, Crohn's disease. While the dynamic T1w-VIBE sequences perfectly demonstrate the anatomy of the organs and vessels as well as the pathologic enhancement areas, DWI sequences can be added to further assess the bowel wall and to characterize potential inter-enteric abscesses. As a matter of course the higher robustness and SNR of DWI with Skyra is a valuable tool for the detection and characterization of complex renal masses such as complex renal cysts. The new extremity coils e.g. allow the acquisition of high-resolution images of the knee or the shoulder with an acquired slice thickness of 2 mm and inplane resolutions of 0.3–0.5 mm². In imaging of the wrist even 1.5 mm

thin slices can be acquired with excellent image quality. Imaging of the shoulder, elbow and wrist reveal a homogenous fat-saturation even though they have to be positioned off-center, which clearly differentiates the MAGNETOM Skyra from conventional 3T MR-scanners. Overall, this excellent quality of DWI studies in the body opens the field for 3T MRI as the leading tool for cancer diagnosis and response evaluation of innovative therapies.

Summary

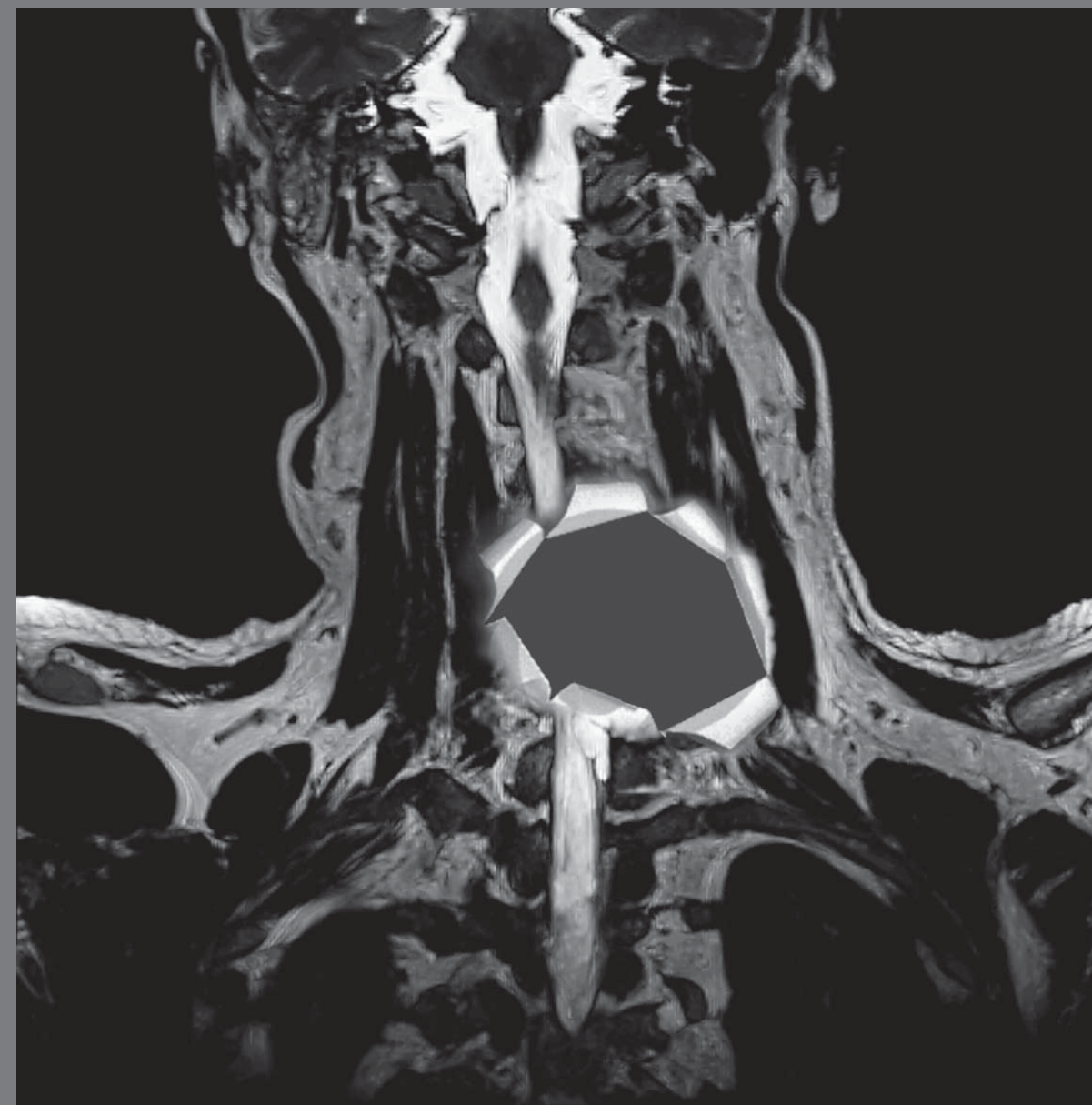
MAGNETOM Skyra is a well-balanced MR-system with the highest technical standards that allows imaging with high reliability and highest image quality throughout the body, thanks mainly to the new coil design in combination with the TimTX TrueForm technology. The new UI in combination with the Dot engines elevate also the user performance to a higher level and allow for better image consistence with less user-

interference. As successful image acquisition is ultimately dependent on patients' corporation, the wide and short bore with internal and exterior illumination takes patients' fear away and guarantees in combination with the fast protocols high patient satisfaction. Its unique image quality, versatility and standardization of complex exams make it particularly attractive as a state-of-the-art system for both research and clinical studies.

Contact

Henrik Michaely, MD
Institute of Clinical Radiology and
Nuclear Medicine
University Medical Center Mannheim
Theodor-Kutzer-Ufer 1–3
68167 Mannheim
Germany
Phone: +49 621 383 2067
henrik.michaely@umm.de

Missing information?



To make sure you have all the information you need, register for our free monthly newsletter on clinical MRI information. Check out case reports from MAGNETOM users around the world and stay up-to-date with Siemens software applications.

Register at
www.siemens.com/magnetom-world
Go to
Publications > Subscriptions

Towards Clinical 7T MRI

Graham C. Wiggins, D Phil; Daniel K. Sodickson, MD, PhD

Center for Biomedical Imaging, Department of Radiology, New York University Langone Medical Center, New York, NY, USA

Introduction

Many researchers in the field of ultra-high-field magnetic resonance have become accustomed to bracing themselves for an oft-repeated question. This question may arise during lulls in conversation with clinical colleagues, or during interviews with interested visitors from the press or the lay public, or, more delicate still, during reviews of our applications for research funding. The question is brief, and to the point: 'When will 7 Tesla scanners be ready for clinical use?' Each of us has his or her own variant on a standard answer to this question, citing particular populations or disease processes in which we have obtained extraordinarily promising images, and outlining the technical hurdles which are gradually falling behind us as research advances. This twofold answer actually encapsulates two distinct strains of 7T research, each of which has an important part to play in defining the eventual clinical role of 7T MR. The first involves identification of unique information available only at ultra-high field strength, enabled for example by extremely high spatial and spectral resolution or by contrast mechanisms which are enhanced as field strength increases. The potential to access this unique information helped to motivate the original development of commercial 7T scanners, and fueled a great sense of enthusiasm as the first whole-body 7T systems arrived on the scene and the first jaw-dropping images began to emerge from those systems. This initial period of exuberant discovery was followed by an equally fascinating but also laborious period of extended basic development, during which 7T research teams began to grapple with the fact that not only the potential infor-

mation content but also the routine operations of 7T scanners differed from what we had come to expect with lower-field scanners. Coils and pulse sequences required careful redesign and optimization, artifacts only hinted at in low-field settings became critical determinants of image quality at 7T, and new constraints on sequence types and parameters changed both the workflow and the content of day-to-day imaging protocols. In the past several years, a growing cadre of high-field researchers has risen to these challenges, seeking to identify the novel RF structures, calibration procedures, and spin manipulations that can eke the best performance out of 7T scanners. The goal of this second strain of research, occurring in parallel with the first, is to replicate some of the breadth and routine image quality of low-field scans, overcoming any and all practical obstacles along the way. Such nominally replicative research has actually spurred a remarkable range of technological and methodological innovation: witness the rise of parallel transmission techniques, reported in previous editions of this magazine, which have become a common component in many 7T research programs but which have already begun to have an impact on lower field strengths. Perhaps of equal importance, however, is the fact that research aimed at achieving high image quality across multiple examination types and body regions addresses an important requirement for what might be considered an ideal clinical 7T imaging platform: the ability to provide unique clinically-relevant information for

a variety of disease processes without sacrificing traditional clinical image content in routine examinations. A 7T scanner with this ability need not be relegated to research tool or niche diagnostic device, but can take its place as a valuable component of the day-to-day clinical arsenal. This article reports on recent developments in the twofold pursuit of unique information content and routine usability at 7T, drawing examples from imaging experience at our institution. The clinical transformation of 7T scanning is by no means complete, but the picture that has begun to emerge is striking.

Unique clinical potential: A gallery of pathology-targeted 7T images from toe to head

The principal advantages of ultra-high field strength for MR imaging are **a)** increased signal-to-noise-ratio (SNR), which can be used to increase spatial resolution, to shorten scan time, and/or to enable imaging of low-sensitivity nuclei other than hydrogen; and **b)** enhanced contrast mechanisms such as those based on susceptibility-related effects. The corresponding challenges associated with 7T MRI include increased inhomogeneity of the RF transmit and the B_0 fields (which result in increased artifacts in various classes of pulse sequence) and increased RF energy deposition into tissue, as quantified by specific absorption rate (SAR), which can limit the range of sequence parameters which may safely be employed. 7T MRI of the brain has now become fairly routine, with the availability of reliable high-performance head coils, and high quality images in a variety of contrasts can be obtained. We will demonstrate later

how a standard 3T clinical neuro imaging protocol can be translated to 7T, illustrating both advantages and challenges of ultra-high-field imaging, and presenting the opportunity to obtain familiar image contrasts while also exploring higher resolution and new contrast mechanisms in a single 7T scan session. The musculoskeletal system has become another highly fruitful area of 7T application, and we begin our catalogue of images there, proceeding from foot to head. Body imaging at 7T (e.g. targeting the heart, abdomen, or pelvis) continues to present unique challenges at 7T. However, 7T body imaging has been the subject of intensive recent attention, with striking examples provided and creative approaches undertaken by various ultra-high-field research groups. As mentioned earlier, parallel transmission and other related methods are currently under investigation to mitigate the particularly substantial B_1 inhomogeneities observed over large fields-of-view in the torso, and also to control SAR. Meanwhile robust imaging of selected body areas such as the breast may already be obtained at 7T with conventional single channel excitation.

At our institution, the past year or two has seen a surge of clinical interest in our 7T scanner, as clinical colleagues in our Department of Radiology and elsewhere have partnered with our basic researchers to probe anatomical details and pathologic processes for which key information has proven to be elusive at lower field strength. The backlog and hours of use of our 7T system have both increased markedly, and it has become an increasingly commonplace occurrence to find a radiologist at the console. The images that follow, all obtained on the Siemens MAGNETOM whole-body 7T scanner at the Center for Biomedical Imaging at NYU School of Medicine (Fig. 1), illustrate some of the multifaceted clinical promise of 7T MRI. These images, which we have sorted by body region and, when appropriate, disease process, are intended to indicate the image quality which may now be achieved at 7T with modern RF coil arrays and pulse sequences. The examples shown here represent only a subset of *in vivo* 7T scans at our center, and an even smaller subset of the work

being done at a growing number of Siemens 7T sites around the world.

Ankle

Figure 2 shows a sagittal image of the ankle obtained at $0.23 \times 0.23 \text{ mm}^2$ in-plane resolution in a healthy adult subject using a custom-designed transmit-receive extremity coil array [1]. Note the high-resolution depiction both of cartilage and of trabecular bone in this image. Although no particular pathology is evident in this example, the ability to resolve cartilage and bone structure at this level becomes a powerful asset for the detection and characterization of disease processes like those in the examples to follow.

Knee Osteoarthritis

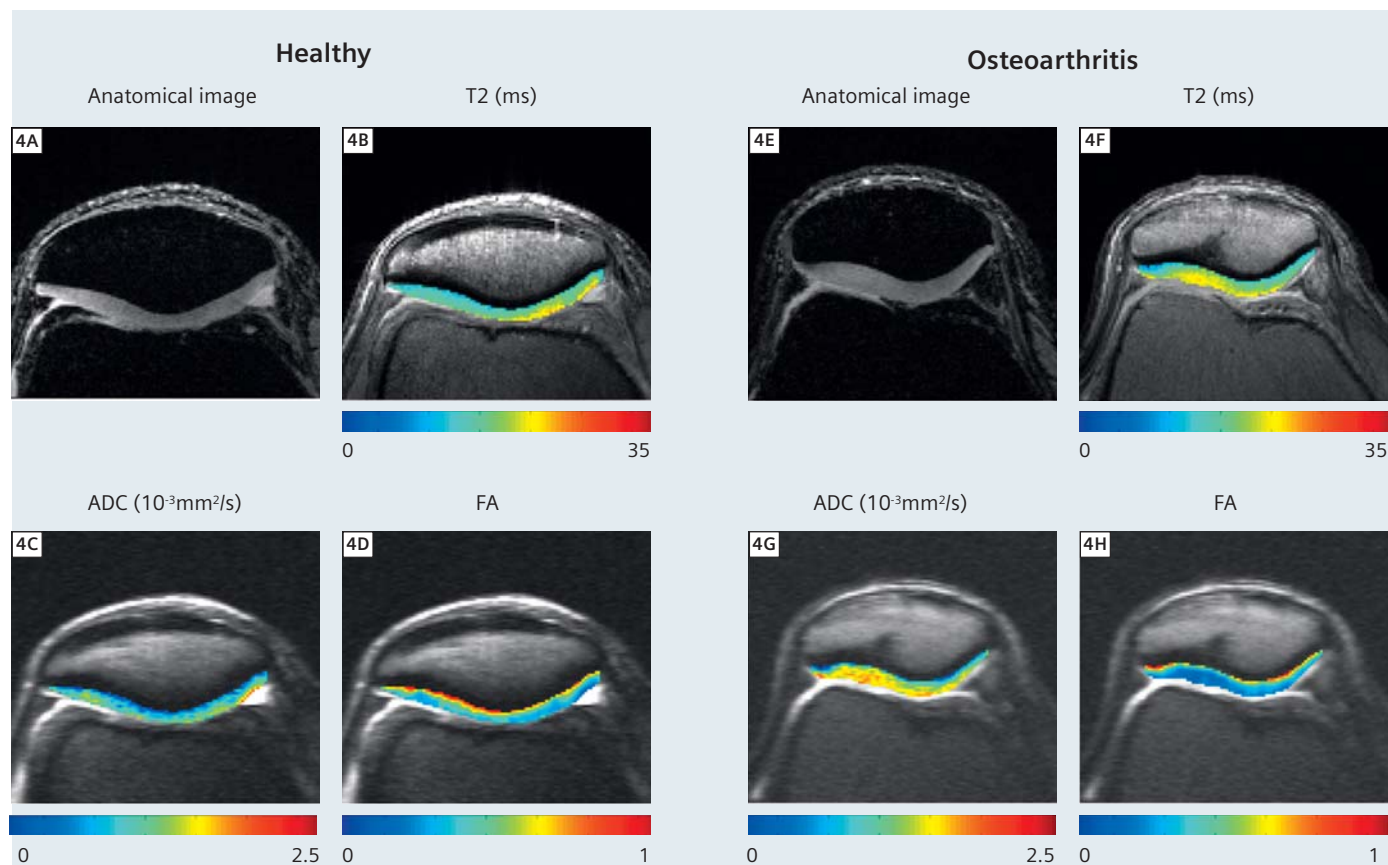
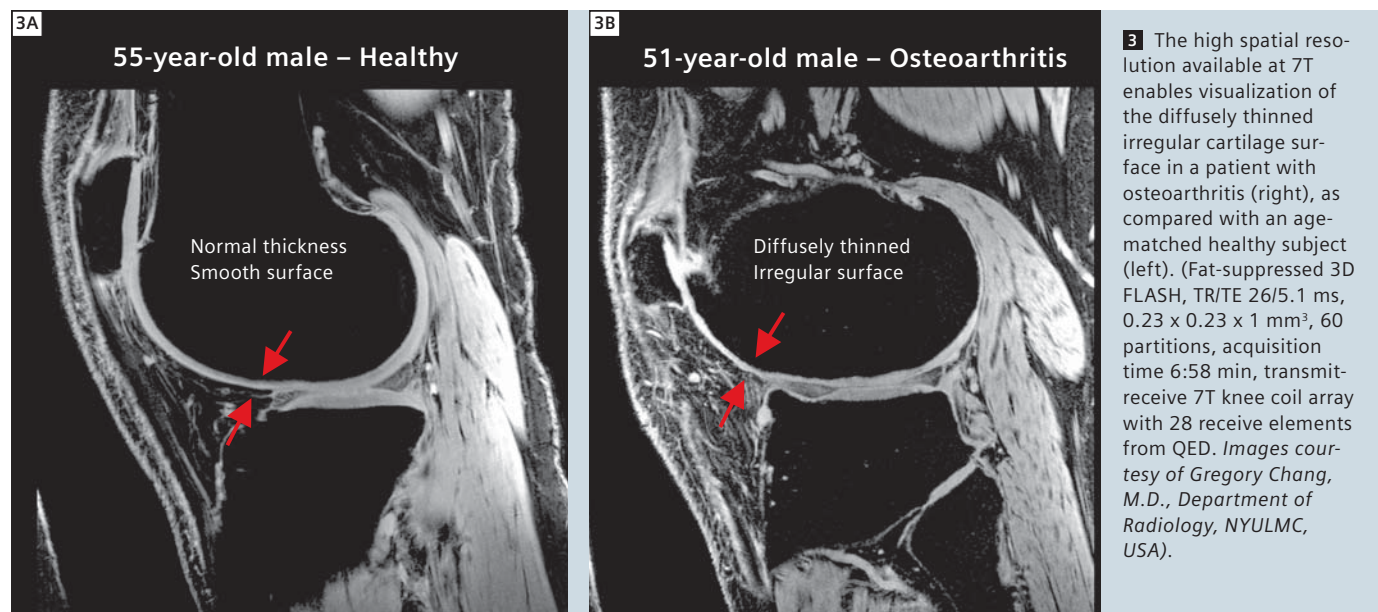
Figures 3 and 4 compare 7T scans of healthy adult subjects with corresponding scans of patients with radiographically documented osteoarthritis. Each of these images was obtained using a 28-element 7T knee coil array developed by Quality Electrodynamics (QED), LLC [2] and expected to be available com-



1 The NYU 7 Tesla scanner.



2 Sagittal image of the ankle of a healthy adult subject. Note high-resolution depiction of cartilage and trabecular bone. (Fat-suppressed 3D FLASH, $0.23 \times 0.23 \times 1 \text{ mm}^3$, TR/TE 26/5.1 ms, 60 partitions, acquisition time 6:58 min, custom-designed transmit-receive extremity coil array with 8 receive elements.)

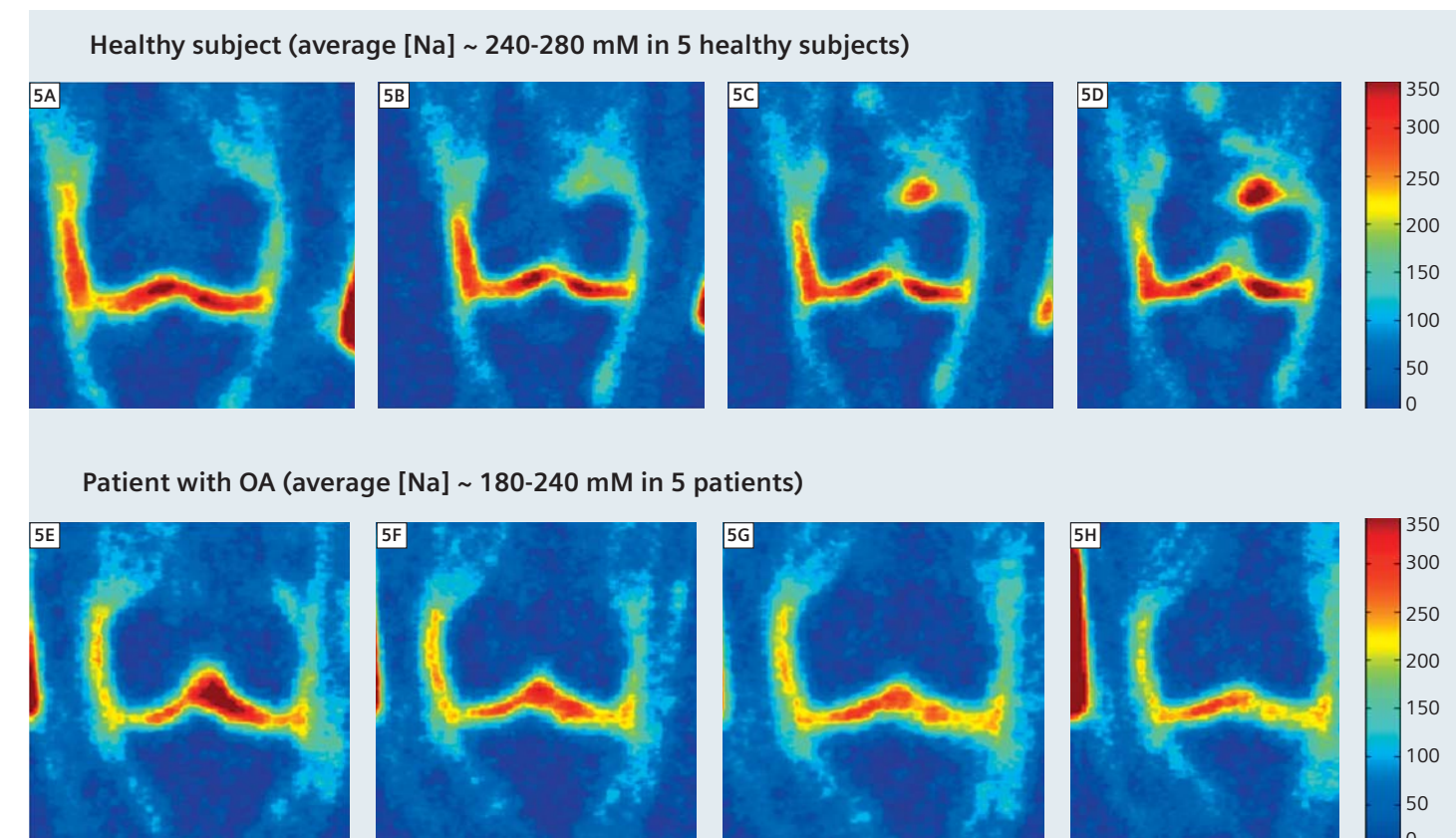


4 Apparent diffusion constant (ADC) and fractional anisotropy (FA) maps derived from line-scan diffusion acquisitions (bottom row) juxtaposed to anatomical images and T_2 maps in the knees of a healthy adult subject (left) and a patient with osteoarthritis (right). Increased ADC and decreased FA are seen in diseased tissue, reflecting microscopic changes in the fiber structure of the cartilage. (Line Scan Diffusion Tensor Imaging sequence: TE/TR/T_{Reff} 46/180/2890 ms, $0.6 \times 0.6 \times 2 \text{ mm}^3$, 5 slices, b-values 5, 450 s/mm², 6 directions, fat-saturation, acquisition time 14:00 min; Anatomical images: T_2^* -weighted fat-saturated GRE, TE/TR 9.2/40 ms, $0.5 \times 0.5 \times 0.5 \text{ mm}^3$, acquisition time 10:00 min; T_2 -mapping acquisitions: multi-slice 2D multi-echo fat-saturated sequence with stimulated echo suppression, TE/TR 16/3500 ms, $0.6 \times 0.6 \times 2 \text{ mm}^3$, 5 slices, echo train length 8, acquisition time 13:35 min. QED 28-element 7T knee array used in all cases. Images courtesy of Jose Raya, Ph.D., NYULMC, USA.)

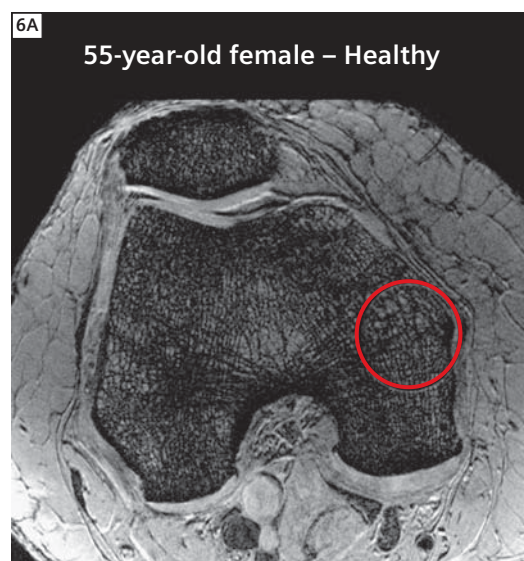
mercially in the near future. The $0.23 \times 0.23 \text{ mm}^2$ in-plane spatial resolution of the sagittal images in Figure 3 is sufficient for direct visual appreciation of the diffusely thinned and irregular cartilage surface in the osteoarthritic patient. The images in Figure 4, on the other hand, are targeted to microscopic changes in cartilage structure and function. In addition to anatomical images and T_2 maps, maps of apparent diffusion constant (ADC) and fractional anisotropy (FA) are shown, derived from line-scan diffusion acquisitions. The decreased FA in the cartilage of subjects with osteoarthritis is consistent with structural damage to the collagen network. The increased ADC, on the other hand, may be shown to result

from reduced proteoglycan content. Figure 5 illustrates the potential value of 7T scanning for a complementary evaluation of proteoglycan content, and therefore of cartilage function. These images represent various slices through 3D volumetric sodium concentration maps encompassing the whole knee in a healthy subject as compared with a patient with osteoarthritis (OA). The enhanced SNR available at 7T enabled whole-knee acquisitions at 2 mm isotropic resolution in less than 15 minutes. Such acquisitions would not be possible at lower field strengths, given inherently low MR sensitivity to sodium nuclei. Through appropriate calibration, sodium images were converted into quantitative

sodium concentrations, which may be seen to be generally decreased in the osteoarthritic as compared with the healthy knee cartilage. Indeed, the average sodium concentration across the knee cartilage in 5 patients with OA was noticeably lower than that in a group of 5 healthy controls. This change reflects a loss of proteoglycans, the removal of whose net negative charge results in a corresponding loss of positively-charged sodium ions to preserve charge balance.



5 7T sodium imaging of cartilage in a healthy subject (top) and a patient with osteoarthritis (bottom). 7T field strength enabled whole-knee 3D volumetric sodium concentration maps at comparatively high resolution in less than 15 minutes. Note reductions in average sodium concentration in arthritic versus healthy cartilage, both in the individual knees shown and in ensembles of 5 patients and 5 controls. (Undersampled 3D radial pulse sequence, TR/TE 80/0.2 ms, $2.0 \times 2.0 \times 2.0 \text{ mm}^3$, single-tuned quadrature sodium coil custom-designed in collaboration with Rapid Biomedical, GmbH. Images courtesy of Ravi Regatte, Ph.D., Department of Radiology, NYULMC, USA.)

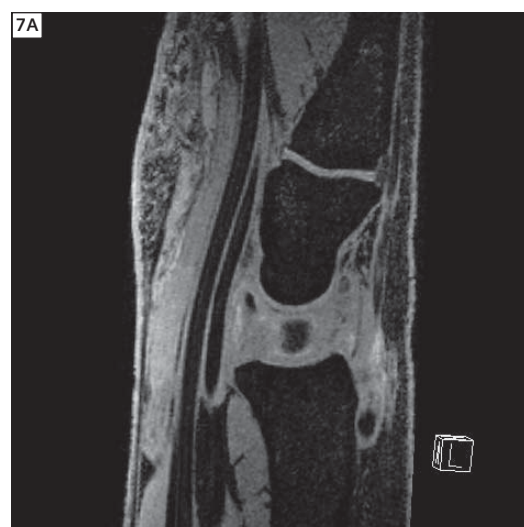


6A 55-year-old female – Healthy

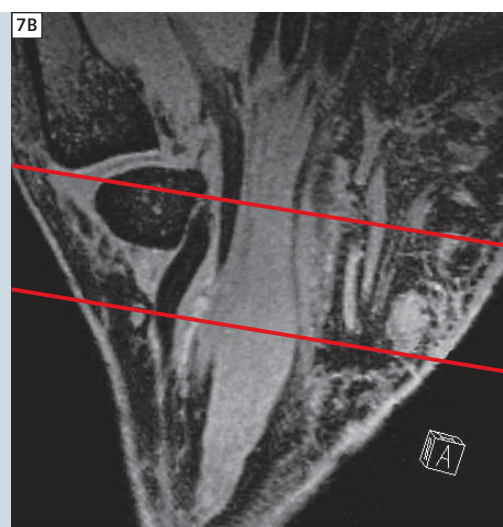


6B 76-year-old female – Osteoporosis

6 Images of the distal femur of a healthy subject (left) and a patient with osteoporosis (right). Note the reduction in density of trabecular bone structure in the patient as compared with the control (for example, in the circled regions of interest). (3D FLASH, TR/TE 20/5.1ms, $0.23 \times 0.23 \times 1.0 \text{ mm}^3$, 80 partitions, acquisition time 7:09 min, QED 28-element knee coil array. Images courtesy of Gregory Chang, M.D., Department of Radiology, NYULMC, USA.)



7A

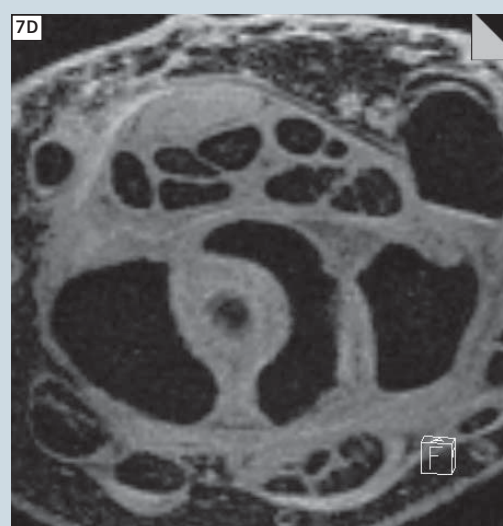


7B

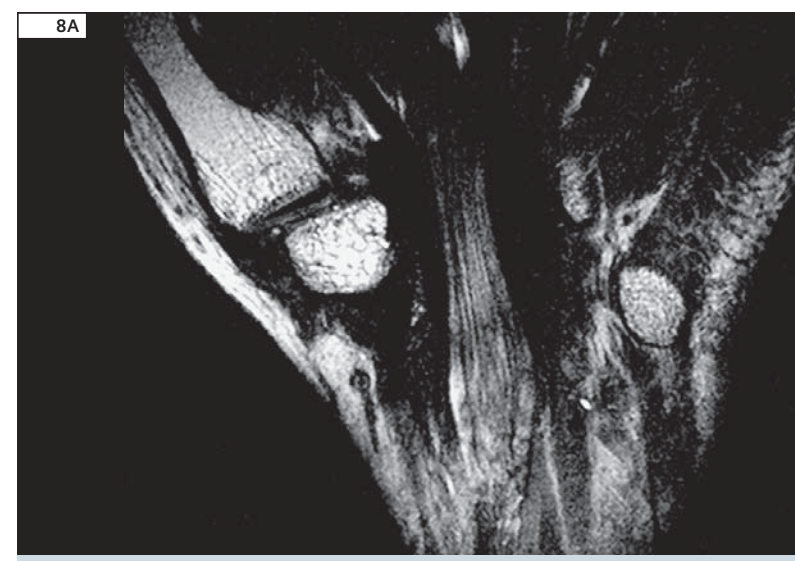
7 Images from a 0.33 mm^3 isotropic 3D gradient-echo acquisition in a patient with Carpal Tunnel Syndrome. The red lines in the top right image indicate the image plane geometry of the bottom two images. The anatomy within the carpal tunnel is clearly delineated, and pronounced swelling of the median nerve may be appreciated. (3D FLASH, TR/TE 40/3.2 ms, $0.33 \times 0.33 \times 0.33 \text{ mm}^3$, 128 partitions, acquisition time 7:10 min, custom-built 8-element 7T extremity coil array. Images obtained as part of a collaboration with Dr. David Chiu, Department of Surgery, NYULMC, USA.)



7C

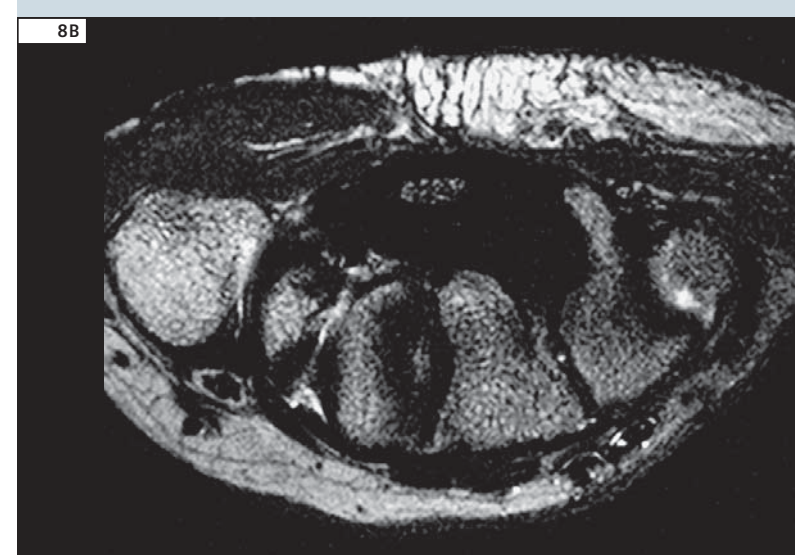


7D

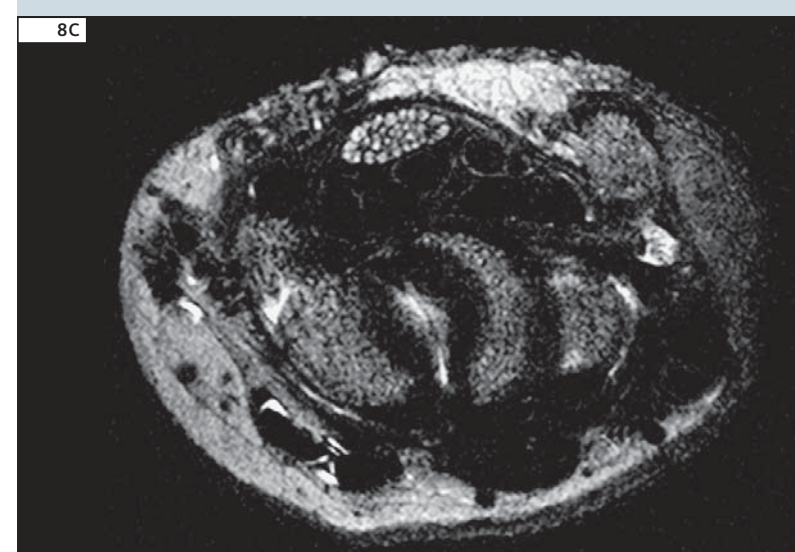


8A

8 2D spin-echo images of a patient with Carpal Tunnel Syndrome. Individual fascicles of the inflamed median nerve can be tracked even through the constriction at the carpal tunnel. (2D TSE, TR/TE 5500/87 ms, $0.2 \times 0.2 \times 1 \text{ mm}^3$, 13 slices, Turbo Factor 13, acquisition time 3:35 min, custom-built 8-element 7T extremity coil array. Images obtained as part of a collaboration with Dr. David Chiu, Department of Surgery, NYULMC, USA.)



8B



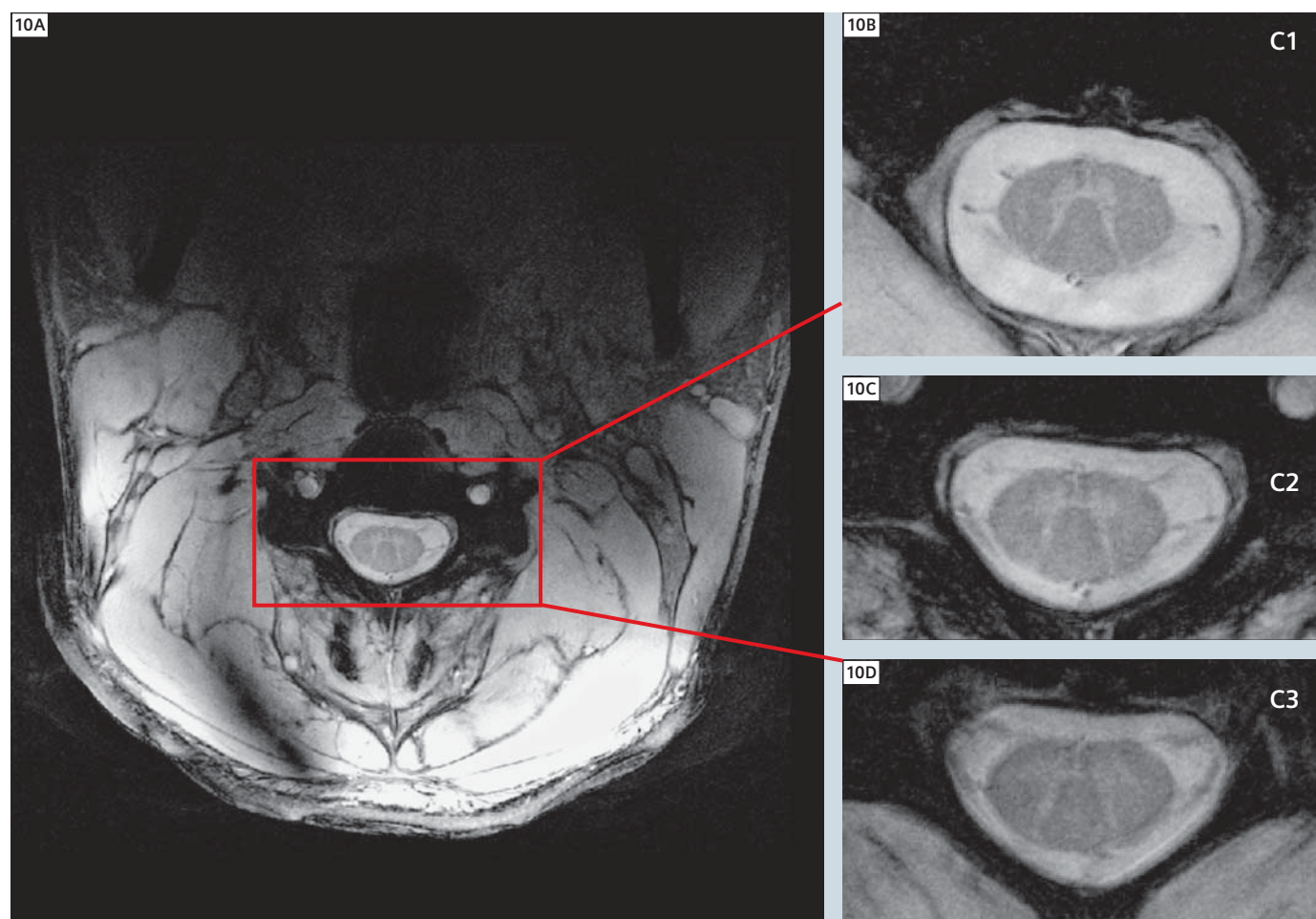
8C

Osteoporosis

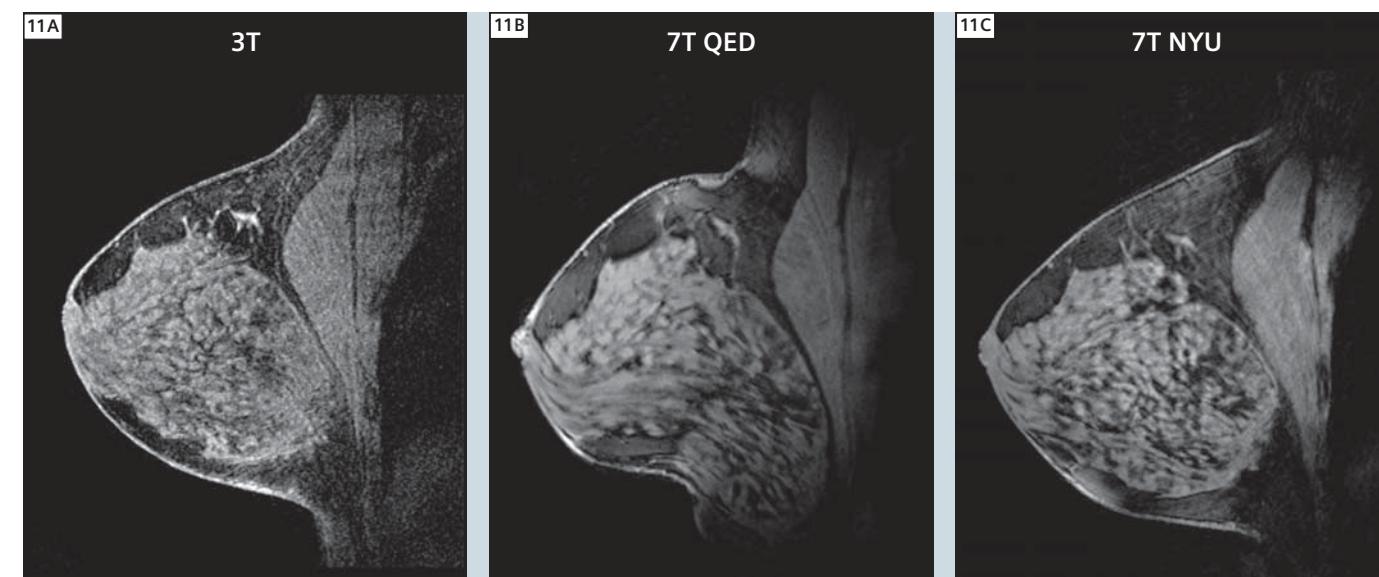
In Figure 6, osteoporotic changes in trabecular bone structure may be appreciated directly from axial 7T images, rather than being probed indirectly through projection-based densitometry. This enables assessment not only of bone density but also of bone quality [3, 4]. The image of the osteoporotic patient shows fewer and more widely-separated dark trabeculae with larger marrow spaces between them. This structure reflects a reduced bone strength and a correspondingly increased fracture risk. In fact, it is believed that bone density alone accounts for only 50–60% of the fracture risk in osteoporotic patients, with the remaining risk attributable to bone quality [3]. Thus, 7T imaging has the potential to improve our ability to assess bone strength and clinical fracture risk.

Wrist Carpal Tunnel Syndrome

In collaboration with interested surgeons at our institution, we have begun to study patients with Carpal Tunnel Syndrome at 7T. The resulting high-resolution depiction of structures surrounding and running through the carpal tunnel, as exemplified in Figures 7 and 8, will enable definitive diagnosis, as well as helping to define surgical approaches and allowing the creation of detailed anatomical atlases in the presence and the absence of pathology.



10 High spatial resolution enables noninvasive visualization of spinal cord structure with unprecedented detail. (2D gradient echo, 0.18 x 0.18 x 3.0 mm³, TR/TE 500/4.91 ms, 5 slices, 4 element transmit-receive C-spine array from Rapid Biomedical GmbH. Images courtesy of Eric Sigmund, Ph.D., Department of Radiology, NYULMC, USA.)



11 Comparison of 3T (left, In Vivo Corp. 4-element receive coil array) and 7T breast images (middle: QED 16-element coil array; right: NYU custom-designed 2-element coil array). 7T images have significantly higher SNR for the same image resolution and total acquisition time. (3D GRE with Fat Saturation, TR/TE 4.37/1.92 ms, 0.6 x 0.6 x 0.6 mm³, 208 partitions, acquisition time 4:28 min. Images courtesy of Ryan Brown, Ph.D., NYULMC, USA.)

Thoracic Spine Cavernoma

Figure 9 documents the case of a 19-year-old patient whose cavernous angioma at thoracic spinal level T5 was discovered incidentally on a 1.5T MR scan at another institution following a sporting accident. Subsequent 3T imaging was also performed in an attempt to determine the feasibility and advisability of surgery for this otherwise asymptomatic young man, but image quality was insufficient to define the detailed internal structure of the lesion and the surrounding spinal cord. The family came to our center in the hope that 7T imaging could further inform their decision and guide a potential surgical approach. A team of physicists, RF engineers, technologists, neuroradiologists, and spinal surgeons was mobilized to address this challenging question. Figure 9 shows sagittal images at two magnifications highlighting the lesion. Using a custom-built 8-channel transmit-receive 7T spine array [5] and optimized gradient-echo and spin-echo pulse sequences, nearby cord structure could be defined with unprecedented detail. Unfortunately,

residual blood products in the vascular lesion resulted in susceptibility-related signal voids in the immediate vicinity of the lesion, preventing ideal delineation. Work is now underway to apply susceptibility-insensitive approaches for further improved visualization. This example highlights both the promise and some of the ongoing practical challenges associated with clinical 7T studies.

Cervical Spine

Figure 10, on the other hand, shows the exquisite delineation of spinal cord substructure which may be achieved at 7T in regions not subject to high susceptibility gradients. In these images, obtained with a 4-element transmit-receive C-spine coil array from Rapid Biomedical, GmbH, excellent spatial detail is observed, differentiating gray/white matter tissue, dorsal and ventral nerve roots, denticulate ligaments, dura mater, pia mater, and rostral-caudal blood vessels.

Breast

Figure 11 compares breast images obtained in the same healthy adult subject at 3T and at 7T. Substantial increases in SNR are evident for the same spatial resolution and total acquisition time in the 7T images. 3T images were acquired using a commercially-available 4-element receive-only 3T breast array from In Vivo Corp. 7T images were acquired both with a commercial transmit-receive breast coil array with 16 receive elements from QED and with a custom-designed 2-element transmit-receive breast array developed at our Center. Our custom-designed 7T coil array has also been used to characterize the distribution of T₁ and T₂ values and B₀ field distribution in healthy breast tissue [6], in preparation for clinical studies to come. Some further development and pulse sequence optimization is called for to reap the full benefits of 7T SNR enhancements, but 7T imaging may be expected to shift favorably the balance of spatial and temporal resolution which is so crucial for characterization of breast cancer.

Brain

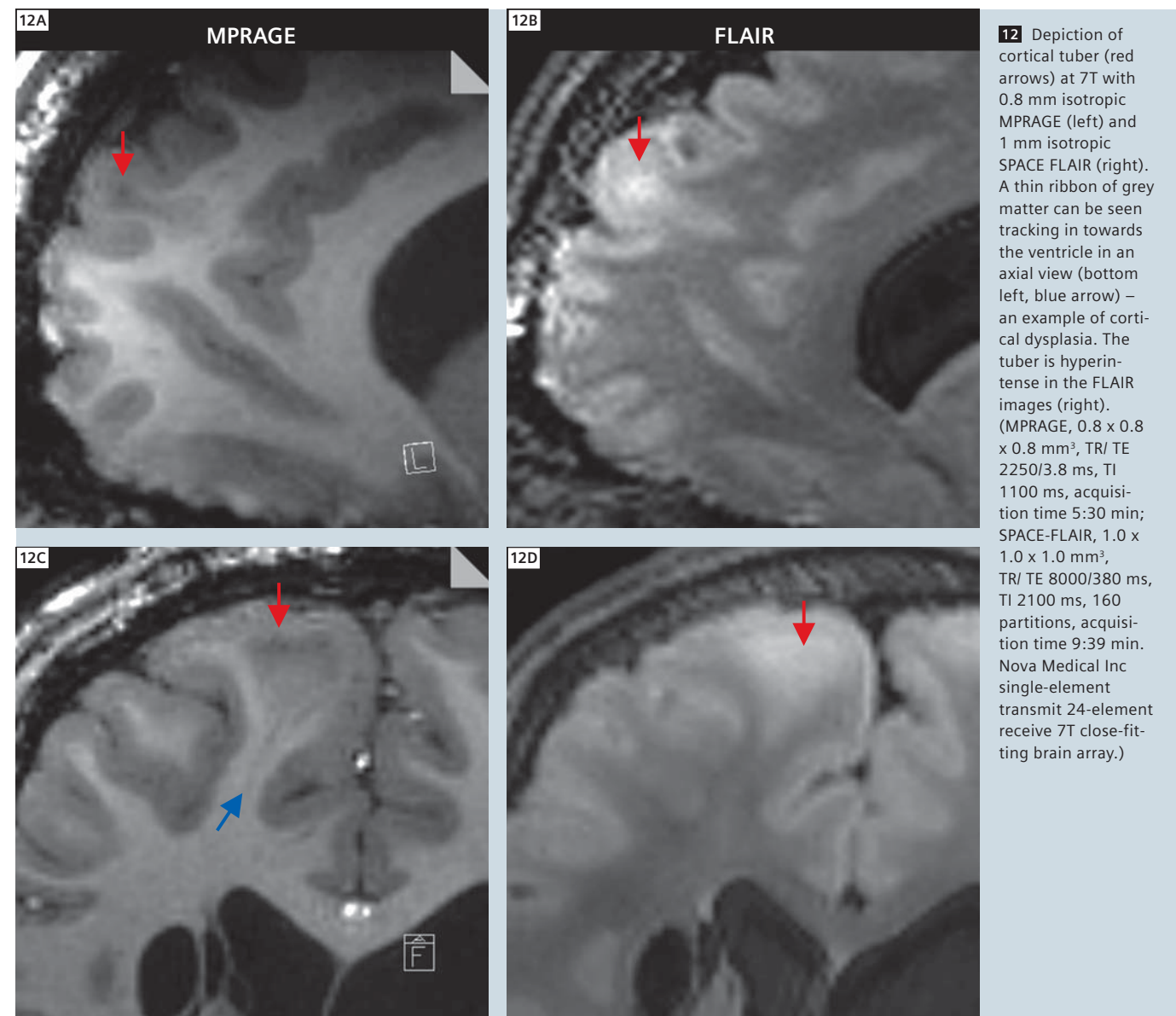
For neurological applications, the high intrinsic SNR and the correspondingly high achievable spatial resolution at 7T may be used to resolve brain structures which have until now eluded direct visualization with MR. Susceptibility- or T_2^* -weighted images in particular can provide extraordinarily high levels of anatomical detail, in addition to affording striking tissue contrast, some of whose precise physical sources are still being investigated. At NYU we have

begun to scan volunteers with a variety of known brain diseases to begin exploring what new clinically- and biologically-relevant information may be found at 7T.

Tuberous sclerosis

Recently, a collaboration has arisen between basic researchers, pediatric neuroradiologists, pediatric neurosurgeons, and epileptologists at our institution, aimed at investigating the biological substrate of tuberous sclerosis, a group of genetic disorders with a spec-

trum of symptoms including potentially intractable seizures. Figure 12 shows images from a patient with tuberous sclerosis. This patient was imaged first with a high resolution T_1 -weighted MPRAGE sequence and then with a 3D FLAIR sequence. The high isotropic spatial resolution of these images allows visualization not only of tubers (like the one indicated by red arrows in the figure), but also of subtle signs of cortical dysplasia (blue arrow).

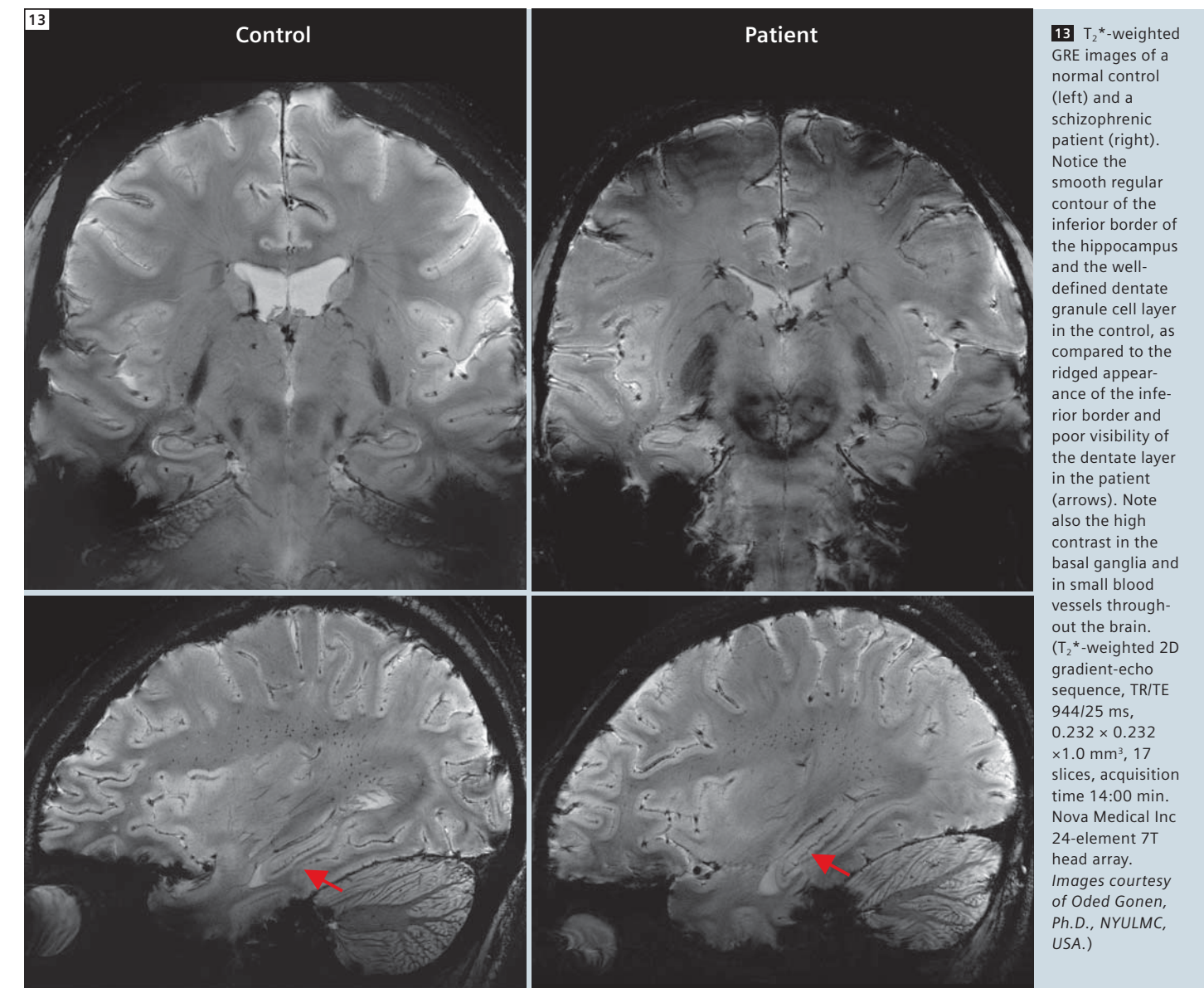


Schizophrenia

Another collaboration between the Departments of Psychiatry and Radiology at our institution resulted in the recent publication of 7T images of the human hippocampus *in vivo* [7], with spatial resolution sufficient to visualize directly such small but important structures as the dentate granule cell layer, which is known to be a locus of neural stem cells. Figure 13 extends this work, showing a direct comparison of coronal

and sagittal images between a schizophrenic patient and a healthy control. The smooth regular contour of the inferior border of the hippocampus and the well-defined dentate granule cell layer in the healthy subject may be compared to the ridged appearance of the inferior border and general poor visibility of the dentate layer in the patient. Note that the dentate granule cell layer cannot be seen in images taken at lower magnetic field strengths. The use of images such

as these is now being contemplated to identify prodromal individuals at risk of developing schizophrenia, in time to initiate preventive treatment before development of chronic life-altering mental illness. Considering the early age of onset of schizophrenia (typically in the late teens to early 20s), prevention has significant social and economic consequences.



Capturing routine clinical information:

Towards a general purpose clinical 7T neuroimaging protocol

Despite the extraordinary image quality available for selected applications, as evidenced by the examples provided earlier in this article, potential clinical enthusiasm for 7T imaging has been hindered by concerns about its ability to support the range of sequence types and provide the range of image contrasts used for routine clinical evaluations at lower field strengths. In this section, we demonstrate that, with appropriate RF coils and pulse sequence modifications, 7T can in fact provide image quality at least equivalent to that available at 3T for a typical clinical neuroimaging protocol. We have developed a set of protocols at 7T which aim to match or exceed the image quality and coverage of the standard 3T clinical protocol within the same total scan time. This makes it possible to obtain a set of images which correspond closely to familiar 3T scans, but also to take advantage of the unique benefits of 7T through increased resolution or through adding on to the protocol specific scans of interest such as T_2^* -weighted GRE, very high resolution MP2RAGE, or Time-of-Flight angiography, obtaining precisely co-registered images in a single scan session. We have chosen certain strategies for optimization of the 7T protocols, but make no claim that these are the optimum sequences for the purpose and offer them primarily as an example and a starting point for others.

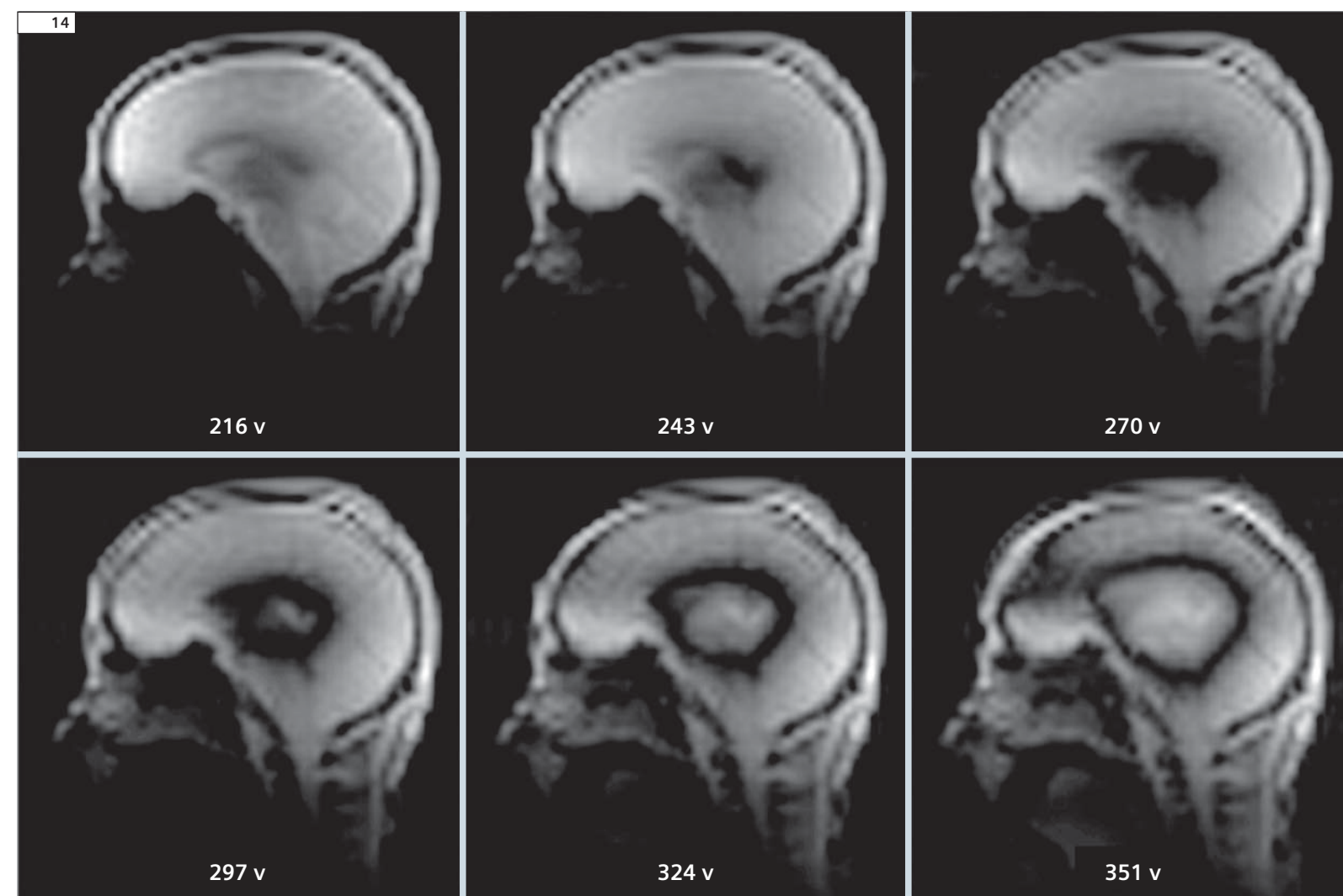
While there are particular sequences which routinely produce superior results at 7T than at lower field strength, for maximum diagnostic power the clinician would like to have images of the whole brain in a number of standard contrasts and formats. A typical 3T clinical brain protocol at NYU includes axial T_2 -weighted TSE, axial FLAIR, axial

T_1 -weighted MPRAGE, axial HemoFLASH, axial Diffusion, and possibly also sagittal FLAIR. Imaging with this 3T protocol is typically performed using the standard Siemens 12-channel Matrix head coil. At 7T we use what has become our work-horse 7T head coil array – a single-element transmit, 24-element receive head array from Nova Medical, Inc (the same coil used to obtain the images in Figures 12–13). Note that Nova Medical has also developed a 32-element head array of similar design for use at 7T, and this array is available as part of the Siemens 7T coil portfolio. Both 7T arrays have very close-fitting geometries, which gives them an advantage in SNR compared to the larger Matrix coil, above and beyond the SNR increase due solely to the increased magnetic field strength.

Our image comparisons, therefore, should not be taken as a strict study of field-strength-related behavior, but rather as an investigation into whether we can use available equipment at 7T to match or exceed the accepted clinical standard at 3T. One additional caveat regarding presentation of the images to follow involves image intensity normalization, which we have used in most cases to remove the variation in brightness caused by the sensitivity profiles of the receive array. At lower field strength, the body coil can be used as a relatively uniform reference to determine the bias field, but there is no clear uniform reference at 7T. While there is a 2D normalization filter on the scanner, it is not always able to correct for steep intensity gradients near the receive elements, and it is not appropriate for 3D scans. Therefore, for this article we have processed 7T images with an off-line intensity normalization algorithm provided with the Firevoxel software, a data analysis tool developed by researchers at NYU [8].

For the interested reader, detailed scan parameters for 3T and 7T protocols will be provided in an online supplement to this article (see URL reference at the end). By leveraging the increased SNR at 7T and by carefully calibrating the required transmit power, we can trade

off parameters in the various imaging sequences to address issues of inhomogeneity and SAR. To this end, one addition we have made to the standard 3T protocol is an in-house-developed ‘ B_1 scout,’ which uses a nonselective preparation pulse and a TurboFLASH readout to determine what scanner transmitter calibration voltage will produce a 90 degree flip in the center of the head [9]. The standard scanner transmitter calibration routine can provide widely varying estimates of the transmitter calibration voltage, depending on head placement relative to isocenter and other issues. We set the transmitter calibration by hand to an expected value based on previous scans (in this case to 270 volts) and then run our B_1 Scout, which acquires a series of 6 images with different preparation pulses (Fig. 14). The RF voltage for the nominally 90 degree preparation pulse is varied from 80% of the value corresponding to the current transmitter calibration value up to 130% in 10% steps, and the entire series is obtained in 10 seconds. When this series is analyzed with the Mean Curve task card we see that the center of the head reaches a 90 degree flip angle when the transmitter calibration voltage is 270. Looking at the series of B_1 Scout images we can also see that more peripheral regions of the brain do not receive the prescribed excitation even with 130% of the manually entered transmitter calibration voltage. This is the familiar B_1^+ inhomogeneity problem, and we keep this in mind as we optimize our acquisitions during the scan session. After acquisition of localizers and the B_1 scout, the first clinical sequence we run at 7T is a 3D MPRAGE with a sagittal slice prescription (adjusted to match the head orientation as seen in the initial 3-plane localizers). The sagittal orientation and 3D nature of this first scan facilitates slice prescriptions for subsequent scans based on anatomical landmarks in the brain such as the anterior commis-

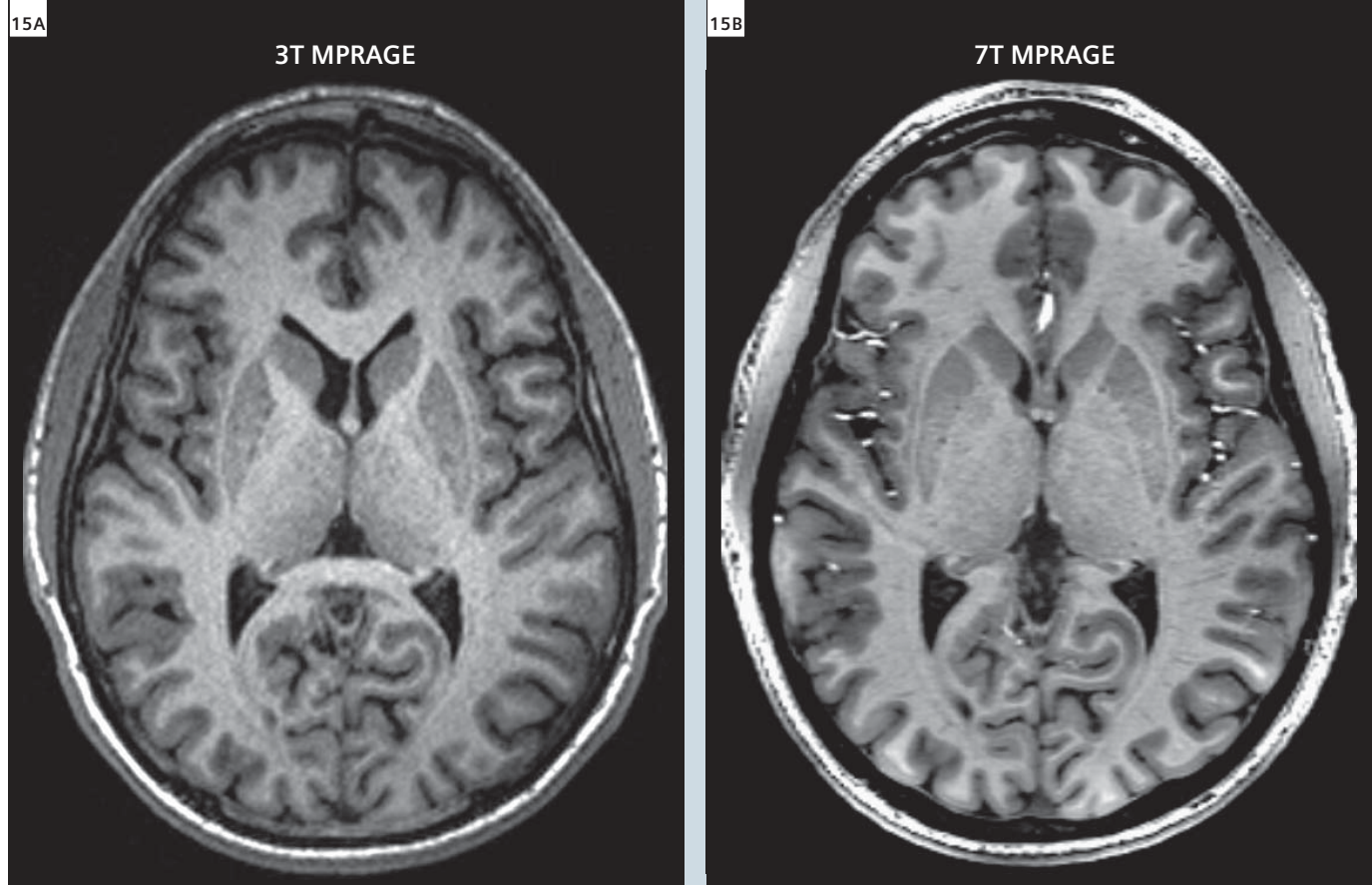


14 In-house-developed ‘ B_1 Scout’, which applies a non-selective preparation pulse of different magnitudes before a TurboFLASH readout. The preparation pulse corresponds to 90 degrees flip at the transmitter reference voltage listed below each image. Black areas represent regions where the preparation pulse achieved a 90 degree excitation. With a transmitter reference of 270 volts we achieve the prescribed flip angle at the center of the head. (TR/TE 2000/1.3 ms, BW 2000, flip angle 8°, 4.7 x 4.7 x 8 mm³, acquisition time 0:12 min.)

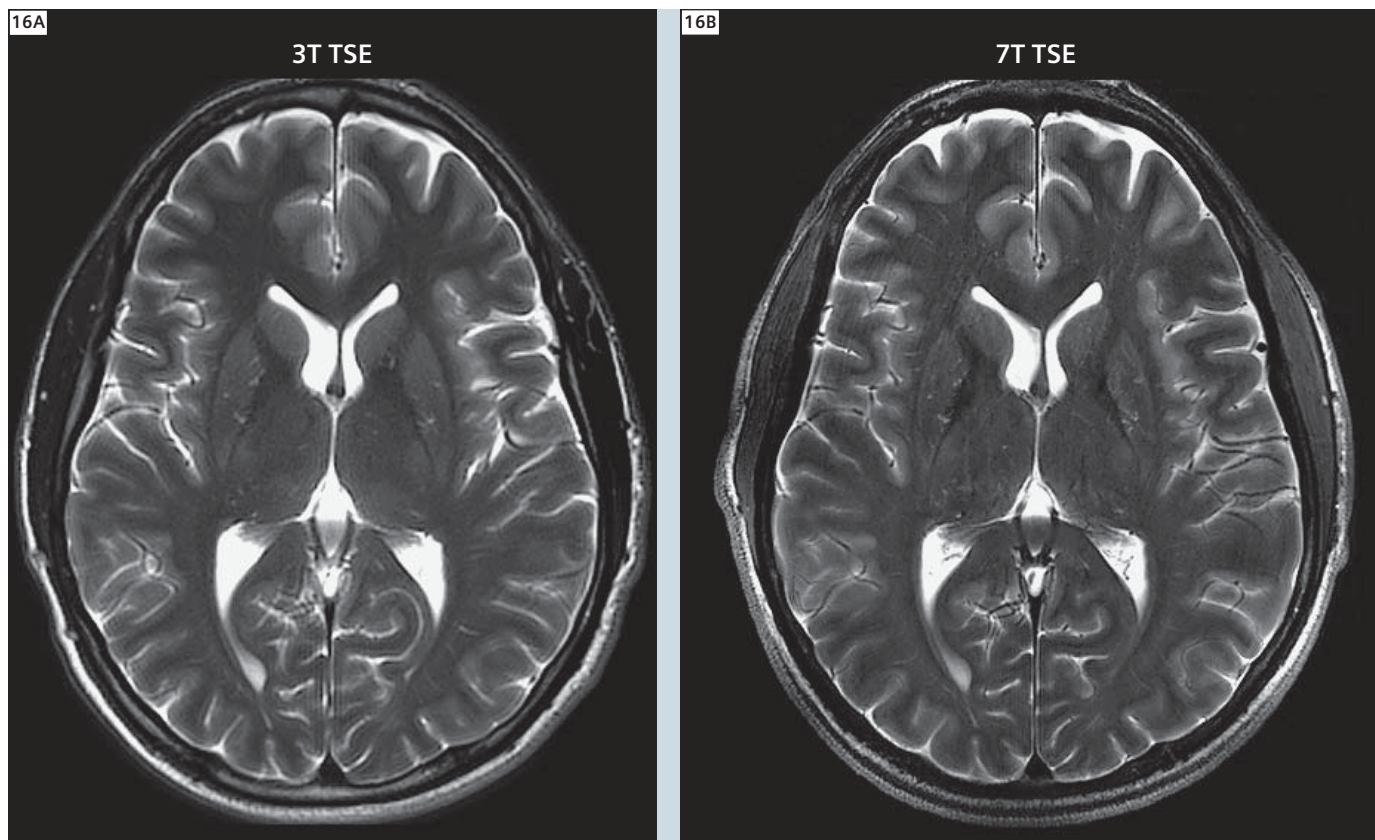
sure – posterior commissure (AC-PC) line. Given that MPRAGE is a low SAR sequence, and that we know the transmitter reference voltage needed to reach the target flip angle in peripheral brain regions is higher than for central regions, we open the adjustments task card before running the scan and set the transmitter reference voltage to 375 for this scan. For comparison to the 3T standard, we reformat the scan into 1 mm thick axial planes, as shown in

figure 15. Even with the higher resolution at 7T the SNR clearly exceeds that of the 3T image, and lengthening the inversion time (TI) to 1100 ms maintains good grey-white contrast. The 7T image clearly depicts thin perivascular spaces in the white matter which are lost in the noise in the 3T image. It should be noted, however, that while the MPRAGE sequence produces high quality T_1 -weighted images at 7T, there are some issues such as loss of contrast immediately superior to the nasal and auditory sinuses (due to B_0 variation)

and in the inferior temporal lobes and inferior cerebellum (due to weak RF transmit field in these regions). These artifacts may be reduced through sequence modifications [10, 11] but we have used the standard (“product”) sequence here.



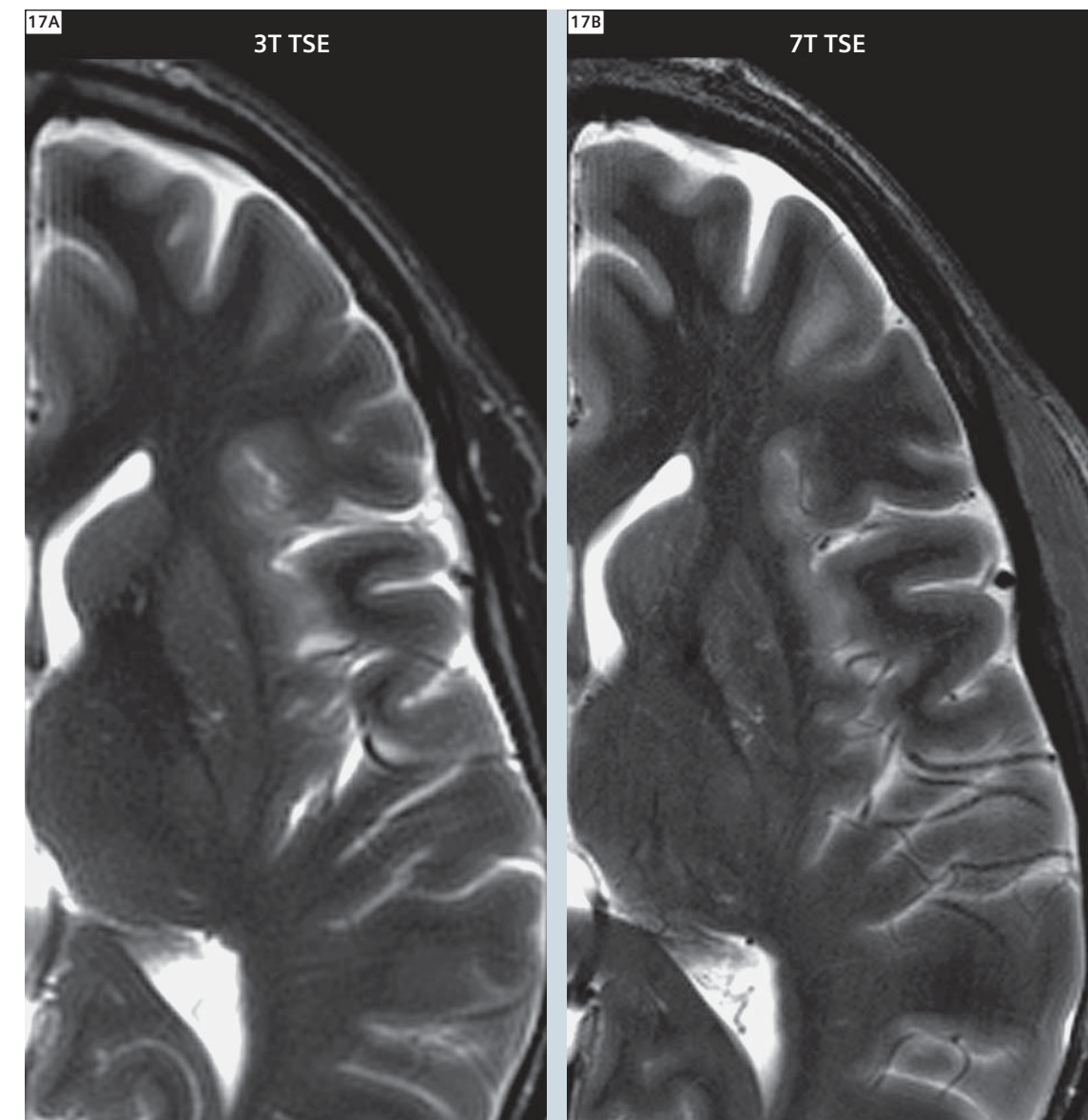
15 Comparison of 3T and 7T MPRAGE scans. Left: 3T, $1.0 \times 1.0 \times 1.0 \text{ mm}^3$ isotropic resolution, acquisition time 4:31. Right: 7T, reformatted to $0.7 \times 1.0 \times 1.0 \text{ mm}^3$, acquisition time 4:38.



16 Comparison of 3T and 7T TSE images. Left: 3T, $0.7 \times 0.7 \times 5.0 \text{ mm}^3$, 30 slices, acquisition time 3:16 min. Right: 7T, $0.5 \times 0.5 \times 3.5 \text{ mm}^3$, 40 slices, acquisition time 3:06 min.

The next sequence is a T_2 -weighted TSE. The TSE sequence is a high SAR sequence due to its series of refocusing pulses. However, thanks to the high SNR provided by our 7T system we can lengthen TR and reduce the field of view, still reaching higher resolution than at 3T within the same total scan time. With regards to the transmitter reference voltage, here our strategy is

to use the highest voltage that can be set without triggering the SAR monitor, so that we can get the full number of slices we desire. In this case we set the transmitter reference voltage to 230 volts. The comparison images (Fig. 16, details in Fig. 17) show that we have achieved very similar contrast and superior image quality with the 7T image.



17 Details from images in Figure 16.

Standard FLAIR sequences are difficult to utilize at 7T because their inversion pulse and multiple refocusing pulses result in very high SAR. We have achieved similar image contrast to 3T FLAIR images with 2D sequences, but only with a limited number of slices in the standard scan time due to SAR restrictions. However, a Siemens works in progress (WIP) sequence is available based on the 3D SPACE sequence which provides FLAIR-like contrast. We run this at 1 mm isotropic resolution, and the scan time is roughly equivalent to the

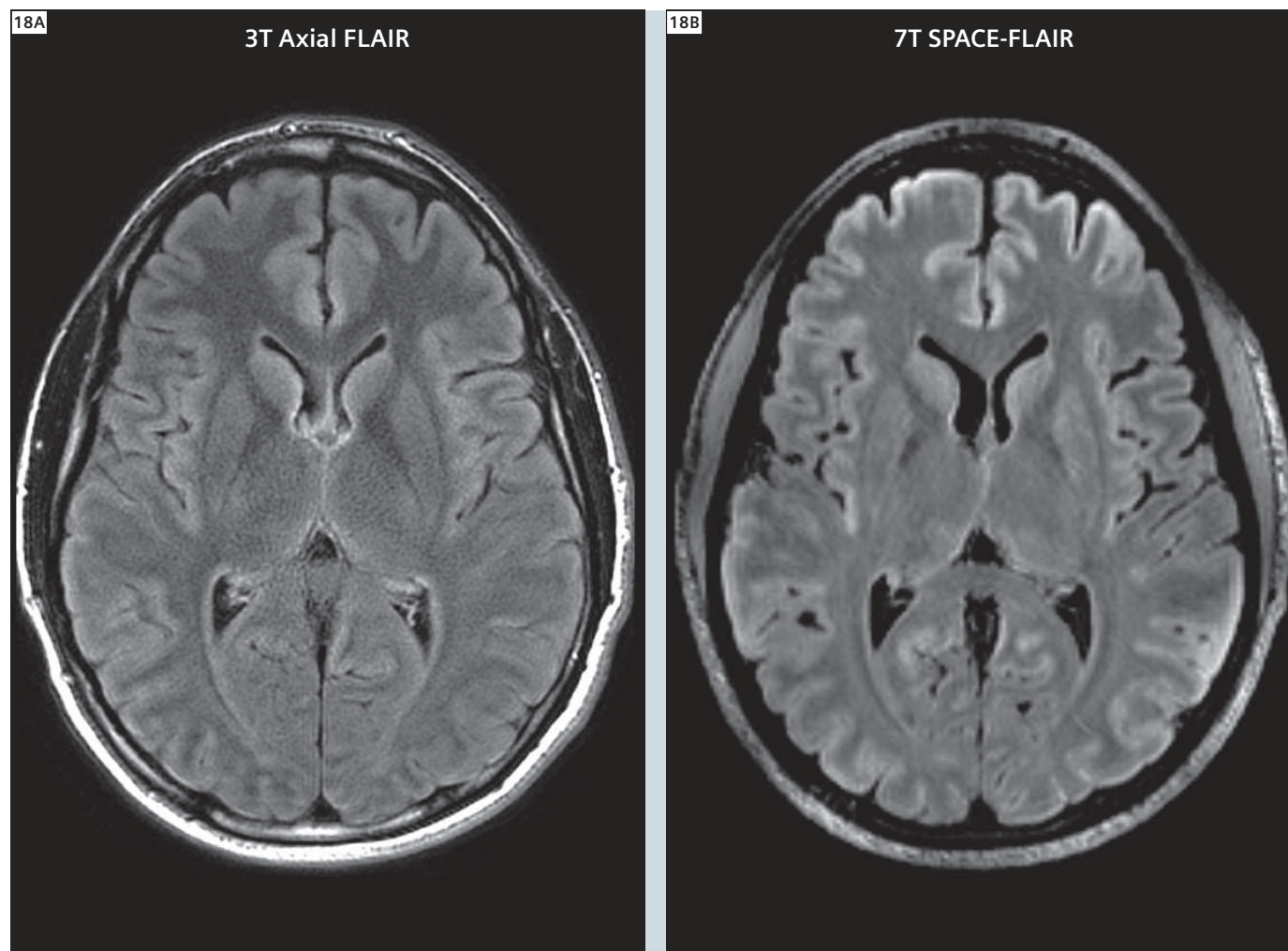
combined time taken for axial and sagittal FLAIR scans at 3T. The isotropic 7T data set can then be reformatted into any plane. With this set of parameters we are able to boost the transmitter reference voltage again without exceeding the SAR limits, in this case to 350 volts. We compare 3T images with corresponding 7T reformats in Figures 18–19. There are some differences in the contrast and image quality between the 3T and 7T scans, but with this new sequence we can add FLAIR contrast to our standard protocol at 7T. We have not yet evaluated

whether the two approaches yield equivalent diagnostic information about brain lesions, but the 7T SPACE-FLAIR is a powerful addition to the array of sequences which can be run routinely at 7T. HemoFLASH is a 2D FLASH sequence with a relatively long TE to create low signal in regions of high susceptibility, such as where there are blood products from hemorrhage or microbleeds. At 3T a TE of 20 ms is used, with a slice thickness of 5 mm. Given that T_2 in the brain is shorter at 7T than at 3T, we reduce TE to 15 ms, and also reduce the slice thick-

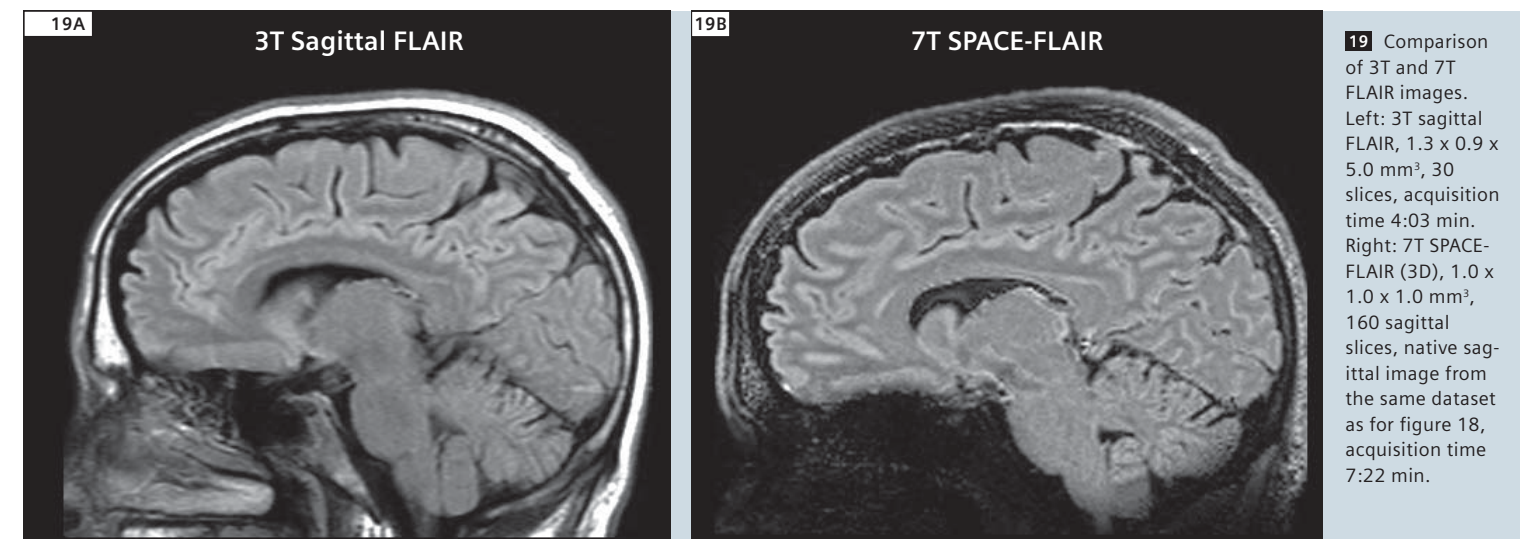
ness to 3 mm to reduce signal dropout over the nasal sinus due to through-plane dephasing. Since FLASH is a low SAR sequence, we leave the transmitter reference voltage at 350. We achieved similar image contrast at higher resolution in the same total scan time as compared to 3T (Fig. 20), though there is still some signal dropout over the nasal sinus at this level of the brain. Further sequence optimization might reduce the sensitivity to susceptibility to a level more similar to 3T if desired. Diffusion-weighted sequences are espe-

cially challenging at 7T. They are particularly susceptible to distortions due to B_0 variations, which are larger at 7T than at 3T even with diligent shimming, and the shorter T_2 at 7T leads to loss of signal because of the long readout time. Various strategies can be employed to overcome these issues, such as using higher acceleration rates with parallel imaging, and using thinner slices. We have reduced the matrix size and increased the acceleration compared to the 3T protocol, resulting in a lower in-plane resolution, and have reduced the slice thick-

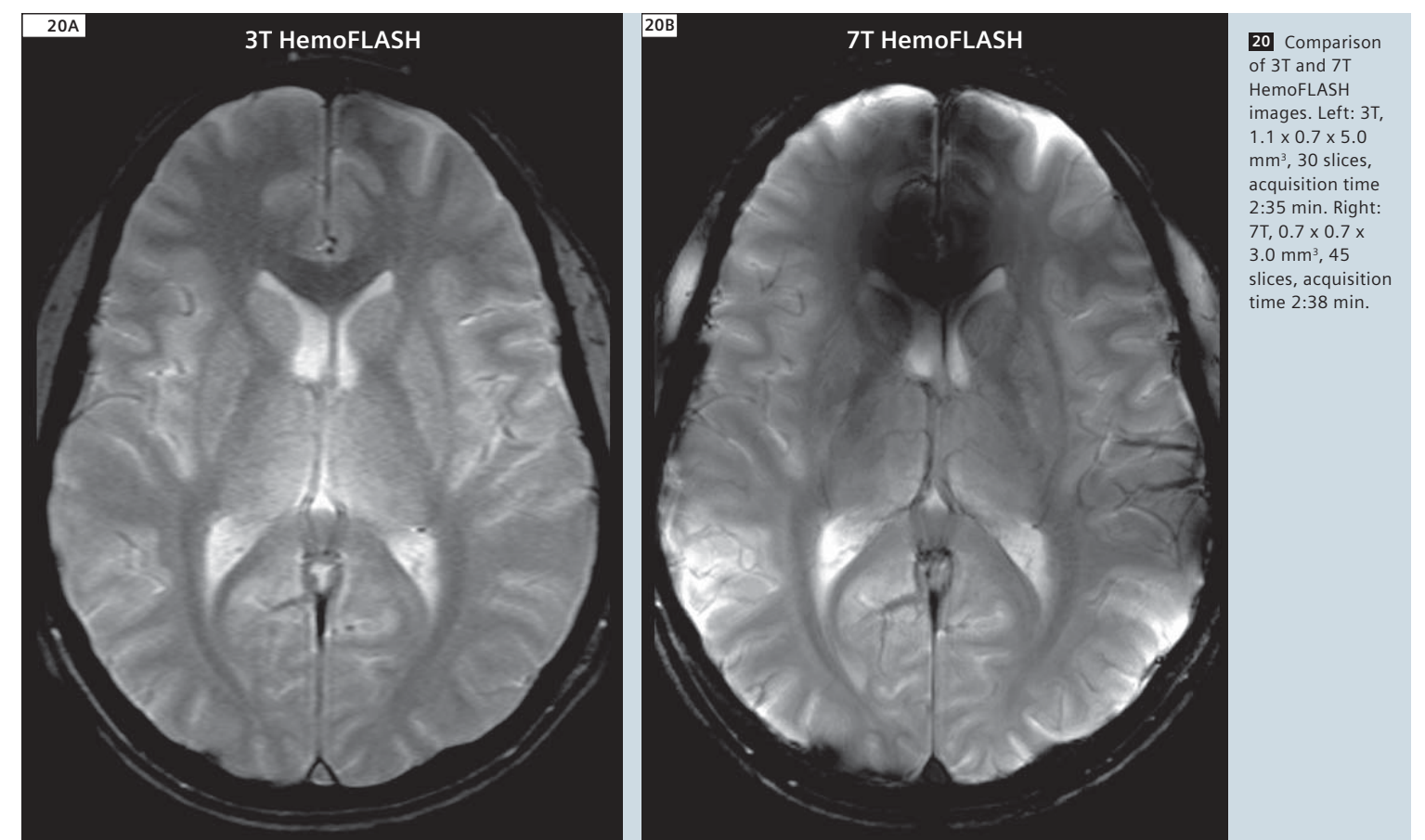
ness to 3 mm from 5 mm to reduce through-plane dephasing. SAR constraints prevented us from obtaining more than 22 slices with the nominal 270 volt transmitter reference. The 7T diffusion images shown in figure 21 are not of equal quality to those that are routinely obtained at 3T. That said, substantial research efforts have been devoted to diffusion imaging at 7T, and specialized sequences may well be able to achieve improved results [12–15].



18 Comparison of 3T and 7T FLAIR images. Left: 3T axial FLAIR, $0.7 \times 0.7 \times 5.0 \text{ mm}^3$, 30 slices, acquisition time 3:02 min. Right: 7T SPACE-FLAIR (3D), $1.0 \times 1.0 \times 1.0 \text{ mm}^3$, 160 sagittal slices, axial reformat, acquisition time 7:22 min.



19 Comparison of 3T and 7T FLAIR images. Left: 3T sagittal FLAIR, $1.3 \times 0.9 \times 5.0 \text{ mm}^3$, 30 slices, acquisition time 4:03 min. Right: 7T SPACE-FLAIR (3D), $1.0 \times 1.0 \times 1.0 \text{ mm}^3$, 160 sagittal slices, native sagittal image from the same dataset as for figure 18, acquisition time 7:22 min.



20 Comparison of 3T and 7T HemoFLASH images. Left: 3T, $1.1 \times 0.7 \times 5.0 \text{ mm}^3$, 30 slices, acquisition time 2:35 min. Right: 7T, $0.7 \times 0.7 \times 3.0 \text{ mm}^3$, 45 slices, acquisition time 2:38 min.

In total, not including time spent on localizers, adjustments and slice placement, the 3T protocol occupies 21 minutes 23 seconds, while the 7T protocol requires exactly 22 minutes. In these essentially equivalent times we have produced improved T₁- and T₂-weighted images at higher resolution, comparable FLAIR images, and higher-resolution HemoFLASH images which suffer from greater artifacts near regions of high susceptibility gradient than corresponding 3T images. Only with diffusion imaging do we encounter a real challenge in matching the image quality routinely obtained at 3T, consistent with the general experience that diffusion imaging requires additional optimization at 7T. There are a few caveats for the 7T protocol. To match the imaging time we often used a reduced phase field-of-view, creating a rectangular field-of-view that requires more careful placement and may not provide sufficient coverage for all heads. We have also been unable within the scope of this article to show the entire set of slices covering the whole brain, and there are a few regions in the inferior portion of the brain where susceptibility and RF inhomogeneity artifacts are more pronounced in the 7T images than in the 3T images. Figure 22 summarizes the results just

presented, illustrating graphically the near-equivalence of routine clinical image content at 3T and 7T, combined, of course, with the potential for unique information only at 7T. Note that similar imaging protocol optimizations are likely to be possible for routine musculoskeletal imaging, and further work may bring other body areas to a similar state.

Conclusions

As is evidenced by the images presented here, unique information relevant to various disease processes is currently available at 7T. There has been some hesitation in the past about clinical use of 7T, given concerns about whether traditional clinical information remained available despite changes in contrast, signal inhomogeneity, SAR limitations, etc. Here we demonstrate for a neuroimaging protocol that, with appropriate RF coils, pulse sequence modifications, and imaging protocol optimizations, 7T scanners may be used without losing most of the key clinical information content present in traditional imaging protocols at lower field strengths. This means that unique information of new clinical value may now be accessed without sacrificing routine clinical information. After a period of exploratory development, a portfolio of robust commercially-avail-

able coils is now available for 7T use. Availability of self-shielded 7T scanner designs should facilitate incorporation into hospital settings, and ongoing work on 7T body imaging should continue to expand the list of indications for 7T imaging.

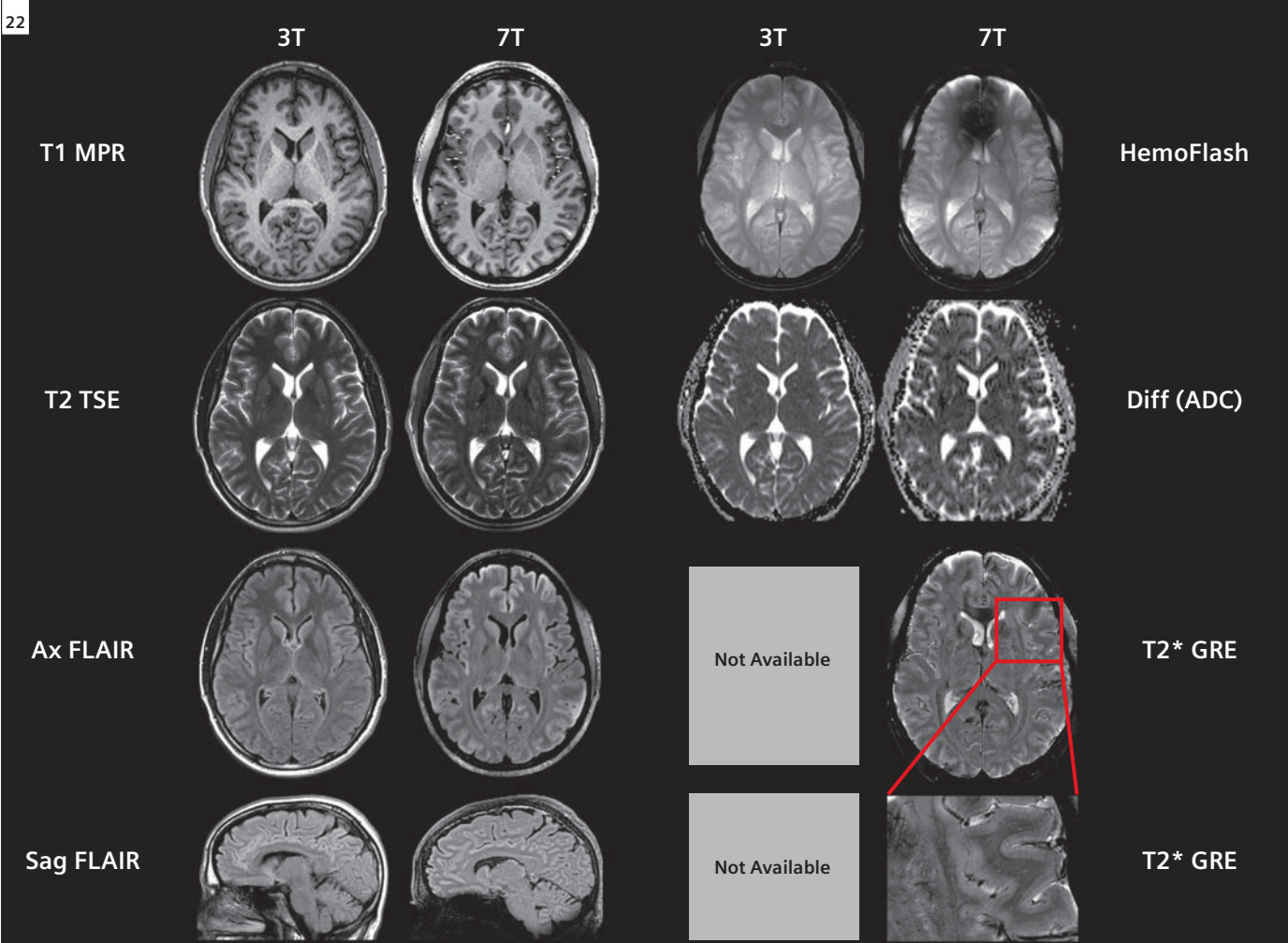
In summary, the tool of 7T MRI has been carefully tuned over the past several years. And increasingly, when we are asked the question ‘When will 7 Tesla scanners be ready for clinical use?’ we may finally respond: ‘Bring on the patients!’

Acknowledgments

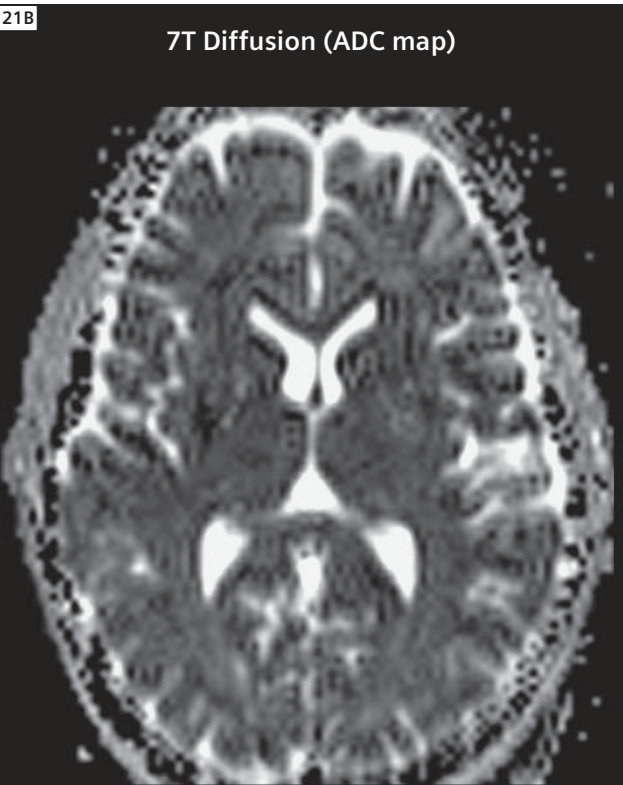
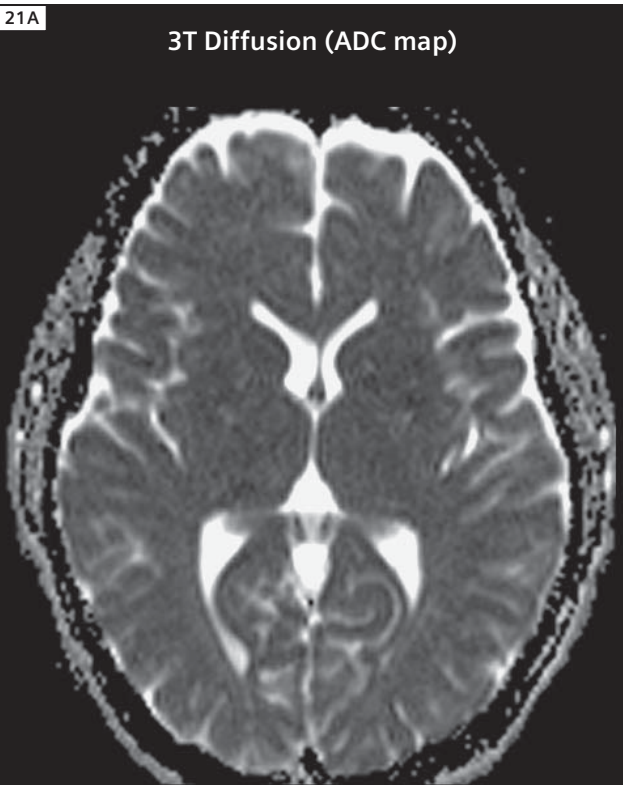
In addition to all of the colleagues who have generously provided images for this article, we would like to thank Dr. Christian Glaser for helpful conversations and consultations. We are also grateful to the Siemens 7T team and particularly to Bernd Stoeckel for his ongoing collaboration, motivation, and support of our 7T work.

Note on online content

Detailed pulse sequence parameters for the images and scanning protocols described in this article may be found at www.siemens.com/magnetom-world



22 Summary of results from 3T and 7T neuroimaging protocols. Images at the bottom right indicate that traditional clinical information, preserved by the 7T protocol, may be supplemented by sequences which provide unique information at 7T.



21 Comparison of apparent diffusion constant (ADC) maps at 3T and 7T. Left: 3T, 1.2 x 1.2 x 5.0 mm³, 30 slices acquisition time 3:56 min. Right: 7T, 1.8 x 1.8 x 3.0 mm³, 22 slices, distance factor 66%, acquisition time 4:06 min.

References

1. Wiggins G, Zhang B, Duan Q, Lattanzi R, Biber S, Stoeckel B, McGorty K, Sodickson D. 7 Tesla Transmit-Receive Array for Carotid Imaging: Simulation and Experiment. Proceedings 17th Scientific Meeting, International Society for Magnetic Resonance in Medicine, 2009:393.
2. Finnerty M, Yang X, Zheng T, et al. A 7-Tesla High Density Transmit with 28-Channel Receive-Only Array Knee Coil. Proceedings 18th Scientific Meeting, International Society for Magnetic Resonance in Medicine. Stockholm, Sweden., 2010:642.
3. Wehrli FW, Song HK, Saha PK, Wright AC. Quantitative MRI for the assessment of bone structure and function. NMR Biomed 2006;19(7):731-64.
4. Chang G, Pakin SK, Schweitzer ME, Saha PK, Regatte RR. Adaptations in trabecular bone microarchitecture in Olympic athletes determined by 7T MRI. J Magn Reson Imaging 2008;27(5):1089-95.
5. Duan Q, Sodickson DK, Lattanzi R, Zhang B, Wiggins G. Optimizing 7T Spine Array Design through Offsetting of Transmit and Receive Elements and Quadrature Excitation. Proceedings 18th Scientific Meeting, International Society for Magnetic Resonance in Medicine. Stockholm, Sweden., 2010:51.
6. Brown R, McGorty K, Moy L, DeGregorio S, Sodickson DK, Wiggins GC. Sub-Millimeter Breast Imaging and Relaxivity Characterization at 7T. Proceedings 19th Scientific Meeting, International Society for Magnetic Resonance in Medicine. Montreal, CA, 2011:3092.
7. Prudent V, Kumar A, Liu S, Wiggins G, Malaspina D, Gonen O. Human hippocampal subfields in young adults at 7.0 T: feasibility of imaging. Radiology;254(3):900-6.
8. Mikheev A, Nevsky G, Govindan S, Grossman R, Rusinek H. Fully automatic segmentation of the brain from T1-weighted MRI using Bridge Burner algorithm. J Magn Reson Imaging 2008;27:1235-1241 (<https://files.nyu.edu/hr18/public/projects.html>).
9. Chung S, Kim D, Breton E, Axel L. Rapid B₁⁺ mapping using a preconditioning RF pulse with TurboFLASH readout. Magn Reson Med 2010;64(2):439-46.
10. Wiggins C. A Simple Method Of Improving MP2RAGE Inversion Coverage at 7T. Proceedings 15th Scientific Meeting, International Society for Magnetic Resonance in Medicine. Seattle, WA, USA, 2007:3448.
11. Marques JP, Kober T, Krueger G, W. van der Zwang W, Van de Moortele P-F, Gruetter R. MP2RAGE contrast optimization at 7T and applications. Proceedings 17th Scientific Meeting, International Society for Magnetic Resonance in Medicine. Honolulu, HI, USA, 2009:2698.
12. Mukherjee P, Hess CP, Xu D, Han ET, Kelley DA,

Imaging and Relaxivity Characterization at 7T. Proceedings 19th Scientific Meeting, International Society for Magnetic Resonance in Medicine. Montreal, CA, 2011:3092.

13. Heidemann RM, Porter DA, Anwender A, Feiweier T, Heberlein K, Knosche TR, Turner R. Diffusion imaging in humans at 7T using readout-segmented EPI and GRAPPA. Magn Reson Med 2010;64(1):9-14.
14. von Morze C, Kelley DA, Shepherd TM, Banerjee S, Xu D, Hess CP. Reduced field-of-view diffusion-weighted imaging of the brain at 7 T. Magn Reson Imaging 2010;28(10):1541-5.
15. Sigmund EE, Gutman D. Diffusion-weighted Imaging of the Brain at 7 T with Echo-planar and Turbo Spin Echo Sequences: Preliminary Results. Magnetic Resonance Imaging 2011:in press.

Vigneron DB. Development and initial evaluation of 7-T q-ball imaging of the human brain. Magn Reson Imaging 2008;26(2):171-80.

Contact
Daniel K. Sodickson, MD, PhD
Vice-Chair for Research, Department of Radiology
Director, Center for Biomedical Imaging
New York University Langone Medical Center
660 First Avenue, Fourth Floor
New York, NY 10016
USA
Phone: +1 212-263-4844
Daniel.Sodickson@med.nyu.edu

MRI-Based Pattern Recognition Methods for Dementia Diagnostics

Stefan Klöppel, MD¹; Richard Frackowiak, MD²

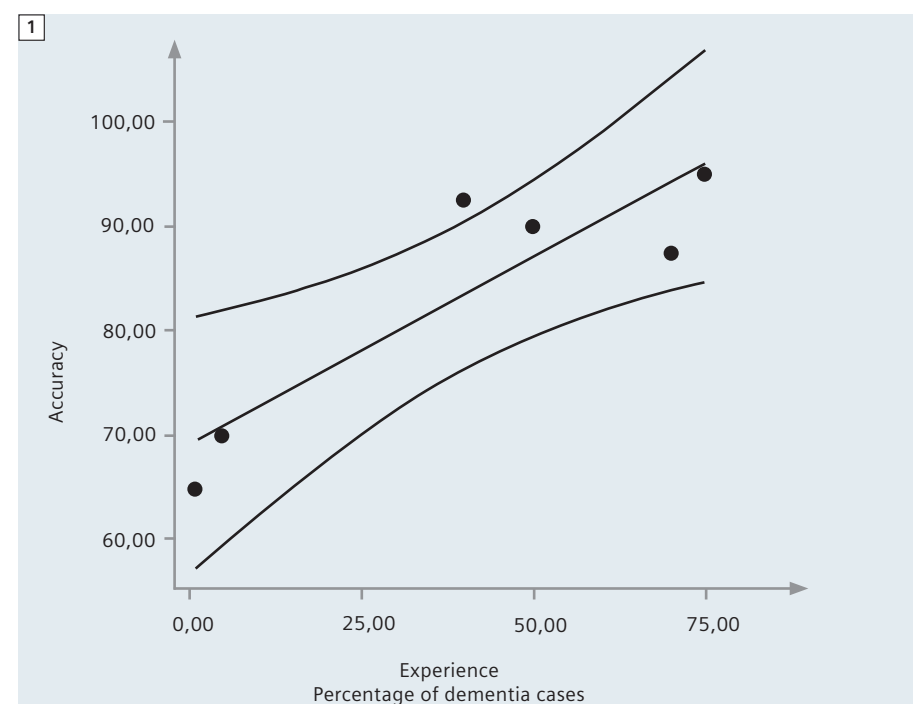
¹Freiburg Brain Imaging, University Hospital Freiburg, Germany

²Centre Hospitalier Universitaire Vaudois, Lausanne, Switzerland

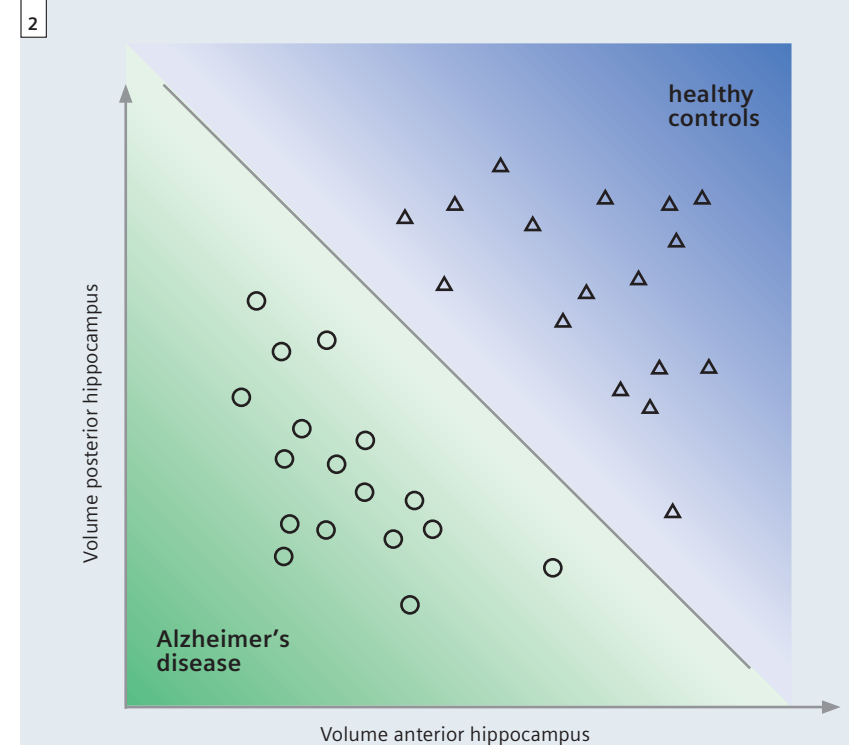
It is estimated that the number of people that will suffer from dementia by 2020 will be more than 40 million, with an increasingly higher proportion coming from developing countries [8]. Historically, brain imaging with CT or MRI has largely been used to rule out alternative and especially structural causes of the dementia syndrome. This approach is consistent with established diagnostic consensus criteria such as those published by the NINCDS-ADRDA [14]. Recently, there has been a realisation that MRI may add positive predictive value to a diagnosis of Alzheimer's disease (AD) [9]. Several studies demonstrate that using MRI to evaluate atrophy of temporal lobe structures can contribute to diagnostic accuracy [2, 22], but these findings have yet to be applied to routine clinical radiological practice, let alone in the general practice or internal medicine setting [22]. Recent developments in machine-learning analysis methods and their application to neuroimaging [4–7, 10, 11, 13, 15, 18–21] are very encouraging in relation to the levels of diagnostic accuracy achievable in individual patients. These multivariate methods promise fully-automated, standard PC-based clinical decisions, unaffected by individual neuroradiological expertise which strongly affects diagnostic accuracy (Fig. 1). They are sufficiently sensitive to successfully separate those with mild cognitive

tively normal [3] or identify those cognitively normal subjects who will convert to MCI [4]. So far, computational anatomy has been used to characterise differences between the brains of patients and normal age-matched volunteers at the group level. What is needed in the clinical setting is a diagnostic method applicable to each and every individual. Multivariate classification methods such as linear support vector machines (SVM)

integrate information from the whole brain. In the context of machine learning, individual MR images are treated as points located in a high dimensional space. Figure 2 illustrates this procedure in an imaginary two-dimensional space: In this example the two groups to be classified are represented by circles and triangles. It can be seen that the groups cannot be separated on the basis of values along one dimension only and that



1 Shows an increasing accuracy of radiologists more experienced in the diagnosis of dementia [10].

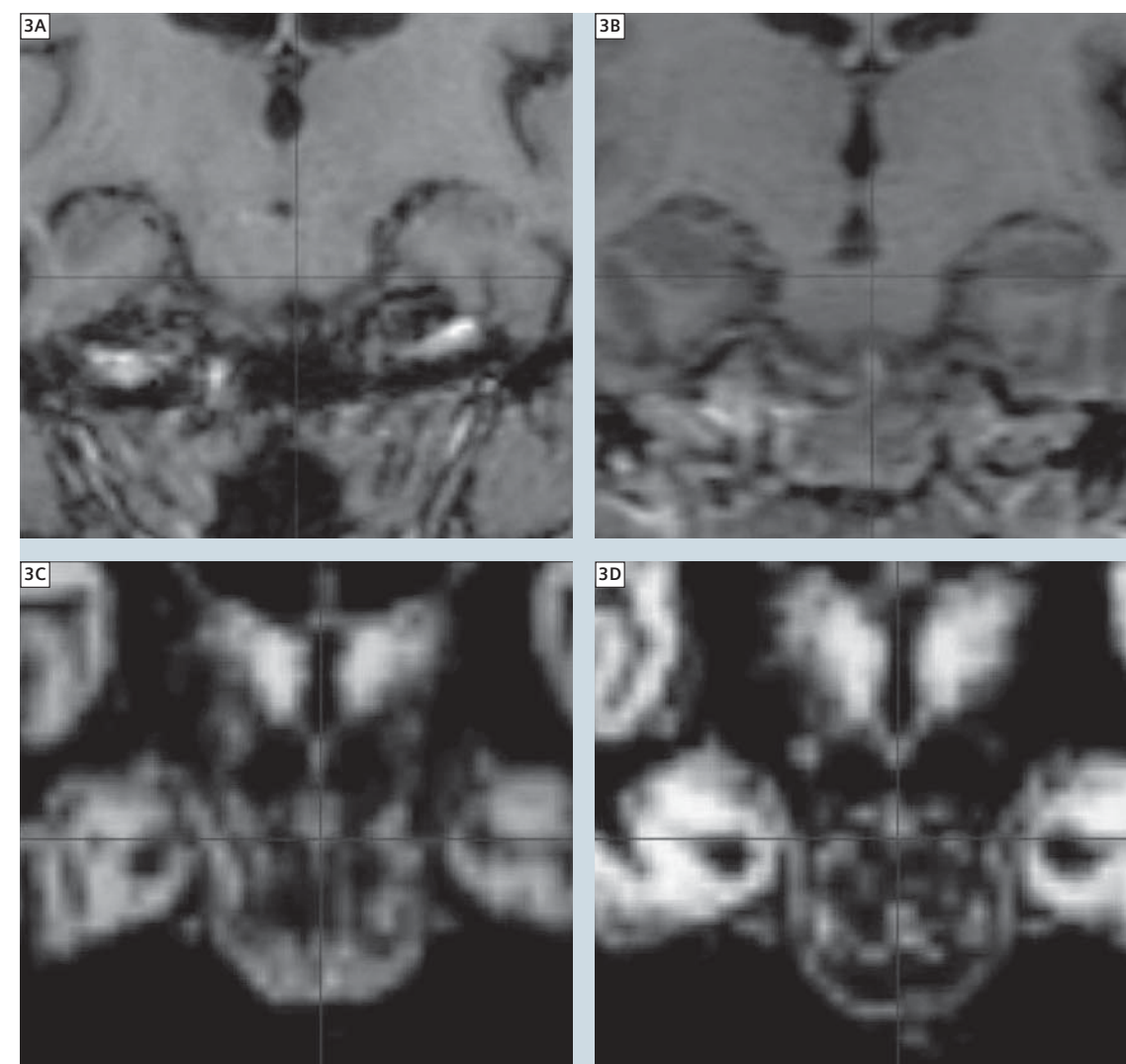


2 Concept of multivariate classification methods in a 2D example.

only a combination of the two leads to adequate separation. The space used for classifying image data is of much higher dimension; the total number of dimensions is determined by the numbers of voxels in each MR image. Related methods have been introduced to aid in breast cancer screening where they are applied to 2D X-rays and are now part of the diagnostic workup. With the advent of faster computer hardware, an accurate spatial transformation of the individual scan to a standard template is possible within minutes.

Image processing pipeline

To apply classification methods successfully it is critical to extract relevant information from the MRI-scan. Figure 3 magnifies the hippocampus area in



3 The hippocampus region is displayed in two example cases before (top row) and after (bottom row) image processing.

two example cases. An observer with some experience may well be able to identify the more atrophic medial temporal lobe areas in figure 3C. Looking at the same images from the feature extraction perspective, it becomes obvious that there are substantial differences between both images, (e.g. regarding brightness, anatomy of the ventricles or differences in non-brain structures) that are unrelated to the diagnostic problem. Those are therefore a source of noise.

Several strategies exist to reduce noise and extract relevant information. Most include a segmentation into grey matter (GM), white matter (WM) and cerebrospinal fluid (CSF) followed by a spatial normalisation of the GM segment to a template. A separate 'modulation' step [1] ensures that the overall amount of each tissue class remains constant after normalization. The bottom row in figure 3 depicts the same two cases as the top row but after applying the preprocessing steps. The brightness of a voxel now codes

the local GM volume and the reduced brightness in figure 3C can easily be identified by an automated method.

Applying the support vector machine

In practical terms, a linear kernel matrix is created from normalised GM segmented images. To this end, each MRI scan undergoes a pair-wise multiplication with all other scans. Each element in the kernel matrix is therefore a dot product of two images. Intuitively, the kernel matrix can be viewed as a similarity measure among subjects belonging to a characterised group. Each scan is effectively treated as coordinate in a high dimensional space and the location is determined by the intensity value at each voxel. The images do not span the whole high dimensional space, but rather cluster in subspaces containing images that are very similar. This is one reason why image normalization into a standard space is an important preprocessing step. Good spatial normalization will tighten clustering and reduce dimensionality.

The use of a support vector machine (SVM) for image classification is an example of a linear discrimination. In the basic model it is a binary classifier, which means it divides the space into two classes by identifying a separating hyper-plane. In a simple two dimensional space, the boundary is represented by a line, but is called a hyperplane in higher dimensional space. Fisher's linear discriminate analysis or linear perceptrons can both identify linear discriminant hyperplanes. However, the motivation behind using an SVM is that it uses the principle of 'structural risk minimization', which aims to find a hyperplane that maximizes the distance between training classes (see Figure 2). Intuitively, it can be seen that the optimal separating hyperplane (OSH) produced by an SVM is defined by those voxels that are closest to the separating boundary between them, i.e., the voxels that are most ambiguous. These voxels are called the 'support vectors'. Voxels

that are further away from a separating boundary are distinctively different, hence are not used to calculate the OSH. This fact suggests that adding more images to a training set will have little effect on an OSH if they are distant from it. After training, an OSH contains learned differences between classes – in our case, AD and control images. That information is then used to assign any new image to its appropriate class (leave-one-out method). This procedure iteratively leaves successive images out of training for subsequent class assignation until each had been used in this way. This validation procedure ensures that a trained SVM can generalize and be used on scans that have never been presented to the SVM algorithm previously.

Clinical applications

We have recently shown that mild to moderately affected individuals with AD and controls can be correctly assigned to their respective group with an accuracy of 95% and a sensitivity of 100%, even when scans come from different scanners to those used to generate the discriminant model that differentiates the categories [11]. A similar accuracy was found when diagnosing two forms of dementia, AD and fronto-temporal lobar degeneration (FTLD), using such computer-based analyses [11]. This performance compares well to that achieved by experienced neuroradiologists [10] (see figure 4). Our preliminary analysis indicates that around 20 subjects per diagnostic group are required to achieve reasonably good performance [12].

Roadmap for future developments

These results have a number of implications that suggest a general adoption of computer-assisted methods for MRI scan-based dementia diagnosis should be seriously considered. The most important of these are:

- improving diagnosis in places where trained neuroradiologists or cognitive neurologists are scarce;
- increasing speed of diagnosis without

compromising accuracy by eschewing lengthy specialist investigations; and

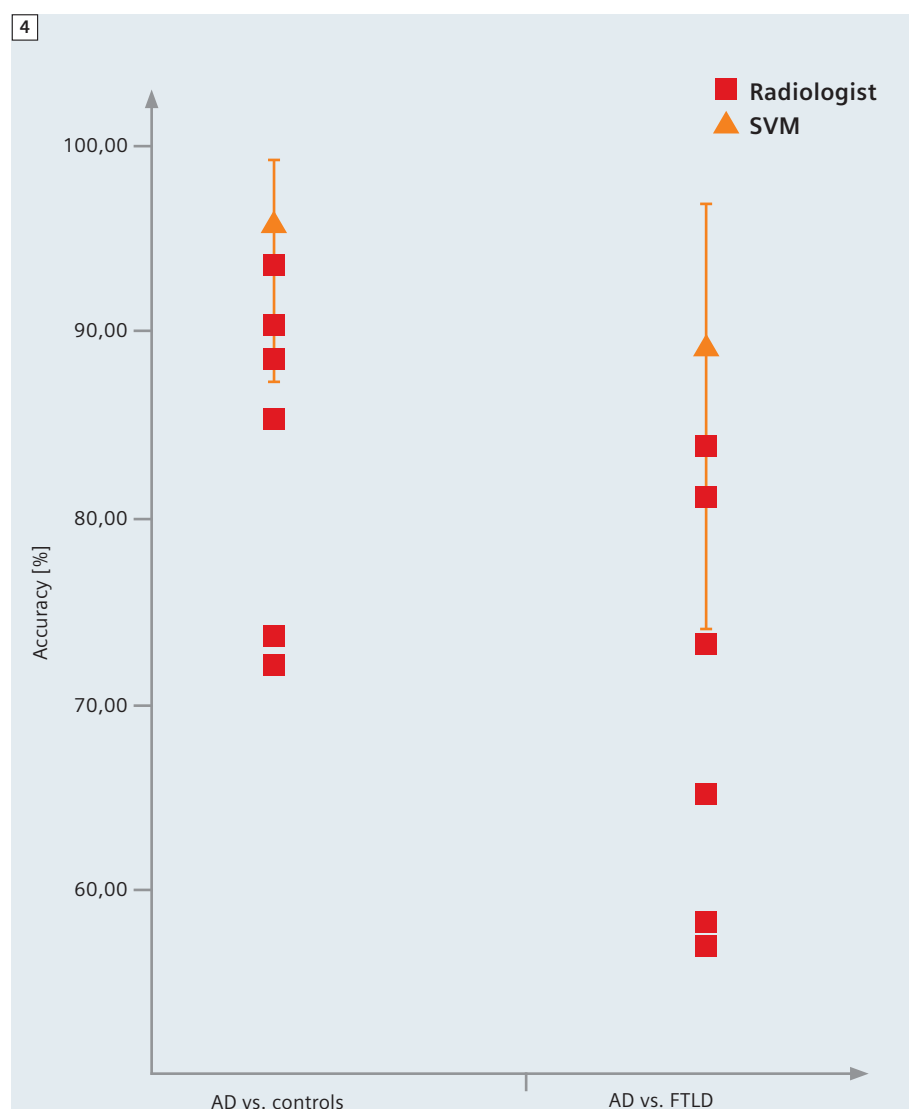
- recruitment of clinically-homogeneous patient populations for pharmacological trials. The following steps should be taken before wide application:

1. Establishment of precise classification techniques with well-established test criteria such as sensitivity and specificity values for each disease and the question under study.
2. Creation of a large database with cases from a high number of disorders diagnosed with certainty.
3. Further optimisation of the ability to combine data from different scanners. Despite encouraging results, scanner differences have effects on imaging [17] and should be corrected if possible.
4. Comparison of present gold standard methods for MRI-based classification methods and examination of combinations of methods.
5. Conclusion as to whether classification methods are capable of creating new gold standards, given limited resources.
6. Implementation of all required image processing steps on the MRI console to facilitate integration into the clinical workflow.

References

- 1 Ashburner J, Friston KJ (2000) Voxel-based morphometry—the methods. *Neuroimage* 11:805-821.
- 2 Barnes J et al. (2004) Differentiating AD from aging using semiautomated measurement of hippocampal atrophy rates. *Neuroimage* 23:574-581.
- 3 Davatzikos C et al. (2008) Detection of prodromal Alzheimer's disease via pattern classification of magnetic resonance imaging. *Neurobiol Aging* 29:514-523.
- 4 Davatzikos C et al. (2009) Longitudinal progression of Alzheimer's-like patterns of atrophy in normal older adults: the SPARE-AD index. *Brain* 132:2026-2035.
- 5 Duchesnay E et al. (2007) Classification based on cortical folding patterns. *IEEE Trans Med Imaging* 26:553-565.
- 6 Fan Y et al. (2006) Diagnosis of Brain Abnormality Using both Structural and Functional MR Images. *Conf Proc IEEE Eng Med Biol Soc* 1:1044-1047.
- 7 Fan Y et al. (2007) Multivariate examination of brain abnormality using both structural and functional MRI. *Neuroimage* 36:1189-1199.
- 8 Ferri CP et al. (2005) Global prevalence of dementia: a Delphi consensus study. *Lancet* 366:2112-2117.
- 9 Fox NC, Schott JM (2004) Imaging cerebral atrophy: normal ageing to Alzheimer's disease. *Lancet* 363:392-394.
- 10 Klöppel S et al. (2008a) Accuracy of dementia diagnosis: a direct comparison between radiologists and a computerized method. *Brain* 131:2969-2974.
- 11 Klöppel S et al. (2008b) Automatic classification of MR scans in Alzheimer's disease. *Brain* 131:681-689.
- 12 Klöppel S et al. (2009) A plea for confidence intervals and consideration of generalizability in diagnostic studies. *Brain* 132:e102.
- 13 Lerch JP et al. (2008) Automated cortical thickness measurements from MRI can accurately separate Alzheimer's patients from normal elderly controls. *Neurobiol Aging* 29:23-30.
- 14 McKhann G et al. (1984) Clinical diagnosis of Alzheimer's disease: report of the NINCDS-ADRDA Work Group under the auspices of Department of Health and Human Services Task Force on Alzheimer's Disease. *Neurology* 34:939-944.
- 15 Mourao-Miranda J et al. (2005) Classifying brain states and determining the discriminating activation patterns: Support Vector Machine on functional MRI data. *Neuroimage* 28:980-995.
- 16 Petersen RC et al. (2001) Current concepts in mild cognitive impairment. *Arch Neurol* 58:1985-1992.
- 17 Stonnington CM et al. (2008) Interpreting scan data acquired from multiple scanners: a study with Alzheimer's disease. *Neuroimage* 39:1180-1185.
- 18 Teipel SJ et al. (2007a) Multivariate deformation-based analysis of brain atrophy to predict Alzheimer's disease in mild cognitive impairment. *Neuroimage* 38:13-24.
- 19 Teipel SJ et al. (2007b) Multivariate network analysis of fiber tract integrity in Alzheimer's disease. *Neuroimage* 34:985-995.
- 20 Vemuri P et al. (2008a) Alzheimer's disease diagnosis in individual subjects using structural MR images: Validation studies. *Neuroimage* 39:1186-1197.
- 21 Vemuri P et al. (2008b) Antemortem MRI based Structural Abnormality iNDex (STAND)-scores correlate with postmortem Braak neurofibrillary tangle stage. *Neuroimage* 42:559-567.
- 22 Wahlund LO et al. (2005) Evidence-based evaluation of magnetic resonance imaging as a diagnostic tool in dementia workup. *Top Magn Reson Imaging* 16:427-437.

Contact
Stefan Klöppel, MD
Brain Imaging
Freiburg University
Breisacher Str. 64
79106 Freiburg
Germany
Email:
stefan.kloepfel@uniklinik-freiburg.de



4 Diagnostic accuracy of radiologists compared to an SVM when separating Alzheimer's Disease (AD) from either healthy controls or cases with fronto-temporal lobar degeneration (FTLD).

STIR versus SPAIR in Breast Imaging: a Case-Based Discussion

Yien Sien Lee, MD; Choon Kuang Low, BSc; Helmut Rumpel, PhD

Department of Diagnostic Radiology, Singapore General Hospital, Singapore

Purpose

The purpose of this article is to illustrate the varying appearances of breast cysts for different inversion recovery imaging sequences such as STIR and SPAIR.

It illustrates a specific pitfall in interpretation of inversion recovery techniques (for lipid void) in breast MR imaging. It includes schematic and pictorial illustrations to describe this pitfall, with imaging from a clinical case.

Introduction

Standard breast MR protocols, e.g. for screening of high-risk patients, encompass methods for water-lipid separation [1]. To optimally assess the water component in fibroglandular tissue, fat suppression scans based on T1 relaxation values are commonly used, namely STIR (short T1 inversion recovery) (Fig. 1A) or SPAIR (spectral selective attenuated inversion recovery) (Fig. 1B). Both sequences embody an inversion recovery scheme and acquire the image data after a time delay (called inversion time TI), when the longitudinal magnetization of the signal from lipids is zero.

What is the difference between STIR and SPAIR?

The inversion-recovery (IR) technique STIR is chemically non-selective, but spatially selective, i.e. the inversion pulse affects all tissues, but only for the respective slice. SPAIR in contrast is chemically selective, but spatially non-selective, i.e. only the fatty tissue is inverted, but this applies to the whole volume of all slices. Consequently, the frequency of inversion pulses for each slice is much higher for SPAIR (TR / num-

ber of slices). The steady-state magnetization of fatty tissue is consequently lower, resulting in a shorter TI for zero crossing of the fat magnetization.

What are the strengths and weaknesses of STIR and SPAIR?

A significant but detrimental feature of STIR is that the water signal follows the

same scheme of inversion recovery although it has a different T1 value. This leads to an intrinsically low signal-to-noise ratio as opposed to SPAIR which leaves the water signal undisturbed. We illustrate this with the following case of breast cysts with short T1.

Pictorial illustration

A 49-year-old patient was selected for high-risk screening in MRI. No prior mammogram or ultrasound of the breasts was performed for the patient. Physical examination found no palpable mass in either breast. MRI was performed on a 3T scanner (MAGNETOM Verio, Siemens Erlangen, Germany). The system was equipped with an open 8-channel breast array coil. The examination protocol consisted of three steps. The first involved STIR / SPAIR. In the second step, dynamic contrast-media enhanced 3D T1-weighted gradient echo images were collected. MRI of the breasts demonstrated two circumscribed oval masses at the 12 o'clock position in the left breast. These two oval masses were isointense to hypointense on the STIR images (Fig. 2A), but hyperintense on SPAIR images (Fig. 2B). Figure 2C shows a pre-contrast T1-weighted image for reference. In the axial subtracted images, these oval masses demonstrated rim enhancement. They probably represent inflamed cysts containing proteinaceous fluid or cysts complicated by hemorrhage.

Discussion

Simple breast cysts are round or oval with sharp margins. Simple cysts have very high T2 signal and display no inter-

nal enhancement with contrast. Breast cysts with proteinaceous content may demonstrate high signal on T1-weighted images with corresponding lower signal on T2-weighted images. In inflamed cysts, enhancement may occur in the tissue around the cyst. This may appear as a mass with rim enhancement on subtracted images.

When water is bound to a hydrophilic macromolecule such as a protein, it forms a hydration layer. This lowers the motional frequencies of water which results in shortening of T1. As a point of reference, proteinaceous fluid has a T1 that is between that of fat (with shortest T1) and bulk water (with longest T1) [2]. The MR signal characteristics are thought to correlate with protein content or hemorrhage within the cysts. There are several reports concerning the relationship between cyst protein concentration and signal intensity on T1-weighted MR images [3]. This is supported by the similarity to CT [4]. An almost linear relationship is reported between protein content and the attenuation value of cyst fluid. The attenuation can be in the range of that of soft tissue and thus mimic a tissue mass.

How do T1 changes affect the STIR image contrast?

Any other tissue with a T1 similar to that of lipids then also appears strongly attenuated (Fig 1A). This inconsistency may confuse the unwary when looking at the same tissue in a different way, e.g. on T1-weighted MRI. On the other hand, STIR is insensitive to B₀ inhomogeneity, and thus potentially permits larger fields-of-view when com-

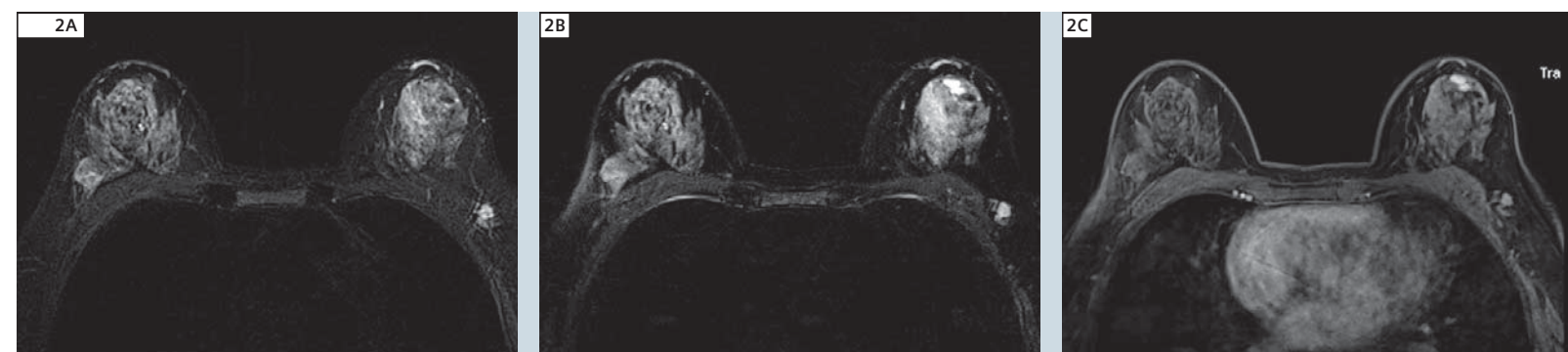
pared to conventional fat suppressed images and also has the ability to scan off-center; SPAIR may not work well in regions with reduced homogeneity, e.g. due to proximity to clips or generally susceptibility changes [5]. But as shown in this exemplary case, SPAIR should be used in cases where water-based tissue lesions may have a T1 similar to that of lipids, because the non-selective scheme of STIR can provide misleading results.

References

- 1 Kuhl CK. Concepts for Differential Diagnosis in Breast MR Imaging, MRI Clinics 2006; 305-328.
- 2 Rakow-Penner R, Daniel B, Yu H, Sawyer-Glover A, Glover GH. Relaxation times of breast tissue at 1.5T and 3T measured using IDEAL. JMIR 2005; 23: 87-91.
- 3 Hayashi Y, Tachibana O, Muramatsu N, et al. Rathke. Cleft cyst: MR and biomedical analysis of cyst content. J Comput Assist Tomogr 1999; 23: 34-38.
- 4 Stafford-Johnson DB, Helvie MA, Hilborn MD, Wilson TE, Goodsitt MM, Bude RO. CT attenuation of fluid in breast cysts. Acad Radiol. 1998; 5: 423-6.
- 5 Bley TA, Wieben O, François CJ, Brittain JH, Reeder SB. Fat and Water Magnetic Resonance Imaging. JMIR 2010; 31: 4-18.

Contact

Helmut Rumpel, PhD
Department of Diagnostic Radiology
Singapore General Hospital
Outram Rd
Singapore 169608
Phone (65)63266774
helmut.rumpel@sgh.com.sg



2 Breast MR images of a 49-year-old woman with cysts containing proteinaceous fluid. **2A:** STIR with TR/TE/TI 4200/93/230, **2B:** SPAIR with TR/TE 4000/86, **2C:** T1-weighted gradient echo image TR/TE 4.9/1.9.

Fat Suppression Techniques – a Short Overview

Wilhelm Horger; Berthold Kiefer

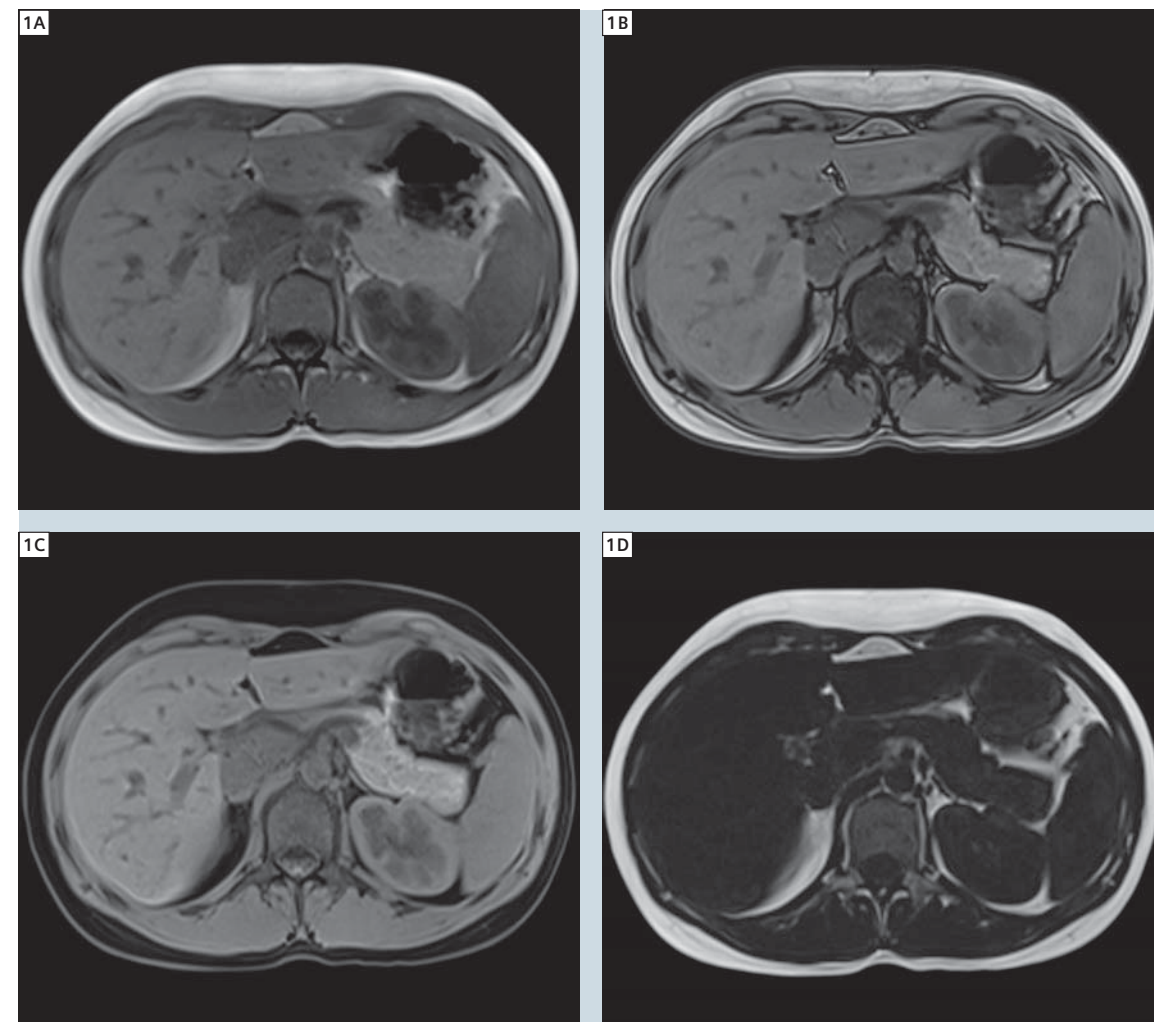
Siemens Healthcare, Erlangen, Germany

Introduction and background

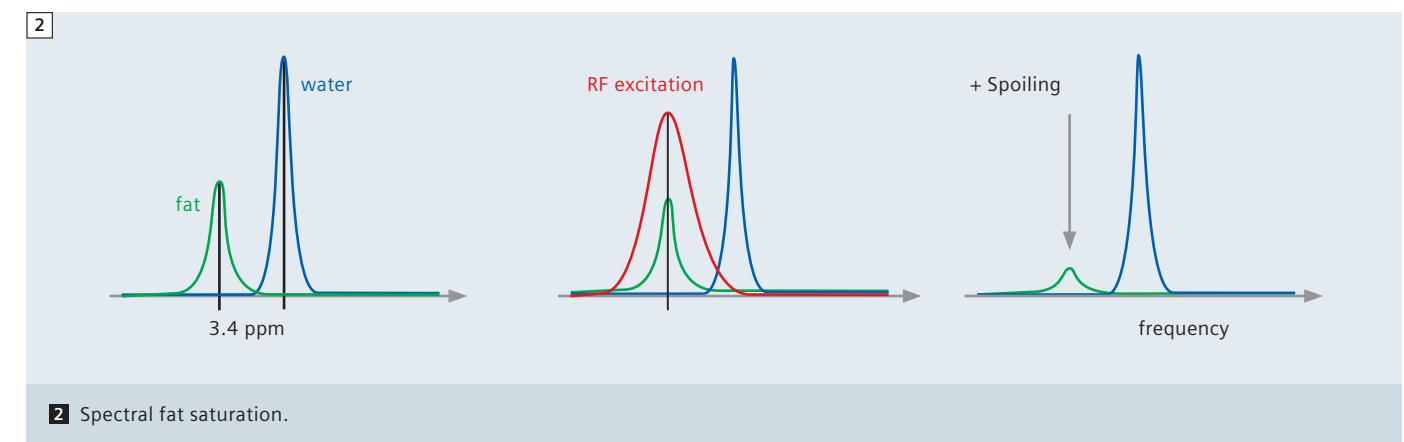
Fat-suppression is an integral part of nearly any routine MR application. Insufficient elimination of the fat signal or even saturation of tissue of interest in an MR image can have severe consequences and therefore the knowledge

about available fat-suppression techniques and their individual advantages and disadvantages are required. The purpose of this article is to provide a short technical overview of the main fat-suppression techniques available for clinical routine.

All techniques for fat suppression are based on the fact that – due to the different chemical environment – hydrogen nuclei in water and in fat-tissue have different values for some MRI-relevant parameters, mainly the relaxation time and the resonance frequency



1 Dixon technique (VIBE). Four contrasts generated in one breathhold:
1A: in-phase
1B: opposed-phase
1C: water image
1D: fat image



2 Spectral fat saturation.

(chemical shift). These differences can be used to selectively suppress or reduce the signal of fat bound protons. Thus one can differentiate between two types of fat-suppression techniques:

- a) Relaxation-dependant (e.g. STIR)
- b) Chemical shift-dependant methods (e.g. Dixon technique (available for VIBE and TSE sequence techniques), spectral fat saturation, water excitation and SPAIR).

Dixon technique

The Dixon technique is based on the chemical shift i.e. the difference in resonance frequencies between fat and water-bound protons. With this technique two images are acquired. In the first image the signal from fat-protons and from water-protons are 'in phase'; in the second they are 'opposed phase'. A separate fat and water-image can then

be calculated. The Dixon method is integrated into the VIBE sequence and TSE sequence (compare Fig. 1).

Dixon delivers up to 4 contrasts in one measurement: in-phase, opposed-phase, water and fat images.

Advantages of the Dixon technique:

- Insensitive to B_0 and B_1 inhomogeneities.
- 4 contrasts delivered in one measurement.

Disadvantage of the Dixon technique:

- Increases minimal TR because in- and opposed phase data must be acquired. This can be compensated by using integrated Parallel Acquisition Techniques (iPAT).

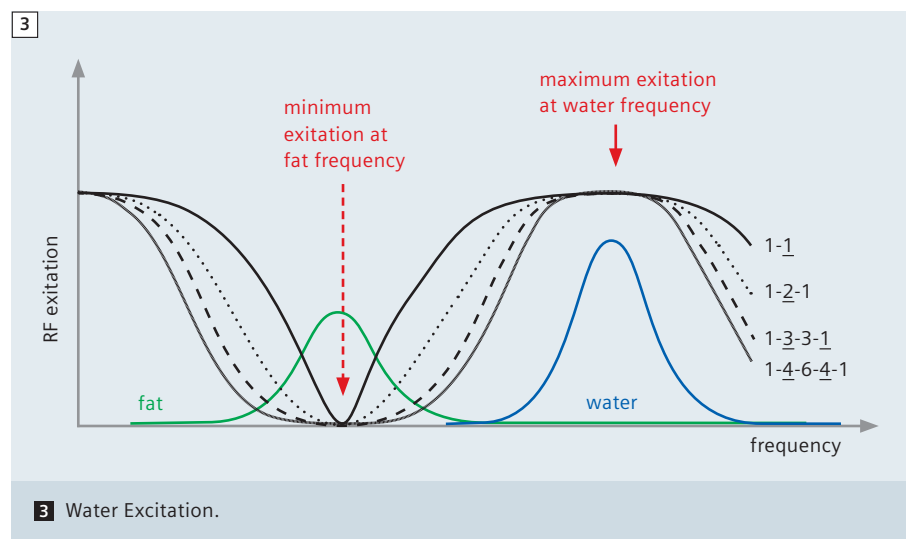
Spectral fat saturation

This technique is based on the chemical shift (3.4 ppm) i.e. the difference in resonance frequencies between fat- and water-bound protons. The application of a narrow band frequency selective radio-frequency (RF) pulse excites mainly fat-

bound protons. This transversal magnetization is destroyed afterwards by spoiler gradients, thus no fat magnetization is left for imaging (compare figure 2).

For spectral fat saturation, a 'Quick-Fat-Sat' setting is available. If this feature is selected, not every slice excitation is preceded by a preparation pulse. This means:

- Shorter possible TR;
- Shorter breath-hold examinations (e.g. VIBE, recommended 40 lines/shot). Two FatSat modes (strong/weak) are also available. Basically, the user can select how much of the fat signal is contributing to the MR image. In the 'strong' mode a nearly full suppression is achieved, whereas in the 'weak' modus, anatomical information of fatty tissue is partially preserved.



Advantages of spectral fat saturation:

- Tissue contrast is not affected;
- Quick-FatSat can be applied for increased performance.

Disadvantages of spectral fat saturation:

- Sensitive to B_0 and B_1 inhomogeneities;
- Additional preparation pulse increases minimal TR and total measurement

time or reduces maximum number of slices (partially compensated by Quick-Fat Sat).

Water excitation

This technique is based on the chemical shift i.e. the difference in resonance frequencies between fat and water-bound

protons. No additional preparation pulse is necessary. Instead, a special excitation pulse (binomial pulse) is used with the spectral excitation profile (minimum excitation of fat bound protons, maximum excitation of water-bound protons) (compare Fig. 3).

Advantages of water excitation:

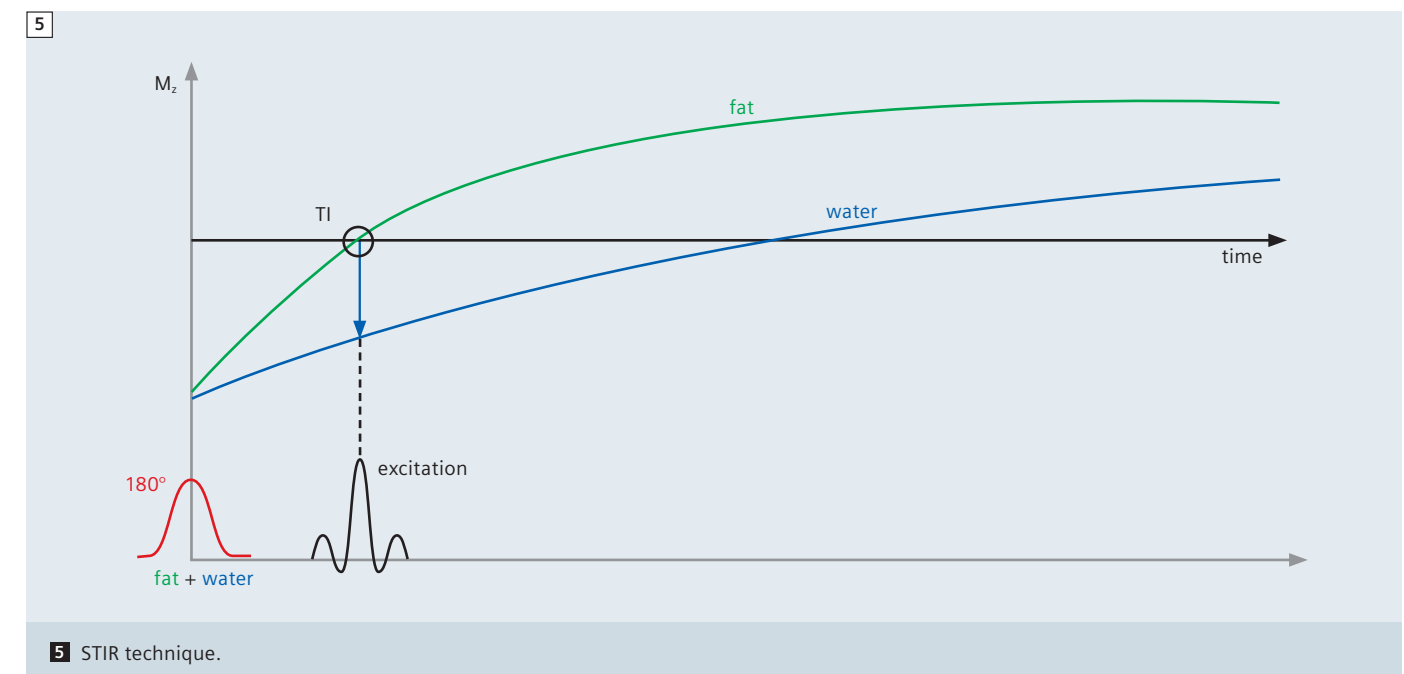
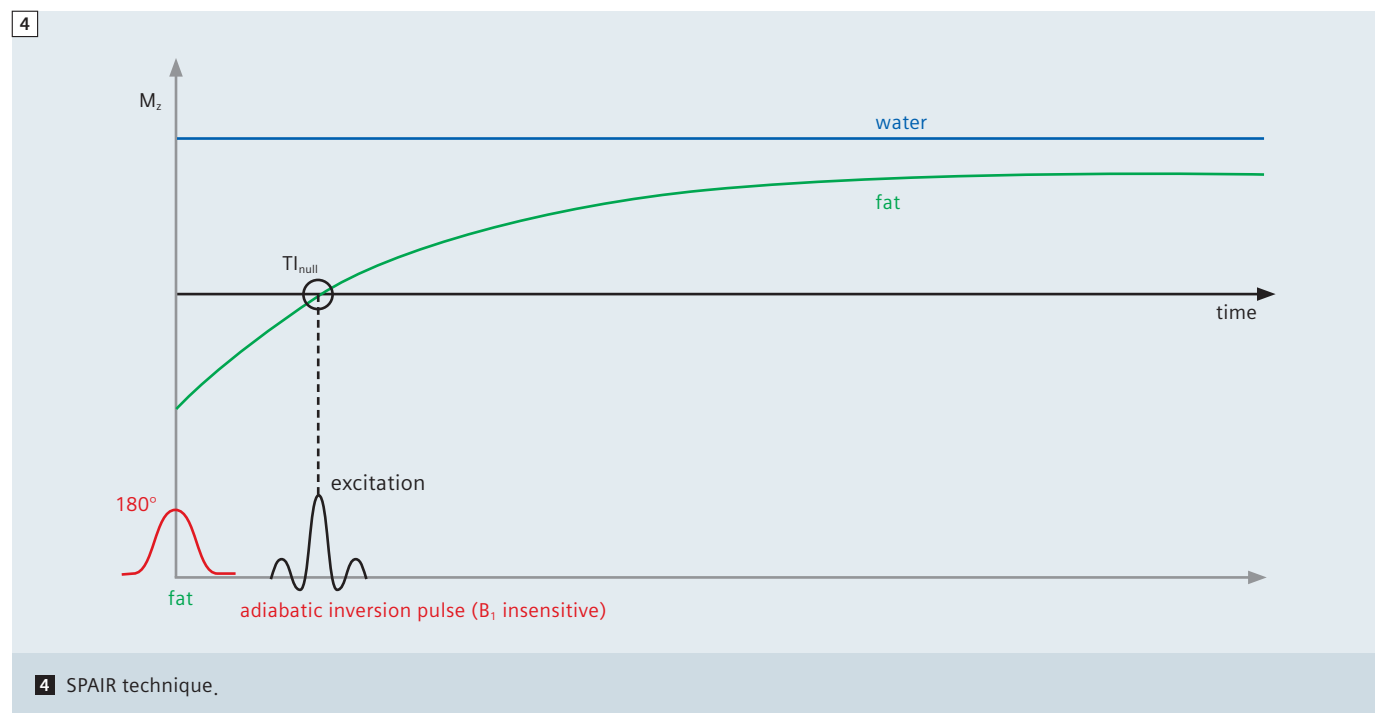
- Reduced sensitivity to B_1 inhomogeneities.

Disadvantages of water excitation:

- Increased min TE, TR and total measurement time or reduced maximum number of slices.

Fat suppression with Inversion Recovery

In clinical routine, two types of inversion recovery techniques are applied: SPAIR (Spectrally Adiabatic Inversion Recovery) method, and Short TI Inversion Recovery (STIR; in principal identical to TIRM (Turbo Inversion Recovery Magnetization) technique).



SPAIR technique (Spectrally Adiabatic Inversion Recovery)

SPAIR is an alternative to the conventional spectral fat saturation. A spectrally selective adiabatic inversion pulse excites only fat spins, thus no STIR like contrast is created. With gradient spoiling the transverse magnetization is destroyed. The inversion time T_I is such that the longitudinal magnetization of fat at the time when the excitation pulse is applied is zero, so fat spins will not contribute to the MR signal (compare Fig. 4).

Advantages of SPAIR:

- Insensitive to B_1 inhomogeneity;
- Tissue contrast is not affected.

Disadvantages of SPAIR:

- Increased minimal TR or reduced maximal number of slices due to more complex preparation pulse (partially compensated by Quick-Fat Sat).

STIR (Short TI Inversion Recovery)

This relaxation-dependant technique is based on the different relaxation behavior of water and fat tissue. Fat has a much shorter T_1 relaxation time than other tissues. Prior to the excitation pulse of the sequence an inversion pulse ($= 180^\circ$) is applied which inverts the spins of all tissue and fat protons. This is followed by T_1 relaxation. When choosing T_I such that the longitudinal magnetization of fat at the time when the excitation pulse is applied is zero, the fat spins will not contribute to the MR signal. STIR images have an inverted T_1 contrast: Tissue with long T_1 appears brighter than tissue with short T_1 (compare Fig. 5).

Advantages of STIR:

- Insensitive to B_0 inhomogeneities.

Disadvantages of STIR:

- Additional inversion pulse increases minimal TR and total measurement time or reduces maximum number of slices;
- Tissue contrast is affected, SNR is reduced.

Contact

Wilhelm Horger
Siemens AG
H IM MR PLM-AW ONCO
Allee am Roethelheimpark 2
D-91052 Erlangen
Germany
wilhelm.horger@siemens.com



→ In this article, the Siemens nomenclature is used. A list of MRI acronyms for a variety of MR techniques and different vendors as well as a booklet with detailed description of MR terms can be found at our MAGNETOM World Internet site. Follow the QR code or visit us at www.siemens.com/magnetom-world and go to MR Basics under Publications.

Case Report:

Snowboarding Injuries to the Middle Subtalar Joint. The Sustentacular Talocalcaneal Articulation

Anna K. Chacko, MD; Charles P. Ho, PhD, MD
Steadman Philippon Research Institute, Vail, Colorado, USA

In this case report we present two cases of injuries to the subtalar joint, specifically chondral defects of the middle facet of the talus and concomitant involvement of middle talocalcaneal or sustentacular articulation. These injuries were both sustained during snowboarding.

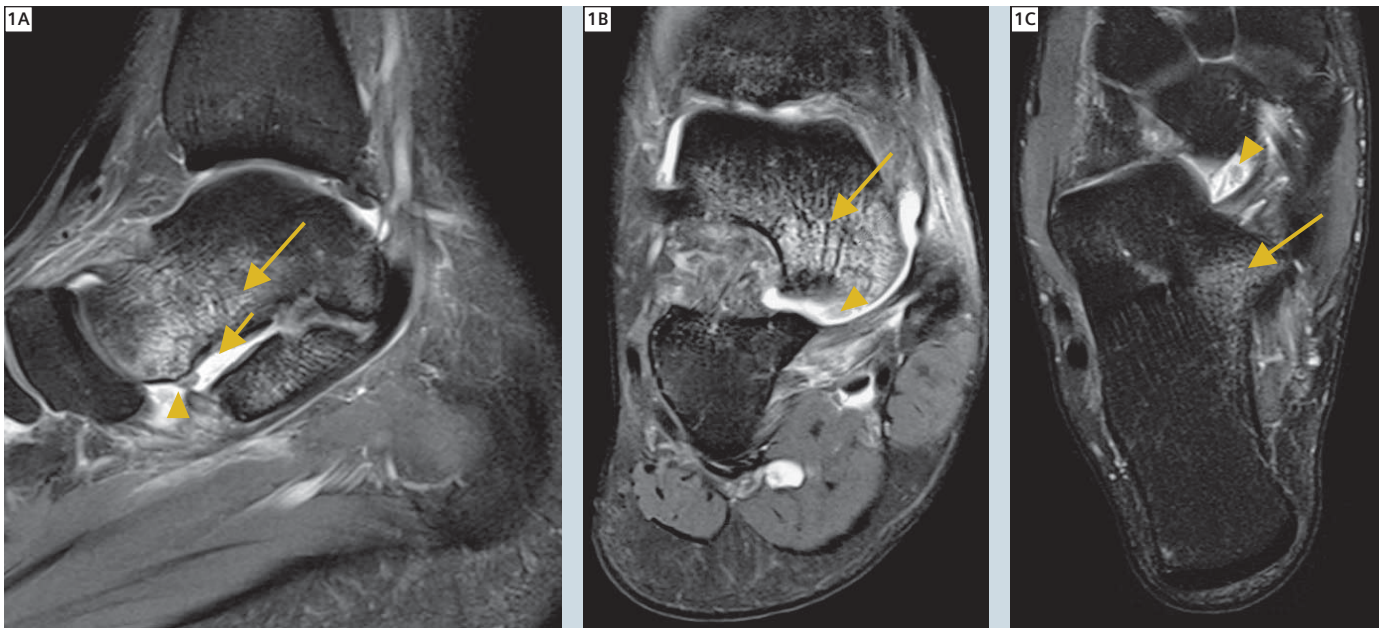
Patient history and imaging findings

A 26-year-old male snowboarder presents with a history of snowboarding injury 3 weeks prior to being scanned. Scarring and sprain of the anterior talofibular and calcaneofibular ligaments is

observed. There is sprain and contusion of the deltoid ligament complex. A small talocrural effusion is seen with capsular sprain and scarring. Synovitis and debris are also seen in the anterior and posterior recesses. Bone edema and impaction fracture of the plantar medial aspect of the talar neck and head are seen with extension to the middle facet. At the sustentacular (middle facet) articulation an impaction fracture of the plantar medial aspect of the talar neck and head is observed (Fig. 1A). Chondral contusion, fracture and focal defects are also noted (Fig. 1B). There is ligamentous injury and partial tearing with sprain

involving the talocalcaneal and interosseous cervical ligaments of the sinus tarsi. Bone edema, and impaction injury of the adjacent sustentaculum tali to medial portion of the body of the calcaneus are observed. Multiple chondral fragments are observed adjacent to the sustentaculum tali (Fig. 1C).

A 27-year-old male snowboarder presents with history of recent snowboarding injury. Clinically, a lateral process fracture was suspected. Mild impaction injury of the plantar aspect of the talar head with extension to the middle facet is seen (Fig. 2A). A focal sharply margin-



1 26-year-old snowboarder presents with subtalar injury. **1A:** PD-weighted Turbo Spin Echo fat suppressed sagittal images through the ankle demonstrate the multiple components of this injury. Bone marrow edema shows the site of the impaction fracture of the middle facet of the talus (long arrow). Chondral defect is noted in the articular cartilage of the middle facet on the inferior aspect of the talus (short arrow). Chondral fragment (arrow head). **1B:** PD-weighted Turbo Spin Echo fat suppressed coronal images through the ankle demonstrate bone marrow edema at the site of the impaction fracture of the middle facet of the talus (long arrow). Chondral fragment (arrow head). **1C:** PD-weighted Turbo Spin Echo fat suppressed axial images through the ankle. Bone marrow edema shows the site of the impaction fracture at the sustentaculum tali (long arrow). Chondral fragment (arrow head).

Table 1: Sequence details							
Weighting and planes	FOV	TR	TE	Sequence	Slice thickness	Gap	Matrix size
T2- weighted axial	100	3860	108	Turbo Spin Echo	3 mm	0.3 mm	640 x 640
PD- weighted FS axial	100	3730	43	Turbo Spin Echo Fat suppressed	3 mm	0.3 mm	640 x 640
PD-weighted coronal	100	4340	33	Turbo Spin Echo	3 mm	0.3 mm	768 x 768
PD-weighted FS coronal	100	4660	43	Turbo Spin Echo Fat suppressed	3 mm	0.3 mm	640 x 640
PD-weighted sagittal	100	2840	34	Turbo Spin Echo	3 mm	0.3 mm	640 x 640
PD-weighted FS sagittal	100	2910	43	Turbo Spin Echo Fat suppressed	3 mm	0.3 mm	640 x 640

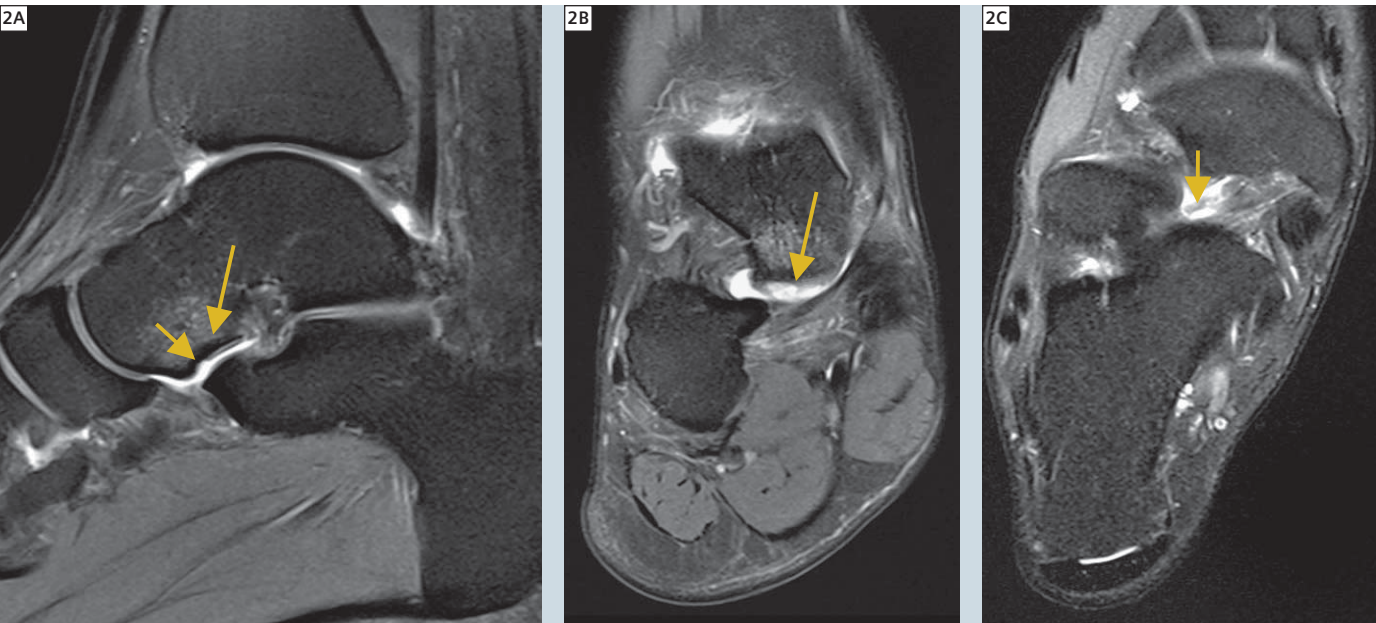
ated chondral defect is observed (Fig. 2B) with adjacent chondral fragment (Fig. 2C). For the MR evaluation of the ankle joint on the 3T MAGNETOM Verio MR scanner (Siemens Healthcare, Erlangen, Germany), the first of our axial image set is routinely a T2-weighted Turbo Spin Echo (TSE) sequence, paired with an axial Proton Density (PD) TSE fat suppressed (FS) sequence. These are then followed by PD-weighted TSE sequences with and without fat suppression in the sagittal and coronal planes. Details of our imaging parameters are presented in Table 1.

Discussion

There is a large body of radiologic literature describing both osseous and ligamentous injuries, to the ankle and hind-foot particularly involving athletic endeavours such as skiing, basketball, football etc. However, injuries to the subtalar joints do not find their way into these

discussions. Furthermore, discussions of involvement of the middle facet of the talus and the middle talocalcaneal sustentacular articulation are even more sparse. This may very well have been due to the “inaccessibility” of the area to imaging examination. The advent of MR imaging and the ability to achieve finer resolution and better signal-to-noise ratios may have changed the landscape. Snowboarding is significantly so different from skiing that the prevalence and distribution of injuries are commensurately different. Snowboarders stand on their boards very similar to skateboarders or surfers. They stand sideways on their board with the rear foot at 90 degrees to the long axis of the board and the front foot positioned between 45 and 90 degrees to the long axis of the board. The snowboarder executes turns by shifting body weight to the front foot and by swinging the tail of the

board to swing out. Since poles are not used, the arms and hands are used to break a fall. The bindings, the type of boot, the patterns of the lead foot etc. are believed to be responsible for the patterns of injury. Upper limb and ankle injuries are more common among snowboarders than skiers. Ankle injuries are the third most common injuries in snowboarders (16%) versus skiers (6%). These ankle injuries which are torsional could be accompanied by talocalcaneal/subtalar injuries which may go undetected. Undetected subtalar injuries and attendant instability can set the stage for significant chronic problems. These injuries are better dealt with acutely rather than chronically. The talus and the subtalar joints are part of a complex biomechanical entity with multiple degrees of freedom where the talocrural (ankle) joint acts in concert with the subtalar and talocalcaneonavicular



2 27-year-old snowboarder presents with subtalar injury. **2A:** PD-weighted Turbo Spin Echo fat suppressed sagittal images through the ankle demonstrate bone marrow edema at the site of the impaction fracture of the middle facet of the talus (long arrow). Chondral defect is noted in the articular cartilage of the middle facet on the inferior aspect of the talus (short arrow). **2B:** PD-weighted Turbo Spin Echo fat suppressed sagittal images through the ankle demonstrate the chondral defect in the articular cartilage of the middle facet on the inferior aspect of the talus (arrow). **2C:** PD-weighted Turbo Spin Echo fat suppressed axial images through the ankle demonstrate single chondral fragment adjacent to the sustentaculum tali (arrow).

ular joints providing significant complexity and multiaxiality of function. This allows the foot to accommodate to irregular terrain. Patients presenting with ankle/talocrural joint injuries must be examined carefully for subtalar injuries. The three talocalcaneal articulations can be visualized on standard planes on MR. However, subtle injuries with osteochondral fractures require greater attention to detail with high resolution. The talus is shaped like a truncated cone and ligament stability of the talocrural and subtalar joints is dependent on the lateral collateral, the cervical and the talocalcaneal interosseous ligaments.

References

1 PinoColville: Snowboard Injuries. American Journal of Sports Medicine: Vol 17, No 6, 1989.
2 Bladin C et al: Australian snowboard injury database study: A four year prospective study. American Journal of Sports Medicine: Vol 21, 701, 1993.
3 Ligamentous injuries about the ankle and subtalar joints. Zwipp H Clin Podiatr Med Surg 2002 Apr; 19 (2): 195-229.
4 Challenging fractures of the foot and ankle Proszki LJ, Saltzman CL Radiol Clin North Am: 1997 May; 35 (3): 655-70.
5 Ankle and foot trauma. Mulligan ME. Semin Musculoskelet Radiol. 2000; 4 (2): 241-53.
6 Chronic ankle instability: biomechanics and Pathomechanics of ligamentous injury and associated lesions. Bonnel F, et al: Orthop Traumatol Surg Res 2010 Jun; 96 (4): 424-32.
7 Lateral ankle sprains: a comprehensive review, Part 1: etiology, pathoanatomy, histopathogenesis and diagnosis. Med.Sci. Sports Exerc., Vol 31, no. 7 (Suppl.) pp S429-S437, 1999.
8 Fractures of the talus Skeletal Radiology Volume 26, Number 3, 137-142, DOI: 10.1007/s002560050209.
9 Wechsler RJ et al Helical Ct of fractures of the talus Skeletal Radiol (1997) 26:137-142 International skeletal Society 1997.
10 Osteochondral lesions of the talus – Canale and Belding RH JBJS Am 1980;62:97-102.
11 Osteochondral Lesions of the Talus Schachter et al. J Am Acad Orthop Surg.2005; 13: 152-158.
12 Characterizing osteochondral lesions by magnetic resonance imaging DiPaola JD et al Arthroscopy: The Journal of Arthroscopic and related Surgery VOL 7 Issue 1 March 1991 101-104.
13 Osteochondritis dissecans: a review and new MRI classification Bohndorf K VOL 8 Number 1 103-112.
14 Osteochondral lesions of the talus in a sports medicine clinic. A new radiographic technique and surgical approach Thompson JP et al Am Journal of Sports Medicine December 1984 vol 12 no 6 460-463.
15 Challenging fractures of the foot and ankle Proszki LJ, Saltzman CL Radiol Clin North Am: 1997 May; 35 (3): 655-70.
16 JBJS: Mulfinger GL and Trueta J Blood supply of the talus VOL 52B No. 1 February 1970.
17 Ankle and foot trauma. Mulligan ME. Semin Musculoskelet Radiol. 2000; 4 (2): 241-53.
18 Chronic ankle instability: biomechanics and Pathomechanics of ligamentous injury and associated lesions. Bonnel F, et al: Orthop Traumatol Surg Res 2010 Jun; 96 (4): 424-32.
19 Lateral ankle sprains: a comprehensive review, Part 1: etiology, pathoanatomy, histopathogenesis and diagnosis. Med.Sci. Sports Exerc., Vol 31, no. 7 (Suppl.) pp S429-S437, 1999.
20 Solomon MA et al CT scanning of the Foot and Ankle: I Normal anatomy AJR 146: 1192-1203 June 1986.

Contact

Charles P. Ho, PhD, MD
Steadman Philippon Research Institute
181 W. Meadow Dr. Suite 1000
Vail, CO 81657
USA
Karen.briggs@sprivail.org

Case Report:

Chondral Fracture of the Talar Dome and Diastasis of the Os Trigonum

Anna K. Chacko, MD; Charles P. Ho, PhD, MD

Steadman Philippon Research Institute, Vail, Colorado, USA

Patient history

We present the magnetic resonance (MR) images of the right ankle of a 34-year-old male police officer complaining specifically of pain deep in the right ankle for 4 years. He has had a history of several small uneventful injuries over the past several years, since high school. Physical activity such as running is hampered by the pain in the right ankle as well as the right knee. On physical examination of his ankles, there is mild tenderness along the anterior aspect of the ankle joints. He is more tender on the anterolateral ankle joint and lateral gutter. He has negative tenderness pos-

terior to his peroneal tendons. Anterior drawer and tilt tests were negative.

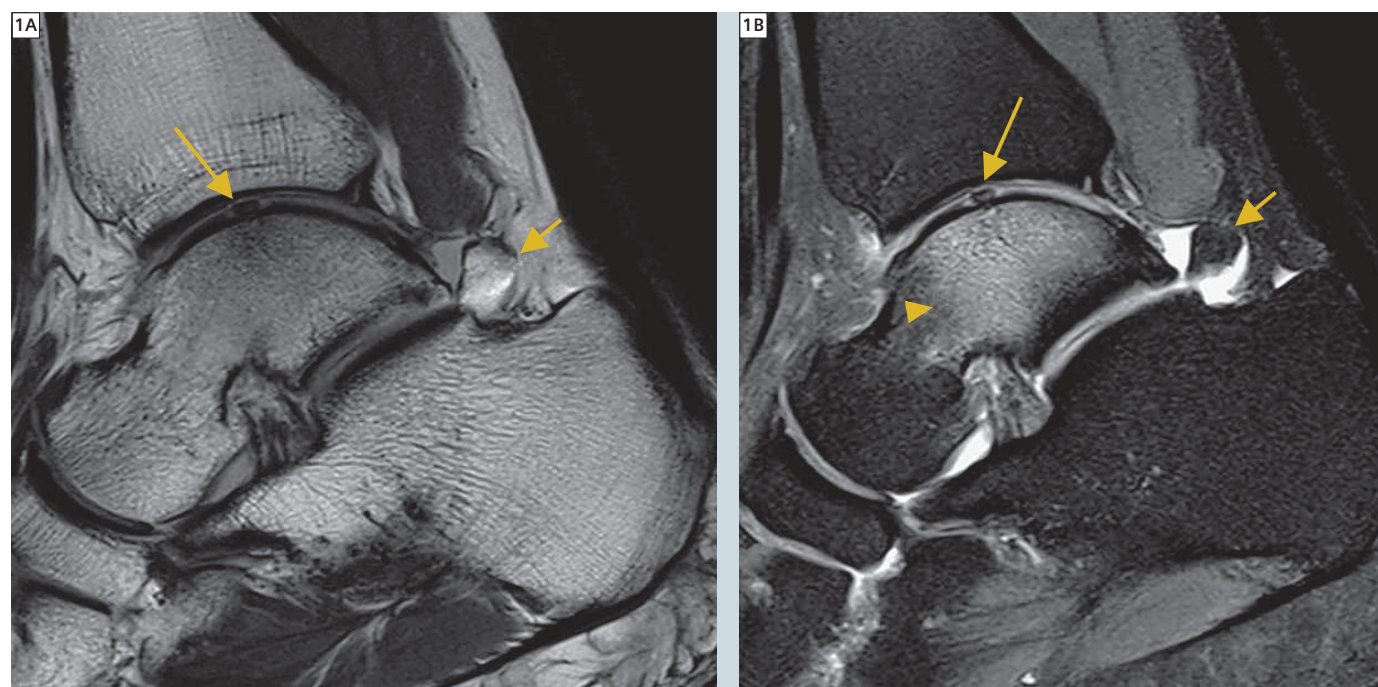
Imaging findings

We present Magnetic Resonance images of the right ankle with significant findings related to his complaints in his right ankle. The right ankle was imaged using a 3T MAGNETOM Verio MRI scanner (Siemens Healthcare, Erlangen, Germany) with a dedicated 8-channel ankle coil. The ankle was imaged in the sagittal, coronal and axial planes. These included proton density (PD), T2-weighted non fat sup-

pressed as well as fat suppressed images for the coronal and sagittal planes. Axial images were obtained with T2-weighting for the non-fat-suppressed images and PD-weighting for the fat suppressed images. We utilized slice thicknesses of 3 mm in all planes. Details of the techniques used are outlined in Table 1. Several abnormalities involving the ligaments in and around the ankle joint were noted on multiple images. However, there are two findings which are well demonstrated in this case. The first is the presence of the chondral fragment in situ noted on the images

Table 1: Sequence details

Weighting and planes	FOV	TR	TE	Sequence	Slice thickness	Gap	Matrix size
T2-weighted axial	100	3860	108	Turbo Spin Echo	3 mm	0.3 mm	320 x 256
PD-weighted axial fat suppressed	100	3730	43	Turbo Spin Echo fat suppressed	3 mm	0.3 mm	320 x 256
PD-weighted sagittal fat suppressed	100	2910	43	Turbo Spin Echo fat suppressed	3 mm	0.3 mm	320 x 256
PD-weighted sagittal	100	2660	35	Turbo Spin Echo	3 mm	0.3 mm	384 x 326
PD-weighted coronal fat suppressed	100	4660	43	Turbo Spin Echo fat suppressed	3 mm	0.3 mm	320 x 256
PD-weighted coronal	100	4340	35	Turbo Spin Echo	3 mm	0.3 mm	384 x 326



1 Sagittal images of the ankle. **1A:** PD-weighted sagittal image which shows the chondral fragment on the talar dome (long arrow) and the diastased os trigonum (short arrow). **1B:** Fat suppressed PD-weighted TSE image which again demonstrates the chondral fragment (long arrow) and the diastased os trigonum (short arrow). The increased signal in the body of the talus (arrowhead) is consistent with edema in the bone marrow as a result of the repetitive irritation caused by instability and ongoing motion of the chondral fragment.

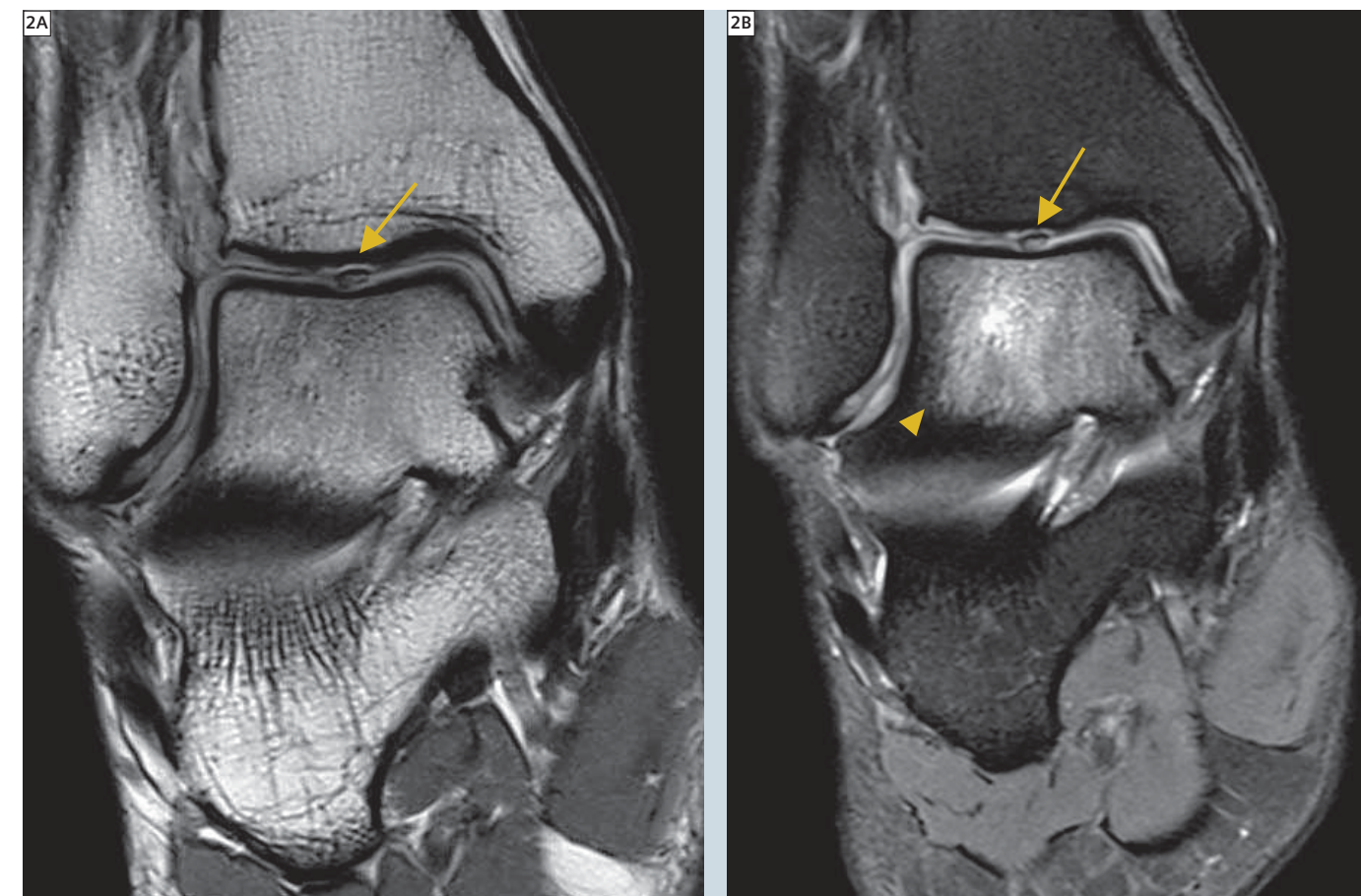
displayed in Figures 1 and 2. The chondral fragment is particularly well delineated by the contrast provided by the effusion surrounding the fragment and the extensive prominent underlying bone edema in the ankle joint and talar dome areas. The chondral fragment measures approximately 3–4 mm and is seen along the mid talar dome. There is underlying osseous irregularity, surrounding chondral focal fissuring. Extensive prominent increased signal is noted in the talar dome and the body which may be reactive stress-related edema and/or contusion and possible ongoing motion/instability of the fragment. The adjacent tibial plafond demonstrates chondral thinning and fissuring to bone (Grade IV – Outerbridge). Cortical irregularity, sclerosis and remodeling are also noted. The presence of increased signal in the body of the talus on the fat suppressed Turbo Spin Echo images (Figs. 1B and 2B) signifies the presence of bone edema which is most likely due to the irritation of the chondral fragment which is located at a

strategic point trapped at the mid weight bearing portion of the talar dome. The second is the separation and posterior tilting of the os trigonum. The os trigonum appears diastased by approximately 3 mm from the lateral tubercle of the posterior process with high signal widening of the synchondrosis. This is most likely related to injury and chronic separation at the synchondrosis. The findings of the diastased os trigonum are visualized on the sagittal images seen in Figures 1A and B.

Discussion

1. Chondral or osteochondral fracture of the talar dome: Ligamentous injuries of the ankle are among some of the most common sports related injuries involving the ankle. When the pain becomes chronic or persistent, associated osteochondral contusion or fracture should be considered. Opposing lesions which involve the plafond and the adjacent talar dome as in this patient should be sought. While the clinical significance of bone contusion

has not been established [1] osteochondral fractures do need to be treated. Of the 146 ankles imaged in the series analyzed by Sijbrandij et al., it was found that bone contusion occurred in the tibial plafond while osteochondral fractures occurred more commonly in the talar dome. They conclude that the opposing lesions occur due to impaction of the talus on the tibia. In this case, however the lack of bone contusion in the plafond suggests that the plafond injury is chronic with resolution of the edema. The presence of the talar edema with the osteochondral fracture of the talar dome suggests that ongoing local movement and instability of the osteochondral fragment could be producing a localized bone injury and consequent stress related edema. Sijbrandij also opined that the explanations for the higher occurrence of the subchondral fractures in the talus rather in the plafond is most likely due to the fact that the osteochondral lesions are more commonly observed on convex



2 Coronal images of the ankle. **2A:** PD-weighted image which shows the chondral fragment on the talar dome (long arrow). **2B:** Fat suppressed PD-weighted TSE image which again demonstrates the chondral fragment (long arrow). The increased signal in the body of the talus (arrowhead) is consistent with edema in the bone marrow as a result of the repetitive irritation caused by the chondral fragment.

surfaces with preferentially sparing of the concave surfaces.

2. Os trigonum injury: The os trigonum is believed to be analogous to a secondary ossification center being formed from a cartilaginous extension of the posterior portion of the talus [2, 3]. It appears between 7–13 years of age, fusing with the posterior process of the talus within 1 year of appearance. In 7–14% patients it remains as a separate ossicle – often present bilaterally. A cartilaginous synchondrosis develops in this region in those adults where it remains separate. A painful os trigonum may be due either from an acute injury or, as likely in this case from a chronic repetitive micro-trauma and resulting chronic diastasis of the synchondrosis [4]. The proximity of the flexor hallucis long tendon is a

feature of which one has to be mindful since pressure from the diastased os trigonum can lead to tenosynovitis. When the involvement of the flexor hallucis tendon becomes chronic and there is degeneration/tendinosis and fibrosis of the tendon between the medial and lateral tubercles of the talus, there can be reduced flexion of the great toe.

References

- 1 Sijbrandij ES, van Gils APG et al Posttraumatic Subchondral Bone Contusions and Fractures of the Talotibial Joint: Occurrence of “Kissing” Lesions. *AJR* 2000; 175: 1707-1710.
- 2 Magee TH, Ginson GW Usefulness of MR Imaging in the detection of talar dome injuries. *AJR* 1998; 170: 1227-1230.
- 3 Karasick D, Schweitzer ME Pictorial Essay The Os trigonum Syndrome: Imaging Features *AJR* 1996; 166: 125-129.
- 4 Grogan DP, Walling AK et al Anatomy of the os trigonum *J Pediatr Orthop* 1990; 10:618-622
- 5 Hedrick MR, McBryde AM Posterior ankle impingement *Foot Ankle* 1994; 15: 2-8.

Contact

Charles P. Ho, PhD, MD
Steadman Philippon Research Institute
181 W. Meadow Dr. Suite 1000
Vail, CO 81657
USA
Karen.briggs@sprvill.org

Long Bone Imaging Distal Lower Limbs utilizing Tim Technology and the Tim User Interface

James Hancock

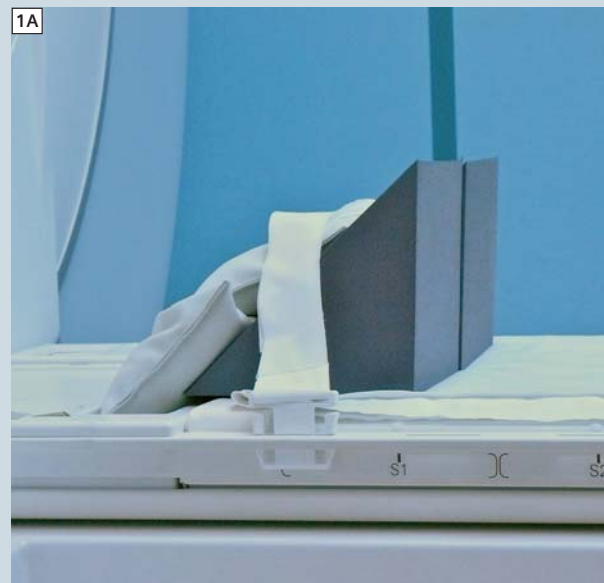
Benson Radiology, Adelaide, South Australia

Distal lower limbs with Tim

Positioning technique

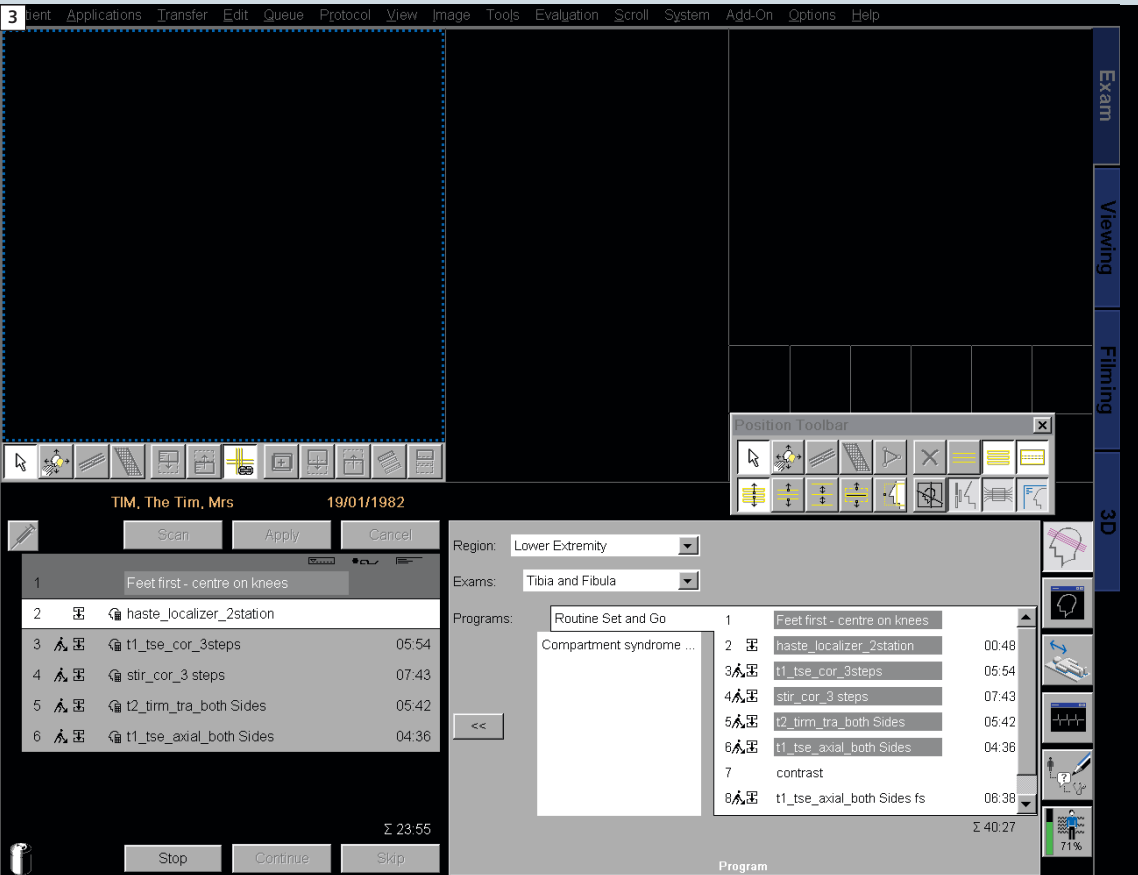
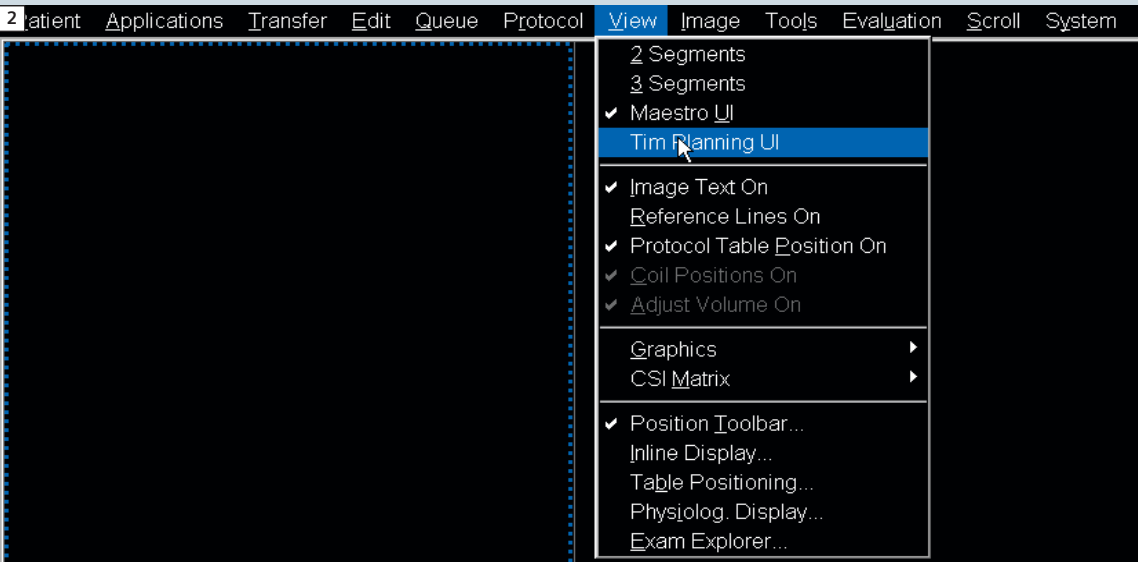
- Head coil and C-spine coil removed from table.
- Spine coil on the table and plugged in.
- Create a bolster for the patient's feet using two triangular pads and sandbags to support them as shown in figure 1. This support needs to be placed in the region of the first spine element as indicated on the table.
- Position the patient on the examination table feet first with their feet dorsiflexed and placed on the support pads.
- Ensure the patient is in the middle of the table and that their legs are as close together as possible without actually touching.
- Place the two Body Matrix coils over the patient's lower limbs strap down and plug in.
- Use the laser to centre to the patients knee joint.
- Press the isocenter button to move the patient in to the magnet bore.

Set up the triangular sponges as shown in these images. Pay attention to the 1st spine element as you want to position them in that region. This allows you to position the patient with their feet dorsiflexed and in the correct anatomical position.



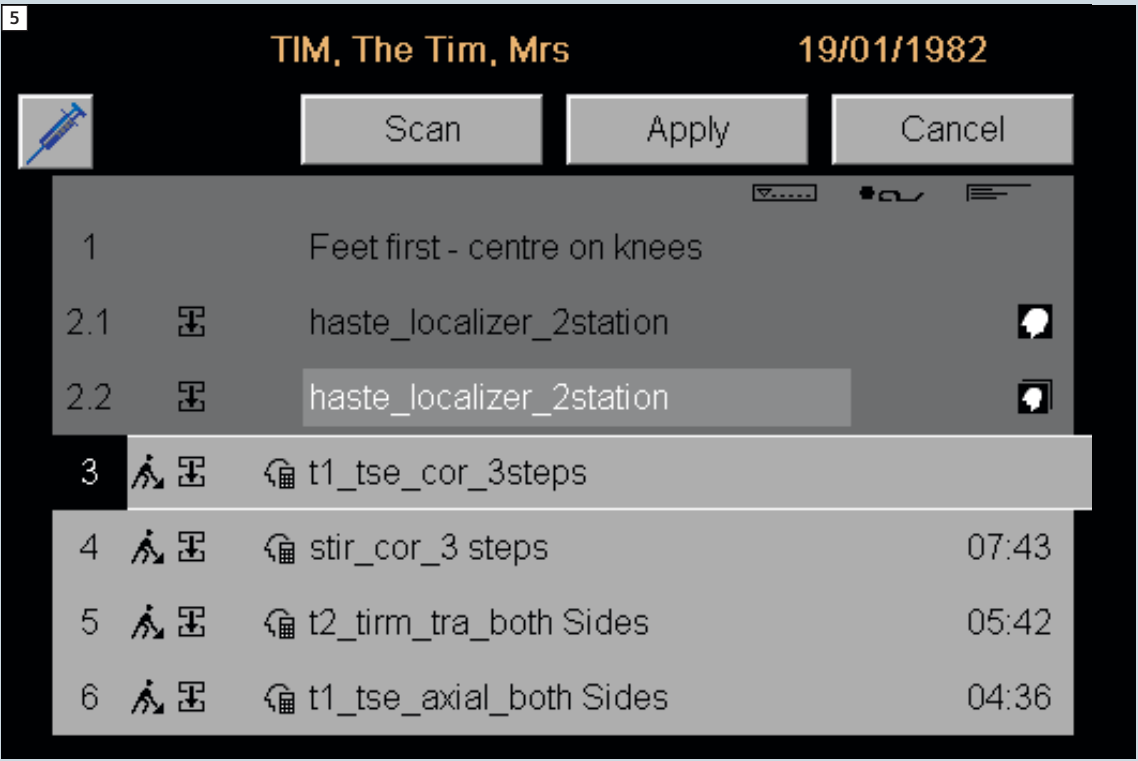
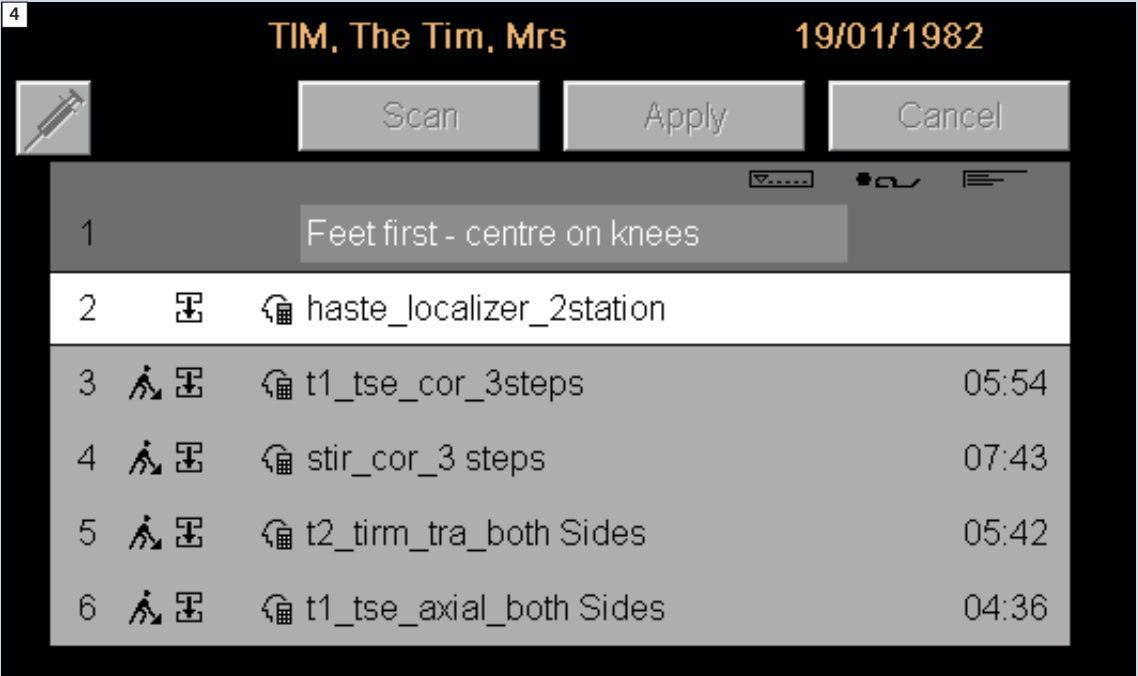
Tim planning

- When running a lower limb protocol it is useful to activate the Tim Planning Suite user interface.
- Figure 3 demonstrates the layout for the Tim User Interface. At our institution the protocol for lower limb MRI is saved under the MSK protocols within the Lower Extremity subsection.



Running the localizers

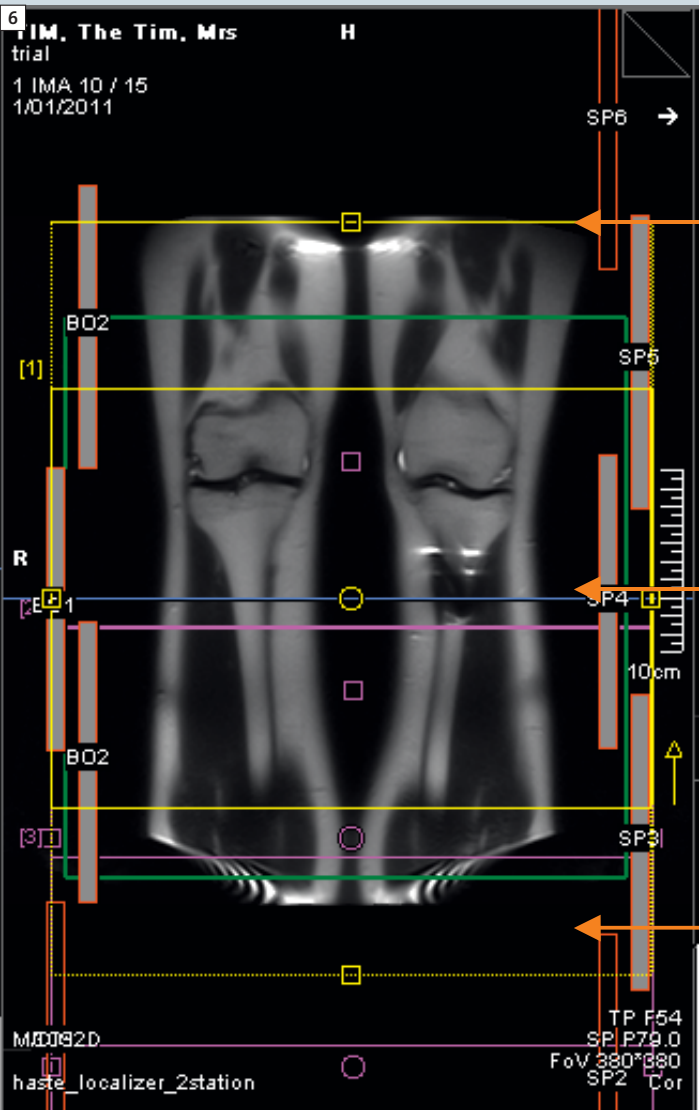
- First step to planning is to run the localizers. Drag the appropriate HASTE localizer into the queue for running. You can bring the other sequences you will run over at the same time. This localizer begins running from the knee down to mid tibia/fibula then moves the table before running localizers from the mid tibia/fibula down to the ankle. We end up with two localizers in the running queue. Once complete the two stations are automatically composed Inline into one complete image for the entire lower limbs in both sagittal and coronal planes. These images allow us to plan the setup for the rest of the scans.



Coronal acquisitions

Setting up the correct fields-of-view

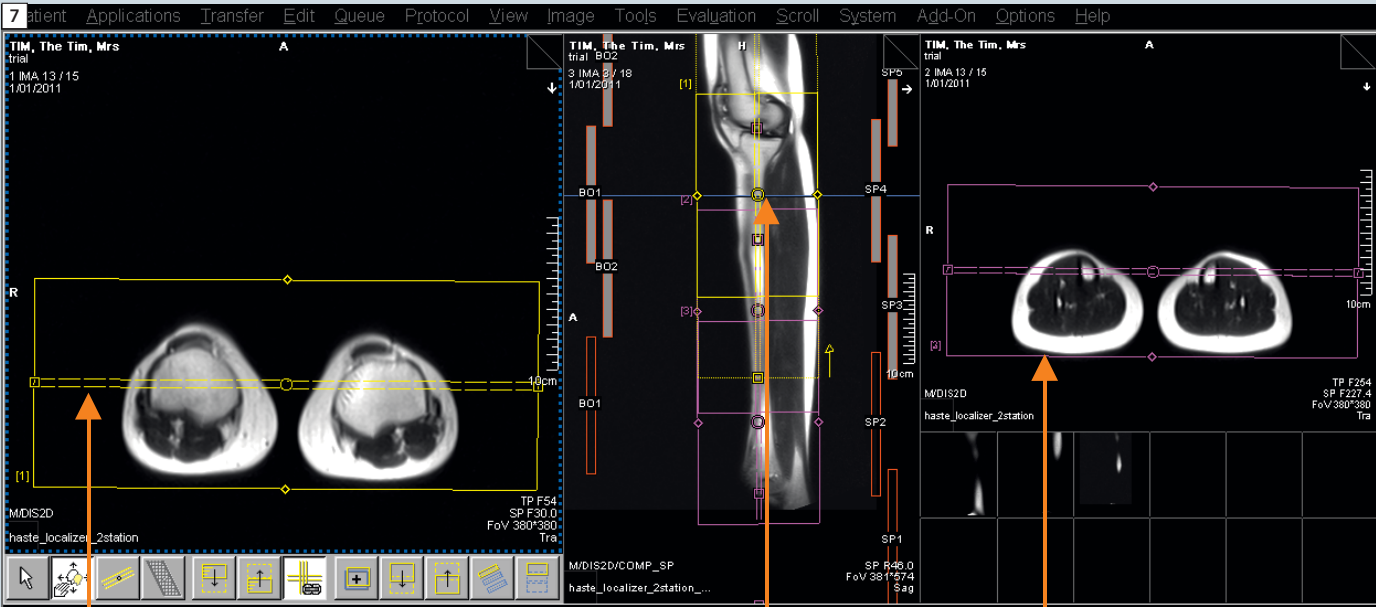
- Drag the T1 coronal sequences across into the queue and open it. This sequence displays three separate sub protocols. This ensures maximum coverage with minimal distortion.
- When setting up for any long bones it is best to take a systematic approach.
- Initially set up your FOV to ensure that you are going to cover the entire region. This involves placing a composed coronal image of the lower limbs into the middle rectangular window.
- When setting up your FOV coverage ensure **coupled graphics is on**. This can be achieved by right clicking in any of the three boxes and selecting the option.
- With coupled graphics on you can then move your FOV and position it appropriately for the correct coverage (Fig. 6).



Note the three separate FOV boxes. The upper FOV is yellow and this indicates that it is currently active. By utilizing coupled graphics you can grab and drag all of the three and move them as one. This makes setting up your coverage very easy. Each FOV is also numbered and you can select them by clicking on the little numbers.

Setting up the slice positions

- Once the FOV has been set you need to set the slice group locations for each of the subgroups.
- The best way to do this is to load your individual axial station localizers into the two square windows. This helps you to visualize your coronal slices.
- In the rectangular window place a composed sagittal image. This gives you an indication of the relationship between each subgroup of slices.
- Unlike the spinal cord almost all patients' long bones are relatively straight. This makes setting the slice positions easy. You can leave coupled graphics on and move the slices as one. Our protocol is set up with plenty of slices to allow easy complete coverage in the coronal plane.



By having an axial localizer of the proximal tibia in this box you can keep an eye on your slice coverage for the proximal portion of the lower legs. Note that there is rotation of this sub-protocol about the H-F axis. This needs to be done with **coupled graphics on** so all sub-protocols match otherwise composition will fail.

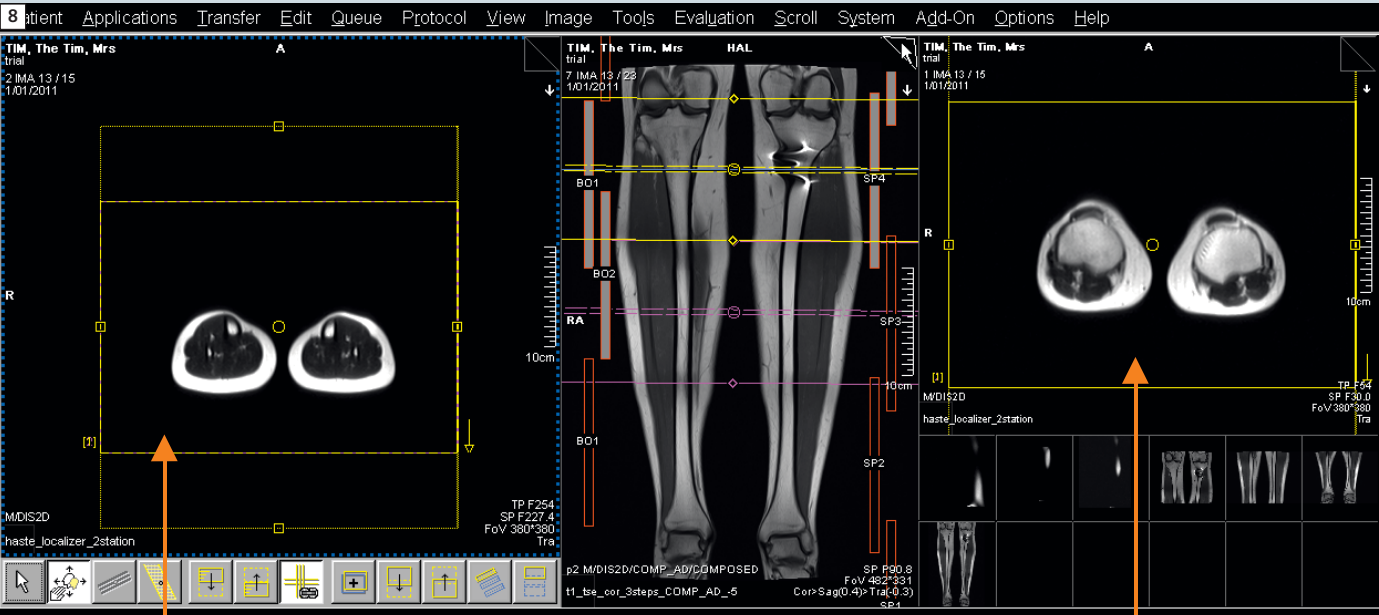
A composed sagittal gives you an indication of both the position of your subgroup slice positions and also a good overview of your total FOV.

By having an axial localiser of the distal tibia in this box you can keep an eye on your slice coverage for the distal portion of the lower legs. Note that there is rotation of this sub-protocol about the H-F axis. This needs to be done with **coupled graphics on** so all sub-protocols match otherwise composition will fail.

Axial acquisitions

Setting up the correct fields-of-view

- Drag the T1 Axial sequences across into the queue and open it. This sequence displays two separate sub-protocols. This ensures we have maximum coverage with minimal distortion.
- To allow for the correct FOV you should again have a separate proximal and distal axial localizer in each of your square windows. This makes it easy to ensure your anatomy is in the middle of the FOV and that you will not cut off anatomical regions as your slices progress down the leg. When adjusting leave **coupled graphics on**.

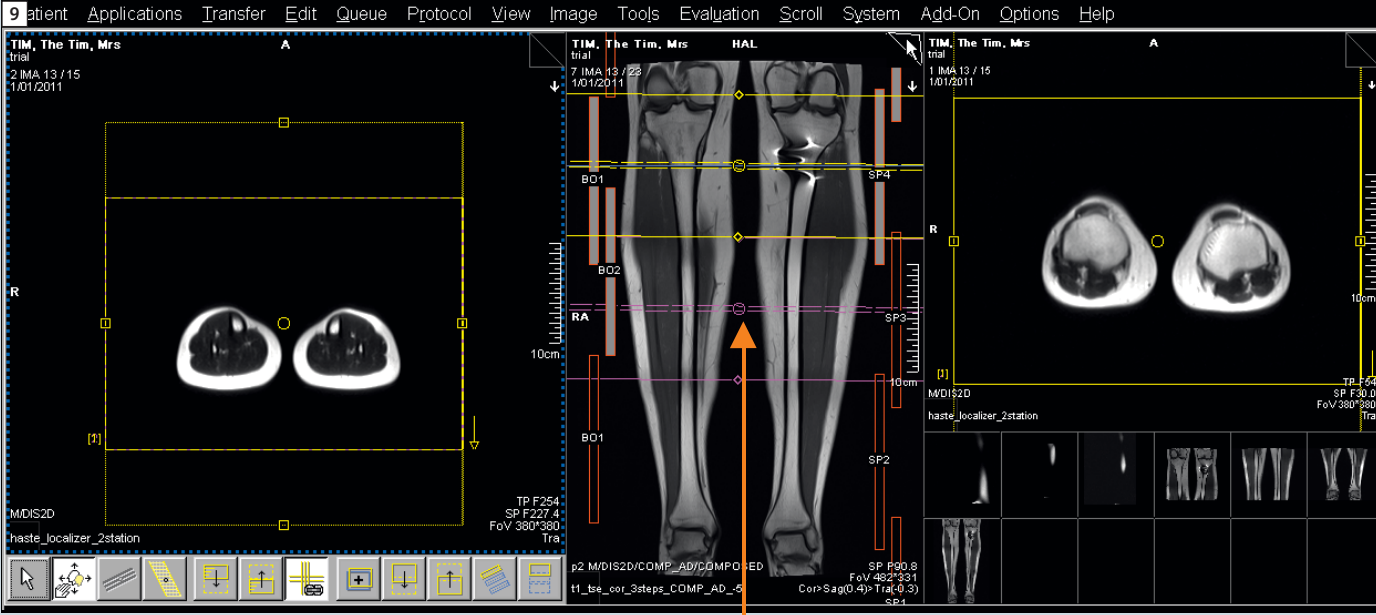


Distal axial localizer. This allows you to position the FOV to ensure you cover the entire distal portion.

Proximal axial localizer. This allows you to position your FOV to ensure you cover the entire proximal portion.

Setting up the slice positions

- Once the FOV has been set you need to set the slice group locations for your axials.
 - In the rectangular window place a composed coronal image which you can use to position your slices. Position your slices to cover the area of interest and within this window
- switch between the coronal and sagittal composed images to ensure your slices are perpendicular and true axials.
- You do this with **coupled graphics on** as the two slice groups are linked and this ensures a contiguous run of axial slices.



Switch between the coronal composed and sagittal composed images when setting up your slice groups. Obviously tailor your slice group to cover the region of interest.



You can see how each subgroup for the T1 coronals has its own number 3.1, 3.2, 3.3 etc. Thus if you need to rerun a region simply hold shift and click the one you need to repeat. Drag and drop that region back into the queue. A cross will run through the compose indicator, this shows that it is only going to run that one region again.

Important notes

- Any presets that you position will affect all three subgroups. As such if you use presets you must pay attention to their positioning.
- Changes made to one subgroup will not affect the other groups so never assume!
- Pay attention to the position of the patient on the table, they need to be close to the middle otherwise you are likely to encounter artifacts on your coronal images.
- Overlaps are built into the protocols, be careful when setting up your FOV. Keep these overlaps in place to ensure smooth composing of final images. Thus when setting up your FOV leave coupled graphics on.
- Avoid in-plane rotation when planning your sequences as this will affect the composing of the final images.
- For coronal and sagittal sequences you may angle your sub-protocols in either the A-P (coronal) or R-L (sagittal) planes when using these 2D protocols. However be aware of the previous point. Thus if setting up a coronal sequence you could angle in the sagittal plane to acquire well placed slices but obviously you need to avoid rotation in the coronal plane as this would correspond to in-plane rotation.
- Rotation of sub-protocols in the F-H (axial) plane should be avoided unless absolutely needed. A difference of just 1 degree between sub-protocols will cause composing to fail. If you do rotate in this plane make sure **coupled graphics is on** as this will ensure any changes you make in this plane apply to all sub-protocols.
- At our institution the axial sequences have been optimized to ensure the maximum coverage with minimal distortion. If you need more coverage consider adding a subgroup rather than increasing the number of slices.
- If you need to repeat a subgroup due to patient movement you only need select the region affected by the movement and rerun that particular subgroup. See the example in figure 10.

Contact

James Hancock
Benson Radiology MRI Department
Ground Floor, 57-59 Anzac Highway
Ashford 5035
South Australia
James.Hancock@bensonradiology.com.au

Long Bone Imaging Proximal Lower Limbs utilizing Tim Technology and the Tim User Interface

James Hancock

Benson Radiology, Adelaide, South Australia

Proximal Lower Limbs with Tim

Positioning technique

- Head coil and C-spine coil removed from table.
- Spine coil on the table and plugged in.
- Create a bolster for the patients' feet using two triangular pads and sandbags to support them as shown in the images. This support should be placed as close to the opening of the bore as strapping will allow. This support helps the patient keep their legs still.
- Position the patient on the examination table feet first with their feet dorsiflexed and placed on the support pads.
- Ensure the patient is in the middle of the table and that their legs are as close together as possible.
- Place the two Body matrix coils over the patient's upper limbs strap down and plug in. Start from the patella apex as a guide.
- Use the laser to centre to the patients symphysis.
- Press the isocentre button to move the patient in to the magnet bore.

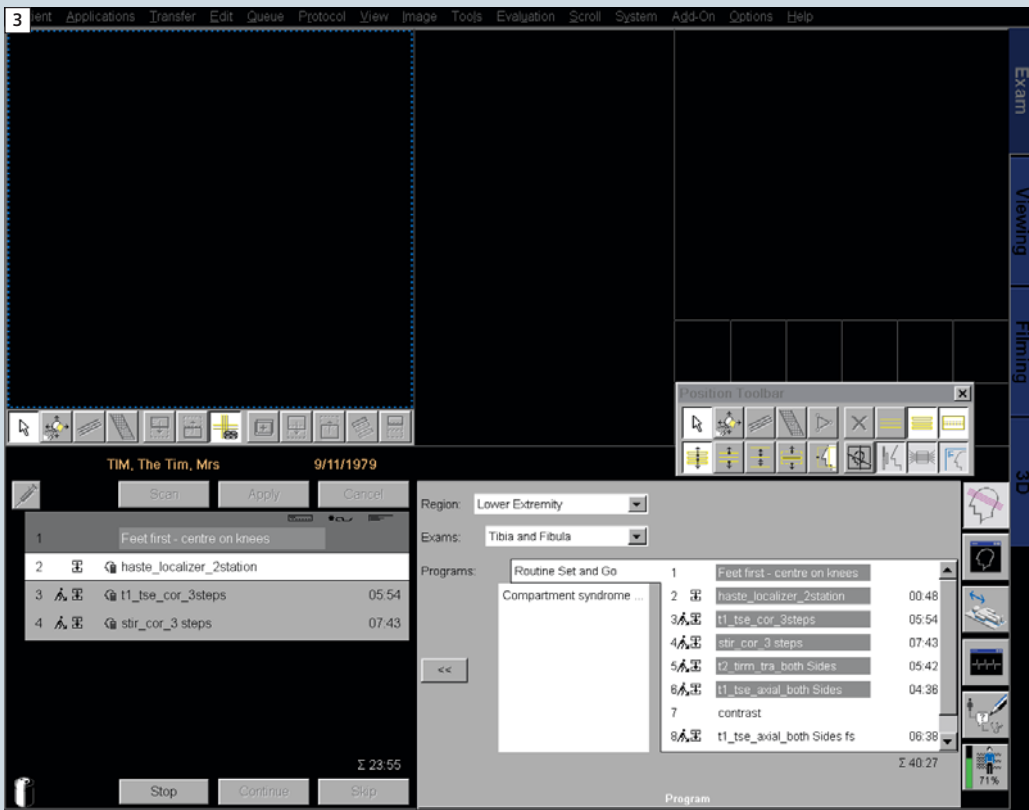
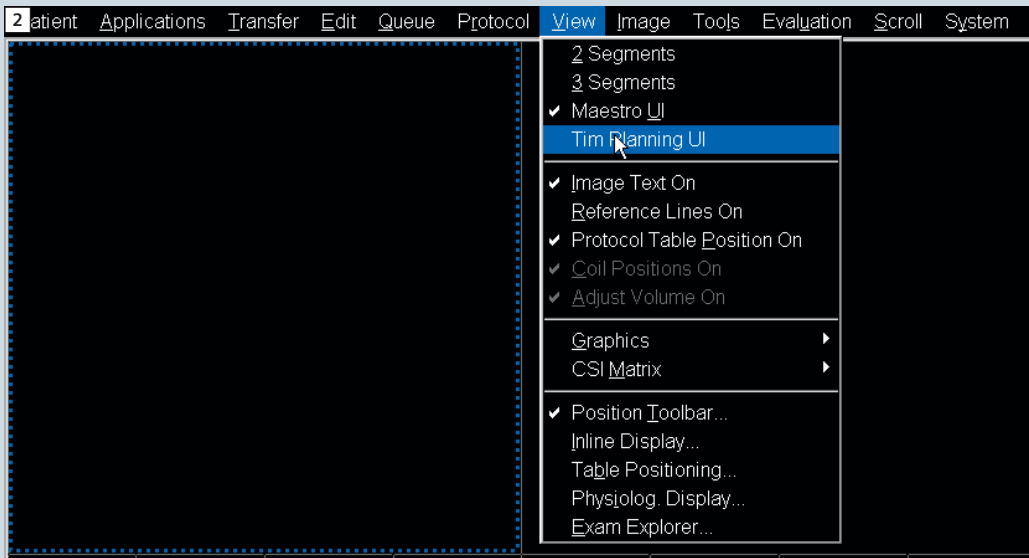
Set up the triangular sponges as shown in these images. You can move this support even closer to the bore than in this image as you can see there is still one more distal strapping point. This allows you to position the patient comfortably with a high degree of immobilisation.





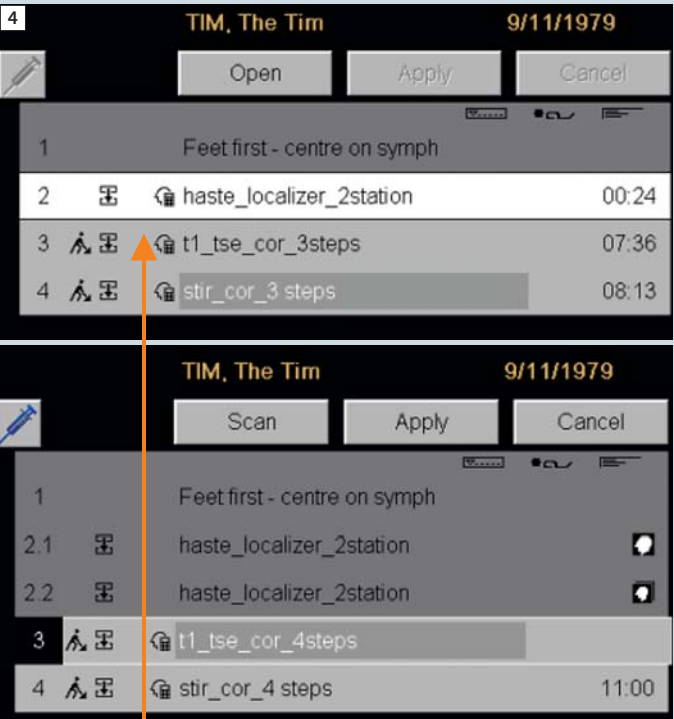
Tim planning

- When running a lower limb protocol it is useful to activate the Tim Planning Suite user interface.
- Figure 3 demonstrates the layout of the Tim User Interface. At our institution the protocol for lower limb MRI is saved under the MSK protocols within the Lower Extremity subsection. Generally for the proximal lower limb you will either be looking at the hamstrings or the femur and surrounding soft tissues.

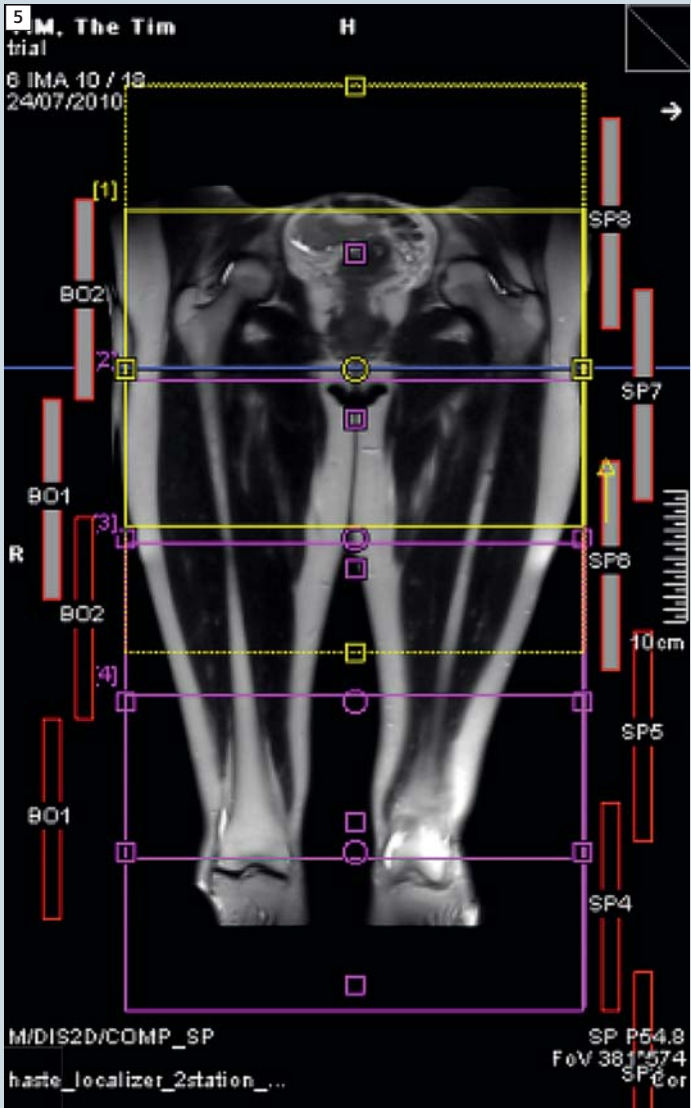


Running the localizers

- First step to planning is to run the localizers. Drag the appropriate HASTE localizer into the queue for running. You can bring the other sequences you will run over at the same time. This localizer begins running from the symphysis down to mid femur then moves the table before running localizers from the mid femur down to the knee. We end up with two localizers in the running queue and thus a two station localizer. Once complete these two stations are automatically composed Inline into one complete image for the entire proximal lower limbs in both sagittal and coronal planes. These images allow us to plan the setup for the rest of the scans.



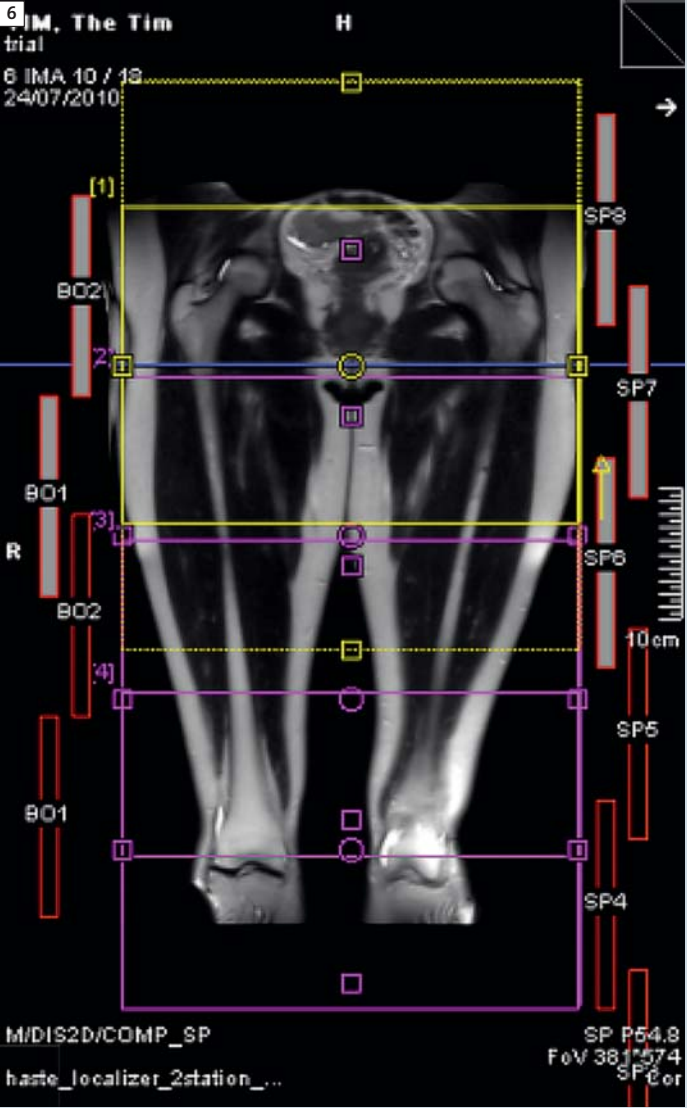
In this example localizer the patient has very long femurs. As such the Technologist has switched from a 3 step protocol to a four step protocol.



Coronal acquisitions

Setting up the correct fields-of-view

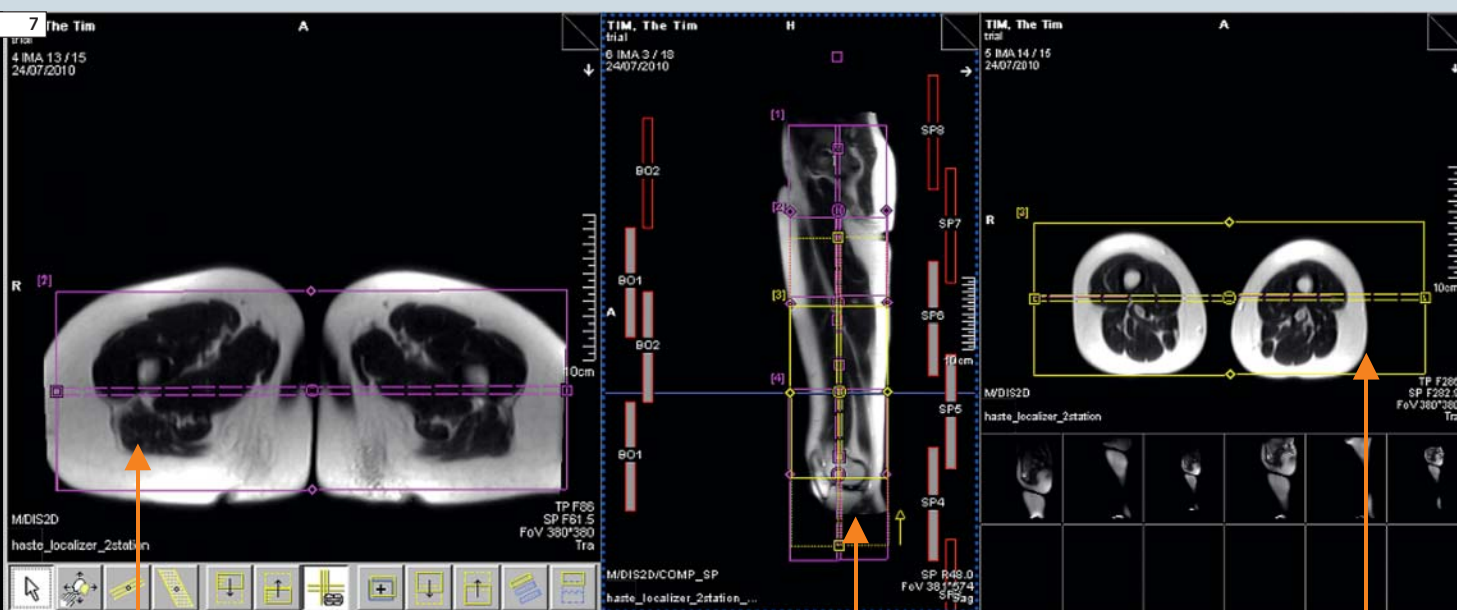
- Drag the T1 coronal sequences across into the queue and open it. The default is a 3 step protocol. This sequence displays three separate sub-protocols. This ensures we have maximum coverage with minimal distortion. If upon opening this sequence it becomes obvious that you will not have enough coverage then there is also a four station sub protocol available. Some people have very long legs!
- When setting up for any long bones it is best to take a systematic approach.
- Initially set up your FOV to ensure that you are going to cover the entire region. This involves placing a composed coronal image of the lower limbs into the middle rectangular window.
- When setting up your FOV coverage ensure **coupled graphics is on**. This can be achieved by right clicking in any of the three boxes and selecting the option.
- With coupled graphics on you can then move your FOV and position it appropriately for the correct coverage (Fig. 6).



Note the four separate FOV boxes. The upper FOV is yellow and this indicates that it is currently active. By utilizing coupled graphics you can grab and drag all of four and move them as one. This makes setting up your coverage very easy. Each FOV is also numbered and you can select them by clicking on the little numbers.

Setting up the slice positions

- Once the FOV has been set you need to set the slice group locations for each of the subgroups.
- The best way to do this is to load your individual axial station localizers into the two square windows. This helps you to visualise your coronal slices.
- In the rectangular window place a composed sagittal image. This gives you an indication of the relationship between each subgroup of slices.
- Unlike the spinal cord almost all patients' long bones are relatively straight. This makes setting the slice positions easy. You can leave coupled graphics on and move the slices as one. The protocol is set up with plenty of slices to allow easy complete coverage in the coronal plane.



By having an axial localizer of the proximal femur in this box you can keep an eye on your slice coverage for the proximal portion of the lower legs. This sub-protocol is not rotated about the H-F axis which is ideal. However if this needs to be done do so with **coupled graphics on** so all sub-protocols match. Otherwise composition will fail (see important notes).

A composed sagittal gives you an indication of both the position of your subgroup slice positions and also a good overview of your total FOV.

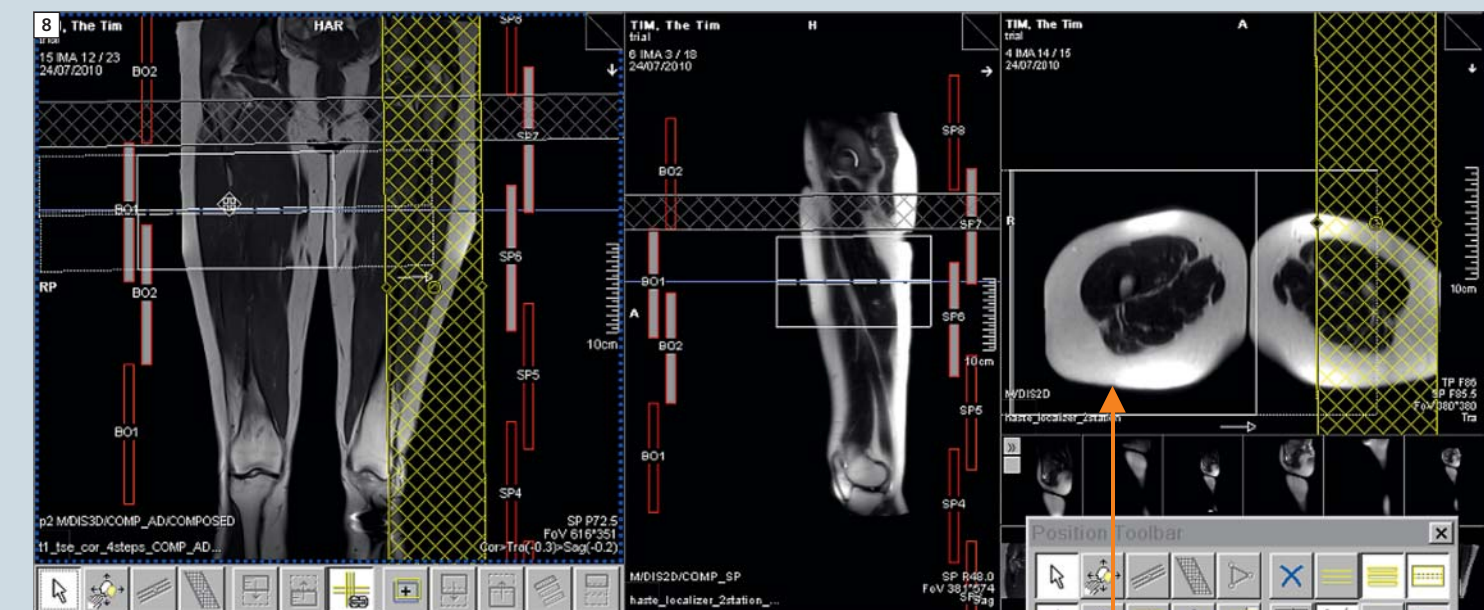
By having an axial localiser of the distal femur in this box you can keep an eye on your slice coverage for the distal portion of the lower legs. This sub-protocol is not rotated about the H-F axis which is ideal. However if this needs to be done do so with **coupled graphics on** so all sub-protocols match otherwise composition will fail (see important notes).

Axial acquisitions

Setting up the correct fields-of-view

- Drag the T1 axial sequence across into the queue and open it. This is a single slice group.
- To allow for the correct FOV you can place a coronal, sagittal and axial set of images in each window. This makes

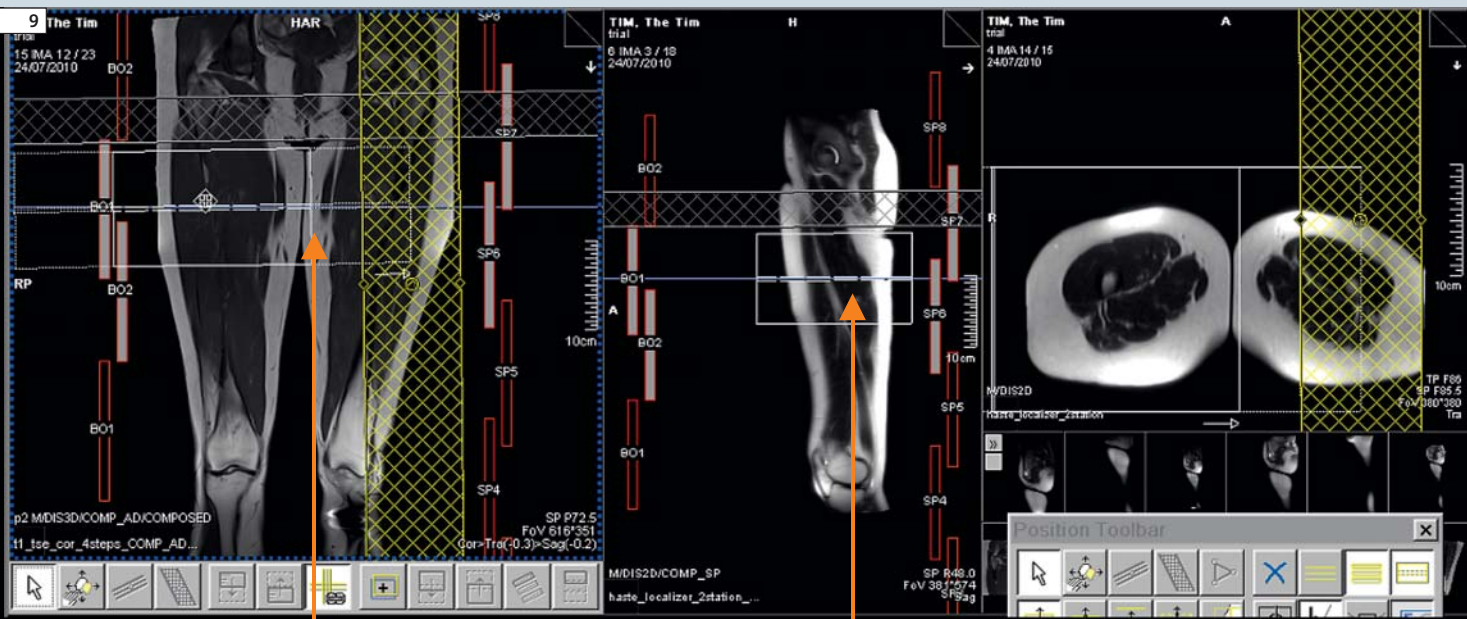
it easy to ensure your anatomy is in the middle of the FOV and that you will not cut off anatomical regions as your slices progress down the leg.



The proximal axial localizer allows you to position your FOV to ensure you cover all of the proximal portion assuming of course that the region of interest lies in this region.

Setting up the slice positions

- Once the FOV has been set you need to set the slice group locations for your axials.
 - Making use of the three windows place coronal sagittal and axial slice groups into each. You can then easily identify the relevant region of interest and ensure your slice groups are running through that region. If there is concern over coverage consider turning the single slice group into a multi-
- step protocol by adding a sub-protocol from the Tim planning suite toolbar.
- Depending on your choice of axials if you need to cover a large region then you will be using a multi group sequence. In this case when setting up do so with **coupled graphics on** as the two slice groups are linked and this ensures a contiguous run of axial slices.



Coronal and sagittal slices make it very easy to identify the region your slices should cover in the axial plane.

Important notes

- Any presets that you position will affect all three subgroups. As such if you use presets you must pay attention to their positioning.
 - Changes made to one subgroup will not affect the other groups so never assume!
 - Pay attention to the position of the patient on the table, they need to be close to the middle otherwise you
- coronal sequence you could angle in the sagittal plane to acquire well placed slices but obviously you need to avoid rotation in the coronal plane as this would correspond to in-plane rotation.
- Rotation of sub-protocols in the F-H (axial) plane should be avoided unless absolutely needed. A difference of just 1 degree between sub-protocols



You can see how each subgroup for the T1 coronals has its own number 3.1, 3.2, 3.3 etc. Thus if you need to rerun a region simply hold shift and click the one you need to repeat. Drag and drop that region back into the queue. A cross will run through the compose indicator, this shows that it is only going to run that one region again.

- are likely to encounter artefacts on your coronal images.
- Overlaps are built into the protocols, be careful when setting up your FOV. Keep these overlaps in place to ensure smooth composing of final images. Thus when setting up your FOV leave coupled graphics on.
 - Avoid in-plane rotation when planning your sequences as this will affect the composing of the final images.
 - For coronal and sagittal sequences you may angle your sub-protocols in either the A-P (coronal) or R-L (sagittal) planes when using these 2D protocols. However be aware of the previous point. Thus if setting up a
- will cause composing to fail. If you do rotate in this plane make sure **coupled graphics is on** as this will ensure any changes you make in this plane apply to all sub-protocols.
- The axial sequences have been optimised to ensure the maximum coverage with minimal distortion. If you need more coverage consider adding a subgroup rather than increasing the number of slices.
 - If you need to repeat a subgroup due to patient movement then you only need select the region affected by the movement and rerun that particular subgroup. See the example in figure 10.

Contact
James Hancock
Benson Radiology MRI Department
Ground Floor, 57-59 Anzac Highway
Ashford 5035
South Australia
James.Hancock@bensonradiology.com.au

Frequently Asked Questions: Diffusion-Weighted Imaging (DWI)

Joachim Graessner, Dipl. Ing.

Siemens Healthcare, Hamburg, Germany

Background

MR diffusion-weighted imaging (DWI) has ceased to be used only in brain applications for several years. The utilization of whole body DWI is becoming a standard application in routine imaging.

Whole body DWI has become as valuable as T2 contrast in tumor imaging and it allows to characterize tissue properties. Due to the more frequent use of DWI, questions are often asked with regard to the background, application, and interpretation of whole body DWI and its calculated Apparent Diffusion Coefficient (ADC) images.

The following will answer some of these questions.

What is diffusion?

Molecular diffusion is the random movement of molecules – in our case water (H₂O) – within tissues propelled by thermal energy. The contribution of intra- and extra-cellular (interstitial) movement to the total diffusion is still under investigation.

How is MR sensitizing the tissue for diffusion effects?

Within the spin echo preparation period of an EPI sequence, two strong gradient pulses are played out around the 180° pulse. The first pulse dephases the magnetization of moving and static spins and the second pulse rephases only static spins 100% while moving i.e. diffusing spins acquire non-zero phase dispersion, resulting in a stronger signal dampening of tissues with fast diffusion compared to tissues with slow diffusion. Free water experiences the strongest signal attenuation at higher b-values.

What does the b-value mean?

The b-value identifies the measure-

ment's sensitivity to diffusion and determines the strength and duration of the diffusion gradients. It combines the following physical factors into one b-value and is measured in s/mm² [1].

$$b = \gamma^2 G^2 \Delta (\Delta - \frac{1}{3})$$

The signal ratio diffusion-weighted to non diffusion-weighted signal is:

$$\frac{S}{S_0} = e^{-\gamma^2 G^2 \Delta (\Delta - \frac{1}{3}) D} = e^{-bD}$$

- S₀ – signal intensity without the diffusion weighting
- S – diffusion-weighted signal
- γ – gyromagnetic ratio
- G – amplitude of the two diffusion gradient pulses
- Δ – duration of the pulses
- Δ – time between the two pulses
- D – diffusion coefficient is a measure of the strength (velocity) of diffusion

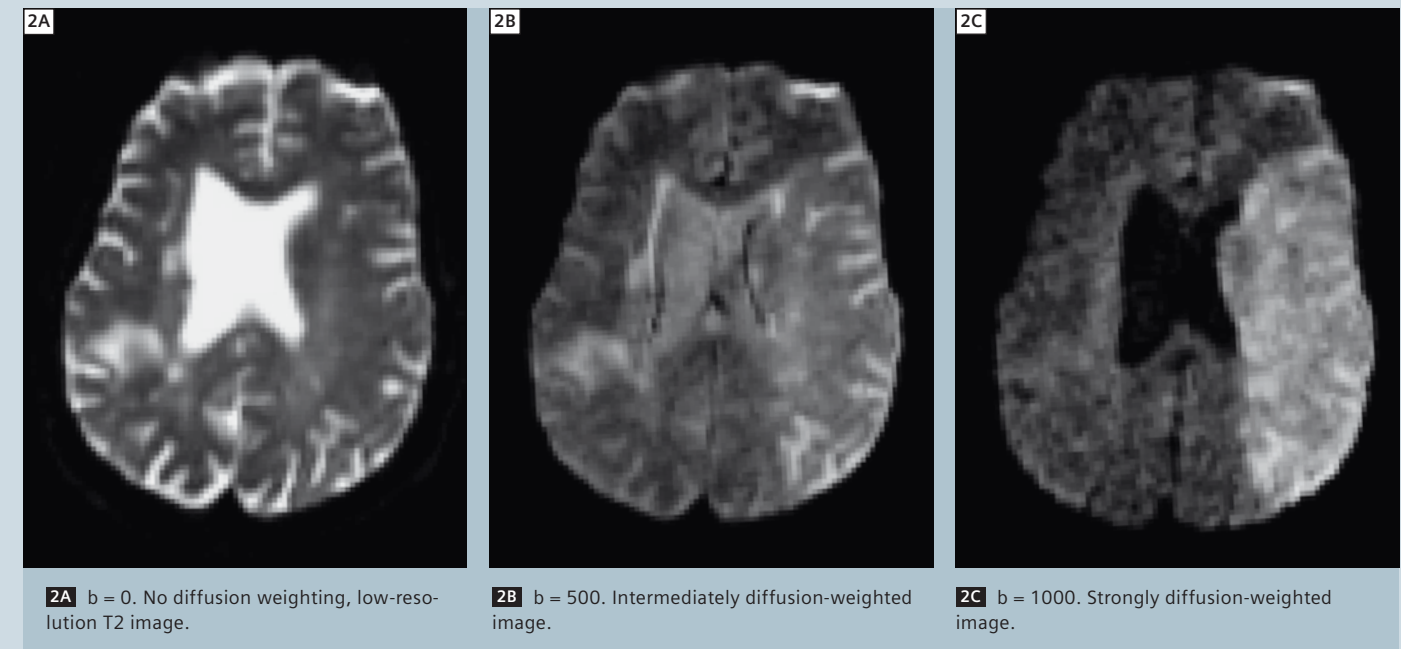
in tissue. The stronger the diffusion, the greater the diffusion coefficient, i.e. the ADC in our in vivo case.

If you choose the b-value the reciprocal magnitude of the expected ADC (D) in the focus tissue you make the exponent of the exponential function being '-1'. This means your signal S is reduced to about 37% of its initial value S₀.

What is the optimum b-value?

A b-value of zero delivers a T2-weighted EPI image for anatomical reference. The b-values should attenuate the healthy background tissue more than the lesion at a level so that the intensity differences are about a factor of two at a comfortable signal-to-noise ratio (SNR) level i.e. there is signal left in the highest b-value image.

In the range of clinically-relevant b-values (up to approximately 1,000), then the greater the b-value, the stronger the diffusion weighting and the higher



the contrast in pathogenic regions. Shown below are examples of three b-values: b 0, b 500, and b 1000 s/mm². The proper b-value has approximately 80% of the reciprocal ADC value of normal background tissue. Keep in mind that higher b-values may pronounce lesions even more at the price of poor SNR due to longer TEs and increased susceptibility. This can be compensated by increasing averages, which result in longer scan times. Changing the b-value immediately influences other parameters like minimal TE, slice thickness and FOV as well as maximum matrix at a given optimal bandwidth. Furthermore anisotropy of tissues, like white matter, also influences the choice [2].

Why are a minimum of three directions measured for each high b-value?

Diffusion may be different in all three dimensions, like in white matter. Fibers exhibit longer free path in the longitudinal direction than perpendicular to it. The ADC images are therefore different depending on the sensitizing direction. This information is collected by applying diffusion gradients in all three dimensions. For example, in the case of commissures, diffusion is severely limited perpendicular to the fibers due to the surrounding myelin layer. In contrast, there are few or no limitations along the fibers. Anisotropy may have a strong effect

on measurement results. To measure the diffusion strength independent of anisotropy, diffusion images of different orientation are measured and averaged.

Why should I measure three b-values for a DWI protocol when two would be enough for calculating ADC?

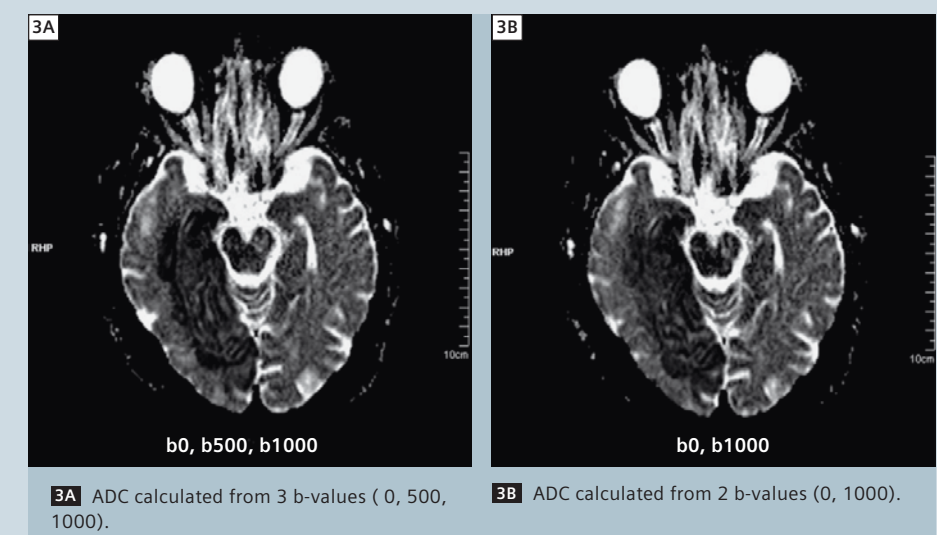
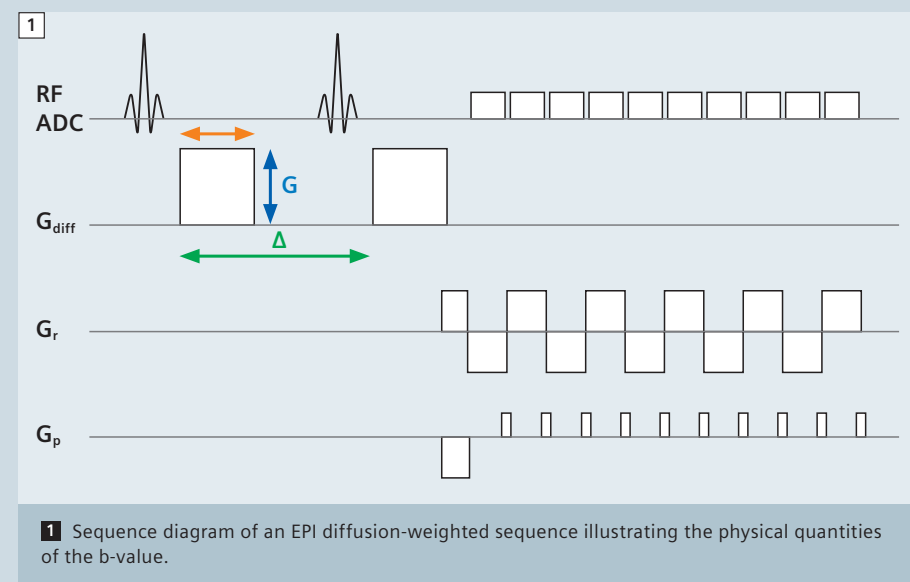
While two b-values are sufficient for creating an ADC image, the selection of three b-values (b 0, b 500, b 1000) delivers a more accurate calculation of the ADC values. The lower SNR of the b 1000 images introduces a higher standard deviation of the ADC which is partially compensated by the median value of b500. Here is an example of two ADC images,

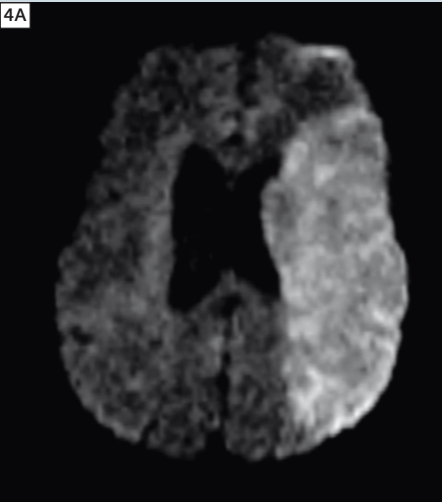
the first acquired with three b-values and the second with two b-values.

What is a trace image?

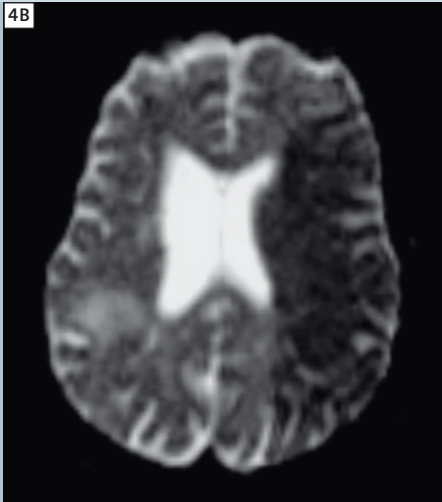
The 'trace image' displays the geometric averaging of all three directional measurements, resulting in trace-weighted images. It suppresses to some extent anisotropy information and focuses on differences in signal attenuation. Like the ADC map, the trace-weighted map shows the strength of the diffusion and not its orientation.

Why do we need ADC images, and what does the 'A' in ADC stand for?
In addition to diffusion contrast, diffu-

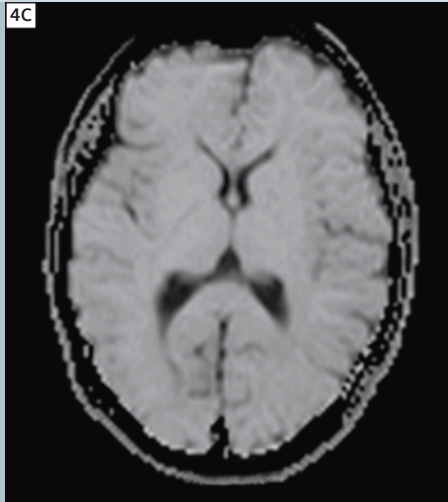




4A b1000 image; infarct is brighter than normal tissue.



4B ADC Image; infarct appears darker than normal tissue.



4C Exponential-Map

sion images also have an overlaying T2 contrast. In regions with long T2, this can simulate reduced diffusion (‘T2 Shine-Through’). These portions of the signal can be eliminated by calculating a pure diffusion coefficient. The ‘A’ stands for apparent because we do not measure the pure diffusion coefficient (D or DC). In living tissue the diffusion process is superimposed by capillary pseudo diffusion and gross motion to which the MR measurement is also very sensitive.

How is the ADC calculated?

Having measured a set of at least 2 different b-value images (e.g., b 0 and b 1000 s/mm²) the system calculates pixel by pixel the ADC by linear regression. The ADC pixel values together form the ADC map. On a half logarithmic scale, the signal decay delivers a straight tilted line whose slope provides the ADC. The faster the signal decay the steeper the slope and the higher the ADC. The Diffusion image (b 1000) below displays reduced diffusion as hyperintense (brighter pixels); in contrast the ADC map displays it as hypointense (darker pixels).

Why are some lesions typically brighter than the background brain tissue on the higher b-value image and darker on the ADC map?

Due to the nature of certain lesions and their missing perfusion, the cells swell and hinder a normal diffusion; i.e.,

the mean free path is shorter. Water molecules cannot move as far in the damaged tissue as in normal tissue. As a result, the ADC is lower and appears darker than the surrounding normal tissue.

Which benefit does the calculation of an exponential map deliver?

The exponential map or image is calculated by dividing the maximal b-value diffusion-weighted image by the b₀ image. Mathematically the exponential map displays the negative exponential of the ADC; it is a synthetic diffusion-weighted image without T2 ‘shine-through’ effect. The contrast behaviour is similar to the high b-value image [3].

How do I get the ADC value out of my ADC image and what is the right unit?

Place a region of interest (ROI) on the ADC map and record the mean value in that ROI. A value of 850 intensity points is to be interpreted as 0.85 10⁻³ mm²/s. This is valid for software versions since *syngo* MR B13. Systems with A-level software (e.g., *syngo* MR A30) and *syngo* MR B11, a mean value of 85 delivers the result above.

There are many publications on DWI and ADC. But why are there so many different unit and digits used for ADCs?

Currently, there is no consensus about applied units in DWI. You will find all

of the following units which are equal (*syngo* MR B13).

A mean intensity of 1000 is equal to:

1.0*µm²/ms or intensity times 10⁻³

1.0*10⁻³ mm²/s or intensity times 10⁻⁶

1.0*10⁻⁵ cm²/s or intensity times 10⁻⁸

1.0*10⁻⁹ m²/s or intensity times 10⁻¹²

Also found:

1000*10⁻⁶ mm²/s

1000*µm²/s

Why does the ADC have a unit of an area/time although diffusion occurs in all three dimensions?

By definition, the diffusion coefficient is defined as the product of 1/3 times medial velocity times mean free path:

D = 1/3 * v * l

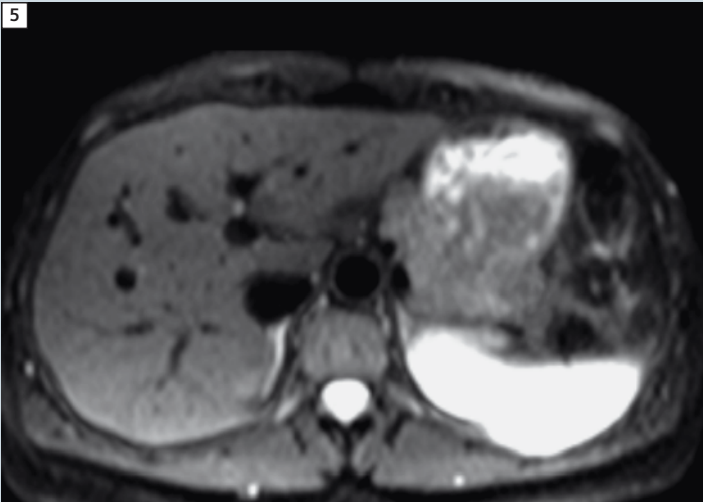
The unit is an area per time.

Why is there a lack of standardization for the choice of b-values in whole body DWI?

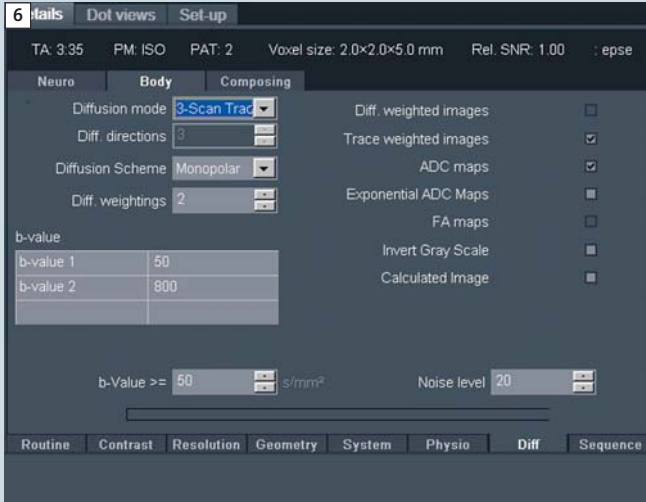
As a relatively new application body DWI is on its way to become a technique with recommended b-values and measurement conditions. See cited reference [4] for further information.

Why do most body and liver DWI protocols start with b-value 50 s/mm²?

The selection of a low b-value larger than zero provides suppression of large vessels which makes lesions more con-



5 b50 image of normal liver at 3T.



6 syngo body-diffusion card in software version syngo MR D11A.

spicuous. The calculation of the tissue ADC can be more accurate when starting with even higher b-values like 100 or 200 to omit the contribution of flow and micro vascular effects. Low b-values more often serve as anatomical reference. In software level *syngo* MR D11A and above you can delimit the b-values for ADC calculation on the body diffusion application card of the protocol.

Why do liver diffusion-weighted images look darker on 3T than 1.5T?

The T2 and T2* relaxations times for liver tissue, and other tissues as well, are considerably shorter as the field strength increases. The overall signal is therefore diminished at 3T, even at lower b-values, due to the relatively long echo times (TE) used in DWI [5].

Which new DWI features are introduced with software version syngo MR D11A for MAGNETOM Aera and Skyra?

- There is a new ‘body diffusion’ application card with many new applications:
- diffusion scheme monopolar/bipolar
 - start ADC calculation for b > = ...
 - exponential ADC; no T2 shine-through
 - invert gray scale (“PET-like” image)
 - calculated image of artificial b-values plus
 - choice of dynamic field correction
 - improved fat saturation schemes

What should I know when scanning liquids in phantoms with DWI sequences?

Firstly, the liquids should not move in the phantom bottle. Flowing liquid in the phantom would cause artificially strong diffusion and results in low intensity DWI images with inaccurately long ADC values. Secondly, the diffusion coefficient is also strongly temperature dependent. Pure water has a diffusion coefficient of about 3 * 10⁻³ mm²/s (exactly: 2.96) at body temperature of 37 °C (98.6 °F). Water of 0 °C (32 °F) has a diffusion coefficient of 1.12 * 10⁻³ mm²/s. This could serve as a standard for different machines.

Additional reading

In addition to the comprehensive Siemens applications guide, “Diffusion/Perfusion Imaging”, there is literature [6] available which covers neuro and body diffusion. (Listed according to year of publication): **Derek K. Jones:** Diffusion MRI: Theory, Methods, and Applications; Oxford University Press **Bachir Taouli:** Extra-Cranial Applications of Diffusion-Weighted MRI; Cambridge University Press **Dow-Mu Koh:** Diffusion-Weighted MR Imaging: Applications in the Body; Springer **Heidi Johansen-Berg:** Diffusion MRI: From Quantitative Measurement to In-Vivo Neuroanatomy; Academic Press

References

- 1 Le Bihan D, Breton E, Lallemand D, Grenier P, Cabanis E, Laval-Jeantet M (1986). MR imaging of intravoxel incoherent motions; application to diffusion and Perfusion in neurologic disorders. Radiology. 161: 401-407.
- 2 Kingsley PB, Monahan WG (2004) Selection of the Optimum b Factor for Diffusion-Weighted Magnetic Resonance Imaging Assessment of Ischemic Stroke. MRM 51: 996-1001.
- 3 Provenzale JM, Engelter ST, Petrella JR, Smith JS, MacFall JA (1998). Use of MR Exponential Diffusion-Weighted Images to eradicate T2 “Shine-Through” Effect. AJR. 172:537-539.
- 4 Padhani AR, Liu G, Mu-Koh D, Chenevert TL, Thoeny HC, Takahara T, Dzik-Jurasz A, Ross BD, Van Cauteren M, Collins D, Hammoud DA, Rustin GJS, Taouli B, Choyke PL (2009). Diffusion-Weighted Magnetic Resonance Imaging as a Cancer Biomarker: Consensus and Recommendations. NEOPLASIA.11 (2): 102-125.
- 5 de Bazelaire CMJ, Duhamel GD, Rofsky NM, Alsop DC (2004).MR Imaging Relaxation Times of Abdominal and Pelvic Tissues in Vivo at 3.0 T. Radiology 230: 652-659.
- 6 Hagmann P, Jonasson L, Maeder P, Thiran JP, Van Wedeen J, Meuli R (2006). Understanding Diffusion MR Imaging Techniques: From Scalar Diffusion-weighted Imaging to Diffusion Tensor Imaging and Beyond. Radiographics 26: 205-223.

Contact

Joachim Graessner, Dipl. Ing.
Siemens Healthcare
GER H IM BM MR
Lindenplatz 2
20099 Hamburg
Germany
joachim.graessner@siemens.com

Whole-Body MR/PET Hybrid Imaging: Technical Considerations, Clinical Workflow, and Initial Results

Harald H. Quick, PhD¹; Ralf Ladebeck, PhD²; Jens-Christoph Georgi, PhD²

¹Institute of Medical Physics (IMP), Friedrich-Alexander University Erlangen-Nürnberg, Erlangen, Germany

²Siemens AG Healthcare Sector, Erlangen, Germany

MR/PET – Advent of a new hybrid imaging modality

These days we are eyewitnesses to an exciting new hybrid imaging modality to enter the clinical arena, namely simultaneous whole-body MR/PET imaging. Envisioning the combination of the excellent soft tissue contrast, high spatial and temporal resolution, and functional tissue parameters that MR provides with the high sensitivity of PET, different technical approaches have been pursued by researchers and by the industry to work on the integration of two formerly 'non-integrable' imaging modalities. With the recent introduction of the Biograph mMR, Siemens has launched a 3.0 Tesla whole-body MR hybrid system that hosts in its isocenter a fully integrated PET detector and that with its 60 cm patient bore enables whole-body simultaneous MR/PET imaging.

Researchers, radiologists, and nuclear medicine physicians have been waiting and actively been working on the advent of this hybrid imaging modality for a long time [1–3]. A detailed overview about the pre-clinical developments, the

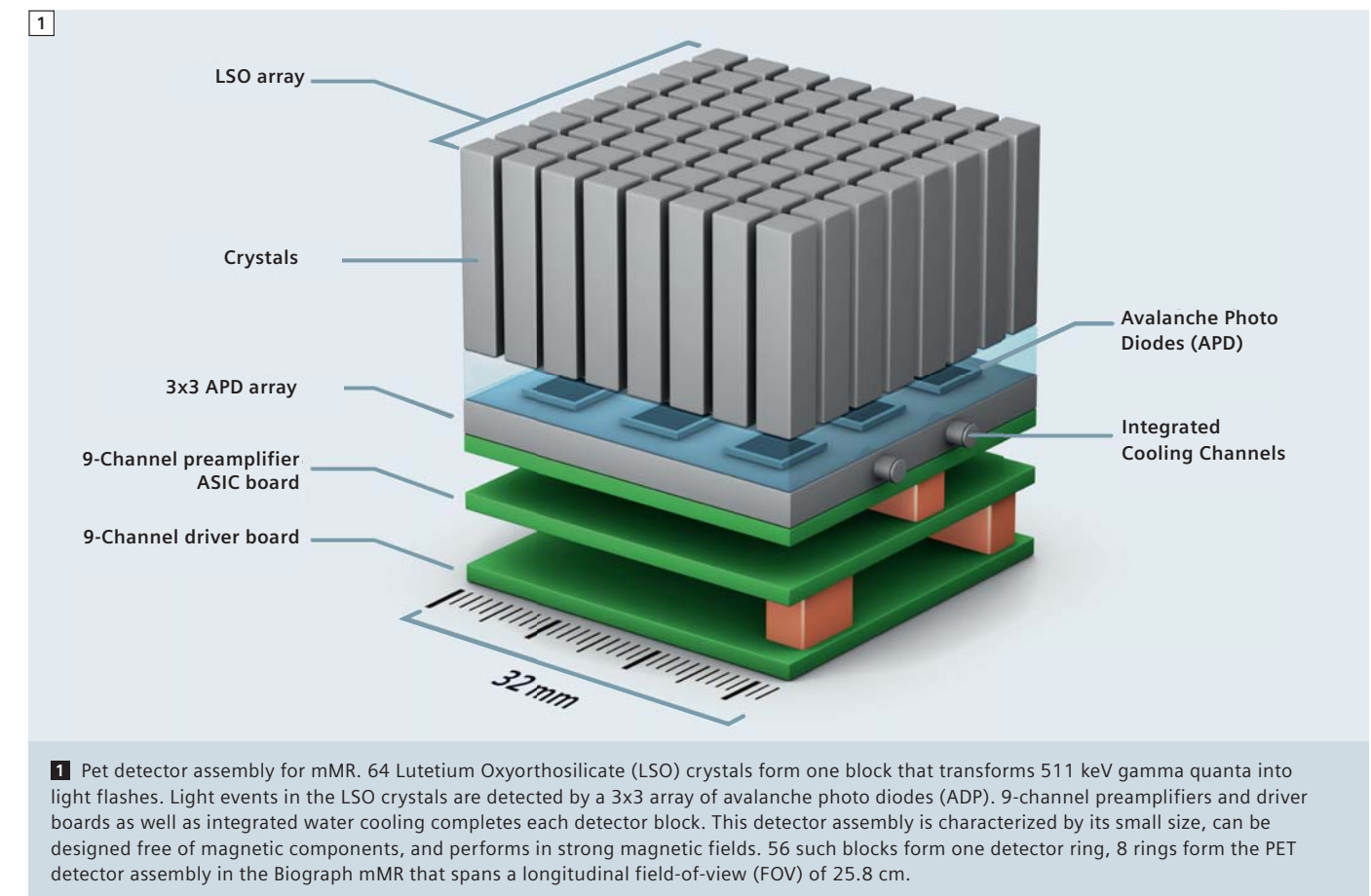
rationale to combine MR and PET as well as the steps which were necessary for integrating these imaging modalities to allow simultaneous scanning can be found in the article by Beyer et al. 'MR/PET – Hybrid Imaging for the Next Decade', published in the supplement of issue 3/2010, RSNA edition of MAGNETOM Flash. Now that whole-body MR/PET has entered clinical practice, we have a starting point to evaluate the full clinical potential of the modality, to research for and to validate new imaging applications, and to ultimately establish this imaging modality in early diagnosis of oncologic, neurologic, cardiologic, and many more diseases.

As more and more research and clinical sites come on board during the months and years ahead, let's take a first look into the technology and explore what specifics such an integrated MR/PET hybrid system brings with it. We will then also explore the workflow of a MR/PET whole-body hybrid exam and present first image examples from clinical findings.

Technical integration of MR and PET

The Biograph mMR hybrid imaging system fully integrates the MR and the PET imaging modality into one imaging system. In order to ensure such a high level of integration, we have to overcome numerous physical and technical preconditions and challenges. The potential physical interactions of both modalities in both directions – PET on MRI and MRI on PET – are manifold. Full integration of a PET system into an MRI environment requires technical solutions for three groups of potential electromagnetic interaction:

- 1) the strong static magnetic B_0 -field for spin alignment,
- 2) the electromagnetic changing fields of the gradient system (G_{xyz}) for spatial signal encoding, and
- 3) the radiofrequency (RF) B_1 -field for MR signal excitation and MR signal readout.



PET hardware and PET signals must not be disturbed by any of these fields. Equally, for full and unlimited MRI system performance, PET must not disturb any of these electromagnetic MR fields and signals.

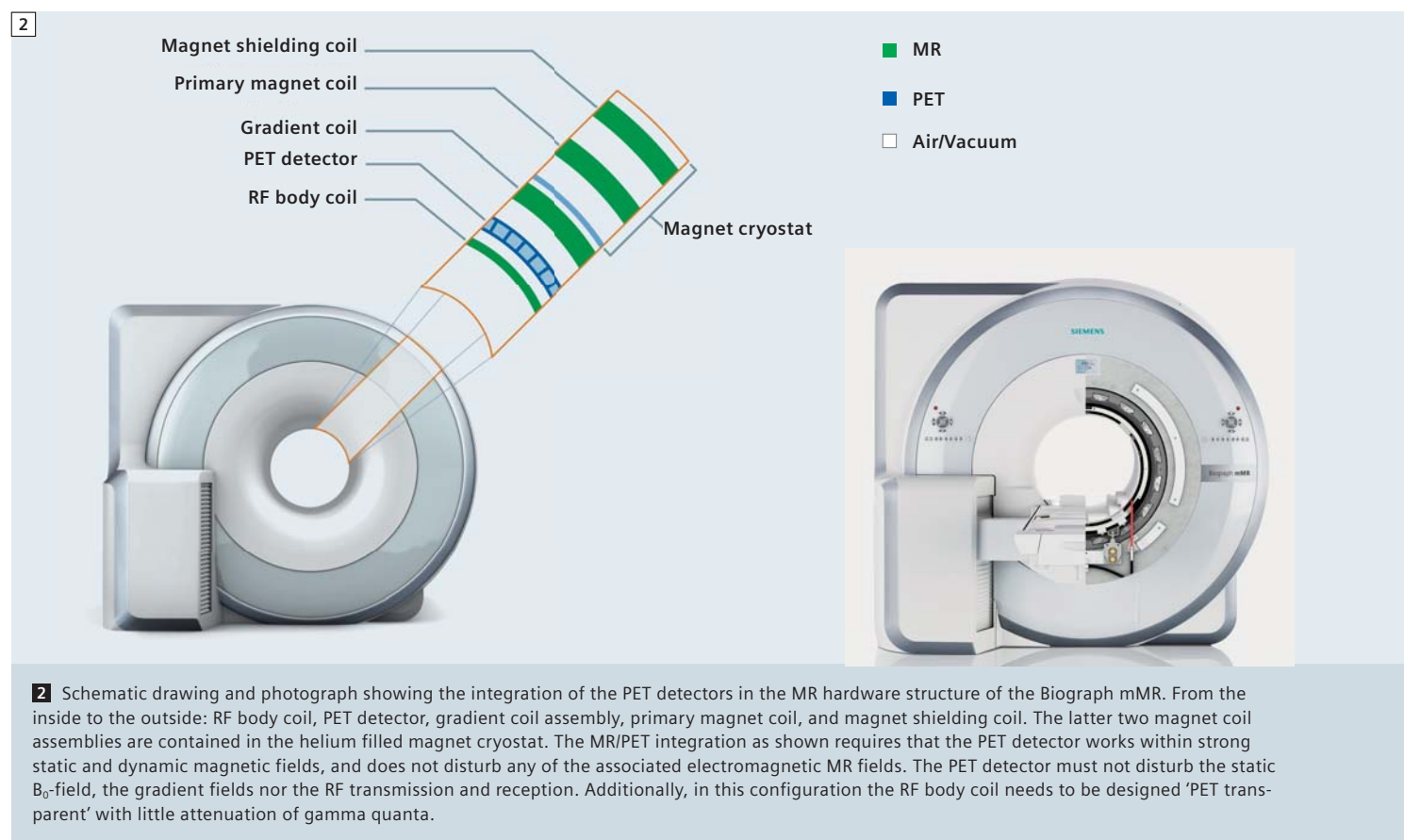
Numerous technical solutions were thus required for PET integration into an MRI system. The most important key technology enabler was the development of detectors and photo diodes that are able to detect the 511 keV PET gamma quanta following an annihilation event inside of a strong magnetic field. What worked well in established PET and in hybrid PET/CT systems in the form of scintillation crystal blocks read out by photomultiplier tubes (PMT), had to be

replaced for the MR/PET integration since the PMTs are very susceptible to magnetic fields. The current detector solution for simultaneous MR/PET is a combination of Lutetium Oxyorthosilicate (LSO) crystals and Avalanche Photo Diodes (APD) able to detect gamma quanta even inside strong magnetic fields and convert the detected events from scintillation light to electrical signals (Fig. 1A) [4]. Another advantage of the combination LSO crystal and APD diodes compared to PMT is that they do not require as much space and thus can be integrated inside of an MRI bore. Siemens' 70 cm magnet bore technology is clearly another precondition to integrate the PET detectors inside the limited space of an MRI system and at the same time to leave enough space to eventually end up with an inner whole-body bore diameter of 60 cm – as has been clinical standard for MRI magnet bore

diameter in the past. In the Biograph mMR hybrid system, 56 LSO-APD detector blocks, each with a block area of 32 x 32 mm², are aligned circumferentially to form one PET detector ring. 8 rings form the full PET detector unit, spanning a length of 25.8 cm in z-direction (for comparison: conventional/standard PET-CT systems have an axial field-of-view (FOV) of less than 20 cm and high-end PET-CT systems nowadays have a FOV of approximately 22 cm). Each LSO crystal, which are put together to form than the LSO-APD block, has a size of 4 x 4 x 20 mm³ which is the finest crystal dimension in the market for clinical PET systems; the crystal size has a direct impact on the achievable PET resolution.



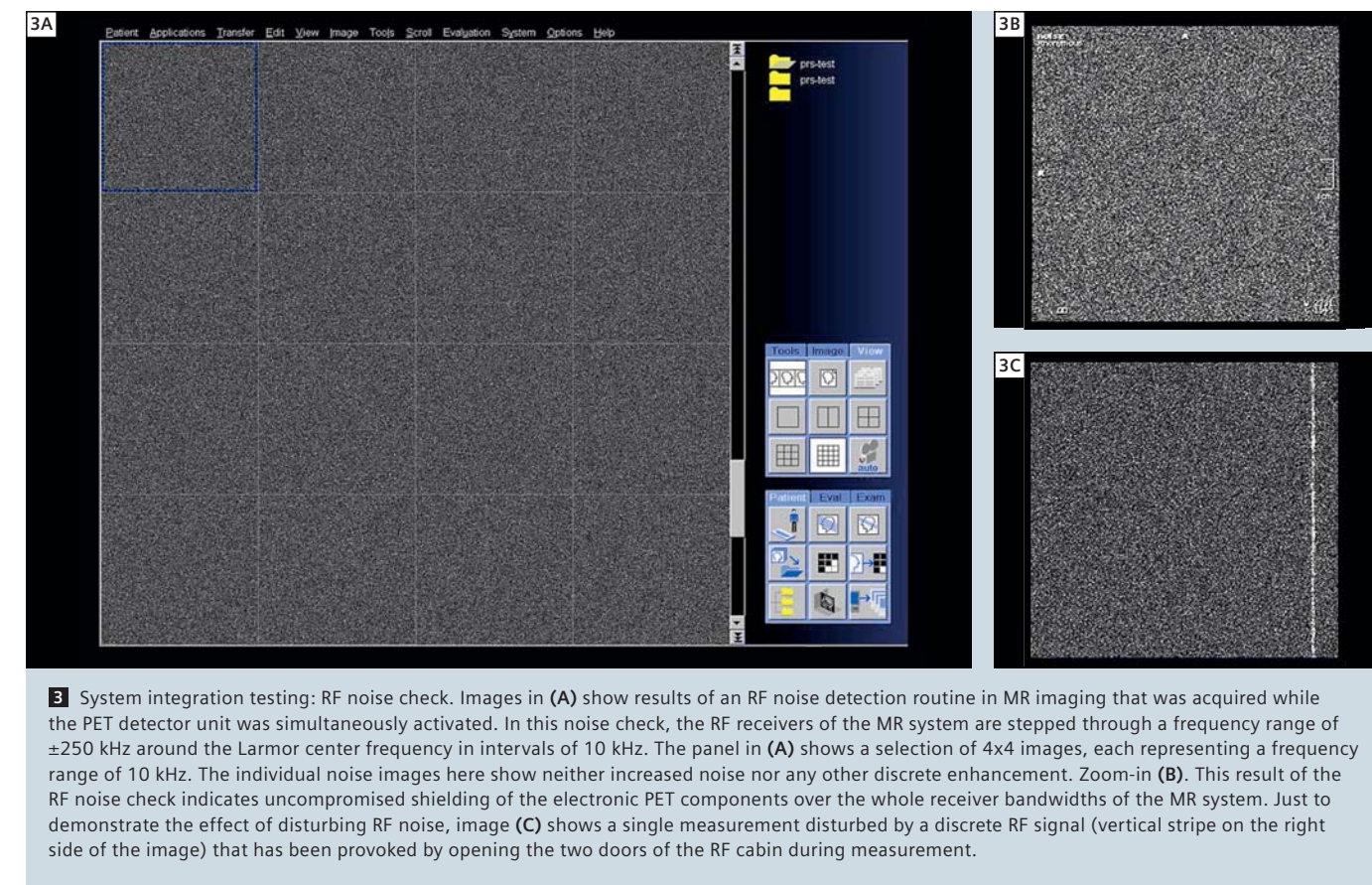
→ The QR code is your direct link to Thomas Beyer's article on the history of combining PET with MRI, the rationale to do so and challenges which had to be overcome. You will also find the article at www.siemens.com/magnetom-world



How has the integration of the PET detector unit into the MR environment been performed technically? Seen from the perspective of the signals emitting patient, the hardware layer structure of the hybrid system is as follows: The innermost layer in the magnet bore is formed by the signal transmitting and receiving RF body coil with its RF shield, shielding the RF coil towards the other structures in the bore. The PET detector rings are located behind the RF coil and its RF shield. The layer behind the PET detector unit is formed by the gradient coil assembly encompassing gradient coils for spatial MR signal encoding in all three dimensions of the scanner coordinate system. The outer layer structure is formed by the magnet cryostat containing the liquid helium for magnet cooling as well as the superconducting magnet winding producing the 3.0 Tesla static magnetic B_0 -field (Fig. 2). The individual hardware components as well as the whole hardware assembly are optimized

towards MR and PET signal detection with no signal disturbances in either direction. A technical precondition to fulfill these requirements is that the RF body coil should be 'PET transparent' such that gamma quanta emitted by the patient are not attenuated by the RF body hardware. An additional consequence is that the PET detectors need to be non-magnetic and 'gradient transparent' in order to not distort the linearity of the fast switching gradient fields. The PET detectors require stable temperatures over time of around 20°C temperature, which has been achieved by implementing water cooling into the APDs (Fig. 1). Analog electrical signals and water cooling are conducted from the PET detector in the isocenter of the magnet bore to the back end of the MR/PET system. All PET detector electronics are hermetically shielded by copper elements in order not to emit RF signals that potentially could disturb the weak MR RF signals or contribute to increased

overall RF noise, leading to decreased signal-to-noise-ratio (SNR) in MRI measurements. With regard to potential interaction with the three groups of electromagnetic fields in an MRI surrounding, all components of the PET detector and electronics must be absolutely non-magnetic, must be absolutely RF shielded and must be optimized to eliminate susceptibility to eddy currents. Eddy currents potentially interact with the strong and fast switching magnetic gradient fields for spatial MR signal encoding. When switching gradient fields, according to Lorentz' induction law, eddy currents are induced into neighboring electrically conducting structures. Unwanted eddy currents thus counteract the effect of fast switching linear gradient fields, potentially leading to reduced rise times, reduced amplitudes, and reduced gradient linearities, resulting in an overall reduced gradient performance and non-linear geometrical distortions in MR imaging.



System integration testing

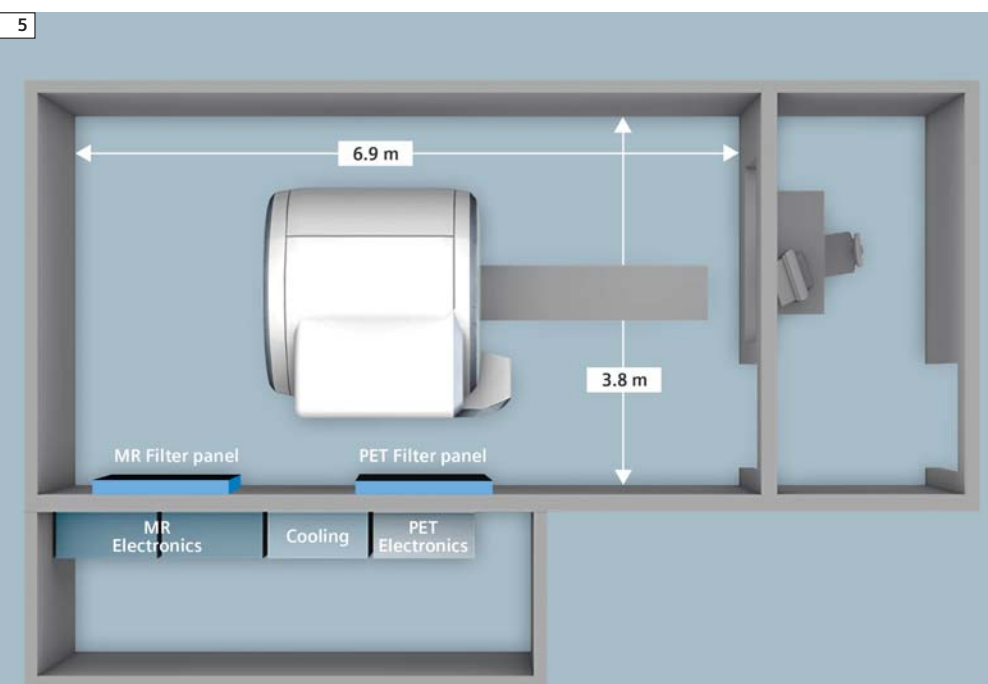
Early system integration testing of the Biograph mMR hybrid MR/PET system has been performed at the Institute of Medical Physics (IMP), University of Erlangen, Germany, in close collaboration with Siemens Healthcare, Erlangen, Germany. Successful system integration needs to be explored and verified in numerous systematic technical and phantom testing experiments. This requires testing in both directions to answer the following questions: Is PET performance influenced by the MR? Is MR performance influenced by the PET? MR testing encompasses testing for potential interactions with RF, B_0 , and G_{xyz} and related artifacts. PET testing encompasses testing for count rates, detector performance, signal homogeneity, and artifacts [5]. Figure 3 shows RF noise testing – a routine system performance test in MRI. In this test, the RF receiver chain is set to a high receiver gain and then stepped in

steps of 10 kHz through a varying bandwidth ranging from -250 kHz to +250 kHz around the Larmor center frequency of the 3.0 Tesla MR system. This is performed twice: Once with PET switched off, and again with the PET hardware switched on. Thus subtle differences in the overall noise level or discrete RF noise frequencies with/without PET can be detected. Static magnetic B_0 -field homogeneity testing encompasses measurements of the static magnetic field homogeneity with/without PET detectors inside of the system. The difference between both measurements can be visualized and evaluated in B_0 difference field maps in three spatial dimensions. Thus subtle differences in the B_0 static magnetic field homogeneity can be detected and displayed within ppm accuracy. In the Biograph mMR system the magnetic field homogeneity is specified with ≤ 6 ppm standard deviation V_{rms} (volume root-

mean square) over an elliptical volume of 50 cm diameter in the x-y-plane and 45 cm in z-direction. In system integration testing the measurements with/without PET detector installed did not reveal any influence of the PET detector on the B_0 -field homogeneity of the MR system. Also the gradient system performance with its parameters amplitude (mT/m), slew rate (T/m/s) and overall linearity has to be evaluated twice with/without PET detectors to determine possible variations from the gradient systems specifications. Measurements have confirmed that the gradient systems performance in the Biograph mMR system is in the specifications – 45 mT/m maximum amplitude for all three gradient axes, 200 T/m/s maximum slew rate, and thus compares well to a system without PET integrated in the magnet bore. This is a major precondition to take full advantage of numerous whole-body imaging



4 The Biograph mMR system installation at the Institute of Medical Physics, University of Erlangen. Both imaging modalities – MR and PET – are fully integrated into one MR/PET hybrid system.



5 Schematic showing the compact siting of the Biograph mMR system and its hardware components. In comparison to an MR-only installation, the MR/PET installation adds only another filter panel and one extra cabinet for the PET electronics to the installation site.

sequences providing anatomical and functional tissue information simultaneously with a combined data acquisition with PET: Diffusion-weighted imaging (DWI), diffusion tensor imaging (DTI), arterial spin labeling (ASL), functional MRI (fMRI), MR spectroscopy, time-of-flight angiography (TOF-MRA), dynamic cardiac acquisitions, etc., to name only a few. Finally the PET systems performance has also to be tested for the potential influences of the strong magnetic field by gradient fields, or by RF interactions. Such testing performed according to NEMA standards [5] twice outside and inside of the MRI system and during system integration testing did not reveal any deviations from the PET performance without MRI surrounding.

Siting specifics

With this new hybrid imaging systems generation, combining the non-radiating imaging modality MRI with the nuclear medicine imaging modality PET, a couple of technical and logistical particularities have to be considered when it comes to siting of such a hybrid system. The high degree of system integration in case of the Biograph mMR helps to reduce the space that is required for system installation. This holds true for the scanner room as well as for the technical equipment room. The installation only requires a minimum of 33 m² of installation space for the scanner, electronics and console room. Figure 4 shows the Biograph mMR installation at the Institute of Medical Physics (IMP), University of Erlangen, Germany. When compared to the installation of a conventional standalone MR system, the MR/PET hybrid system does not require additional space in the scanner room and only requires one additional cabinet in the technical equipment room (Fig. 5). Water cooling infrastructure is shared for both the gradient system and for the PET detectors. The additional cabinet in the technical equipment room contains the PET electronics and computers for signal processing and image reconstruction, respectively. Another requirement for the MR/PET hybrid system installation is a second filter panel in the RF cabin to

feed the PET signals and associated cables through the wall between the system room and the technical equipment room. During the MR/PET systems installation at the Institute of Medical Physics, University of Erlangen, a second RF shielded door was installed in the RF cabin. Although not a necessity, this installation at the IMP enables a patient to be brought directly from the 'active waiting' controlled area into the scanner room which then becomes a temporal control area and thus not affecting the operator room with radiation at any time. Thus personnel, researchers and potential visitors can stay in the operator room while switching patients in the scanner room.

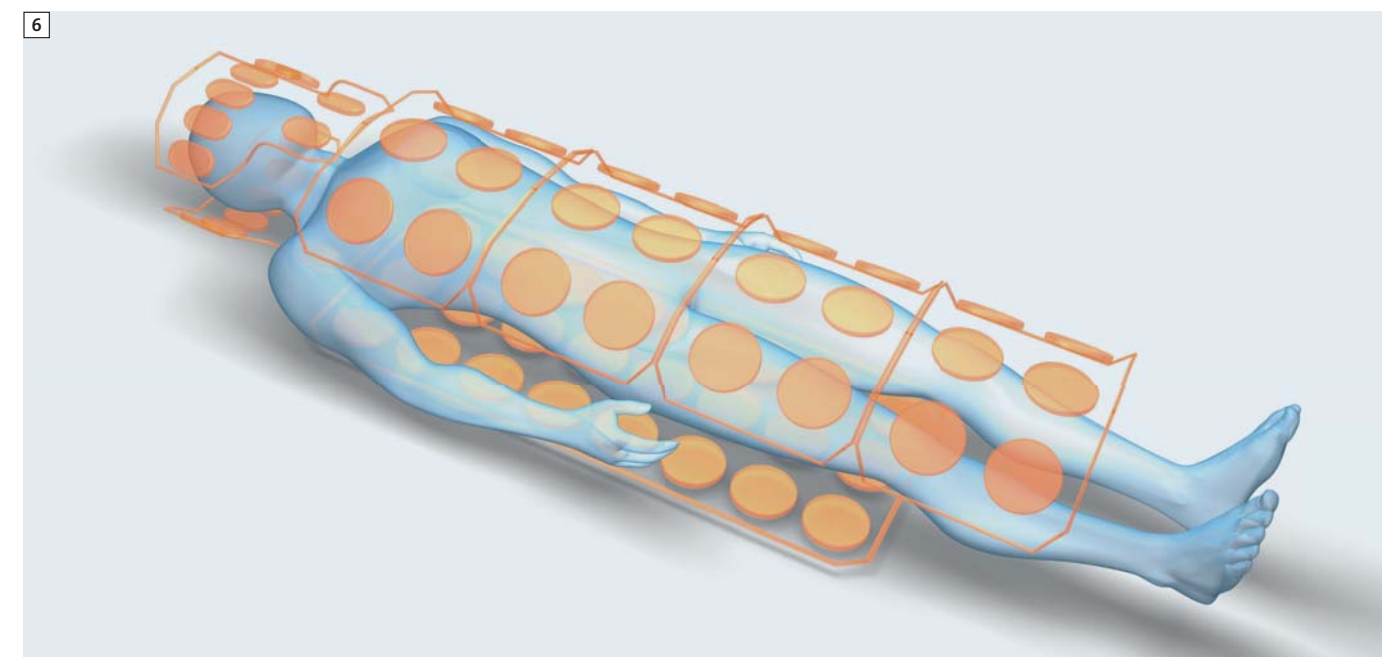
RF coils and associated attenuation correction

Like its MR-only siblings, the Biograph mMR MR/PET hybrid system is equipped with a full set of RF coils and associated RF architecture – the well established

Tim technology (Tim, Total imaging matrix, Siemens Healthcare). The Tim RF system provides seamless coverage of the patient's body with integrated surface coils from head to toe (Fig. 6). The coils are each equipped with multiple RF coil channels providing a high coil element density for high SNR gain as well as parallel imaging capabilities with high acceleration factors in three spatial dimensions. While this integrated RF surface coil concept today is well established in MRI, its use in a combined MR/PET hybrid imaging system is a novelty and prerequisite for seamless whole-body MR/PET acquisitions. The RF surface coils that cover the patient's body for optimal MR signal performance are at the same time in the FOV of the PET detectors. Thus all RF surface coils now have to be also optimized towards PET-transparency, i.e. such coils should attenuate gamma quanta to only a minor extent, for optimized PET performance. This also holds true for all other

hardware equipment – MR or PET related – that potentially accompanies the patient's body when traveling through the PET-FOV, e.g. RF surface coils, the patient table, cables, connectors, patient monitoring equipment, etc. [6]. Here one can differentiate between 'rigid and stationary' equipment such as the patient table, the RF spine array coil as well as the RF head coil, and between 'flexible and non-stationary' equipment such as the flexible RF Body Matrix array coils. 'Rigid' here means stable in its form and geometry. 'Stationary' in this context means non-moving relative to the patient table whose position is known to the imaging coordinate system at any point in time when moving in the scanner bore.

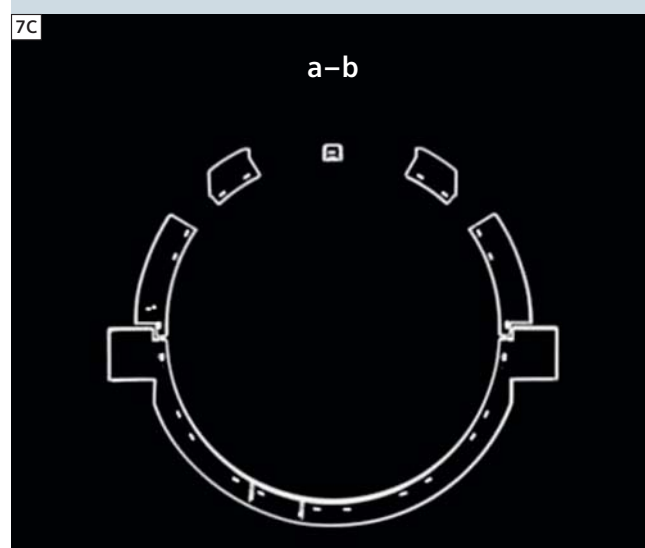
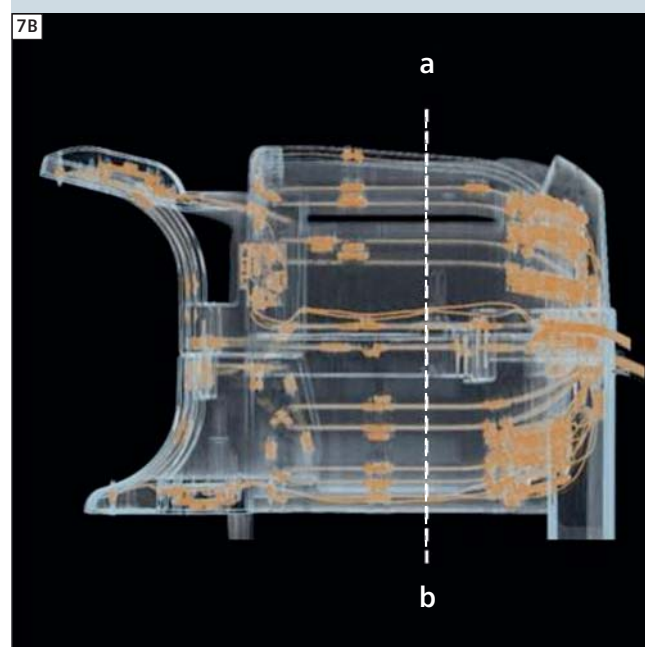
The PET signal attenuation and scatter of rigid and stationary equipment can be compensated for by straightforward attenuation correction (AC) methods. For example, the RF head coil (Fig. 7A) is scanned in a CT (computed tomography)



6 The Biograph mMR is equipped with the Tim (Total imaging matrix) RF coil technology consisting of multiple integrated surface coils that cover the patient's body from head to toe with up to 102 RF coil elements connected to 32 RF receivers. This multi-channel phased array RF coil configuration enables parallel imaging and whole-body MR data acquisition with optimized signal-to-noise (SNR) performance. In simultaneous MR/PET hybrid imaging, the surface RF coils are located between the radioactivity emitting patient and the PET detectors. As a consequence, the RF coils should be designed to be as PET-transparent as possible.



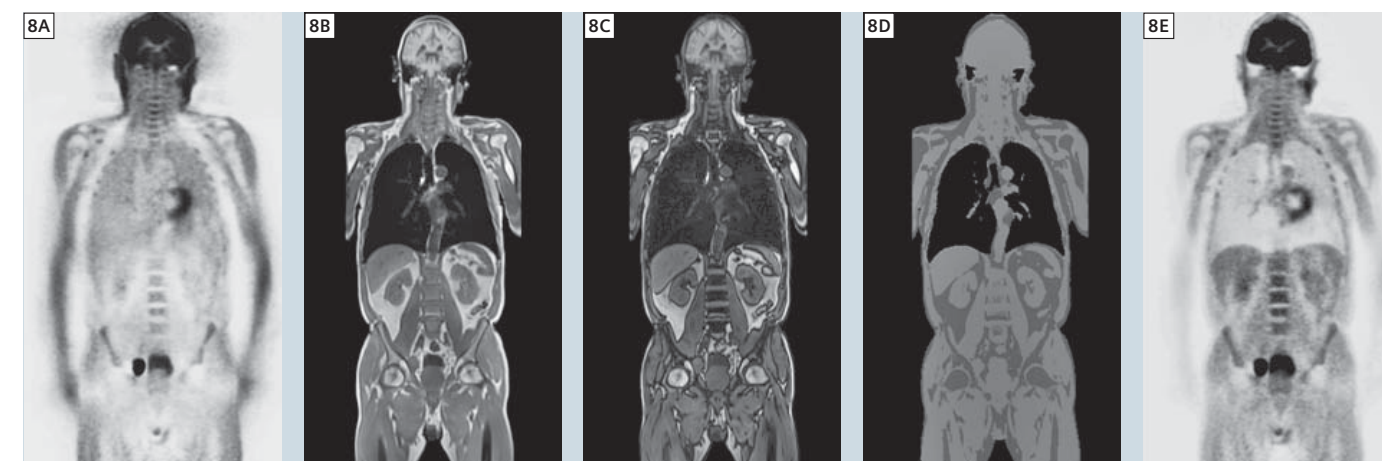
7A (A) A head/neck RF coil that was designed and optimized towards PET-transparency for use in simultaneous MR/PET hybrid imaging. This RF coil serves as an example of a rigid hardware component that is stationary at its known position with regard to the patient table. (B) 3D CT-scan of this rigid RF coil. Such a CT-scan provides hardware attenuation values that can be transformed from the CT's 100 keV energy level to the 511 keV energy level of PET in order to derive a PET-equivalent attenuation map (μ -map), shown in image (C). The μ -map in (C) has been acquired at level a-b as shown in image (B).



system once and a 3-dimensional map of attenuation values is thus generated (Fig. 7B). X-ray based CT attenuation values in general are in the energy range of about 70–120 keV and thus have to be converted to the 511 keV energy level of the gamma quanta emitted in PET. A 3D graphical representation of the obtained attenuation values ' μ -map' with 511 keV attenuation values is then generated (Fig. 7C). This CT-based registration of 3D attenuation values has to be performed once for each rigid hardware component and then the according μ -map becomes part of the PET image reconstruction process. By linking the RF spine – or RF head coils – position relative to the patient's table position, the relevant AC μ -map for each table position is automatically selected by the system for PET image reconstruction. The flexible and non-stationary Body Matrix RF array coils covering the patient's body cannot be attenuation-corrected in the same manner. Here the geometry and position of the coils attenuating structures depend on the patient's individual anatomy and on the individual situation of the patient exam and thus cannot be easily predicted by MR imaging. Here the emphasis lies on designing flexible and moving RF coils as PET-transparent as possible. For the Biograph mMR system, the associated RF coils have been further optimized in this regard. Potential design parameters for RF coil optimization are the choice of materials, the geometry, and the overall assembly. The ultimate goal of such an RF coil design optimization process is to maximize SNR and signal performance for MR while not disturbing PET-imaging.

Attenuation correction for tissue

A necessity in PET-based imaging is the correction for attenuation and scatter resulting not just from the hardware in the PET FOV (e.g. patient table, and RF coils as described above) but also from the patient's body, i.e. the anatomic distribution of soft tissues, air, and bones in the individual patient. Such tissue AC in PET-only systems traditionally has been performed by rotation of radioac-



8 Soft-tissue attenuation correction (AC) based on MR imaging. (A) Uncorrected whole-body PET scan showing relative activity enhancement in the lungs and on the outer contours of the patient. (B and C) Dixon MR sequence providing separate water/fat 'in-phase' and 'opposed phase' images that serve as basis for soft-tissue segmentation. (D) Segmented tissue groups (air, fat, muscle, lungs) that can be assigned to 511 keV attenuation maps. (E) Resulting attenuation corrected whole-body PET scan of the initial data set (A).

tive ^{68}Ge 511 keV sources around the patient and detection of the attenuated transmission signals 'behind' the patient. From a number of projections, a topography of attenuation values (μ -map) could be reconstructed. This was a relatively time-consuming process, since the ^{68}Ge -source needed to be rotated at a relatively slow speed in order to achieve a significant count rate for each projection angle.

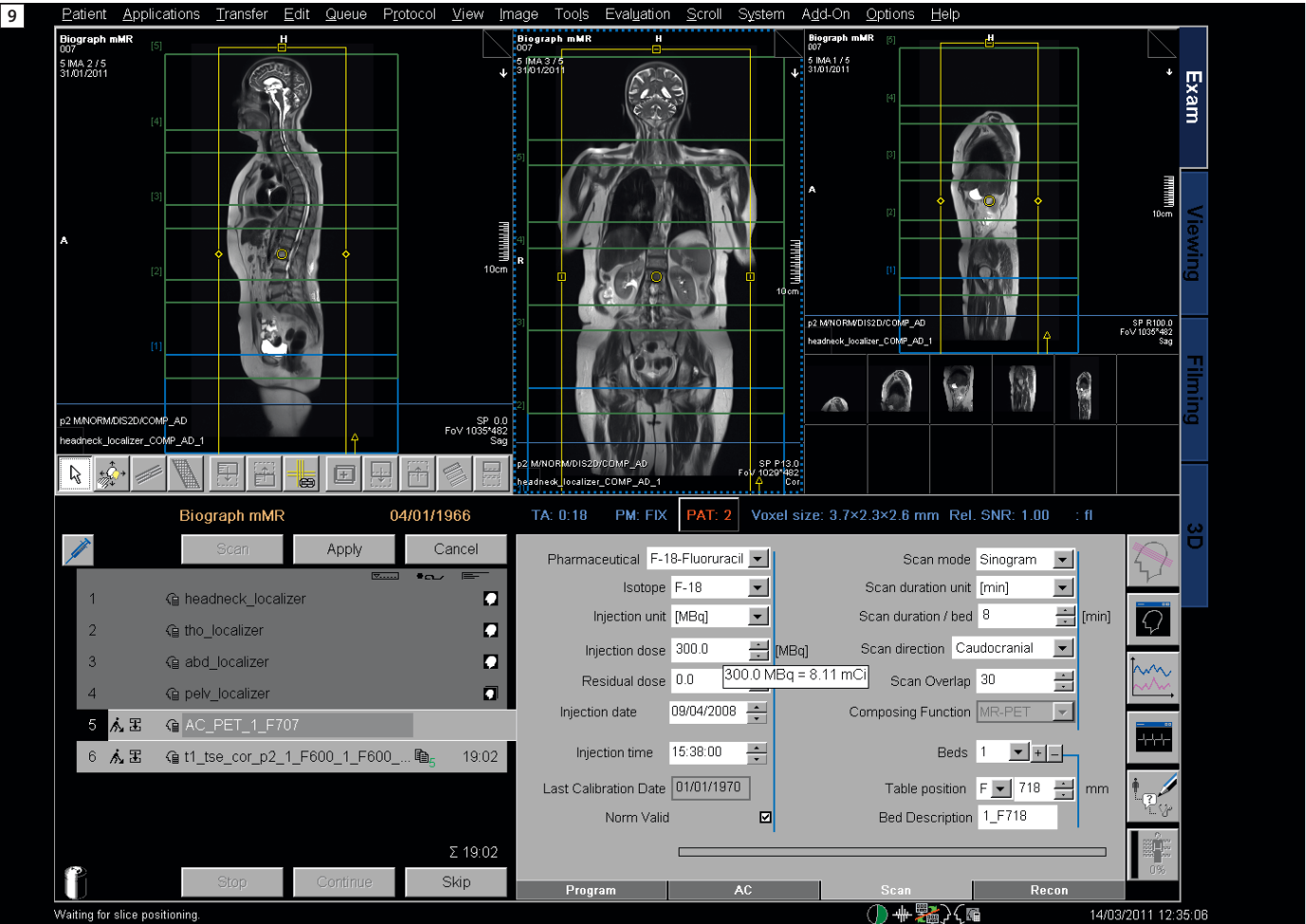
In modern PET/CT hybrid systems, the hardware (e.g. patient table) and the patient tissue μ -map are generated straightforwardly from a fast (potentially low-dose) 3D CT scan provided by the build-in CT scanner. Attenuation values are converted from the 70–120 keV energy level to 511 keV and thus a fast individual and reliably AC μ -map of the patient and any hardware accessories in the PET FOV is obtained.

In a combined MR/PET hybrid system tissue attenuation has to be obtained in a completely different way. Since no CT-like attenuation information is available in such a hybrid system, tissue AC necessary for PET image reconstruction needs

to be based on MR images. The problem is the non-irradiative nature of MR imaging, based on proton densities and T1 and T2 relaxation parameters, rather than on the attenuation of radiation in tissue. MR-based AC of tissues also leads to the problem that air and bone are depicted in black the vast majority of MR imaging sequences turning air and bone hardly distinguishable, in CT and PET imaging on the other hand air and bone show minimal and maximal attenuation values, respectively. Different methods have been described in the recent literature, that deal with MR-based AC for tissue [7–9]. Those methods can be separated in atlas-based or atlas-supported methods and in image segmentation based efforts. In the latter, the gray values provided by selected sequences are registered to different tissue classes resulting in tissue segmentation.

Depending on the sequence type used, air, lung, fat, muscle, and bones might be segmented and provided with according PET correction values. In the current implementation of the Biograph mMR system, tissue attenuation and scatter correction is performed twice. The head/neck region is attenuation-corrected with the help of a UTE (ultrashort echo

time) sequence [10, 11] providing segmentation also of the bone which in this region takes a large percentage of the imaged volume. All other body parts are attenuation-corrected by a Dixon technique providing two images where water and fat are 'in phase' and in 'opposed phase'. This allows for reconstruction of fat-only, water-only and of fat-water images and results in tissue segmentation of air, fat, muscle, and lungs (Fig. 8) [8]. Bone is not accounted for in this approach. Initial results in patient imaging have shown that this approach works reliably and provides results that are comparable to corrected images from PET/CT in the same individual. The ultimate impact of this and other MR-based AC methods on PET-quantification and determination of standard uptake values (SUV) has not yet been determined and is subject to current investigations and further research efforts.



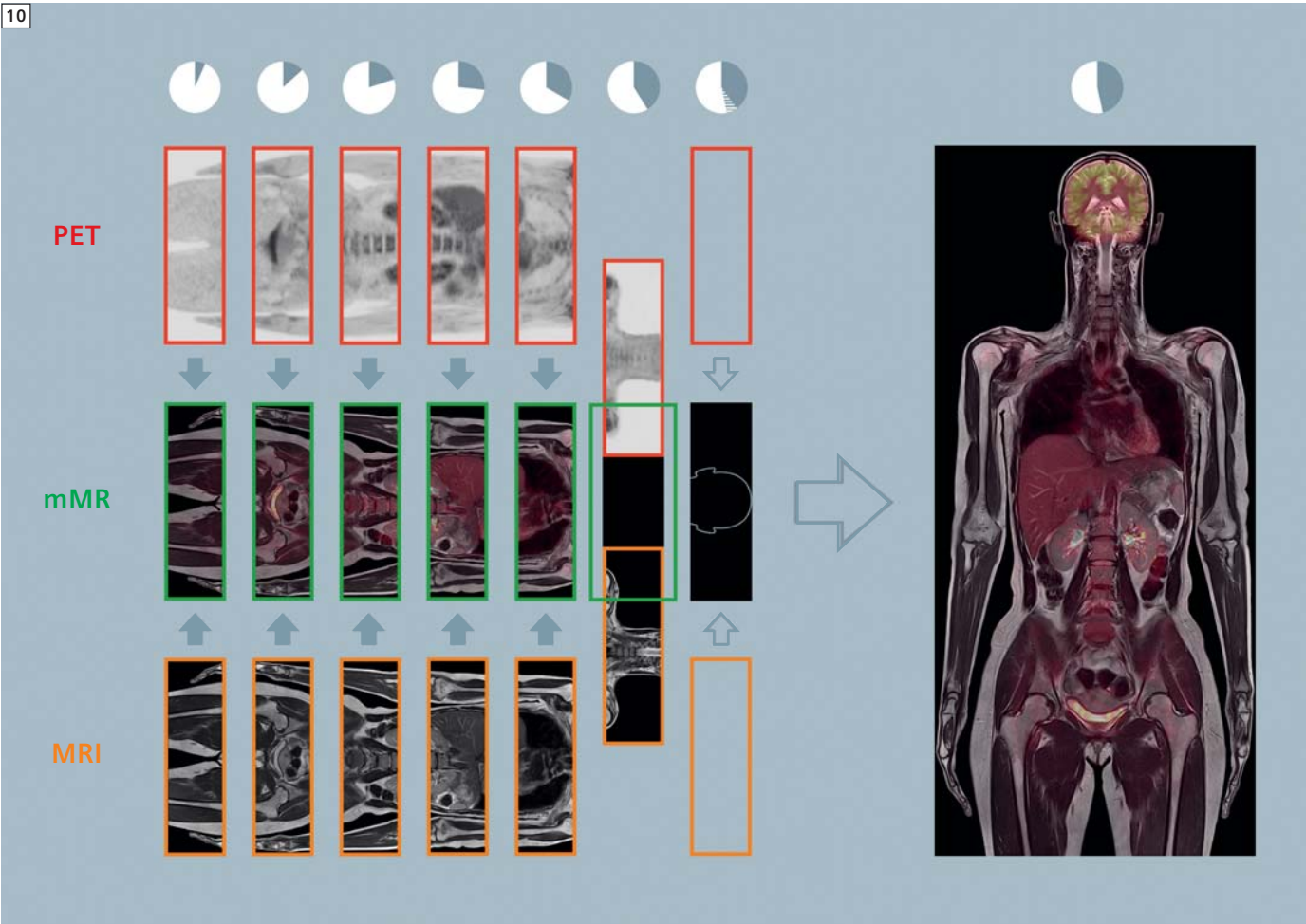
9 Screenshot of the syngo user interface during planning of a MR/PET examination. The image panel shows multi-station MR localizers in sagittal (left and right) and coronal (middle) orientation. Displayed with a yellow frame is the FOV of the AC MR sequence for tissue attenuation correction. Green and blue frames show graphical planning of the individual bed positions of the MR and PET data acquisition. In the lower half the planning of the MR/PET acquisition is currently ongoing.

Imaging workflow

From a procedural point-of-view the imaging workflow of a whole-body MR/PET examination on the Biograph mMR is very similar to a whole-body MRI examination. First the patient is prepared on the patient table. For that purpose the earlier described dedicated mMR Tim RF coils (head and neck coil, spine coil, and up to four body matrix coils) are positioned underneath, on and around the patient's body, respectively. In this context the Tim RF coil technology is a prerequisite for seamless whole-body imaging without RF coil replacement and patient repositioning. Following patient preparation a localizer MR scan is performed covering the

region to be examined. Making use of the syngo software functionality the localizer scan, as well as any further MR scan can be loaded per drag and drop from a predefined list of protocols and can also be adjusted according to the user's specific needs and saved afterwards as individualized protocols, similar to customization of MR protocols. Based on the localizer scan the combined MR/PET scan then is planned. Figure 9 shows the user interface for examination planning. The yellow boxes in the graphical slice positioning section indicate the acquisition volume for the MR sequences used in the attenuation and scatter correction. The green and blue boxes indicate the acquisition vol-

ume of the respective PET bed positions. The overlap between the bed positions is variable. When the planning for the AC sequence is finished and the scan is started, automatically the simultaneous acquisition of the PET starts as well and – bed position per bed position – the simultaneous acquisition of PET, MR AC scan, and any further MR scan for anatomy and function is performed (Fig. 10). Additional MR sequences (beyond the AC scans) for assessment of anatomy and function can be chosen individually for each bed position. For a typical MR/PET scan using ¹⁸F-FDG for tumor staging, the overall scan time is defined not necessarily only by the PET acquisition time per bed and number of required



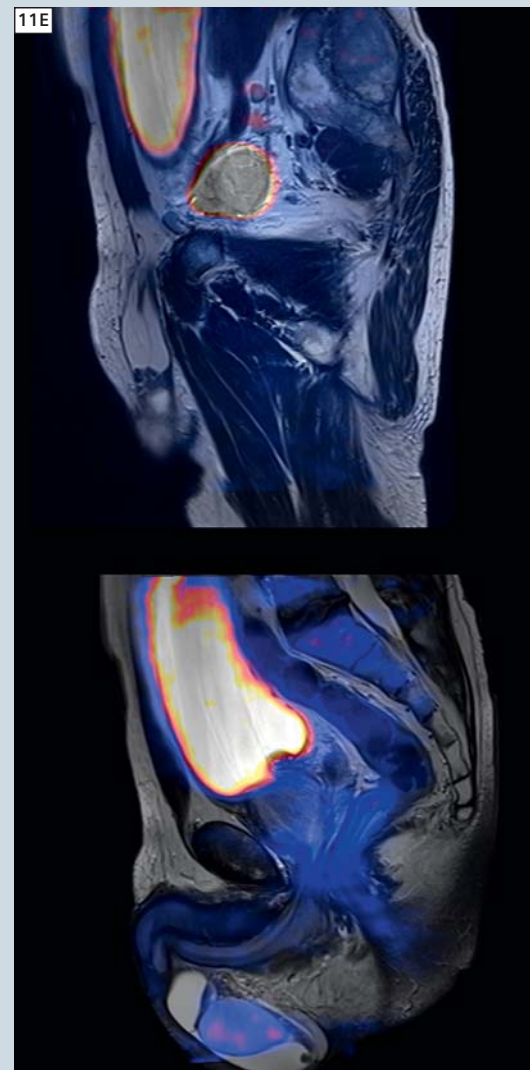
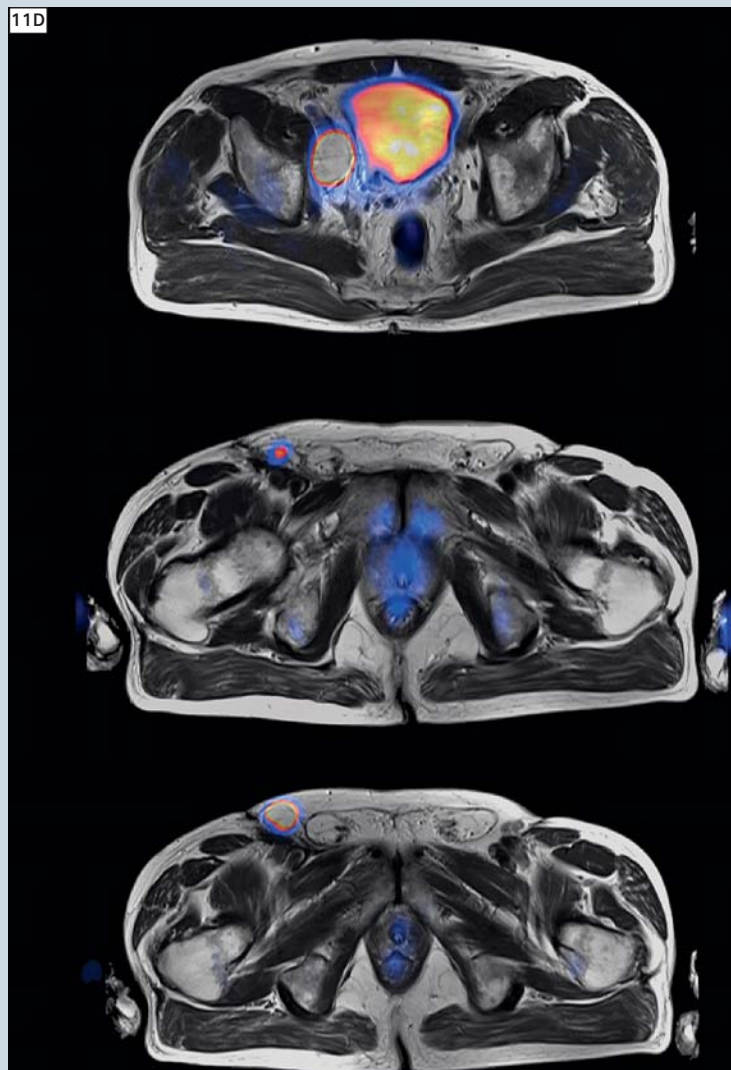
10 MR/PET simultaneous imaging workflow. MR and PET data acquisition is performed simultaneously during a multi-step examination with 6–7 bed positions for whole-body coverage. Depending on the selection of MR imaging sequences, such a whole-body MR/PET hybrid imaging study is regularly completed in about 20–30 minutes.

bed positions to cover the region-of-interest; in contrast to PET/CT, the acquisition time necessary for MR imaging can be the limiting factor with respect to the total scan time of a mMR exam. However, the additional MR scan time is not lost: Further MR sequences may add to the acquisition time of a specific bed position. This additional time can then directly be used for longer PET data acquisition, translating not only into improved PET image quality but allowing the collection of dynamic PET data (this includes also gating / triggering of PET data). The acquisition of single bed positions for simultaneous MRI and PET, e.g. for dynamic MR/PET studies of the brain, is clinically possible and it should be

emphasized that this possibility is also a direct consequence of the large z-axis coverage by the PET detectors, allowing to scan the whole brain or the liver without the need of repositioning over a longer time-period. Combining PET data and multiple MR sequences will increase the amount of images and complexity of reading, not only for whole-body applications. Therefore an intuitive and powerful tool for evaluating mMR examinations was developed in parallel to the scanner hardware. After the acquisition of the MR/PET data the dedicated mMR Reader based on syngo.via and delivered with the Biograph mMR system can be used for image reading and diagnosis. It has

been developed for efficient and seamless integration of the new modality into clinical workflow; this includes automatically loading and displaying images for the whole body and specific anatomical regions in MR only, PET only and MR/PET fusion. The client-server-based software supports reading and diagnosing by an MRI and a PET expert (also on different days and in different rooms) in several regards including advanced findings navigation and also by automatically merging these individual findings into one joint report.

11 Patient with lymph node filiae following a history of a penis carcinoma. Images (A–C) show whole-body T1-weighted MR image (A), attenuation corrected PET (B), and MR/PET hybrid images (C) in a coronal orientation, that were all simultaneously acquired in a multi-station/multi-bed acquisition mode. MRI in this whole-body study (A) displays anatomical structures with exquisite detail and excellent soft-tissue contrast. PET (B) and the combined MR/PET hybrid image (C) in this coronal overview show enhanced tracer activity in one lymph node on the right side of the patient. The axial and sagittal reformates of the MR/PET hybrid data (D, wE) reveal two additional lymph nodes with focal tracer activity on the right side.

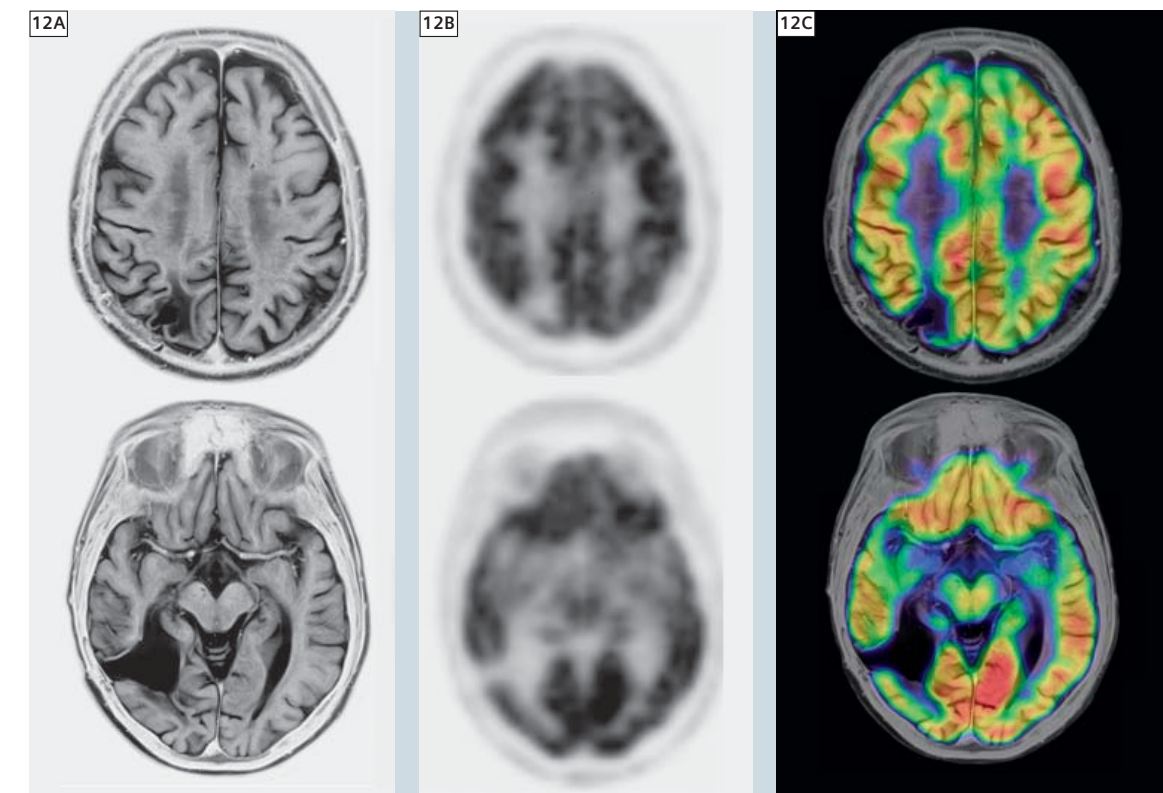


First clinical examples

An early study was initiated in 2010 at the Institute of Medical Physics (IMP), University of Erlangen, in cooperation with Siemens AG Healthcare Sector, Erlangen. This study aimed at system integration testing and at showing system performance and full operability by scanning first patients. For acquiring these images, the study was setup as follows: Patients referred to PET/CT scanning were recruited from the Nuclear Medicine Department of the nearby University Hospital Erlangen. Patients had been injected the radioactive tracer ^{18}F -Fluorodesoxyglucose (FDG) and had already undergone their PET/CT examination immediately before participating in the MR/PET hybrid imaging examination. This study design thus also had the

benefit that the preceding PET/CT examination could serve as a 'gold standard' comparison for subsequent MR/PET imaging. No additional FDG injection or increased radiation dose was necessary. Due to the scanning PET/CT first, however, patients involved in this study had their MR/PET examination on average about 120 min after the injection of FDG. This is about 60 min later than the PET scan would usually have been performed after ^{18}F -FDG-injection. With the given half life time of 108 min for ^{18}F -FDG, this has the effect that activity and thus count rate have already decreased since the PET/CT examination and additionally, FDG has been metabolized during a longer time window than usual. In our study, the effect of decreased activity has been compensated for by longer PET measurement times per bed position (i.e. 6 minutes instead of 2–3 minutes per bed position).

Figure 11 shows a whole-body MR/PET study of a patient with a history of a penis carcinoma with R0 resection of the tumor and now suspicion of tumor recurrence (lymph node metastases). The MR/PET study in this case revealed multiple lymph node filiae inguinal and iliacal, which can be displayed in fine detail in PET and in MRI. These findings correlate well with the findings of the preceding PET/CT examination (not shown). Figure 12 shows a brain MR/PET study of a lung cancer patient for therapy effectiveness control with a history of 2 resected brain metastases. No increased activity or any other signs of recurrence or malignancy could be observed – neither in the PET nor in the MR images. This also correlates with the findings of the associated PET/CT examination (not shown).



12 Case of a patient with successfully treated lung carcinoma and with two resected brain metastasis (both right side). The axial slices show MR (A) and PET (B) images simultaneously acquired at each position of the resected brain metastasis. The T2-weighted and inverted MR data set (A) shows the anatomical structures in fine detail and with excellent soft tissue contrast. The PET images (B) and the resulting MR/PET data set (C) does not show any signs of recurrence.

Status and outlook

The long-awaited hybrid imaging modality enabling simultaneous whole-body MR/PET imaging has entered the clinical arena. On the physics and hardware level, this opens up completely new options for clinical imaging research. MR-based hardware and tissue attenuation correction (AC) and MR-based motion correction (MC) for PET imaging are only two examples of current active fields of research. The development of RF coils intended not only for their intended diagnostic application and MR imaging performance but also for their PET-transparency is another research field. On the clinical imaging level, this new hybrid imaging modality demands clinical evaluation especially given the wealth of new diagnostic information generated by the integration of both imaging modalities. Here a special area of interest will focus on the streamlining and optimization of the imaging workflow of simultaneous MR and PET imaging. The ultimate goal is the maximization of multi-modal diagnostic information within a minimum of acquisition time.

Acknowledgements

The authors would like to thank Dr. Matthias Lichy, Dr. Jürgen Kampmeier, and Heike Weh, all Siemens Healthcare Sector, Erlangen, Germany, for in depth discussions and for their support in preparing figures for this article. The authors are also grateful to Prof. Dr.

Torsten Kuwert, Prof. Dr. Michael Uder, Dr. Michael Lell, all University Hospital Erlangen, Germany, and to Dr. Alexander Cavalaro, ISI Erlangen, for their help in patient recruitment and personal support.

References

- Pichler BJ, Judenhofer MS, Wehr HF. PET/MRI hybrid imaging: devices and initial results. *Eur Radiol.* 2008; 18:1077-86. Review.
- Antoch G, Bockisch A. Combined PET/MRI: a new dimension in whole-body oncology imaging? *Eur J Nucl Med Mol Imaging.* 2009; 36 Suppl 1:S113-20. Review.
- Wehr HF, Sauter AW, Judenhofer MS, Pichler BJ. Combined PET/MR imaging--technology and applications. *Technol Cancer Res Treat.* 2010; 9:5-20.
- Pichler BJ, Wehr HF, Kolb A, Judenhofer MS. Positron emission tomography/magnetic resonance imaging: the next generation of multimodality imaging? *Semin Nucl Med.* 2008; 38:199-208. Review.
- Delso G, Martinez MJ, Torres I, Ladebeck R, Michel C, Nekolla S, Ziegler SI. Monte Carlo simulations of the count rate performance of a clinical whole-body MR/PET scanner. *Med Phys.* 2009; 36:4126-35.
- Delso G, Martinez-Möller A, Bundschuh RA, Ladebeck R, Candidus Y, Faul D, Ziegler SI. Evaluation of the attenuation properties of MR equipment for its use in a whole-body PET/MR scanner. *Phys Med Biol.* 2010; 55:4361-74.
- Beyer T, Weigert M, Quick HH, Pietrzyk U, Vogt F, Palm C, Antoch G, Müller SP, Bockisch A. MR-based attenuation correction for torso-PET/MR imaging: pitfalls in mapping MR to CT data. *Eur J Nucl Med Mol Imaging.* 2008; 35:1142-6.
- Martinez-Möller A, Souvatzoglou M, Delso G, Bundschuh RA, Chefd'hotel C, Ziegler SI, Navab N, Schwaiger M, Nekolla SG. Tissue classification as a potential approach for attenuation correction in whole-body PET/MRI: evaluation with PET/CT data. *J Nucl Med.* 2009; 50:520-6.
- Schulz V, Torres-Espallardo I, Renisch S, Hu Z, Ojha N, Börner P, Perkuhn M, Niendorf T, Schäfer WM. Automatic, three-segment, MR-based attenuation correction for whole-body PET/MR data. *Brockmann H, Krohn T, Buhl A, Günther RW, Mottaghy FM, Krombach GA. Eur J Nucl Med Mol Imaging.* 2011; 38:138-52.
- Waldman A, Rees JH, Brock CS, Robson MD, Gatehouse PD, Bydder GM. MRI of the brain with ultra-short echo-time pulse sequences. *Neuroradiology.* 2003; 45:887-92.
- Robson MD, Bydder GM. Clinical ultrashort echo time imaging of bone and other connective tissues. *NMR Biomed.* 2006; 19:765-80. Review.

Contact

Prof. Dr. Harald H. Quick, PhD
Director of MR-Imaging
Institute of Medical Physics (IMP)
Friedrich-Alexander-University (FAU)
Erlangen-Nürnberg
Henkestr. 91
91052 Erlangen
Germany
Phone: +49 9131 85 25900
Harald.Quick@imp.uni-erlangen.de

Dr. Jens-Christoph Georgi, PhD
Global Product Manager Biograph mMR
Siemens AG Healthcare Sector
MR MK O
Karl-Schall-Str. 6
91052 Erlangen
Germany
Phone: +49 9131 84 4701
Jens-Christoph.Georgi@siemens.com

Don't miss the talks of experienced and renowned experts covering a broad range of MRI imaging

Jörg Barkhausen, M.D.
University Hospital Essen

Dynamic 3D MRA – Clinical Concepts
(syngo TWIST)



John A. Detre, M.D.
University of Pennsylvania

Clinical Applications of Arterial Spin Labeling
(syngo ASL)



Tammie L. S. Benzinger, M.D., Ph.D.
Washington University School of Medicine

Clinical Applications of Diffusion-Tensor Imaging
(syngo DTI)



John F. Nelson, M.D.
Battlefield Imaging

Breast Cancer Management –
Cross Modality Approach



John A. Carrino, M.D., M.P.H.
Johns Hopkins University, School of Medicine

MRI in Sports Medicine



Visit us at
www.siemens.com/magnetom-world
Go to
Education > e-trainings & Presentations

Integrated Whole Body MR/PET Imaging. First Examples of Clinical Application

A. Drzezga; A.J. Beer; S. Fürst; S. Ziegler; S.G. Nekolla; M. Schwaiger

Technische Universität München, Klinik und Poliklinik für Nuklearmedizin, Klinikum rechts der Isar, Munich, Germany

Introduction

Over the last decade, development of hybrid-imaging instrumentation has been among the innovations with the strongest impact on diagnostic imaging in clinical everyday routine. The driving force behind these developments is the considerable extent to which several different imaging modalities show complementary rather than redundant features. Consequently, it is logical to bundle the particular strengths of different modalities, and to compensate particular deficits of one modality with capabilities of another by combination of the different modalities into one hybrid instrument. Hybrid PET/CT entered the market in around 2000 and became a major success, thereby quickly obviating the demand for PET-only scanners. This success has been strongly driven by oncological applications, combining the high sensitivity of PET with the anatomical precision of CT. The coupling of ^{18}F -FDG, a tracer for metabolic activity with CT, has especially proved highly valuable: FDG-PET allows the sensitive detection of tumor cells and the estimation of their viability (e.g. for therapy control); CT complements the exact anatomic localization of suspect lesions and has a very high sensitivity for small

lesions which are missed by PET due to limited resolution or movement artifacts (e.g. in the lung).

However, CT has some specific limitations, the most apparent being the relatively low soft-tissue contrast. This represents a disadvantage particularly for diagnostic questions directed to body regions which are defined by a complex regional arrangement of different adjacent soft tissue structures, e.g. the brain, the head-and-neck region or the pelvis. In contrast to CT, MR-imaging is distinguished by the ability to provide excellent soft-tissue contrast. This is the main reason why corresponding diagnostic problems are typically directed to MRI as the first-line imaging procedure of choice rather than to CT. This includes questions concerning e.g. neurological disorders, brain tumors, conditions in the head and neck region, abdominal/hepatic and pelvic masses and musculoskeletal problems.

For many of these diagnostic questions, PET has demonstrated a high added value as a complementary test in itself, whilst frequently being performed in addition to mandatory MRI-tests (see A. Padhani 'Multiparametric imaging of tumors – an emerging paradigm', MAGNETOM Flash #45 3/2010, Research Supplement). Thus, the value of a combination of PET with MRI seems obvious. However, the development of such hybrid MR/PET instrumentation has been

hampered for a long time primarily by technical obstacles which have been harder to overcome compared to the combination of PET and CT. Whereas the latter both represent modalities working with radiation (although in different wavelengths) and can thus be combined more easily, PET and MRI are based on entirely different image acquisition principles. The strong magnetic field required for MR-image acquisition is severely affecting the acquisition of the PET-signal. In particular, the conventional photomultiplier technique commonly used for obtaining the PET signal does not work properly in a magnetic field. To circumvent this limitation, platforms have been developed in which spatially separate MR- and PET-scanners are connected by means of a moving table. The patient is positioned on this table and undergoes first PET and then MR imaging, without having to get up from the table between the scans. However, these solutions do not allow simultaneous image acquisition and they are of course associated with lengthy examination protocols and with the risk of patient movement.

With the introduction of the so-called APDs (Avalanche Photodiodes) into PET-

instrumentation this problem has been solved more elegantly. APDs function in strong magnetic fields and can be used to substitute conventional photomultipliers to acquire information in the MR-scanner. The advent of this technology has allowed the industry to produce a first generation of hybrid MR-scanners in which a true integration of both modalities in a single machine has been realized (see H. Quick 'Whole-body MR/PET hybrid imaging' page 88 in this issue of MAGNETOM Flash). This principle was first successfully demonstrated by means of small head-only PET-scanners (PET-insert) which have been installed in conventional MR-scanners (see T. Beyer et al. 'MR/PET-hybrid imaging for the next decade', MAGNETOM Flash #45 3/2010 Research Supplement). Several studies have been performed in this prototype system since and proved the practicability of the concept [1–4]. On the basis of this prototype, a dedicated whole-body MR/PET system has now been developed. In November 2010, the world's first integrated clinical whole-body MR/PET scanner (Siemens Biograph mMR) was installed in the Department of Nuclear Medicine at the Technische Universität München (TUM), in Munich, Germany. The scanner is now operated by a consortium between the directors of Nuclear Medicine (Prof. Dr. Markus Schwaiger) and Radiology (Prof. Dr. Ernst Rummeny) from TUM and the directors of Nuclear Medicine (Prof. Peter Bartenstein) and Radiology (Prof. Dr. Maximilian Reiser) from the Ludwig-Maximilians-Universität, München. The setup of the first scanner of this type in Germany (and of three identical scanners which will be established in 2011 in Essen, Leipzig and Tübingen) has been made possible by funding of the German Research Foundation (DFG, Deutsche Forschungsgemeinschaft). The Biograph mMR MR/PET-scanner is constituted by a high end 3T MR-scanner which harbours a fully functional state-of-the-art PET system within the gantry. The PET-system covers a field of view (25.8 cm) which is larger than in any other existing PET-camera. This allows to

obtain multimodal (MR&PET) image information simultaneously in an extended region and to cover the entire body with a limited number of bed positions in short time. For further technical details on the system see page 88 in this issue of MAGNETOM Flash.

Opportunities of the MR/PET-system

From a clinical point of view, this system offers a number of obvious advantages:

1. Reduction in examination time

In comparison to clinical CT-examinations, MR-scans can often be relatively time-consuming. The recently introduced whole-body MR/PET scanner now allows the acquisition of MR and PET information in a truly simultaneous approach, i.e. in regional alignment at exactly the same time, thereby reducing not only the number of examination appointments (i.e. the visits patients have to make to the imaging department) but also cutting the required examination time approximately in half (as compared to two separate examinations). This option of 'one-stop shop' examinations represents a major gain in patient comfort for patients requiring both MR and PET examinations and also reduces the required time of the medical personnel to acquire the requested imaging information.

2. Regional coregistration

The acquisition of PET and MR-information in exactly overlapping anatomical positions also offers clear advantages: Precise coregistration of the PET-signal with the underlying anatomical information is assured as the risk of patient movement or changes in organ position (e.g. in bowel positions, different bladder filling status) between the acquisition of the two modalities is reduced, and thus potential misalignment is minimized. Due to the lack of radiation exposure by the MR-image acquisition, anatomical scans can be added/repeated to achieve optimal anatomical information.

3. Simultaneity of acquisition

The newly introduced integrated MR/PET scanners for the first time allow truly simultaneous acquisition of imaging information from two different modalities of the same region at the same time. This opens a completely new dimension in hybrid imaging. Even established PET/CT technology only allows the acquisition of CT and PET in the same system but not at exactly the same time and region, as the two modalities/acquisition procedures are cascaded one after the other. The simultaneous acquisition of MR and PET information opens the opportunity to address many new scientific questions, which may be translated into clinical application, e.g. to cross-evaluate the value of different imaging tests under identical examination conditions or to improve understanding of disease pathophysiology by shedding light on the interrelation between different pathological processes. Simultaneous acquisition may also allow the following of organ and/or patient movement over time allowing for motion correction [2] and also the combination of information on motility with other functional information provided by PET (e.g. information on viability/perfusion derived from PET-imaging with information on wall movement in cardiac examinations).

4. Exposure to ionizing radiation

Radiation exposure based on clinical imaging tests is currently a much-discussed topic. Compared to PET/CT, hybrid MR/PET offers the chance to reduce ionizing radiation exposure without loss of diagnostic information. MRI will probably allow anatomical allocation of the PET-signal with comparable precision as known from CT. In some cases the combination of PET-imaging with appropriate diagnostic MR-imaging procedures may be of superior diagnostic value with considerably lower radiation exposure as compared to the combination of PET and diagnostic CT.

5. Complementary/superior diagnostic value of MR/PET compared to PET/CT

It is well known that MRI has complementary features to CT. The most obvious being the higher soft-tissue contrast. As mentioned above, combined MR/PET may be of obviously higher diagnostic value compared to PET/CT for indications and in body regions which would usually be approached using MRI rather than CT (see clinical examples below). In this regard MR/PET may represent a complementary imaging technique to PET/CT in the future just as MR itself represents a complementary imaging technique to CT nowadays.

6. Opportunities for scientific applications

The MR/PET-system opens a large number of potential scientific applications. Among these is the unique option to establish previously unknown interrelations between different measures of pathology and physiology in the human body such as structure and function, perfusion and metabolism, tissue diffusivity and cell proliferation etc. This may allow to improve the understanding of healthy organ function and to detect causal relationships in disease pathogenesis potentially leading to new therapeutic approaches.

For clinical diagnosis, combined MR/PET may allow the development of integrated multiparametric markers for more sensitive and more specific diagnosis, therapy planning and evaluation [5]. Several previous studies using separate modalities point to a potentially high scientific and clinical benefit from multimodal imaging approaches using MR/PET [e.g. 5–7].

Challenges of the MR/PET system

Like every new system, combined MR/PET still has a number of apparent challenges:

1. Attenuation correction

In PET/CT systems, low-dose CT scans are used to estimate the expected

attenuation of the radiation emitted from a specific body region. In contrast to CT, MR imaging does not provide information on tissue specific photon absorption, but rather on tissue type/class. However, it has been demonstrated that by means of a set of specific MR-sequences (Dixon imaging or chemical shift imaging) suitable attenuation maps can be calculated, which allow an approximation of 511 keV photon attenuation correction with sufficient reliability [8]. The dual point VIBE T1-weighted Dixon sequence used for attenuation correction in the Biograph mMR can be acquired quickly for each bed position (e.g. in the thorax during one breath-hold), practically not increasing the examination time. However, the current approach of tissue classification with the Dixon sequence is not yet fully satisfying, it is prone to metal artifacts, attenuation by bones is not considered and truncation artifacts may occur due to the limited transaxial field-of-view of the MR/PET scanner (particularly of the upper limbs). The compensation for these artifacts is currently a matter of ongoing research. Moreover, it can be anticipated that different sequences for attenuation correction will be used in specific areas of the body. For the head e.g., bone probably cannot be neglected completely for truly accurate AC, especially for the skull base. Therefore in this region, the application of ultrashort TE (UTE) sequences might be favourable, which allows for delineation of the bone, thus leading to more exact attenuation maps (μ -maps) as compared to the Dixon imaging approach.

2. Anatomical allocation of PET-findings

The low dose CT scan of the whole body as acquired in conventional PET/CT provides limited diagnostic information but it allows a rough anatomical allocation of suspect PET-findings with sufficient reliability in many cases. For precise attribution diagnostic contrast-enhanced CT scans can be acquired in very short time and provide excellent anatomical information. By contrast, MR-sequences can be comparably slow and it may not be feasible to always acquire whole-body MR-information with high resolution in due time. However, it seems likely that the Dixon-sequences used for attenuation correction of the PET-data also can be used for anatomical allocation of PET-findings with very satisfying results. These whole-body images can then be complemented by added high-resolution MR-sequences in particular regions of interest.

3. MR-specific diagnostic limitations

It is expected that MR/PET will be inferior to PET/CT for indications which are commonly addressed with better diagnostic value by CT, e.g. small pulmonary lesions. It remains to be evaluated for which indications MR/PET is superior or equal to PET/CT and for which indications PET/CT will remain the method of choice.

4. Workflow

The high costs for this type of imaging instrumentation will require elaborate logistics regarding patient flow, occupancy of the scanner, selection of examination procedures etc., to assure efficient utilization of the scanner. The combined acquisition of MR and PET information defines the need for specially educated medical personnel experienced with both modalities.

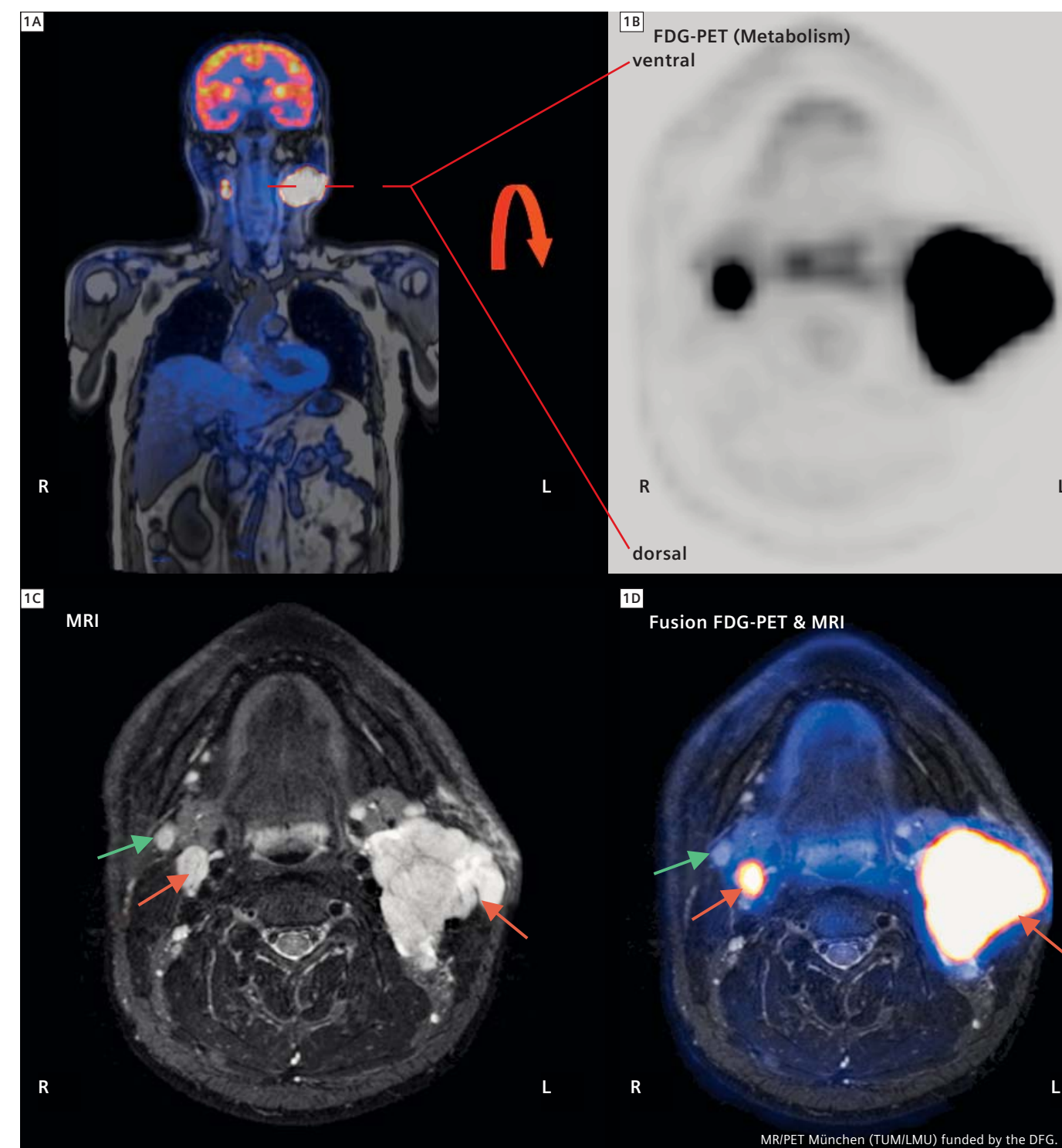
5. Design of suitable imaging protocols

The large number of available MR-sequences and of different PET-tracers exponentiates the number of potential combinations of imaging tests. This will define the need to develop optimized imaging algorithms for specific diagnostic questions, which ensure the selection of the most beneficial combinations.

Examples for clinical applications

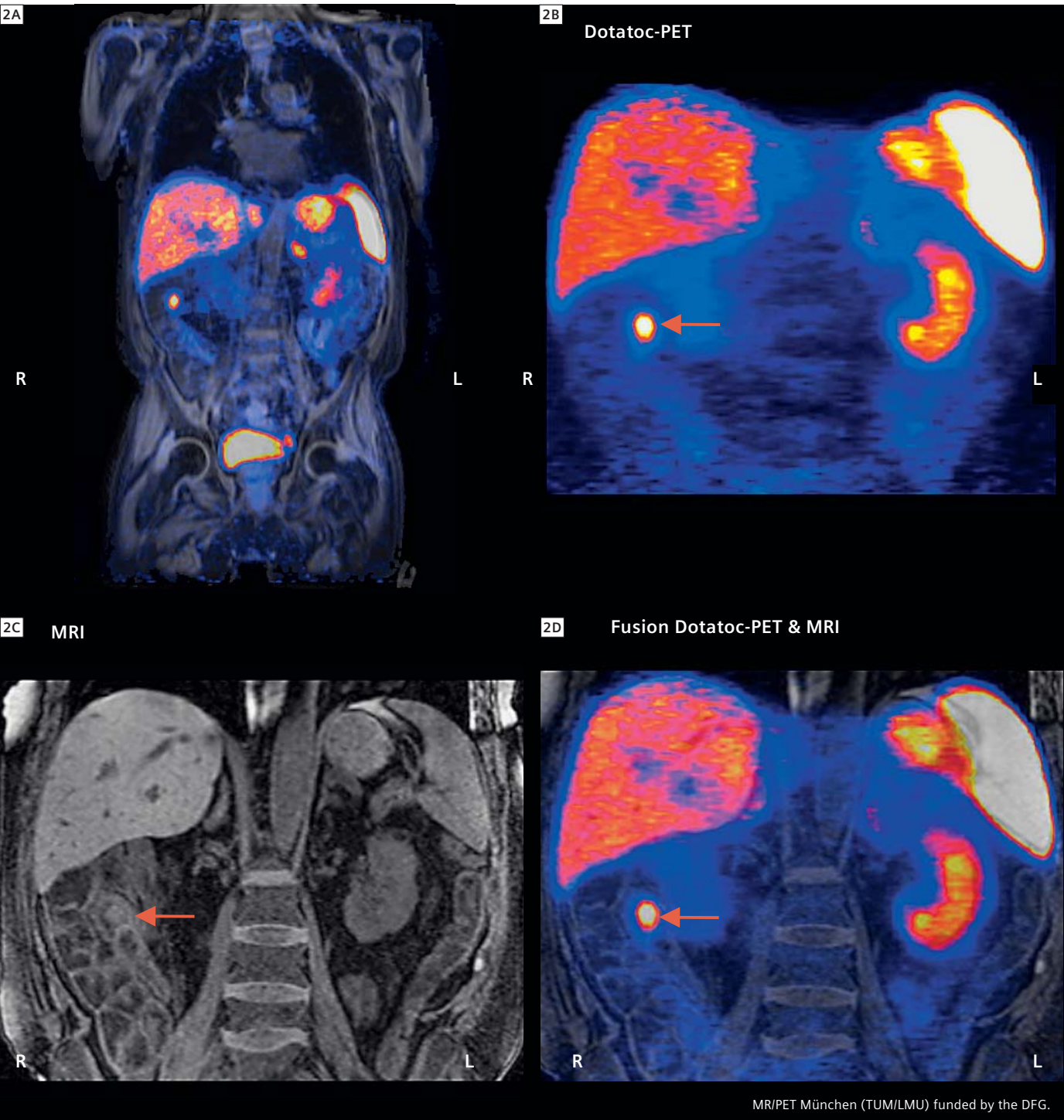
1. Oncology

Case 1 Patient with a cervical Non-Hodgkin lymphoma.



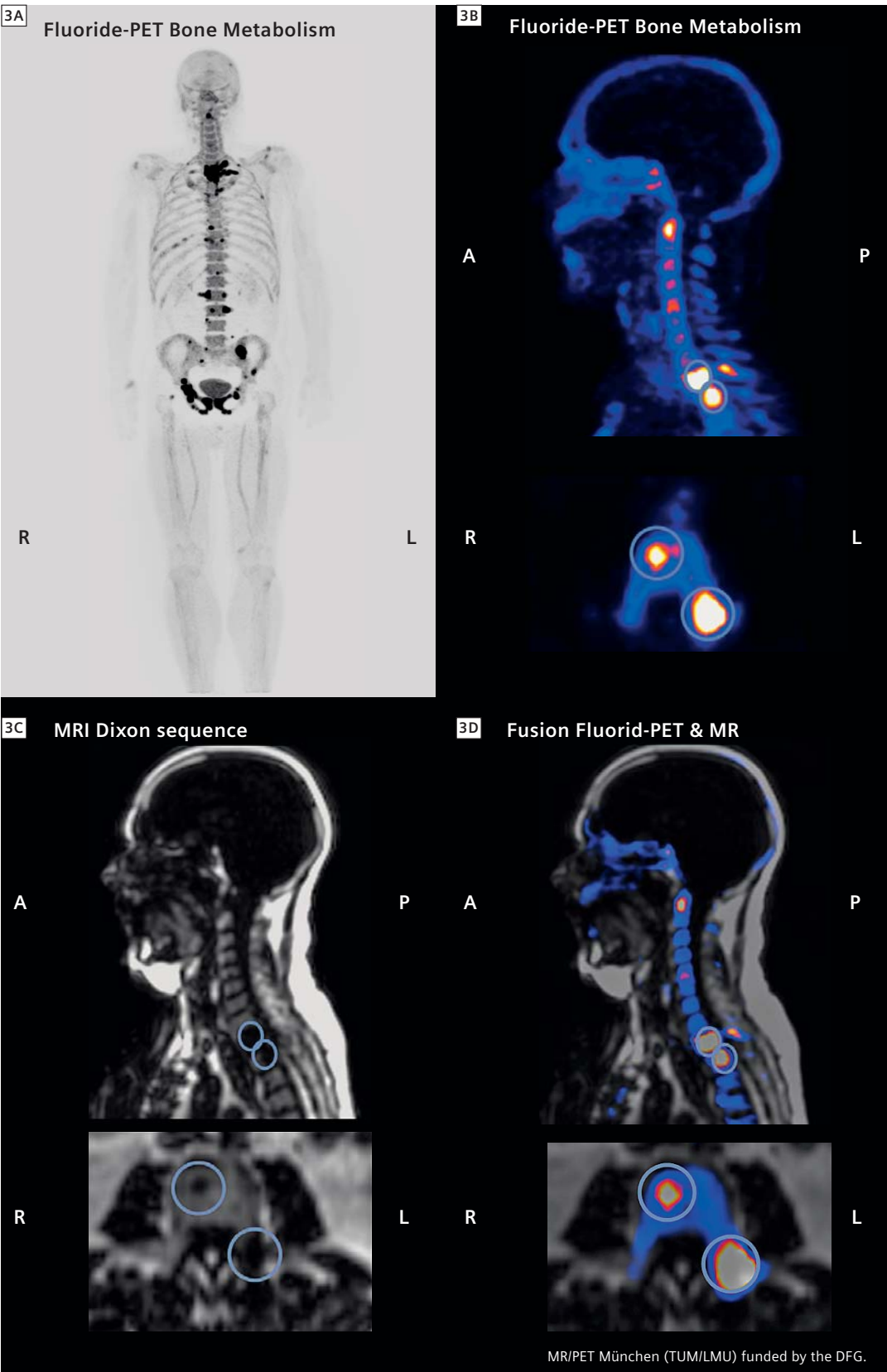
1 A: Overview using the opposed phase of the MR AC Dixon sequence. B: Axial slice of the ^{18}F -FDG-PET image, demonstrating tumor-suspect increased metabolism in two lesions (left and the right lateral). C: Axial MRI (STIR sequence) demonstrating the high tissue contrast. Several cervical lymph nodes are apparent, some enlarged. D: Overlay of PET and MRI, easily tumor-typical (red arrows) and non tumor-typical findings (green arrow) can be identified and allocated anatomically.

Case 2 Patient with a Neuroendocrine tumor.



2 A: Overview using the water image of the MR AC Dixon sequence. Note the area of intense focal tracer uptake in the right upper quadrant of the abdomen, projecting on the region of the terminal ilium. There is a small bladder diverticulum of the left lateral bladder wall with tracer retention as accidental finding. B: PET-findings with ⁶⁸Ga-DOTATOC, a tracer binding to somatostatine-receptors which are expressed frequently on neuroendocrine tumors. An intense focal tracer-uptake can be found in the abdomen. C: MR-image, fat-suppressed coronal T1w breathhold VIBE sequence. D: Fusion of PET and MR-findings. An excellent identification and anatomical allocation of the tumor is possible by combination of PET and MRI findings. No additional suspect lesions are apparent.

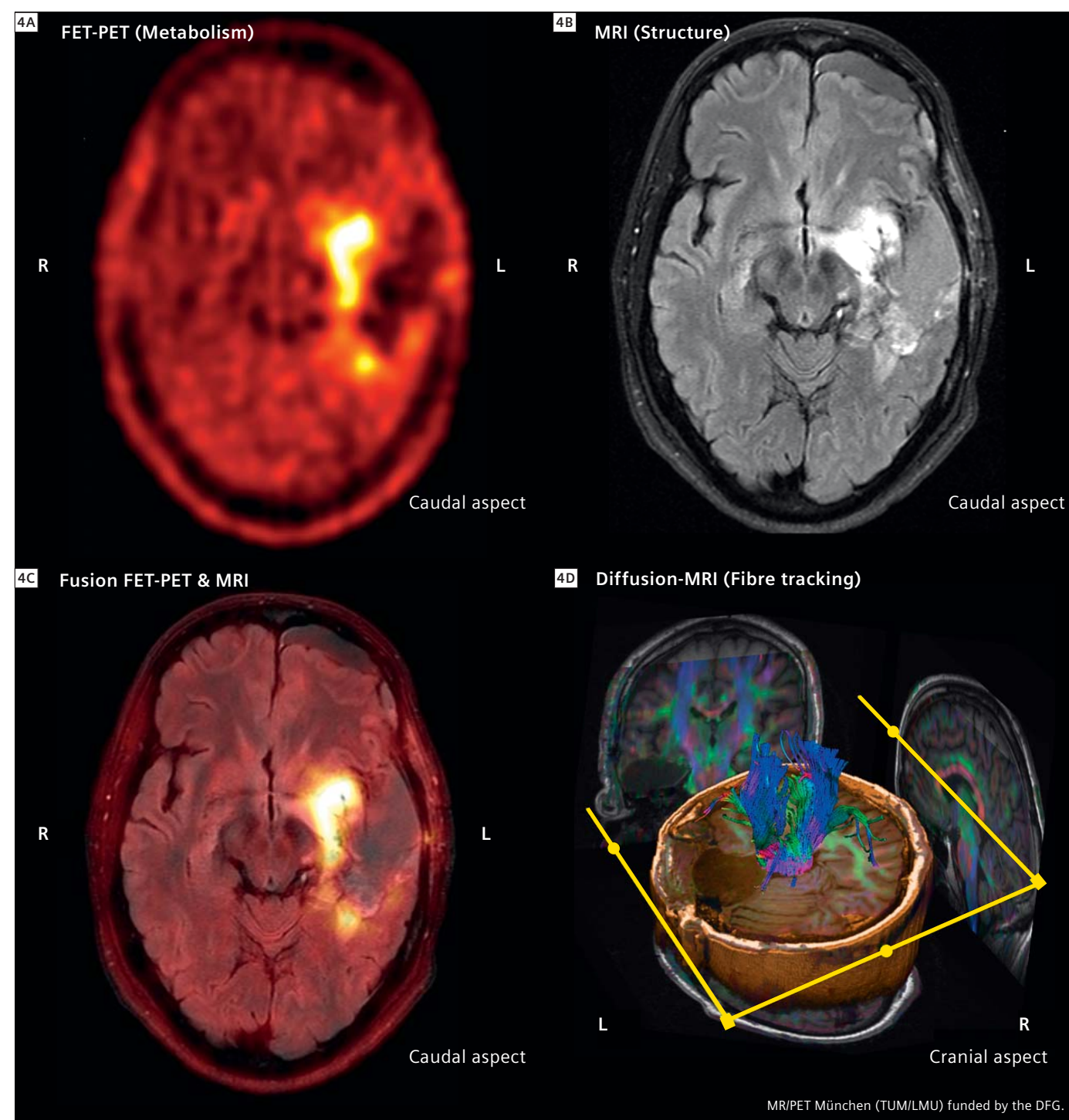
Case 3 Patient with bone metastases of a prostate cancer.



3 A: Overview of the ¹⁸F-Fluoride PET scan. B: PET-findings. C: MR-image, sagittal fat-weighted MR AC Dixon sequence. D: Fusion of PET and MR-findings. Upper row: sagittal slices, Lower row: axial slices. The Fluoride-PET scan shows a number of suspect lesions in the skeleton, likely corresponding to bone metastases of the prostate-cancer. On the MR- and the fusion-images it is apparent that in the region of the increased PET-tracer uptake, displacement of the bone marrow has occurred, underlining the suspicion of bone metastases.

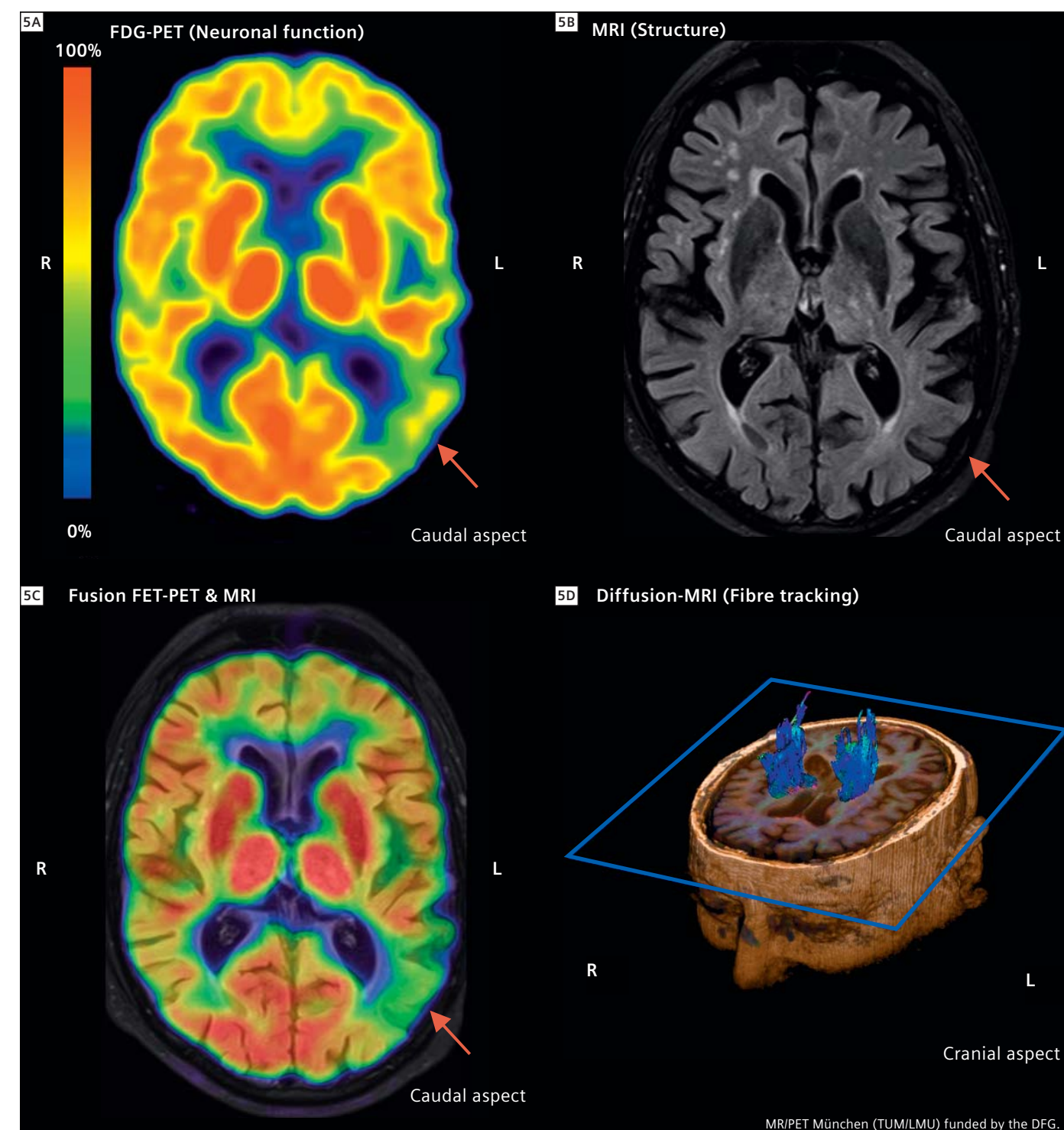
2. Neurology

Case 4 Patient with a glioblastoma multiforme.



4 **A:** ^{18}F -FET PET scan. The tracer FET represents a measure of the amino acid metabolism and allows the sensitive identification of brain tumor tissue which is characterized by high amino acid turnover, in contrast to healthy brain tissue. A strong tracer uptake is visible around a previous resection area, suspect for remaining/recurrent brain tumor tissue. **B:** MR-image, axial FLAIR-sequence, demonstrating a region of hyper intensity around the area of resection, potentially representing edema and/or gliosis, but also vital tumor tissue cannot be excluded. Moreover, a left frontopolar hygroma is seen. **C:** Fusion of PET and MR-findings, allowing excellent anatomical allocation of the vital tumor tissue in reference to anatomical structures and abnormalities in the MR-image. **D:** Fibre-tracking based on a diffusion-tensor MR dataset, demonstrating the course of neuronal axons alongside the resection area.

Case 5 Patient with Alzheimer's disease.



5 **A:** ^{18}F -FDG-PET of the brain, which represents a measure of neuronal function. Areas with reduced neuronal function in consequence of ongoing neurodegenerative processes are displayed in green-yellow (left temporoparietal cortex, see red arrow), healthy brain regions in orange-red. **B:** MR-image, axial FLAIR-sequence. Brain anatomy can be displayed in high resolution, cerebral atrophy is apparent in widespread regions, predominantly on the left side. **C:** In the MR/PET fusion regional allocation of hypometabolism and brain substance loss is possible. **D:** Fibre-tracking based on a diffusion-tensor MR dataset, demonstrating the course of neuronal axons in the brain of the patient.

- First clinical imaging studies demonstrate successful clinical applicability of integrated whole body MR/PET.
- Attenuation correction of the PET signal using appropriate MR-derived attenuation maps appears to be feasible with sufficient reliability for most cases. Some problems (lack of accurate bone-detection, truncation artifacts) are a matter of ongoing research.
- From a diagnostic perspective, superiority of MR/PET compared to PET/CT can be foreseen for indications/body regions, which would preferably be approached by MRI rather than by CT, due to the superior soft tissue contrast of MRI. Examples are:
 - Oncology:** Head and neck tumors, masses in the pelvis/abdomen (e.g. prostate cancer), carcinoma of unknown primary, whole-body imaging
 - Neurology:** Brain tumors, epilepsy, dementia, stroke
 - Cardiology:** Regional function (wall motion) and scar detection (late enhancement) versus myocardial perfusion and tissue viability
- It remains to be evaluated for which indications MR/PET is superior or equal

- to PET/CT and for which indications PET/CT will remain the method of choice. MR/PET will probably be inferior to PET/CT for indications which are commonly addressed with better diagnostic value by CT, e.g. pulmonary lesions.
- The expected high costs for this type of imaging procedure will require elaborate logistics regarding patient flow, examination procedures, occupancy of the scanner etc., to ensure efficient utilization.
- The large number of available MR-sequences and of different PET-tracers exponentiates the number of potential combinations of imaging tests. This will define the need to develop optimized imaging algorithms for specific diagnostic questions.

- 1 Catana, C., et al., MRI-assisted PET motion correction for neurologic studies in an integrated MR-PET scanner. *J Nucl Med.* 52(1): p. 154-61.
- 2 Catana, C., et al., Toward implementing an MRI-based PET attenuation-correction method for neurologic studies on the MR-PET brain prototype. *J Nucl Med.* 51(9): p. 1431-8.
- 3 Herzog, H., et al., High resolution BrainPET combined with simultaneous MRI. *Nuklearmedizin.* 50(2).
- 4 Schlemmer, H.P., et al., Simultaneous MR/PET

Alexander Drzegza, MD
Technische Universität München
Klinik und Poliklinik für Nuklearmedizin
Klinikum rechts der Isar
Ismaninger Str. 22
D-81675 Munich
Germany
phone: +49 89 4140 7722
a.drzegza@lrz.tum.de

- 5 Beer, A.J., et al., Radionuclide and hybrid imaging of recurrent prostate cancer. *Lancet Oncol.* 12(2): p. 181-91.
- 6 Metz S, Ganter C, Lorenzen S, van Marwick S, Herrmann K, Lordick F, Nekolla SG, Rummeny EJ, Wester HJ, Brix G, Schwaiger M, Beer AJ. Phenotyping of tumor biology in patients by multimodality multiparametric imaging: relationship of microcirculation, alphavbeta3 expression, and glucose metabolism. *J Nucl Med.* 2010 Nov; 51(11):1691-8. Epub 2010 Oct 18.
- 7 Drzezga A, Becker AJ, Van Dijk K, Sreenivasan A, Talukdar T, Sullivan C, Schultz AP, Sepulcre J, Putcha D, Greve D, Johnson KA, Sperling RA. Neuronal dysfunction and disconnection of cortical hubs in non-demented subjects with elevated amyloid-burden. *Brain.* 2011, in press.
- 8 Martinez-Moller, A., et al., Tissue classification as a potential approach for attenuation correction in whole-body PET/MRI: evaluation with PET/CT data. *J Nucl Med.* 2009. 50(4): p. 520-6.

[illegible]

For the whole range of clinical MR information
visit us at
www.siemens.com/magnetom-world



The 7th MAGNETOM World Summit took place in Shenzhen, China.

Clinical Perspective of the MAGNETOM World Summit

Matthias P. Lichy, MD, M.Sc.

Siemens Healthcare, Erlangen, Germany

It is crucial to understand clinical needs and opportunities of new imaging technologies to answer the questions of referring clinicians and therefore to provide best patient care. The exchange of knowledge about existing and upcoming technologies, clinical demands and how we as radiologists and industry can answer these demands is at the heart of the MAGNETOM World Summit, organized by Siemens Healthcare MR.

The following limited overview highlights some of the clinical perspectives discussed at the 7th MAGNETOM World Summit in Shenzhen, China.

Diffusion-weighted MRI (DWI) outside the brain is probably – from a clinical perspective – the most emerging imaging technique within the last years in the field of MRI. Initially intended to improve the detection of suspicious lesions, it was soon used to provide PET-like images with MRI. But with further evolution of sequence techniques and in combination with new coils [1] and parallel imaging [2], DWI can now easily be applied in clinical routine as a real whole-body imaging modality. It can also be used to quantify restriction of diffusion and provides therefore important information for therapy assessment

in a variety of malignancies [3]. In combination with other imaging modalities, DWI can assist in identifying suspicious lesions and therefore potentially increase the sensitivity of these imaging approaches [4]. For the detection of prostate cancer within the gland, in particular, integration of DWI including the calculation of the ADC (apparent diffusion coefficient) value has now to be regarded as clinical standard [5, 6].

References

- [1] Daniel K. Sodickson. Parallel imaging.
- [2] Jürgen Hennig. High density coils and Tim4G.
- [3] Anwar Padhani. Why and when to use diffusion-weighted imaging outside the brain.
- [4] Jelle Barentsz. Lymph node imaging with MR.

[5] Heinz-Peter Schlemmer. Prostate cancer – when MRI should be used.

[6] Anwar Padhani. Prostate cancer – state-of-the-art imaging techniques.

Clinical indications, **comparability and standardization of MR protocols** and the resultant quality of care was one of main topics discussed, ranging from pediatric imaging [7–10], oncology (the imaging of breast cancer with MRI [11–13]) to dementia and vascular diseases [14–16].

References

- [7] Michael Ditchfield. Imaging of the young brain – which technique for which referral?
- [8] Michael Ditchfield. Why, when and how to image joints in childhood.
- [9] Charuta Dagia. Staging and therapy follow-up of malignancies in childhood.
- [10] Jeannette Schulz-Menger. Imaging of the young heart – the role of MRI in congenital cardiac malformations.
- [11] Gladis Lo. When should MRI of the breast be the standard?
- [12] Mitsuhiro Tozaki. DWI and MR spectroscopy of the breast.
- [13] Mitsuhiro Tozaki. MRI biopsy of the breast – indications and techniques.
- [14] Li Kun-Cheng. MR imaging of the ischemic brain.
- [15] Alma Gregory Sorensen. Imaging of dementia – when MR beats molecular imaging.
- [16] Feng Xia-Yuan. Imaging brain tumors – a necessity to combine morphology with function.

The value of **cardiovascular MRI** is already well recognized. However, especially for elderly patients with potentially impaired physiological capabilities, the appropriate selection of imaging protocols and realization of stress cardiac exams in a realistic and tolerable examination time and the implementation of low-dosage or even contrast-media free MR angiography are challenges in clinical routine and were therefore covered in detail [17–22].

References

- [17] Jens Vogel-Claussen. Imaging of the heart – the role of MRI compared to ultrasound and molecular imaging.
- [18] Jens Vogel-Claussen. Heart perfusion – when should I stress the heart?
- [19] Russel Bull. Increasing productivity with the Cardiac Dot Engine – the Bournemouth experience.
- [20] Li Kung-Cheng. Coronary MRA at 3T.
- [21] Henrik Michaely. Low dose and large field-of-view MR angiography.
- [22] James C. Carr. Non-contrast enhanced MR angiography – when contrast matters.



The MAGNETOM World Summit is a valuable source of detailed information about clinical applications and upcoming developments. The talks given at the MAGNETOM World Summit and additional, clinically relevant information is available online at www.siemens.com/magnetom-world.

For an **optimal clinical application of MRI** it is also important to optimally utilize already existing technologies. This makes a clinically relevant difference in diagnoses as demonstrated for liver imaging [23–24] including dynamic scans; and for emerging indications like imaging of rheumatism [25] and peripheral nerves [26, 27].

References

- [23] Puneet Sharma. T1w liver dynamics.
- [23] Jeong-Min Lee. Imaging of the liver and the biliary system with MR.
- [24] Zheng Meng-Su. SWI of the liver – clinical applications.
- [25] John A. Carrino. Imaging of rheumatoid arthritis.
- [26] Meng Quan-Fei. Peripheral nerve imaging from head to toe: role of 3D high resolution DW MRI.
- [27] Mirko Pham. Imaging of peripheral nerves – status quo.

It is not the purpose of this short article to summarize the 7th MAGNETOM World Summit in detail but to show the clinical perspective behind all our conjoined efforts. **Education** plays an important role at each MAGNETOM World Summit. The last Summit not only covered clinical topics such as MR arthrography or

whole-spine imaging [28, 29] but provided a deeper scientific insight into MR technologies like ultra high-field (UHF) [30, 31], pharmacokinetic modelling [32] and MR/PET [33]. These technologies will certainly change our clinical perspective of MRI.

References

- [28] Marco Zanetti. When do I need an arthrogram?
- [29] Marco Zanetti. Whole spine imaging – when is it a clinical must?
- [30] Daniel K. Sodickson. 7T MRI-technology.
- [31] Zang-Hee Cho. Clinical impact of 7T MRI.
- [32] Bernd Pichler. MR-PET-technology

The 8th MAGNETOM World Summit will take place in the USA in 2012. Once details are available we will announce them at: www.siemens.com/magnetom-world

Contact

Matthias Lichy, MD, MSc
Siemens AG
H IM MR MK O AW
Allee am Roethelheimpark 2
D-91052 Erlangen
Germany
matthias.lichy@siemens.com



→ This Quick Response code is your direct link to the clinical talks at www.siemens.com/magnetom-world > Education > e-trainings & Presentations.

Siemens Healthcare Publications

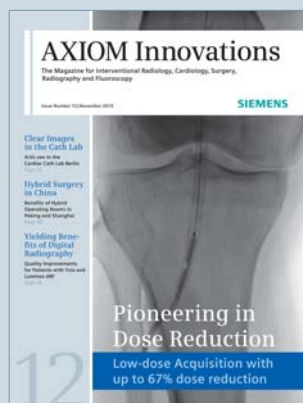
Our publications offer the latest information and background for every healthcare field. From the hospital director to the radiological assistant – here, you can quickly find information relevant to your needs.



Medical Solutions
Innovations and trends in healthcare. The magazine is designed especially for members of hospital management, administration personnel, and heads of medical departments.



eNews
Register for the global Siemens Healthcare News-letter at www.siemens.com/healthcare-eNews to receive monthly updates on topics that interest you.



AXIOM Innovations
Everything from the worlds of interventional radiology, cardiology, fluoroscopy, and radiography. This semi-annual magazine is primarily designed for physicians, physicists, researchers, and medical technical personnel.



MAGNETOM Flash
Everything from the world of magnetic resonance imaging. The magazine presents case reports, technology, product news, and application tips. It is primarily designed for physicians, physicists, and medical technical personnel.



SOMATOM Sessions
Everything from the world of computed tomography. With its innovations, clinical applications, and visions, this semiannual magazine is primarily designed for physicians, physicists, researchers, and medical technical personnel.

For current and past issues and to order the magazines, please visit www.siemens.com/healthcare-magazine.

Cover



Simultaneous MR/PET examination of a male patient with large cortical defect after stroke event. In addition, multiple lymph node filiae of an advanced oropharynxcarcinoma can be seen. This image consists of three data sets, which were superimposed: inverted sagittal T2-weighted turbo spin echo (TSE) MR image, time-of-flight MR angiography (TOF MRA) and the simultaneously acquired PET (^{18}F -FDG) data.

Contact

Dr. Nina Schwenzer, MD
University of Tuebingen
Department of Diagnostic and Interventional Radiology
Hoppe-Seyler-Str. 3
72076 Tuebingen
Germany
nina.schwenzer@med.uni-tuebingen.de

MAGNETOM Flash – Imprint
© 2011 by Siemens AG, Berlin and Munich,
All Rights Reserved

Publisher:

Siemens AG
Medical Solutions
Business Unit Magnetic Resonance,
Karl-Schall-Straße 6, D-91052 Erlangen,
Germany

Editor-in-Chief: PD Dr. Matthias Lichy, MD
(matthias.lichy@siemens.com)

Associate Editor: Antje Hellwich
(antje.hellwich@siemens.com)

Editorial Board: Christiane Bernhardt;
Peter Kreisler, PhD; Wellesley Were;
Milind Dhamankar, MD; Michelle Kessler;
Gary McNeal; Sunil Kumar, MD

Production: Norbert Moser, Siemens AG,
Medical Solutions

Layout: independent Medien-Design
Widenmayerstrasse 16, D-80538 Munich

Printers: Farbendruck Hofmann, Gewerbestraße 5,
D-90579 Langenzenn, Printed in Germany

**MAGNETOM Flash is also available
on the internet:**

www.siemens.com/magnetom-world

Note in accordance with § 33 Para. 1 of the
German Federal Data Protection Law: Despatch is
made using an address file which is maintained
with the aid of an automated data processing
system.

MAGNETOM Flash with a total circulation of
20,000 copies is sent free of charge to Siemens
MR customers, qualified physicians, technolo-
gists, physicists and radiology departments
throughout the world. It includes reports in the
English language on magnetic resonance:
diagnostic and therapeutic methods and their
application as well as results and experience
gained with corresponding systems and solu-
tions. It introduces from case to case new
principles and procedures and discusses their
clinical potential.

The statements and views of the authors in
the individual contributions do not necessarily
reflect the opinion of the publisher.

The information presented in these articles and
case reports is for illustration only and is not
intended to be relied upon by the reader for
instruction as to the practice of medicine. Any
health care practitioner reading this information
is reminded that they must use their own learn-
ing, training and expertise in dealing with their
individual patients. This material does not substi-
tute for that duty and is not intended by Siemens
Medical Solutions to be used for any purpose
in that regard. The drugs and doses mentioned

herein are consistent with the approval labeling
for uses and/or indications of the drug. The treat-
ing physician bears the sole responsibility for the
diagnosis and treatment of patients, including
drugs and doses prescribed in connection with
such use. The Operating Instructions must always
be strictly followed when operating the MR
system. The sources for the technical data are the
corresponding data sheets. Results may vary.
Partial reproduction in printed form of individual
contributions is permitted, provided the custom-
ary bibliographical data such as author's name
and title of the contribution as well as year, issue
number and pages of MAGNETOM Flash are
named, but the editors request that two copies be
sent to them. The written consent of the authors
and publisher is required for the complete reprint-
ing of an article.

We welcome your questions and comments about
the editorial content of MAGNETOM Flash. Please
contact us at magnetomworld.med@siemens.com.
Manuscripts as well as suggestions, proposals
and information are always welcome; they are
carefully examined and submitted to the editorial
board for attention. MAGNETOM Flash is not
responsible for loss, damage, or any other injury
to unsolicited manuscripts or other materials.
We reserve the right to edit for clarity, accuracy,
and space. Include your name, address, and
phone number and send to the editors, address
above.

MAGNETOM Flash

The Magazine of MR

Issue Number 1/2011
ISMRM Edition
Not for distribution in the US.

SIEMENS

Technology

Towards Clinical 7T MRI
Page 32

Clinical

MRI of the Lung
Page 6

MAGNETOM Skyra: The
Mannheim Perspective
Page 24

Snowboarding Injuries
to the Middle Subtalar
Joint
Page 60

Integrated Whole-Body
MR/PET Imaging
Page 102

How I do it

FAQs on Diffusion-
Weighted Imaging
Page 84



Please enter your business address

Institution

Department

Function

Title

Name

Street

Postal Code

City

State

Country

MR system used

Please include me in your mailing list for the
following Siemens Healthcare customer magazine(s):

☐ Medical Solutions

☐ MAGNETOM Flash

☐ SOMATOM Sessions

☐ AXIOM Innovations

Stay up to date with the latest information
Register for:

☐ the monthly e-Newsletter

E-mail

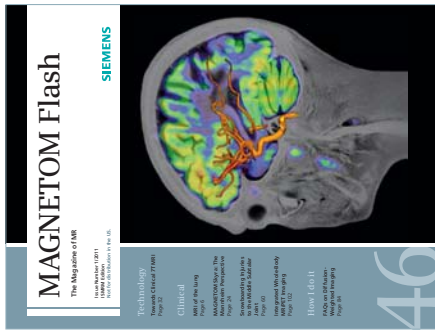
Please print clearly!

☐ Yes, I consent to the above information being used
for future contact regarding product updates and other
important news from Siemens.

☐ unsubscribe from info service

46

MAGNETOM Flash



Siemens AG
Medical Solutions
Magnetic Resonance
Antje Hellwich - Marketing
P.O. Box 32 60
D-91050 Erlangen
Germany



→ Visit www.siemens.com/magnetom-world
for case reports,
clinical methods,
application tips,
talks and much more
clinical information.

SUBSCRIBE NOW!

– and get your free copy of future
MAGNETOM Flash! Interesting information from
the world of magnetic resonance – gratis to your
desk. Send us this postcard, or subscribe online at
www.siemens.com/MAGNETOM-World

Global Siemens Headquarters

Siemens AG
Wittelsbacherplatz 2
80333 Muenchen
Germany

Global Siemens Healthcare Headquarters

Siemens AG
Healthcare Sector
Henkestr. 127
91052 Erlangen
Germany
Phone: +49 9131 84-0
www.siemens.com/healthcare

www.siemens.com/healthcare-magazine

Order No. A91MR-1000-81C-7600 | Printed in Germany | CC MR 01000 ZS 041120. | © 04.11, Siemens AG

On account of certain regional limitations of sales rights and service availability, we cannot guarantee that all products included in this brochure are available through the Siemens sales organization worldwide. Availability and packaging may vary by country and is subject to change without prior notice. Some/All of the features and products described herein may not be available in the United States.

The information in this document contains general technical descriptions of specifications and options as well as standard and optional features which do not always have to be present in individual cases.

Siemens reserves the right to modify the design, packaging, specifications and options described herein without prior notice.
Please contact your local Siemens sales representative for the most current information.

Note: Any technical data contained in this document may vary within defined tolerances. Original images always lose a certain amount of detail when reproduced.

Global Business Unit

Siemens AG
Medical Solutions
Magnetic Resonance
Henkestr. 127
DE-91052 Erlangen
Germany
Phone: +49 9131 84-0
www.siemens.com/healthcare

Local Contact Information

In Asia

Siemens Pte Ltd
The Siemens Center
60 MacPherson Road
Singapore 348615
Phone: +65 6490-8096

In Canada

Siemens Canada Limited
Medical Solutions
2185 Derry Road West
Mississauga ON L5N 7A6
Canada
Phone: +1 905 819-5800

Europe/Africa/Middle East

Siemens AG
Medical Solutions
Henkestr. 127
91052 Erlangen
Germany
Phone: +49 9131 84-0

Latin America

Siemens S.A.
Medical Solutions
Avenida de Pte. Julio A. Roca No 516,
Piso 7
C1067ABN Buenos Aires
Argentina
Phone: +54 11 4340-8400

USA:

Siemens Medical Solutions U.S.A., Inc.
51 Valley Stream Parkway
Malvern, PA 19355-1406
USA
Phone: +1-888-826-9702